Electrodeposition of Zinc Oxide Nanostructured Films

By

Benoit Illy

A Thesis Submitted in Fulfilment of the Requirements for the Degree of Doctor of Philosophy of Imperial College London

Imperial College London

Department of Materials

November 2009

Foreword

This work forms the written component of the research undertaken in the period July 2005 to June 2008, to full the requirements of the Imperial College PhD degree. The work presented in this thesis has also been published in the following publications. Others are in preparation or are planned.

- **Direct observation of distinct nucleation and growth processes in electrochemically deposited ZnO nanostructures using in situ XANES** Ingham, B; Illy, BN; Ryan, MP, Journal of Physical Chemistry C, 112, 8, 2820-2824
- **In situ synchrotron studies of ZnO nanostructures during electrochemical deposition** Ingham, B; Illy, BN; Ryan, MP, Current Applied Physics, 8, 3-4, 455-458, (2008)
- **In situ synchrotron X-ray diffraction experiments on electrochemically deposited ZnO nanostructures,** Ingham, B; Illy, BN; Toney, MF, Ryan, M.P., Journal of Physical Chemistry C, 112, 38, 14863-14866, 2008

Conference Abstracts

- ***In-situ*** **Synchrotron X-ray Absorption Studies of Electrochenically Deposited ZnO Nanostructures** Illy BN, Ingham B, Ryan MP, 5th Spring Meeting of the International Society of Electrochemistry, Nanostructured Materials in Electrochemistry: Biosciences and Molecular Electronics Applications, P-135 (2007)

Acknowledgements

Firstly I would like to thank my supervisor Dr M.P. Ryan for the support, enthusiasm and encouragement she has given me during the course of my PhD. It has been a privilege to work with her and to learn from her. She also gave me the invaluable opportunity to work and learn from a wide range of exceptional people in so many different places of the world. I apologise in advance if I fail to mention some of them.

I am very grateful to Dr B. Ingham for her training, her help and her efficiency during the synchrotron experiments and the analyse of the results.

Thank to Dr. M. Toney; the synchrotron X-ray diffraction work in this thesis would not have been possible without his knowledge and practical experience. Thank to Pr. H. S. Isaacs for all his help during experiments at Brookhaven as well as Dr R. Huang, Mr K. Suter and Mr. L. Fareria.

I would like to thank also all the members of Industrial Research Limited I had the opportunity to meet for sharing their knowledge and their warm welcome in New Zealand, particularly Dr. S.C. Hendy. Thanks to the Foundation for Research, Science and Technology for funding this project.

There are many people I would like to thank from Imperial College. Thanks to Mr. N. Royall, Dr M. Ardakani, Mr R. Chater and Mr R. Sweeney for their assistance on experimental work at Imperial College. I would also like to thank all the past and present members of the Dr. Ryan, Professor McComb, Dr. Riley, Dr Heutz and Dr McLachlan research groups for their fruitful discussions and friendship.

I would like to give a big thanks to all the friends I had the chance to make in London and the ones I left in France for their support, happiness and joy.

Finally, I would like to thank my family for all their support and love during my studies and for encouraging me to do what I want to do.

Abbreviations

1-D	one dimensional
2-D	two dimensional
3-D	three dimensional
Ag/AgCl	silver/silver chloride reference electrode
at%	atomic per cent
BCF	Bessel-Cabrera-Frank
BSE	back-scattered electrons
CBD	chemical bath deposition
CV	cyclic voltammetry
DMS	dilute magnetic semiconductors
EDS	energy dispersive X-ray spectroscopy
EXAFS	extended X-ray absorption fine structure
fcc	face-centred cubic
FESEM	field emission scanning electron microscope
FET	field effect transistor
FWHM	full width at half maximum
GIXS	grazing incidence X-ray scattering
KSV	Kossel-Stranski-Volmer
LED	light-emitting diode
PL	photoluminescence
UV	ultraviolet
VLS	vapour-liquid-solid
VS	vapour–solid
wt%	weight per cent
XANES	X-ray absorption near-edge structure
XAS	X-ray absorption spectroscopy

XRD	X-ray diffraction

Abstract

ZnO nanostructures have great promise in a wide range of applications such as sensors, optoelectronics, piezoelectronics, healthcare. Preparation of oxide films by electrodeposition from aqueous solution presents several advantages over other techniques such as controlling the rate and morphology through several well-defined parameters (electrode potential, current, temperature, pH, etc.), the fact that electrolytic processing is a well-established technology and readily scalable for production, and the non-equilibrium nature of the electrochemical interface often gives rise to morphologies and compositions not attainable through other, usually high-temperature, routes. Despite a large amount of research in this area the detailed mechanism of nucleation and growth is still controversial. Only a good understanding of it will allow the expected industrial applications to be achieved. One of the main difficulties to overcome is that tiny amounts of material are involved and the required in-situ measurements are thus very delicate. The ability of synchrotron radiation to probe material structure during deposition makes it the ideal tool for the study of nucleation and growth of these materials as a function of the processing parameters.

Here we will present two synchrotron-based approaches involving both X-ray absorption and scattering. The first method, together with ex-situ characterisation, provides detailed information about how the kinetics of the growth and/or dissolution is influenced by the electrochemical parameters. The effect of time, potential, zinc ions concentration, oxygen precursor, temperature and electrolyte composition have been studied. Following this understanding of the influence of the parameters, films of desired structure can be synthesised and new structures have been made.

Beside the electrochemical parameters, the growth of the film is influenced by the interaction with substrate in the early stage of nucleation. The second synchrotron technique allows the direct observation of the development of the crystal orientation of

the films during the deposition. It gives promising results to study how the substrate influences the growth and thus the properties of the films.

1 Table of Contents

Acknowledgements 5
Abbreviations 7
Abstract 9
1 Table of Contents 11
2 Table of Figures 17
3 Introduction 25
3.1 Nanotechnology 26
3.2 Properties of ZnO 26
3.2.1 Electrical Properties 26
3.2.2 Optical Properties 27
3.2.3 Crystal Structure 27
3.2.4 Nanostructures 28
3.2.5 Piezoelectricity 29
3.3 Applications 30
3.3.1 Piezoelectricity Applications 30
3.3.2 Photovoltaic (PV) Applications 30
3.3.3 Light-Emitting Diodes (LEDs) 31
3.3.4 Sensing 31
3.3.5 Dilute Magnetic Semiconductors (DMS) 33
3.3.6 Medical Applications 33
3.3.7 Others Applications 34
3.4 Synthesis and Fabrication 34
3.4.1 Vapour Phase Growth 34
3.4.1.1 Vapour-Liquid-Solid Mechanism (VLS) 35
3.4.1.2 Vapour–Solid Mechanism (VS) 35
3.4.2 Solution Processes 35
3.4.2.1 Chemical Bath Deposition (CBD) 35

3.4.2.2 Sol-Gel Method 36
3.4.2.3 Solvothermal Reaction 36
3.5 Electrodepositon 36
4 Literature Review 39
4.1 Electrocrystallisation Process of ZnO 40
4.1.1 Principles of the cathodic electrodeposition 40
4.1.2 Nucleation and Growth 40
4.2 Thermochemical Calculations 44
4.3 Effect of the Deposition Parameters 46
4.3.1 Temperature 46
4.3.2 Applied Potential or Current Density 48
4.3.2.1 High Zn Precursor Concentration 49
4.3.2.2 Low Zn Precursor Concentration 49
4.3.3 Zinc Precursor Concentration 50
4.3.3.1 High Zn Precursor Concentration 50
4.3.3.2 Low Zn Precursor Concentration 51
4.3.4 Oxygen Precursor 51
3.3.4.1 Nitrate 51
3.3.4.1 Oxygen 52
4.3.4.2 Hydrogen Peroxide 52
4.3.5 Substrate 52
4.3.6 Influence of the Anions and Surfactant 53
4.4 Field of Research 54
5 Experimental 57
5.1 Electrochemistry Techniques 58
5.1.1 Experimental Set Up 58
5.1.1.1 Three-electrode Set Up 58
5.1.1.2 Preparation of the Working Electrode 59

5.1.1.3 Electrolyte 59
5.1.2 Electrochemical Methods 60
5.1.2.1 Cyclic Voltammetry (CV) 60
5.1.2.2 Electrodeposition 60
5.2 Electron Microscopy 60
5.2.1 Principle 61
5.2.2 Imaging 63
5.2.3 Energy Dispersive X-ray Spectroscopy (EDS) 63
5.3 X-ray Absorption and Diffraction Studies 63
5.3.1 Tube X-Ray Diffraction 63
5.3.2 Synchrotron Radiation 64
5.3.2.1 Synchrotron Sources 64
5.3.2.2 X-Ray Absorption Spectroscopy (XAS) 66
5.3.2.3 Grazing Incidence X-Ray Scattering (GIXS) 68
5.4 Development of *In-Situ* Characterisation Techniques 69
5.4.1 *In-Situ* X-ray Absorption 69
5.4.2 *In-Situ* Grazing Incidence X-Ray Scattering 70
6 Results and Discussion 73
6.0 Methodology of Study 73
6.1 Electrochemical Studies of the System in the Standard Conditions 75
6.1.1 Cyclic Voltammetry Studies of the Oxygen Reduction 75
6.1.2 Cyclic Voltammetry Studies of the Effect of Nitrate Anions 78
6.1.3 Summary 79
6.2 Evolution of the Films with Time: Nucleation and Growth 80
6.2.1 Microscopy 80
6.2.2 Evolution of the Current 82
6.2.3 Evolution of the Film Thickness 83
6.2.3.1 Principle of the Methods 83

6.2.3.2 Calibration of Signal 85
6.2.3.3 Validity of the Method 86
6.2.3.4 Evolution of the Nominal Thickness with Time 88
6.2.4 X-ray Diffraction 90
6.2.4.1 *Ex-Situ* Measurements 90
6.2.4.2 *In-Situ* Measurements 93
6.2.5 Summary 97
6.3 Effect of Potential 98
6.3.1 Microscopy 98
6.3.2 Electrochemical Measurements 101
6.3.3 X-Ray Diffraction 103
6.3.4 Discussion 104
6.3.5 Summary 105
6.4 Effect of the Cl^- Concentration 106
6.4.1 Microscopy 106
6.4.2 Electrochemical Measurements 107
6.4.3 X-Ray Diffraction 108
6.4.4 Discussion 110
6.4.5 Summary 110
6.5 Effect of $Zn(NO_3)_2$ Concentration 111
6.5.1 Effect of the Zinc(II) Concentration on the Solution pH. 111
6.5.2 Microscopy 112
6.5.3 Electrochemical Measurements 116
6.5.4 X-Ray Diffraction 118
6.5.5 Discussion 121
6.5.6 Summary 123
6.6 Effect of pH, Dissolution and Formation of Nanotubes 124

6.6.1 Effect of pH on the Growth 124
6.6.1.1 Microscopy 124
6.6.1.2 Electrochemical Measurements 125
6.6.1.3 X-Ray Diffraction 127
6.6.2 Dissolution and Formation of Nanotubes 129
6.6.2.1 Introduction 129
6.6.2.2 Microscopy 131
6.6.2.3 X-Ray Diffraction 136
6.6.3 Summary 136
6.7 Effect of Capping Agent 138
6.7.1 X-Ray Diffraction 139
6.7.1 Acetic Acid 141
6.7.1.1 Microscopy 141
6.7.1.2 Electrochemical Measurements 141
6.7.2 Oxalic Acid 142
6.7.2.1 Microscopy 142
6.7.2.2 Electrochemical Measurements 145
6.7.3 Citric Acid 147
6.7.3.1 Microscopy 147
6.7.3.2 Electrochemical Measurements 147
6.7.4 Summary 148
7. Conclusions and Future Work 151
7.1 Conclusions 151
7.2 Further Research and Development of this Topic 153
8. References 155
9. Appendix: 3D schematic views and technical drawings of in-situ GIXS cell 163

2 Table of Figures

FIGURE 3.1 SCHEMATIC REPRESENTATION OF THE WURTZITE ZINC OXIDE STRUCTURE. THE TOP (001) PLANE IS COMPRISED OF EITHER O^{2-} OR Zn^{2+} AND IS CHARGED. THE (1-10), (100) AND (010) PLANES ARE COMPRISED OF AN EQUAL NUMBER OF O AND ZN AND ARE THUS ELECTRICALLY NEUTRAL. 27

FIGURE 3.2 DIFFERENT ZNO NANOSTRUCTURES, FROM TOP LEFT: (A) PARTICLE, (B) ROD, (C) WIRE, (D) PLATE, (E) DENDRITE, (F) TUBE, (G) HIERARCHICAL NANOSTRUCTURE, (H) TETRAPOD, (I) RING , (J) SPRING. 29

FIGURE 3.3 SCHEMATIC DIAGRAM OF THE FORMATION OF A DIPOLE MOMENT P WHEN A STRESS F IS APPLIED TO ZnO_4 TETRAHEDRON OF THE ZNO WURTZITE STRUCTURE (AFTER 20) 30

FIGURE 4.4 SCHEMATIC DIAGRAM OF THE INCORPORATION OF AN ATOM TO A GROWTH CENTRE (FROM [105]). 41

FIGURE 4.5 DRAWING OF THE GENERAL SHAPE OF THE TRANSIENTS OBSERVED FOR ZNO ELECTRODEPOSITION AFTER [107]. I_{MAX} IS THE MAXIMUM CURRENT OBSERVED. T_{PEAK} AND I_{PEAK} ARE THE COORDINATE OF THE PEAK OF CURRENT BEFORE THE PLATEAU WHOSE VALUE IS $I_{PLATEAU}$. 43

FIGURE 4.6 THERMOCHEMICAL CALCULATIONS FROM [109] (A) EFFECT OF TEMPERATURE ON POTENTIAL–PH DIAGRAM IN THE PRESENCE OF 5MM ZN(II) AND 0.1M Cl^- AT 70°C. (B) DISTRIBUTION OF THE SOLUBLE COMPLEXES AS THE FUNCTION OF THE SOLUTION PH AT 60°C. (C) SOLUBILITY OF ZNO (PLAIN LINE) AND $Zn(OH)_2$ (DASH LINE) AT 70°C (D) EFFECT OF TEMPERATURE ON THE SOLUBILITY OF OXYGEN AT SATURATION IN WATER 45

FIGURE 4.7 NUMBER OF PUBLISHED PAPERS FROM CURRENT CONTENTS CONNECT DATA BASE AS A FUNCTION OF ZINC PRECURSOR CONCENTRATION (FROM 1996 TO 2006) 48

FIGURE 4.8 PHASE DIAGRAMS OF THE STRUCTURES OBTAINED BY ELECTRODEPOSITION FROM AN AQUEOUS ELECTROLYTE CONTAINING ONLY $Zn(NO_3)_2$, $ZnCl_2$, O_2 OR KCL AT TEMPERATURE RANGING FROM 60°C TO 80°C. THE COLOUR OF THE PICTURES BORDER INDICATED THE SOURCE OF THE IMAGES: RED[104], PURPLE[11], BLUE[121], GREEN[123], YELLOW[126], ORANGE[127], PINK[129]. 50

FIGURE 5.9 SCHEMATIC DIAGRAM OF EXPERIMENTAL SETUP, SHOWING THE ELECTROCHEMICAL CELL WITH A PT COUNTER ELECTRODE (CE), AG/AGCL REFERENCE ELECTRODE (RE), AND A GOLD COATED GLASS SLICE WHICH ACTS AS THE WORKING ELECTRODE (WE) 58

FIGURE 5.10 SCHEMATIC ILLUSTRATION OF THE ELECTRON COLUMN OF A TYPICAL SEM[178] 61

FIGURE 5.11 PHOTON AND ELECTRON EMISSIONS FROM A SAMPLE HIT WITH AN ELECTRON BEAM[178] 62

FIGURE 5.12 SYNCHROTRON RADIATION EMITTED BY A RELATIVISTIC ELECTRON TRAVELLING ALONG A CIRCULAR ORBIT. THE FORCE IS THE MAGNETIC FIELD PERPENDICULAR TO THE ORBIT. $\Sigma_X\Sigma_Y$ IS THE TRANSVERSE AREA OF THE OPTICAL SOURCE[182]. 65

FIGURE 5.13 TYPICAL X-RAY ABSORPTION SPECTRUM REALISED IN FLUORESCENCE OF AN ZNO SAMPLE DEPOSITED DURING OUR EXPERIMENTS. THE PRE-EDGE, XANES AND EXAFS REGIONS ARE SHOWED. 67

FIGURE 5.14 INCIDENT X-RAY PENETRATION DEPTH AS A FUNCTION OF INCIDENCE ANGLE A FROM [189] 68

FIGURE 5.15 SCHEMA OF THE GEOMETRY ASPECT OF GIXS FROM[189]. 69

FIGURE 5.16 SCHEMATIC PLAN AND PICTURE OF THE CELL OF THE *IN-SITU* XAS SET-UP. 70

FIGURE 5.17 SCHEMATIC SIDE VIEW AND PICTURE OF THE CELL 71

FIGURE 6.18 CV STUDIES OF THE ZN-CL-H_2O SYSTEM 0.1 M OF KCL AT 70°C (A) WITHOUT OXYGEN (BLACK CURVE) AND WITH OXYGEN (RED CURVE) (B) 5 MM $ZnCl_2$ WITHOUT OXYGEN (GREEN CURVE) AND WITH OXYGEN (BLUE CURVE). 76

FIGURE 6.19 CV STUDIES OF THE NITRATE REDUCTION IN THE ZN-CL-H_2O-NO_3 SYSTEM WITH 0.1 M OF KCL AT 70°C (A) WITHOUT OXYGEN, 5MM OF $ZnCl_2$ (BLACK CURVE) AND 5 MM OF $Zn(NO_3)_2$ (RED CURVE) ,(B) WITHOUT OXYGEN (GREEN CURVE) AND WITH OXYGEN (BLUE CURVE), (C) 5 MM $Zn(NO_3)_2$ IN PRESENCE OF OXYGEN. 78

FIGURE 6.20 FESEM CROSS-SECTION OF A SAMPLE AFTER 1 MINUTE. 5 MM OF $Zn(NO_3)_2$ AND 0.1 M OF KCL IN A OXYGENATED AQUEOUS SOLUTION AT 65°C. THE APPLIED POTENTIAL WAS -0.97 V. 80

FIGURE 6.21 STUDY OF THE EVOLUTION OF THE STRUCTURES WITH TIME: FESEM IMAGES OF ZNO NANOSTRUCTURED FILMS DEPOSITED FOR (A) 15 SECONDS, (B) 1 MINUTE, (C) 2 MINUTES, (D) 4 MINUTES, (E) 10 MINUTES AND (F) 45 MINUTES. 5 MM OF $Zn(NO_3)_2$ AND 0.1 M OF KCL IN A OXYGENATED AQUEOUS SOLUTION AT 65°C. THE APPLIED POTENTIAL WAS -0.97 V. 81

FIGURE 6.22 FESEM IMAGES OF SAMPLES AFTER 1 MINUTE (A) AND 10 MINUTES (B). 5 MM OF $Zn(NO_3)_2$ AND 0.1 M OF KCL IN A OXYGENATED AQUEOUS SOLUTION AT 65°C. THE APPLIED POTENTIAL WAS -0.97 V. 81

FIGURE 6.23 EVOLUTION OF THE NANO-STRUCTURES DIAMETER WITH TIME (FROM THE FESEM IMAGES). 5 MM OF $Zn(NO_3)_2$ AND 0.1 M OF KCL IN A OXYGENATED AQUEOUS SOLUTION AT 65°C. THE APPLIED POTENTIAL WAS -0.97 V. 82

FIGURE 6.24 CURRENT DENSITY AS A FUNCTION OF TIME. 5 MM OF $Zn(NO_3)_2$ AND 0.1 M OF KCL IN A OXYGENATED AQUEOUS SOLUTION AT 65°C. THE APPLIED POTENTIAL WAS -0.97 V. INSET : FIGURE 4.25 DRAWING OF THE GENERAL SHAPE OF THE TRANSIENTS OBSERVED FOR ZNO ELECTRODEPOSITION AFTER [107]. I_{MAX} IS THE MAXIMUM CURRENT OBSERVED. T_{PEAK} AND I_{PEAK} ARE THE COORDINATE OF THE PEAK OF CURRENT BEFORE THE PLATEAU WHOSE VALUE IS $I_{PLATEAU}$. 83

FIGURE 6.26 SYNCHROTRON XANES RECORDED DURING THE DEPOSITION OF ZNO. 5 MM OF $Zn(NO_3)_2$ AND 0.1 M OF KCL IN A OXYGENATED AQUEOUS SOLUTION AT 65°C. THE APPLIED POTENTIAL WAS -0.97 V. 84

FIGURE 6.27 SYNCHROTRON XANES RECORDED DURING THE DEPOSITION OF ZNO. IN-SET: REGION OF ENERGY CHOOSE FOR THE MEASUREMENTS. 5 MM OF $Zn(NO_3)_2$ AND 0.1 M OF KCL IN A OXYGENATED AQUEOUS SOLUTION AT 65°C. THE APPLIED POTENTIAL WAS -0.97 V 85

FIGURE 6.28 SELF-ABSORPTION CORRECTION FUNCTION FOR ZNO 88

FIGURE 6.29 NOMINAL FILM THICKNESS (T_N) OBTAINED FROM X-RAY FLUORESCENCE INTENSITY AT 9725 EV. 5 MM OF $Zn(NO_3)_2$ AND 0.1 M OF KCL IN A OXYGENATED AQUEOUS SOLUTION AT 65°C. THE APPLIED POTENTIAL WAS -0.97 V. 89

FIGURE 6.30 FARADAIC EFFICIENCY AS A FUNCTION OF TIME. 5 MM OF $Zn(NO_3)_2$ AND 0.1 M OF KCL IN A OXYGENATED AQUEOUS SOLUTION AT 65°C. THE APPLIED POTENTIAL WAS -0.97 V. 90

FIGURE 6.31 CRYSTALLOGRAPHIC STUDY: (A) XRD PATTERN OF A SAMPLE AFTER A 20 MINUTES DEPOSITION (B) ZNO WURTZITE AND AU FCC XRD PATTERN. 5 MM OF $Zn(NO_3)_2$ AND 0.1 M OF KCL IN A OXYGENATED AQUEOUS SOLUTION AT 65°C. THE APPLIED POTENTIAL WAS -0.97 V. 91

FIGURE 6.32 *EX-SITU* GIXS SCAN OF A SAMPLE DEPOSITED FOR 15 S. THE PEAKS ARE LABELLED ACCORDING TO THE ZNO WURTZITE STRUCTURE OR AU FCC STRUCTURE (ITALICS). INSET: INTENSITY VS. POLAR ANGLE TEXTURE SCAN OF THE (101) PEAK WITH A LORENTZIAN FITTING (RED LINE). 5 MM OF $Zn(NO_3)_2$ AND 0.1 M OF KCL IN A OXYGENATED AQUEOUS SOLUTION AT 65°C. THE APPLIED POTENTIAL DURING THE DEPOSITION WAS -0.77 V. 92

FIGURE 6.33 DIFFRACTION PATTERN FROM AN IN-SITU SCAN. EACH INTENSITY PEAK CORRESPONDS TO A SPECIFIC ORIENTATION OF EITHER ZNO OR AU, AS LABELLED. THE DATA CAN BE READ IN POLAR COORDINATES BY USING THE ANGLE X FROM THE VERTICAL AND THE SCATTERING VECTOR Q. 5 MM OF $Zn(NO_3)_2$ AND 0.1 M OF KCL IN A OXYGENATED AQUEOUS SOLUTION AT 65°C. THE APPLIED POTENTIAL WAS -0.77 V. 93

FIGURE 6.34 GRAPH RESULTING OF THE INTEGRATION OF THE DATA IN FIGURE 6.33 WITH FIT2D. THE POLAR DATA (X, Q) HAVE BEEN CONVERTED TO A CARTESIAN REFERENTIAL. THE HORIZONTAL LINES CORRESPONDING TO THE REFLECTION OF AU AND ZNO HAVE BEEN LABELLED. 5 MM OF $Zn(NO_3)_2$ AND 0.1 M OF KCL IN A OXYGENATED AQUEOUS SOLUTION AT 65°C. THE APPLIED POTENTIAL WAS -0.77V. 94

FIGURE 6.35 INTENSITY VERSUS ANGLE IN OMEGA FOR THE ZNO (101) REFLECTION AT THE END OF A DEPOSITION. 5 MM OF $Zn(NO_3)_2$ AND 0.1 M OF KCL IN A OXYGENATED AQUEOUS SOLUTION AT 65°C. THE APPLIED POTENTIAL WAS -0.77 V. 95

FIGURE 6.36 *IN-SITU* MEASUREMENTS OF THE PEAK INTENSITY (A) AND FULL WIDTH AT HALF-MAXIMUM (B) FOR THE (101) REFLECTION AS A FUNCTION OF TIME. THE APPLIED POTENTIAL WAS -0.77 V 96

FIGURE 6.37 CURRENT DENSITY AS A FUNCTION OF TIME FOR (A) IN-SITU XAS (XAS) SET-UP AND (B) *IN-SITU* XRD SET-UP. 5 MM OF $Zn(NO_3)_2$ AND 0.1 M OF KCL IN A OXYGENATED AQUEOUS SOLUTION AT 65°C. THE APPLIED POTENTIAL WAS -0.97 V. 96

FIGURE 6.38 EVOLUTION OF THE FILM MORPHOLOGY WITH TIME FOR FOUR DEPOSITION POTENTIALS. 5 MM OF $Zn(NO_3)_2$ AND 0.1 M OF KCL IN A OXYGENATED AQUEOUS SOLUTION AT 65°C. 98

FIGURE 6.39 DIAMETER AND DENSITY OF THE NANOSTRUCTURES AS A FUNCTION OF THE POTENTIALS AND TIME. (A) -0.37 V, (B) -0.67 V, (C) -0.77 V AND (D) -0.97 V. 5 MM OF $Zn(NO_3)_2$ AND 0.1 M OF KCL IN A OXYGENATED AQUEOUS SOLUTION AT 65°C. 99

FIGURE 6.40 DIAMETER (RED SQUARES) AND DENSITY (BLUE DIAMONDS) OF THE NANOSTRUCTURES AS A FUNCTION OF THE POTENTIALS. T=4MINUTES. 5 MM OF $Zn(NO_3)_2$ AND 0.1 M OF KCL IN A OXYGENATED AQUEOUS SOLUTION AT 65°C. 99

FIGURE 6.41 SIMULTANEOUS CURRENT DENSITY (A) AND NOMINAL THICKNESS (B) MEASUREMENTS AS A FUNCTION OF TIME AND POTENTIAL: -0.37 V (RED LINE), -0.67 V (BLUE LINE), -0.77 V (BLACK LINE) AND -0.97 V (GREEN LINE). 5 MM OF $Zn(NO_3)_2$ AND 0.1 M OF KCL IN A OXYGENATED AQUEOUS SOLUTION AT 65°C. 101

FIGURE 6.42 CURRENT EFFICIENCIES CALCULATED FOR THE FILMS DEPOSITED IN FIGURE 6.41 : -0.37 V (RED LINE), -0.67 V (BLUE LINE), -0.77 V (BLACK LINE) AND -0.97 V (GREEN LINE). 5 MM OF $Zn(NO_3)_2$ AND 0.1 M OF KCL IN A OXYGENATED AQUEOUS SOLUTION AT 65°C. 103

FIGURE 6.43 *EX-SITU* GIXS SCAN OF A SAMPLE DEPOSITED FOR 1 MINUTE AT A POTENTIAL OF -0.37 V (BLUE) AND -0.97 V (RED). THE PEAKS ARE LABELLED ACCORDING TO THE ZNO WURTZITE STRUCTURE OR AU FCC STRUCTURE (ITALICS). INSET: INTENSITY VS. POLAR ANGLE TEXTURE SCAN OF THE (101) PEAK. GREEN CURVES: 20 MINUTES AT A POTENTIAL OF -0.37. 5 MM OF $Zn(NO_3)_2$ AND 0.1 M OF KCL IN A OXYGENATED AQUEOUS SOLUTION AT 65°C. 103

FIGURE 6.44 *IN-SITU* MEASUREMENTS OF FULL WIDTH AT HALF-MAXIMUM FOR THE (101) REFLECTION AS A FUNCTION OF POTENTIAL: (A) -0.37 V, (B) -0.67 V, (C) -0.77 V AND (D) -0.77 V. 5 MM OF $Zn(NO_3)_2$ AND 0.1 M OF KCL IN A OXYGENATED AQUEOUS SOLUTION AT 65°C. 104

FIGURE 6.45 EFFECT OF THE [Cl^-] ON THE MORPHOLOGY: 0.2 M OF Cl^- (A) AND 0.1 M OF Cl^- (B). THE DEPOSITION TIME WAS 10 MINUTES. 5 MM OF $Zn(NO_3)$ IN A OXYGENATED AQUEOUS SOLUTION AT 65°C. THE APPLIED POTENTIAL WAS -0.97 V. 106

FIGURE 6.46 SIMULTANEOUS (A) CURRENT DENSITY AND (B) NOMINAL THICKNESS MEASUREMENTS AS A FUNCTION OF THE SUPPORT ELECTROLYTE (I) BLUE CURVES, KCL AND (II) RED CURVES, $CaCl_2$. INSET: EVOLUTION OF THE MORPHOLOGY WITH TIMEWITH A $CaCl_2$ SUPPORT ELECTROLYTE. FESEM IMAGES AFTER (A) 25 SECONDS, (B) 4 MINUTES AND (C) 10 MINUTES. 5 MM OF $Zn(NO_3)$ IN A OXYGENATED AQUEOUS SOLUTION AT 65°C. THE APPLIED POTENTIAL WAS -0.97 V. 107

FIGURE 6.47 CURRENT EFFICIENCIES CALCULATED FOR THE FILMS DEPOSITED WITH (A) 0.1 M (BLUE LINE) AND (B) 0.2 M (RED LINE) OF Cl^-. 5 MM OF $Zn(NO_3)$ IN A OXYGENATED AQUEOUS SOLUTION AT 65°C. THE APPLIED POTENTIAL WAS -0.97 V. 108

FIGURE 6.48 *EX-SITU* GIXS SCAN OF A SAMPLE DEPOSITED FOR 4 MINUTE. THE PEAKS ARE LABELLED ACCORDING TO THE ZNO WURTZITE STRUCTURE OR AU FCC STRUCTURE (ITALICS). 5 MM OF $Zn(NO_3)$ AND 0.1 M OF $CaCl_2$ IN A OXYGENATED AQUEOUS SOLUTION AT 65°C. THE APPLIED POTENTIAL WAS -0.97 V. 109

FIGURE 6.49 *IN-SITU* MEASUREMENTS OF FULL WIDTH AT HALF-MAXIMUM FOR THE (101) REFLECTION AS A FUNCTION Cl^- CONCENTRATION: (A) 0.1 M AND (B) 0.2 M. 5 MM OF $Zn(NO_3)$ IN A OXYGENATED AQUEOUS SOLUTION AT 65°C. THE APPLIED POTENTIAL WAS -0.97 V. 109

FIGURE 6.50 CHANGE IN THE SOLUTION PH AS A FUNCTION OF INITIAL CONCENTRATION OF $Zn(NO_3)_2$ AT 65°C. 111

FIGURE 6.51 EFFECT OF THE $Zn(NO_3)_2$ CONCENTRATION ON THE MORPHOLOGY OF THE FILMS. FESEM IMAGES OF FILMS DEPOSITED WITH AN INITIAL CONCENTRATION OF (A) 0.5 MM, (B) 1 MM, (C) 2 MM, (D) 5 MM, (E) 10 MM, (F) 20 MM AND (G) 50 MM. THE TOP INSERT IN FIGURES (C), (D), (E) AND (G) PRESENTS THE FESEM CROSS SECTION OF THE FILMS. THE DEPOSITION TIME WAS 30 MINUTES. 0.1 M OF KCL IN AN OXYGENATED AQUEOUS SOLUTION AT 65°C. THE APPLIED POTENTIAL WAS -0.77 V. 113

FIGURE 6.52 EVOLUTION OF THE FILM MORPHOLOGY WITH TIME AS A FUNCTION OF INITIAL CONCENTRATION OF $Zn(NO_3)$. FESEM IMAGES: TILT VIEW OF A FILM DEPOSITED WITH (A) 1 MM FOR 30 SECONDS, (B) CROSS SECTION AND (C) TOP VIEW OF A FILM DEPOSITED WITH 1 MM FOR 60 MINUTES, (D) TILT VIEW OF A FILM DEPOSITED WITH 50 MM FOR 30 SECONDS AND TOP VIEW OF FILMS DEPOSITED WITH 5 MM FOR (E) 30 SECONDS AND (F) 20 MINUTES. 0.1 M OF KCL IN AN OXYGENATED AQUEOUS SOLUTION AT 65°C. THE APPLIED POTENTIAL WAS -0.77 V. 114

FIGURE 6.53 EVOLUTION OF THE ROD DIAMETER WITH TIME AS A FUNCTION OF $Zn(NO_3)_2$ CONCENTRATION: 1 MM (TRIANGLE) AND 5 MM (SQUARE) OF $Zn(NO_3)_2$. THE ROD DIAMETERS HAVE BEEN MEASURED FROM THE FESEM IMAGES ON TWO SAMPLES DEPOSITED IN THE SAME CONDITIONS. 0.1 M OF KCL IN AN OXYGENATED AQUEOUS SOLUTION AT 65°C. THE APPLIED POTENTIAL WAS -0.77 V. 115

FIGURE 6.54 DISTRIBUTION OF THE NANOROD DIAMETERS AS A FUNCTION OF THE $Zn(NO_3)_2$ CONCENTRATION. (A) 0.5 MM, (B) 1 MM, (C) 2 MM, (D) 5MM AND (E) 10 MM. THE ROD DIAMETERS HAVE BEEN MEASURED FROM THE FESEM IMAGES ON TWO SAMPLES DEPOSITED IN THE SAME CONDITIONS. GAUSSIAN FITS OF THE DISTRIBUTIONS HAVE BEEN INDICATED BY LINES. THE DEPOSITION TIME IS 30 MINUTES. 0.1 M OF KCL IN AN OXYGENATED AQUEOUS SOLUTION AT 65°C. THE APPLIED POTENTIAL WAS -0.77 V. 116

FIGURE 6.55 VARIATIONS OF THE CURRENT DENSITY (A) AND OF THE NOMINAL THICKNESS (B) WITH TIME AS A FUNCTION OF $Zn(NO_3)_2$ CONCENTRATION: (I) 0.5 MM, (II) 1 MM, (III) 2 MM, (IV) 5 MM, (V) 10 MM, (VI) 20 MM AND (VII) 50 MM. 0.1 M OF KCL IN AN OXYGENATED AQUEOUS SOLUTION AT 65°C. THE APPLIED POTENTIAL WAS -0.77 V. 117

FIGURE 6.56 VARIATIONS OF THE FARADAIC EFFICIENCY WITH TIME AS A FUNCTION OF $Zn(NO_3)_2$ CONCENTRATION: (A) 1 MM, (B) 2 MM, (C) 5 MM, (D) 10 MM, (E) 20 MM. 0.1 M OF KCL IN AN OXYGENATED AQUEOUS SOLUTION AT 65°C. THE APPLIED POTENTIAL WAS -0.77 V. 118

FIGURE 6.57 *IN-SITU* GRAZING INCIDENCE XRD SCANS AT THE END OF A 30 MINUTES DEPOSITION AS A FUNCTION OF CONCENTRATION. (A) LOW CONCENTRATION (1 MM), (B) MEDIUM CONCENTRATION (5 MM) AND (C) HIGH CONCENTRATION (50 MM). THE PEAKS CORRESPONDING TO ZNO, AU AND $Zn_5(OH)_8Cl_2$ HAVE BEEN MARKED THE SQUARES, TRIANGLES AND CIRCLE RESPECTIVELY. 0.1 M OF KCL IN AN OXYGENATED AQUEOUS SOLUTION AT 65°C. THE APPLIED POTENTIAL WAS -0.77 V. 119

FIGURE 6.58 SOLUBILITY DIAGRAMS OF ZINC OXIDE AND ZINC HYDROXYCHLORIDE AFTER 11 120

FIGURE 6.59 *IN-SITU* GRAZING INCIDENCE XRD SCANS AT THE END OF A 30 MINUTES DEPOSITION WITH AN APPLIED POTENTIAL OF -0.97 V AND $Zn(NO_3)_2$ CONCENTRATION OF 50 MM. 0.1 M OF KCL IN AN OXYGENATED AQUEOUS SOLUTION AT 65°C. 120

FIGURE 6.60 FULL WIDTH AT HALF-MAXIMUM (FWHM) CALCULATED FROM (101) POLAR ANGLE PLOTS. (A) LIGHT GREY CIRCLES, LOW CONCENTRATION (1 MM), (B) GRAY SQUARES, MEDIUM CONCENTRATION (5 MM) AND (C) BLACK TRIANGLES, HIGH CONCENTRATION (50 MM). 0.1 M OF KCL IN AN OXYGENATED AQUEOUS SOLUTION AT 65°C. THE APPLIED POTENTIAL WAS -0.77 V. 121

FIGURE 6.61 EFFECT OF PH. FESEM IMAGES AFTER A 20 MINUTE DEPOSITION AND THE FILM IMMEDIATELY REMOVED FROM SOLUTION. (A) PH=4, (B) PH=5, (C) PH=5.3 AND (D) PH=6. 5 MM OF $Zn(NO_3)_2$ AND 0.1 M OF KCL IN AN OXYGENATED AQUEOUS SOLUTION AT 65°C. THE APPLIED POTENTIAL WAS -0.97 V. 125

FIGURE 6.62 SIMULTANEOUS CURRENT DENSITY (A) AND NOMINAL THICKNESS (B) MEASUREMENTS AS A FUNCTION OF THE PH (I) PH=2, (II) PH=3, (III) PH=4, (IV) PH=5.3, (V) PH=6. 5 MM OF $Zn(NO_3)_2$ AND 0.1 M OF KCL IN AN OXYGENATED AQUEOUS SOLUTION AT 65°C. THE APPLIED POTENTIAL WAS -0.97 V. 126

FIGURE 6.63 *IN-SITU* END GIXS SCAN WITH REMOVED SOLUTION AS A FUNCTION OF PH: (I) PH=4, (II) PH= 5, (III) PH=5.4. THE PEAKS ARE LABELLED ACCORDING TO THE ZNO WURTZITE STRUCTURE OR AU FCC STRUCTURE (ITALICS). 5 MM OF $Zn(NO_3)_2$ AND 0.1 M OF KCL IN AN OXYGENATED AQUEOUS SOLUTION AT 65°C. THE APPLIED POTENTIAL WAS -0.97 V. 128

FIGURE 6.64 *IN-SITU* MEASUREMENTS OF FULL WIDTH AT HALF-MAXIMUM FOR THE (101) REFLECTION AS A FUNCTION OF PH: (I) PH=4, (II) PH=5 AND (III) PH=5.3. 5 MM OF $Zn(NO_3)_2$ AND 0.1 M OF KCL IN AN OXYGENATED AQUEOUS SOLUTION AT 65°C. THE APPLIED POTENTIAL WAS -0.97 V. 128

FIGURE 6.65 NOMINAL THICKNESS AS A FUNCTION OF TIME, FOR A ZNO FILM DEPOSITED FROM 10 MM ZN(NO3)2 SOLUTION WITH 0.1 M KCL AS THE ELECTROLYTE AT 65°C. THE APPLIED POTENTIAL WAS -0.77 V. REGION (A) CORRESPONDS TO NUCLEATION, (B) TO 1D GROWTH, AND (C) TO OPEN-CIRCUIT DISSOLUTION. THE INSET MICROGRAPHS CORRESPOND TO THE END OF DEPOSITION (20 MINUTES, I) AND DISSOLUTION (40 MINUTES, II). 129

FIGURE 6.66 FORMATION OF TUBE STRUCTURES OCCURS OVER LARGE AREAS. THE DIMENSIONS SUCH AS TUBE DIAMETER, TUBE HIGH AND WALL THICKNESS CAN BE TAILORED BY VARYING THE DEPOSITION PARAMETERS. THE INSETS SHOW CLOSE-UP OF

THE NANOTUBES. (A) THE APPLIED POTENTIAL WAS -870 MV USING A 5 MM $Zn(NO_3)_2$ SOLUTION AND 0.1 M $CaCl_2$ ELECTROLYTE. (B) THE APPLIED DEPOSITION POTENTIAL WAS -770 MV. THE SOLUTION WAS 5 MM $Zn(NO_3)_2$ WITH 0.1 M $CaCl_2$ ELECTROLYTE. THE DISSOLUTION TIME IS 270 MINUTES IN BOTH CASES.....130

FIGURE 6.67 EVOLUTION OF THE FILM MORPHOLOGY WITH INCREASING DISSOLUTION TIME. THE SAMPLES WERE PREPARED FROM A SOLUTION WITH 5 MM OF $Zn(NO_3)_2$ AND 0.1 M OF$CaCl_2$ AT 65^{o}C 132

FIGURE 6.68 EVOLUTION OF THE FILM MORPHOLOGY BEFORE AND AFTER A ONE HOUR LONG DISSOLUTION FOR HIGH DEPOSITION POTENTIAL (-0.37 V). THE SAMPLES WERE PREPARED FROM A SOLUTION WITH 5 MM OF $Zn(NO_3)_2$ AND 0.1 M OF KCL AT 65^{o}C. THE SMALL POTS ON FIG (B) ARE DUE TO THE GOLD COATING. 132

FIGURE 6.69 INFLUENCE OF CHLORIDE ION CONCENTRATION. FESEM IMAGES OF FILMS DEPOSITED AT -0.770 V AT 65^{o}C FROM 5 MM $Zn(NO_3)_2$ SOLUTION FOR 20 MINUTES AFTER 1 HOUR LONG DISSOLUTION: (A) 0.1 M Cl^- (B) 0.2 M Cl^-.....133

FIGURE 6.70 INFLUENCE OF CHLORIDE ION [Zn^{2+}]. FESEM IMAGES OF FILMS DEPOSITED AT -770 MV AT 65^{o}C WITH KCL SUPPORT ELECTROLYTE FOR 20 MINUTES AFTER 1 HOUR DISSOLUTION: (A) 10 MM OF [Zn^{2+}] AND (B) 5 MM OF [Zn^{2+}] 134

FIGURE 6.71 STUDY OF THE DISSOLUTION: INFLUENCE OF CONCENTRATION. DEPOSITION CONDITIONS FOR (A) AND (B): 5 MM $Zn(NO_3)_2$, 0.1 M $CaCl_2$ AT 65^{0}C FOR 90 MINUTES. THE APPLIED POTENTIAL WAS -0.77 V. THE SAMPLES SHOWS IN (B) HAVE BEEN DISSOLVED FOR 3.5 HOURS. DEPOSITION CONDITIONS FOR (C) AND (D): 50 MM $Zn(NO_3)_2$, 0.1 M KCL AT 65^{0}C FOR 30 MINUTES. THE APPLIED POTENTIAL WAS -0.77 V. THE SAMPLES SHOWS IN (D) HAVE BEEN DISSOLVED FOR 1 HOUR.....135

FIGURE 6.72 GRAZING INCIDENCE XRD SCANS OF TWO FILMS DEPOSITED FOR 20 MINUTES FROM A 10 MM $Zn(NO_3)_2$ SOLUTION WITH 0.1 M KCL ELECTROLYTE AT 65^{o}C AND AN APPLIED POTENTIAL OF -770 MV, ONE REMOVED FROM SOLUTION IMMEDIATELY AFTER DEPOSITION BUT BEFORE DISSOLUTION (BLACK), AND THE OTHER SUBSEQUENTLY DISSOLVED FOR 45 MINUTES (RED). THE PEAKS ARE LABELLED ACCORDING TO THE ZNO WURTZITE STRUCTURE OR AU FCC STRUCTURE (ITALICS). NOTE THAT THE INTENSITY IS SHOWN ON A LOG SCALE 136

FIGURE 6.73 COMPARISON OF THE XRD PATTERN FOR DIFFERENT SURFACTANT. (A) NO SURFACTANT, (B) 1 MM OF SODIUM ACETATE, (C) 1 MM OF OXALIC ACID AND (D) 0.1 MM OF CITRIC ACID. RED AND BLUE LINES CORRESPOND TO CUBIC GOLD (FROM THE SUBSTRATE) AND HEXAGONAL ZINC OXIDE PATTERNS RESPECTIVELY. 5 MM OF $Zn(NO_3)_2$ AND 0.1 M OF KCL IN AN OXYGENATED AQUEOUS SOLUTION AT 65^{o}C. THE APPLIED POTENTIAL WAS -0.97 V. 139

FIGURE 6.74 EDS SPECTRUM WITH AND WITHOUT ADDITIVE. (A) NO ADDITIVE, (B) 1 MM OF SODIUM ACETATE, (C) 1 MM OF OXALIC ACID AND (D) 0.1 MM OF CITRIC ACID. THE PEAK ARE INDEXED WITH THE CORRESPONDING ELEMENTS. 5 MM OF $Zn(NO_3)_2$ AND 0.1 M OF KCL IN AN OXYGENATED AQUEOUS SOLUTION AT 65^{o}C. THE APPLIED POTENTIAL WAS -0.97 V. PH WAS 5.4.....140

FIGURE 6.75 EFFECT OF PH ON THE FILM MORPHOLOGY IN PRESENCE OF 1 MM OF SODIUM ACETATE. FESEM IMAGES AFTER A 20 MINUTE DEPOSITION. (A) PH=4, (B) PH=5, (C) PH=5.3 AND (D) PH=6. 5 MM OF $Zn(NO_3)_2$ AND 0.1 M OF KCL IN AN OXYGENATED AQUEOUS SOLUTION AT 65^{o}C. THE APPLIED POTENTIAL WAS -0.97 V. 141

FIGURE 6.76 DEPOSITION STUDIES WITH 1MM OF SODIUM ACETATE SHOWING THE EFFECT OF PH. (A) CURRENT VS. TIME (B) NOMINAL THICKNESS VS. TIME. 5 MM OF $Zn(NO_3)_2$ AND 0.1 M OF KCL IN AN OXYGENATED AQUEOUS SOLUTION AT 65^{o}C. THE APPLIED POTENTIAL WAS -0.97 V. 142

FIGURE 6.77 EFFECT OF PH ON THE FILM MORPHOLOGY IN PRESENCE OF 1 MM OF OXALIC ACID. FESEM IMAGES AFTER A 20 MINUTE DEPOSITION. (A) PH=4, (B) PH=5, (C) PH=5.3 AND (D) PH=6. 5 MM OF $Zn(NO_3)_2$ AND 0.1 M OF KCL IN AN OXYGENATED AQUEOUS SOLUTION AT 65°C. THE APPLIED POTENTIAL WAS -0.97 V. 143

FIGURE 6.78 FESEM IMAGE OF A FILM DEPOSITED IN PRESENCE OF 1MM OF OXALIC ACID AFTER ANNEALING, SHOWING THE FORMATION OF NANOPORES IN THE ZNO SHEETS. 5 MM OF $Zn(NO_3)_2$ AND 0.1 M OF KCL IN AN OXYGENATED AQUEOUS SOLUTION AT 65°C. THE APPLIED POTENTIAL WAS -0.97 V. 144

FIGURE 6.79 EFFECT OF OXALIC ACID CONCENTRATION ON THE FILM MORPHOLOGY IN PRESENCE AT PH 5.3. (A) NO OXALIC ACID (B) 0.1 MM AND (C) 1 MM. 5 MM OF $Zn(NO_3)_2$ AND 0.1 M OF KCL IN AN OXYGENATED AQUEOUS SOLUTION AT 65°C. THE APPLIED POTENTIAL WAS -0.97 V. 145

FIGURE 6.80 DEPOSITION STUDIES WITH 1MM OF OXALIC ACID: EFFECT OF PH. (A) CURRENT VS. TIME, (B) NOMINAL THICKNESS VS. TIME. 5 MM OF $Zn(NO_3)_2$ AND 0.1 M OF KCL IN AN OXYGENATED AQUEOUS SOLUTION AT 65°C. THE APPLIED POTENTIAL WAS -0.97 V. 145

FIGURE 6.81 DEPOSITION STUDIES: EFFECT OF OXALIC ACID CONCENTRATION. (A) CURRENT VS. TIME, (B) NOMINAL THICKNESS VS. TIME. 5 MM OF $Zn(NO_3)_2$ AND 0.1 M OF KCL IN AN OXYGENATED AQUEOUS SOLUTION AT 65°C. THE APPLIED POTENTIAL WAS -0.97 V. 146

FIGURE 6.82 EFFECT OF CITRIC ACID CONCENTRATION ON THE FILM MORPHOLOGY. (A) 0.01 MM, (B) 0.1 MM AND (C) 1 MM. FESEM IMAGES AFTER A 20 MINUTE DEPOSITION. 5 MM OF $Zn(NO_3)_2$ AND 0.1 M OF KCL IN AN OXYGENATED AQUEOUS SOLUTION AT 65°C. THE APPLIED POTENTIAL WAS -0.97 V. 147

FIGURE 6.83 DEPOSITION STUDIES: EFFECT OF CITRIC ACID CONCENTRATION. (A) CURRENT VS. TIME, (B) NOMINAL THICKNESS VS. TIME. 5 MM OF $Zn(NO_3)_2$ AND 0.1 M OF KCL IN AN OXYGENATED AQUEOUS SOLUTION AT 65°C. THE APPLIED POTENTIAL WAS -0.97 V. 148

3 Introduction

The aim of this chapter is chapter is to explain why the electrodeposition of zinc oxide nanostructured films is such an interesting field of research. Firstly, the importance of the nanotechnology market in today's society will be presented. Secondly, we will explain why ZnO is a key material in the development of future nano-technology by presenting its unique properties and applications. Finally a comparison of the electrodeposition process with other methods will show how electrodeposition could become the best method to produce nanostructured zinc oxide.

3.1 Nanotechnology

Nanotechnologies are the design, characterisation, production and application of structures, devices and systems by controlling shape and size at dimensions between approximately 1 and 100 nanometres, where unique phenomena enable novel applications[1]. Nanotechnology has the potential to create many new materials and devices with wide-ranging applications, such as cheap and clean energy, drug delivery and diagnostics system, fast and more advanced computing chips. In the United States, the Federal funding for nanotechnology has increased from approximately $464 million in 2001 to nearly $1.5 billion for the 2009 fiscal year. Private industry is investing at least as much as the government, according to estimates. Estimates from 2005 showed the European Union and Japan invested approximately $1.05 billion and $950 million respectively in nanotechnology[2].

3.2 Properties of ZnO

ZnO is a fascinating material. It has probably one of the richest families of nanostructures among all materials, and has many potential applications owing to its unique physical and chemical properties. It is a large band gap semi-conductor, it has piezoelectric, pyroelectric, photoluminescence (PL) and remarkable wetting properties. Its first applications were related to its optical properties: 300 years ago it was already used as a pigment in paints and as a dermatotherapeutic to protect skin against ultraviolet (UV) radiation[3]. Today, it is one of the most studied materials for future nanotechnology applications: ZnO has found a wide range of application for electronic and photonic devices such as piezoelectric transducers, solar cells, nano-sensors, varistors, phosphors, smart windows, transparent electrodes and light emitting devices.

3.2.1 Electrical Properties

ZnO is a wide band gap (3.4 eV) II–VI compound semiconductor. It is usually an n-type semiconductor which originates from inherent defects such as oxygen vacancies and zinc interstitials. As the defects are usually concentrated in the surface region, they have significant effect on the optical and electrical properties of nanostructured materials due to their large surface to volume ratio[4].

3.2.2 Optical Properties

The optical properties ZnO nanostructures have been extensively studied because of the promising potential of this material in optoelectronics. Compared with other wide bandgap semiconductors, for example GaN or SiC, ZnO has a large exciton binding energy (about 60 meV) which ensures efficient excitonic emission at room temperature and thus ZnO has significant advantages in optoelectronic applications such as for UV lasing[5]. It has also been reported that the exciton binding energy is significantly enhanced due to size confinement in ZnO nanorods with diameter of 2 nm[5]. ZnO has very strong violet luminescence from bound excitonic emission at room temperature[6]. Field effect mobility have been measured by electrical transport studies after configuring individual single crystal ZnO nanowires as field effect transistors (FET)[7]. The mobility typically ranges from 20 to 100 $cm^2.V^{-1}.s^{-1}$. The electron mobility in ZnO nanowires can be dramatically enhanced to exceed 4000 $cm^2.V^{-1}.s^{-1}$ with surface treatment. These results indicate that the ZnO device has exceptional potential in high speed electronic applications.

3.2.3 Crystal Structure

ZnO crystallizes in the Wurtzite structure. This structure is a hexagonal crystal system and consists of tetrahedrally coordinated zinc and oxygen atoms that are stacked in an ABABAB pattern along the major c axis (see Figure 3.1).

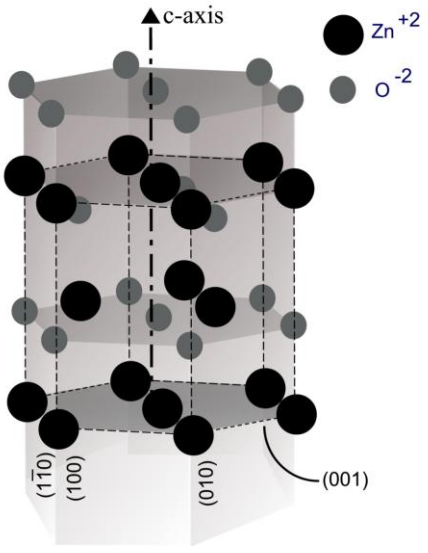


Figure 3.1 Schematic representation of the wurtzite zinc oxide structure. The top (001) plane is comprised of either O^{2-} or Zn^{2+} and is charged. The (1-10), (100) and (010) planes are comprised of an equal number of O and Zn and are thus electrically neutral.

The alternative distance between the close packed oxygen and zinc layers is 0.69 Å and 1.99 Å respectively[8]. The two important characteristics of the wurtzite structure are the noncentral symmetry and the polar surfaces. The surfaces perpendicular to the major axis are composed uniquely by Zn^{2+} or O^{2-} ions to form polar surface while the faces parallel to the c-axis are composed of Zn–O dimers with neutral charge, i.e. non-polar surfaces. For the ZnO nanostructures, with the increased surface-to-bulk ratio, the effect played by the surfaces, especially the polar surfaces, is critically important. Polar faces with surface dipoles are thermodynamically less stable than non-polar faces, often undergone rearrangement to minimise their surface energy and tending to grow more rapidly. Wander and Harrison calculated the surface energies of (100), (110) and (001) faces using an *ab initio* (all-electron) approach[9]. They found 2.32 $J.m^{-2}$, 4.1 $J.m^{-2}$ and 5.4 $J.m^{-2}$ respectively.

3.2.4 Nanostructures

ZnO has a rich family of nanostructures. Various nanostructures such as particles[10], rods[11], wires[12], plates[13], dendrites[14], tubes[15], hierarchical structures[16], nanorings[17], nanohelices[18], tetrapods[19] have been reported for Wurtzite ZnO. A nomenclature for these structures has *not* been well established. A possible classification is the dimensionality of the structures. Figure 3.2 presents the most common structures found in the literature classed according to their dimensionality. These nano-structures exhibit novel physical properties owing to their unique geometry and high aspect ratio.

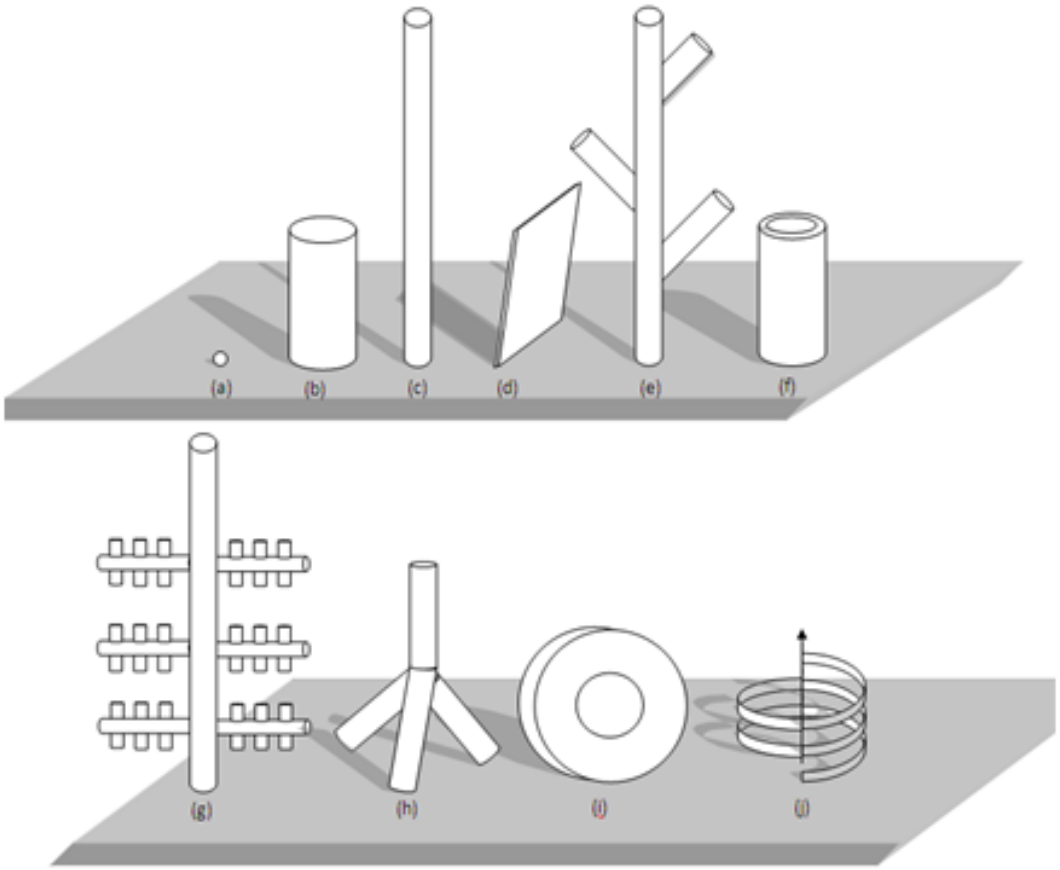


Figure 3.2 Different ZnO nanostructures, from top left: (a) particle, (b) rod, (c) wire, (d) plate, (e) dendrite, (f) tube, (g) hierarchical nanostructure, (h) tetrapod, (i) ring , (j) spring.

3.2.5 Piezoelectricity

Piezoelectricity is the ability to generate an electric potential in response to applied mechanical stress. Piezoelectricity is due to the atomic-scale polarization and directly related to a lack of a centre of inversion symmetry in the crystal structure of ZnO. To understand piezoelectricity one can consider a tetrahedron of the Wurtzite structure (see Figure 3.3). Without applied stress, the centre of gravity of the negative charges coincides with the position of the Zn^{2+} ions. By exerting pressure on the crystal through the apex of a tetrahedron, the tetrahedron will experience distortion, and the centre of gravity of the negative charges will no longer coincide with the position of the positive central atom, an electric dipole is generated. If all of the tetrahedra in the crystal have the same orientation or some other mutual orientation that does not allow for a cancellation between the dipoles, the crystal will have a macroscopic dipole. The two opposite faces of the crystal have opposite electric charges[20].

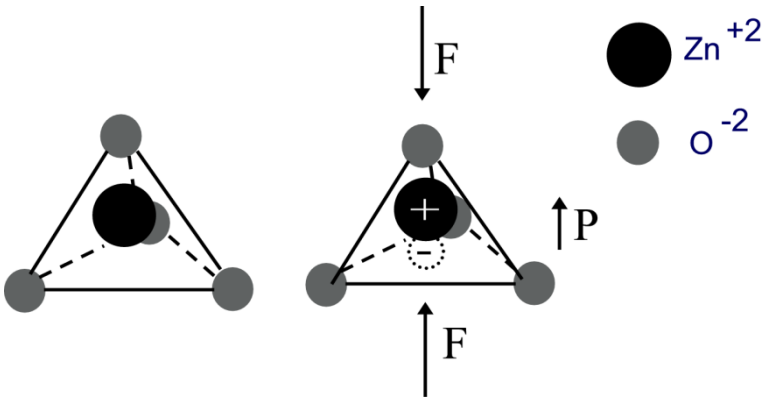


Figure 3.3 Schematic diagram of the formation of a dipole moment P when a stress F is applied to ZnO_4 tetrahedron of the ZnO wurtzite structure (after 20)

3.3 Applications

ZnO has been used in industry for many years in numerous applications such in rubber manufacture, concrete production, cigarette filters, food additives, pigment and coating[21], with tens of thousands of tons produced each year[22]. The development of nanoscience has opened a new field of research the 10 past years. The most promising new applications based on the improved functional properties are listed below.

3.3.1 Piezoelectricity Applications

Piezoelectricity can be used for the production of nano-generator[23]. For example low-frequency vibration/friction energy such as body movement or wind could be used to produce electricity in textile made of ZnO wires[24]. It can also be used for the transduction of acoustic waves in surface acoustic wave devices[25].

3.3.2 Photovoltaic (PV) Applications

Photovoltaics (PV) is the field of technology and research related to the application of solar cells for energy generation by converting sunlight directly into electricity. Due to the growing demand for clean sources of energy, the manufacture of solar cells and photovoltaic arrays has expanded dramatically in recent years. Photovoltaic production has doubled every two years, increasing by an average of 50 percent each year since 2002, making it the World's fastest-growing energy technology[26]. Hybrid photovoltaic cells are a promising new route to the production of low cost PV devices. They typically combine an organic and inorganic material: for example an n-type oxide semiconductor with a p-type polymeric conductor. These hybrid devices can take advantage of the

beneficial properties of both types of materials: solution processing of polymer semiconductors and high electron mobility of inorganic semiconductors. In organic photovoltaic systems excitons in conjugated polymers are harvested *via* charge separation across a donor−acceptor heterojunction with another material. The short exciton diffusion lengths in conjugated polymers, typically 5−20 nm, requires that the blend of the two materials be structured at the nanoscale. Moreover the two materials must percolate to the electrode to ensure a good transport of the charges. Since the morphology of ZnO can be controlled at the nanoscale it is a promising material for hybrid PV applications. Moreover, compared to other metal oxides, ZnO is environmentally friendly and it can be high quality and low cost. Numerous studies have been devoted to increase the efficiency of ZnO based PV devices[27,28,29,30,31,32,33, 34] . These studies have demonstrated the feasibility of the hybrid approach, although the morphologies of the nanostructured inorganic semiconductors have not been optimized, and reported device efficiencies have not so far exceeded 2%[28].

3.3.3 Light-Emitting Diodes (LEDs)

A LED is an electronic light source. LEDs are semiconductor diodes: when the diode is biased, electrons are able to recombine with holes and energy is released in the form of light. This effect is called electroluminescence and the colour of the light is determined by the energy gap of the semiconductor. Y. R. Ryu et al have reported the fabrication of homostructural ZnO p–n junctions[6]. ZnO has optical and structural properties similar to GaN and ZnS, widely use materials for LED for emission between green and UV. However its optical properties are superior and it is easier to obtain high quality ZnO giving ZnO advantages over GaN and ZnS for such devices[6,35,36].

3.3.4 Sensing

A large number of studies have been carried to investigate the properties of nanostructured materials[37] for sensing applications. The interaction of nanostructured materials with the surrounding atmosphere can greatly modify its surface properties. Nanostructured materials have a high surface to volume ratio and their electrical properties can be dominated by surface interactions. Electrical, optical and electrochemical properties of ZnO have been used to produce sensors:

- **DC conductimetric gas sensors**

The sensing mechanism in this type of ZnO nanowire gas sensor is related to the surface absorption of gaseous species. When the charge density is reduced or increased due to surface reactions with atmospheric species, large variations of conductivity are observed. The sensing ability of ZnO has been proven for different gases. Nano-crystalline Cu-doped ZnO thin films shown been proved to be sensing to CO[38]. ZnO nanorods have been reported to be sensitive to H_2 at 112 ◦C or O_3 at room temperature[39]. It has been reported that ZnO thin films of sub-micron rods had a good sensitivity and rapid response–recovery characteristics towards liquefied petroleum gases[40,41]. Zang et al. reported variations in the electrical properties due to humidity changes at room temperature[42]. Wang et al. have studied ZnO as a hydrogen sensor[43]. The detection of ethanol at levels as low as 10 ppm and recovery times faster than 10 s were reported by Jiaquiang et al. [44] who also show sensitivity to CO, H_2S, HCHO and NH_3.

- **Field Effect Transistors based gas sensors**

ZnO nanowires can be mounted as a channel in an FET devices[45]. Because of their large surface-to-volume ratios, the electronic properties can be controlled almost entirely by the chemical processes taking place at the surface. The channel conductance and the FET threshold changes with the absorption of molecules from the gaseous surrounding atmospheres. Gas-sensing properties of ZnO were tested towards O_2 (sensitive to 20% of O_2 at a pressure of 3.10^{-5} atm)[46] NO_2 (sensitive to 10 ppm) and NH_3 (sensitive to 1%)[47] and humidity detection (sensitive to 95% of relative humidity)[48].

- **Photoluminescence based gas sensors**

PL quenching has been investigated as a new detection method. Most of the work in this area has been carried on ZnO due to its unique properties such as lasing but the method is not yet well-explored. Quantum confinement effects and an increase of the surfaces area which is rich in defects, can also lead to a change in PL emission by interactions with the surrounding atmosphere[49]. Lettieri and al. have investigated the gas sensitive light emission properties of zinc oxide nanobelts[50]. They found that the device was sensitive to 5 ppm of NO_2.

- **Biosensing**

ZnO nanostructures possess several unique advantages such as high specific surface area, nontoxicity, chemical stability, electrochemical activity, and high electron mobility. Such properties indicate the potential applications of ZnO as one of the promising materials for biosensor applications[51]. ZnO nanorods showed dramatic changes in conductance upon exposure to polar liquids[52]. The sensing mechanism is based on the polarization-induced change in bound surface charge by interaction with polar molecules in the liquids. ZnO nano-pH electrodes have been made in order to study intercellular pH[53,54,55]. Interaction between the ZnO surface and the solution leads to the formation of hydroxide group and thus a pH-dependent net surface charge. The change in voltage at the electrode/liquid interface can be measured and is found to be linearly proportional to the pH in the range of interest. ZnO nanorods have also been used in reagentless uric acid biosensors[56]. ZnO is also an attractive candidate in immobilizing redox proteins and fabricating biosensors[57,36, 58, 59].

3.3.5 Dilute Magnetic Semiconductors (DMS)

The potential use of both the charge and spin of electrons for spintronic devices has attracted great interest in recent years and a large amount of research is ongoing into DMS materials[60,61]. It is predicted that ZnO-based DMS will have a high Curie temperature and they could lead to new classes of device and circuits, such as spin transistors, ultra-dense non-volatile semiconductor memory and optical emitters with polarized output[62]. Room temperature ferromagnetism in ZnO by introducing manganese (Mn) as a dopant has been reported by Sharma et al.[63]. Room temperature anisotropic ferromagnetic behaviour has also been reported in ZnO nanowires with Fe[64], Co[65] and Ni[66] dopants.

3.3.6 Medical Applications

Anti-irritant and astringent properties as well as UV blocking properties of ZnO nano-particles have long been recognized[67]. UVA radiation is responsible for the photo-aging and skin cancers. Most sunscreens do not protect against long-wave UVA. ZnO nano-particles dispersed into sun-cream can protect the skin against this kind of radiation[68].

ZnO nanoparticles may be a used for the treatment of cancer. Indeed, its photonic properties can be used for the purpose of photodynamic therapy. It is a selective treatment of cancer with low risk for the healthy cells[68]. It is based to the administration of a photosensitizer to a patient which accumulates in the cancer tissues. Therapeutic light is shone on the area to be treated. The photosensitizer molecules are excited and transmit the excess of energy to oxygen molecules to yield first excited state. Singlet oxygen is highly cytotoxic and its formation leads to degradation of the cancerous cells[68].

3.3.7 Others Applications

ZnO is one of the most common materials used in high voltage varistors. With the development of modern electronic industries and communication technology, low voltage applications have to be developed and ZnO has been reported as a good candidate[69]. Zinc Oxide, as a transparent semiconductor, can be used for "smart windows"[70].

3.4 Synthesis and Fabrication

Various methods have been used to deposit ZnO. They can be divided in two main categories: vapour phase growth and solution phase growth. Most ZnO is deposited *via* well-developed vapour phase techniques, which is based on the reaction between metal vapour and oxygen gas. Solution phase depositions are more recent and not as well-developed but are more flexible and lower production costs can be achieved.

3.4.1 Vapour Phase Growth

The reaction between metal vapour source and oxygen gas is controlled by a thermal furnace. In order to control the shape and crystallinity of the material, various techniques have developed including thermal chemical vapour deposition, direct thermal evaporation, pulse-laser-deposition, and metal–organic chemical vapour deposition (MOCVD) etc. These growth methods are based on two mechanisms: vapour–liquid–solid and vapor–solid[71] growth.

3.4.1.1 Vapour-Liquid-Solid Mechanism (VLS)

In 1963, Wagner and Ellis first proposed the VLS mechanism[71]. VLS uses metal nanoclusters or nanoparticles as the nucleation seeds to catalyse the growth process. The process starts with the formation of liquid alloy droplet containing both catalyst and source metal. When the droplet becomes supersaturated with the metal precipitation occurs. Under a flow of oxygen, the metal oxide crystals are formed. This type of growth is epitaxial, thus it results in materials of very high crystalline quality[71]. ZnO films with various morphologies have been synthesised by this method[72-76] .

3.4.1.2 Vapour–Solid Mechanism (VS)

VS is a catalyst-free deposition method. Vaporized source materials are directly condensed on to the substrate placed in a low temperature region. The initial condensed particles serve as nucleation sites. Despite the fact that this is a commonly used method there is still a lack of fundamental understanding[71]. VS has lower growth rates compared to VLS and a poorer control of the deposit dimension because the nucleation process is less controlled. An advantage is the absence of contamination at the top of the nanostructures caused by the presence of the catalyst particles[71]. VS process has been successfully used to produce ZnO nanostructured films[77-82].

3.4.2 Solution Processes

ZnO nanostructures are usually prepared by vapour phase deposition[83]. The nanostructures obtained have generally a good crystalline quality and the morphology can be controlled. However, these techniques require sophisticated and expensive equipment they need to work in vacuum and/or at high temperature. Solution processes usually involve temperatures below 100^{o}C which considerably reduces the complexity and cost of fabrication.

3.4.2.1 Chemical Bath Deposition (CBD)

CBD has been used to deposit ZnO[84-89]. The technique of CBD relies on controlling the precipitation of a compound from solution on to a suitable substrate. Deposition characteristics can be controlled by varying the solution pH, temperature and reagent concentration. CBD can be used to coat large areas at low coast in a reproducible way. The major drawback of the CBD process is the inefficiency of the process. Waste of

product occurs due to precipitation in both the bulk solution and on the wall of the cell in addition of the substrate of interest.

3.4.2.2 Sol-Gel Method

This method is based on the phase transformation of a sol, obtained from metallic alkoxides or organometallic precursors. This sol, which is a solution containing particles in suspension, is polymerized at low temperature to form a wet gel. This gel is then densified by thermal annealing to give an inorganic product like a glass, polycrystals or a dry gel. The advantages of the sol-gel methods are its low cost, its versatility and the possibility to obtain high purity materials (shaped as monolithic blocks, powders or thin layers), the composition of which is perfectly controlled. However, the method does not directly produce crystalline material and it offers poor control of the morphology. This method has been used to produced ZnO thin films[90-94].

3.4.2.3 Solvothermal Reaction

A solvothermal reaction can be described as a chemical reaction involving a solvent either in subcritical or supercritical conditions between different precursors. Such a solvent can act as a chemical component or a fluid phase able, through its physico-chemical properties, to induce the synthesis reaction[95]. Various morphologies of nanostructured ZnO have been successfully produced by this method[96-101] .

3.5 Electrodepositon

Electrodeposition is as old as the production of electricity. Italian chemist, Luigi Brugnatelli invented electroplating in 1805. Brugnatelli performed electrodeposition of gold using the Voltaic Pile, discovered by his college Allessandro Volta in 1800[102]. It is today a widely used industrial process. ZnO has also a long history with electrochemistry and industry. Corrosion-resistant zinc plating of steel has been widely used in the industry. In 1996, two groups discovered independently a method to produce high quality nanostructured ZnO by electrodeposition[103, 104]. Preparation of oxide films by electrodeposition from aqueous solution presents several advantages over other techniques: the thickness and morphology can be controlled using electrochemical parameters, high quality films can be obtained, relatively uniform films can be obtained on substrates of complex shape, the deposition rate is relatively high,

the films can be prepared on substrates with melting point below 100 °C, the equipment is not expensive and already widely used in industry. The principle is simple: as soon as the potential is applied, a current is generated *via* the reduction of an oxygen precursor. Hydroxide ions are produced which increase the local pH in the vicinity of the substrate (cathode) surface and leads to the direct formation of crystalline zinc oxide according to the reaction:

$$Zn^{2+} + 2\ OH^- \rightarrow ZnO + H_2O \qquad \text{Eq 3.1}$$

The great degree of control of the electrodeposition has also its drawbacks: many parameters may have an effect on the deposition: time of electrodeposition, temperature, pH and chemical composition of the deposition bath, type of oxygen precursor, concentration of oxygen precursor, type of zinc precursor, concentration of zinc precursor, type and preparation of substrate onto the films are deposited and post treatments such as annealing. If one wants to optimize this method to reach an industrial scale, a perfect understanding of how the parameters influence the growth is needed. The next chapter will be dedicated to summarizing the results from the literature concerning electrodeposition of ZnO.

4 Literature Review

Electrodeposition is a versatile method for the production of ZnO. The dimensions, morphology and orientation can be controlled by varying the deposition parameters. Electrodeposition of ZnO films was first demonstrated by Lincot and Peulon[103] and by Izaki and Omi[104] in 1996. Since then, the number of publications has soared, revealing an increase of the interest for this method and of the use of ZnO in general. The first part of this chapter will describe the electro-crystallisation process. In the second part, the system will be presented from a thermodynamics point of view. In the third part, we will summarize the results on the influence of growth parameters on ZnO before defining the field of research of this work.

4.1 Electrocrystallisation Process of ZnO

4.1.1 Principles of the cathodic electrodeposition

Many important electrode reactions involve the formation of a solid phase, either as a result of the reduction of ions in solution, or by oxidation at the electrode and subsequent reaction with anions to form an anodic film. The term electrocrystallisation is used to describe electrode processes of that kind[105]. Electrocrystallisation of ZnO involves a number of distinct steps:

1. Diffusion of the hydroxyl precursor molecules toward the surface
2. Diffusion of zinc ions toward the surface
3. Electrochemical reduction at the surface
4. Precipitation of the zinc ions with the hydroxyl anions
5. Spontaneous dehydration into ZnO
6. Development of crystallographic orientation and morphological characteristics of the deposit

The reduction of the hydroxyl precursor is controlled by the potential, it starts when the applied potential E is lower than the redox potential for the cathodic processes at the electrode used. The precipitation is only observed at the electrode: firstly, the critical increase of pH is localised to the vicinity of the electrode, the bulk value remains constant. Secondly, homogenous nucleation of solid phases from solutions requires a higher activation energy barrier and therefore, heteronucleation is promoted and energetically more favourable. Indeed, the interfacial energy between two solids is generally smaller than the interfacial energy between a solid and a solution, and therefore nucleation may take place at a lower saturation ratio onto a substrate than in solution[106]. Nuclei will grow by heteronucleation on to the substrate and various dimensions, morphologies and orientations can be obtained by experimental control of the deposition parameters[106].

4.1.2 Nucleation and Growth

The growth of a film involves nucleation of centres which expand and may coalesce to form various structures. Generally, nucleation involves complex mechanisms which cannot be solved analytically. Nevertheless, it is instructive to consider a simple case which leads to analytical equations to get a better insight in to the mechanism of nucleation and growth. In this section we will present the general model applicable to

the electrocrystailisation of nickel[107]. Figure 4.4 illustrates the simplest case: two dimensional (2-D) growth with a single disc-like nucleus which expands at the periphery by incorporating molecules or atoms[105].

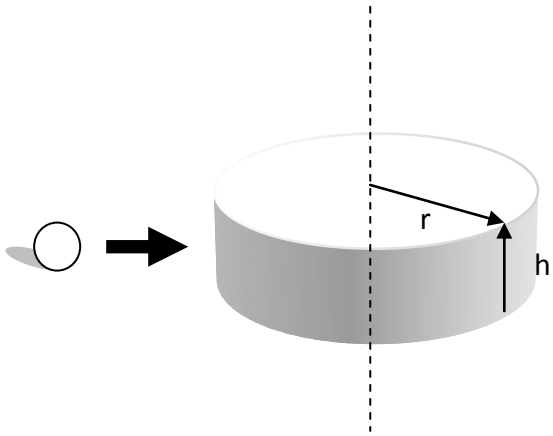


Figure 4.4 Schematic diagram of the incorporation of an atom to a growth centre (from [105]).

If the rate determining step in the electrocrystallisation process is the incorporations of an atom or a molecule, the current can be written:

$$\mathrm{I} = 2\pi\mathrm{rhnFk} \qquad \text{(Eq. 4.1)}$$

Where h the thickness of the monolayer, r is the radius of the nucleus, n the number of electrons involved in the electrode reaction, F the Faraday constant and k the rate of incorporation.

The amount of charge of charge required to form the cylinder of new materials is

$$Q(t) = \frac{\pi r^2 hnF\rho}{M} \qquad \text{(Eq. 4.2)}$$

The differentiation of the equation above gives the instantaneous current into the centre

$$i(r,t) = \frac{2\pi hnF\rho r(t)}{M}\frac{dr(t)}{dt} \qquad \text{(Eq. 4.3)}$$

The rate of radial expansion is equal to:

$$\frac{dr(t)}{dt} = \frac{Mk}{\rho} \qquad \text{(Eq. 4.4)}$$

The integration of that equation gives:

$$r(t) = \frac{Mk}{\rho} t \qquad \text{(Eq. 4.5)}$$

And thus

$$i(t) = \frac{2\pi nFk^2hM}{\rho} . t \qquad \text{(Eq. 4.6)}$$

The current of a single nucleus increases linearly with time. Practically, the nucleation involves the growth of many nucleation centres. If the growth centres are independent the integration of Eq. 4.6 it is trivial for the case of instantaneous and progressive nucleation. If all the N_0 nucleation centres are activated at the same time, the nucleation is called instantaneous and the current is

$$i(t) = N_0 \frac{2\pi nFk^2hM}{\rho} . t \qquad \text{(Eq. 4.7)}$$

If the nucleation centres are activated progressively at a rate A, the nucleation is called progressive and the current is:

$$i(t) = AN_0 \frac{2\pi nFk^2hM}{\rho} . t^2 \qquad \text{(Eq. 4.8)}$$

For a real surface the shape of the nuclei may not be disk-like and the interaction between growth centres has to be taken into account. Figure 4.5 illustrates the general features of the current-time transients which are commonly observed during the initial stages of the electrocrystallisation of ZnO[107].

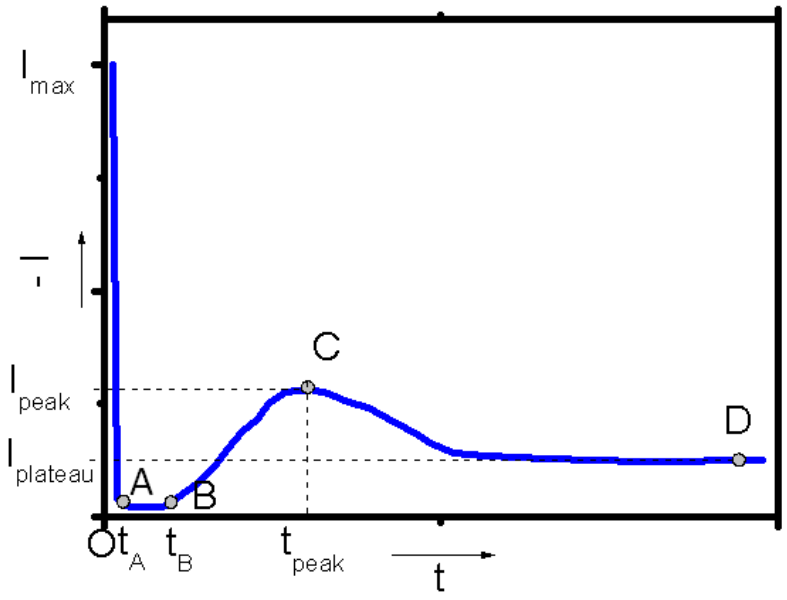


Figure 4.5 Drawing of the general shape of the transients observed for ZnO electrodeposition after [107]. I_{max} is the maximum current observed. t_{peak} and I_{peak} are the coordinate of the peak of current before the plateau whose value is $I_{plateau}$.

The transient is usually divided into the following sections:

1. O-A: After an initial surge, the current decays abruptly. This is related to any cationic species in the close vicinity of the cathode, which discharge immediately after the electrode is polarized[108].
2. A-B: An induction period where the current decreases slowly. The induction time t_b is linked to the temperature (it decreases with the temperature[109]).
3. B-C: three dimensional (3-D) nucleation and crystal growth
4. C-D: Overlap of the growth centres and coalescence of nuclei

Abyaneh and Fleischmann have calculated the expression of current for a nucleation and growth of 3-D conical centres when inclusion is the limiting step [107]:

In the case of instantaneous nucleation:

$$\frac{I}{I_{peak}} = \frac{t}{t_{peak}} \exp\left(-\frac{(t^2 - t_{peak}^2)}{2t_{peak}^2}\right) \qquad \text{(Eq. 4.9)}$$

In the case of a progressive nucleation:

$$\frac{I}{I_{peak}} = \frac{t}{t_{peak}} \exp(-\frac{(t^3 - t_{peak}^3)}{3t_{peak}^3}) \quad \text{(Eq. 4.10)}$$

The expressions for instantaneous nucleation and progressive nucleation with 3-D growth under diffusion controlled are given by the equations 4.10 and 4.11, respectively [110]:

$$\frac{I^2}{I_{peak}^2} = 1.9542 \frac{t_{peak}}{t} (1 - \exp(-1.2564 \frac{t}{t_{peak}}))^2 \quad \text{(Eq. 4.11)}$$

$$\frac{I^2}{I_{peak}^2} = 1.2254 \frac{t_{peak}}{t} (1 - \exp(-2.3367 (\frac{t}{t_{peak}})^2))^2 \quad \text{(Eq. 4.12)}$$

4.2 Thermochemical Calculations

Lincot and co-workers have extensively studied the electrodeposition of ZnO[11, 103, 109, 111, 112]. In reference [109], a thermochemical study of the temperature effect on the deposition is presented. The potential–pH, solubility and species repartition diagrams calculated are presented in fig 4.2 in the domain of temperature 60°C – 70°C. The diagrams are calculated for an initial concentration in $ZnCl_2$ of 5 mM and a concentration in KCl of 0.1 M.

Figure 4.6a presents the potential-pH diagram for Zn in the presence of 0.1M of Cl^-. The domain between the two blue lines represents the domain of thermodynamic stability of water associated with the two following redox reactions:

$$½\ O_{2\,(g)} + 2H^+ + 2\ e^- \leftrightarrow H_2O \quad \text{(Eq. 4.13)}$$

And

$$2H^+ + 2e^- \leftrightarrow H_{2\,(g)} \quad \text{(Eq. 4.14)}$$

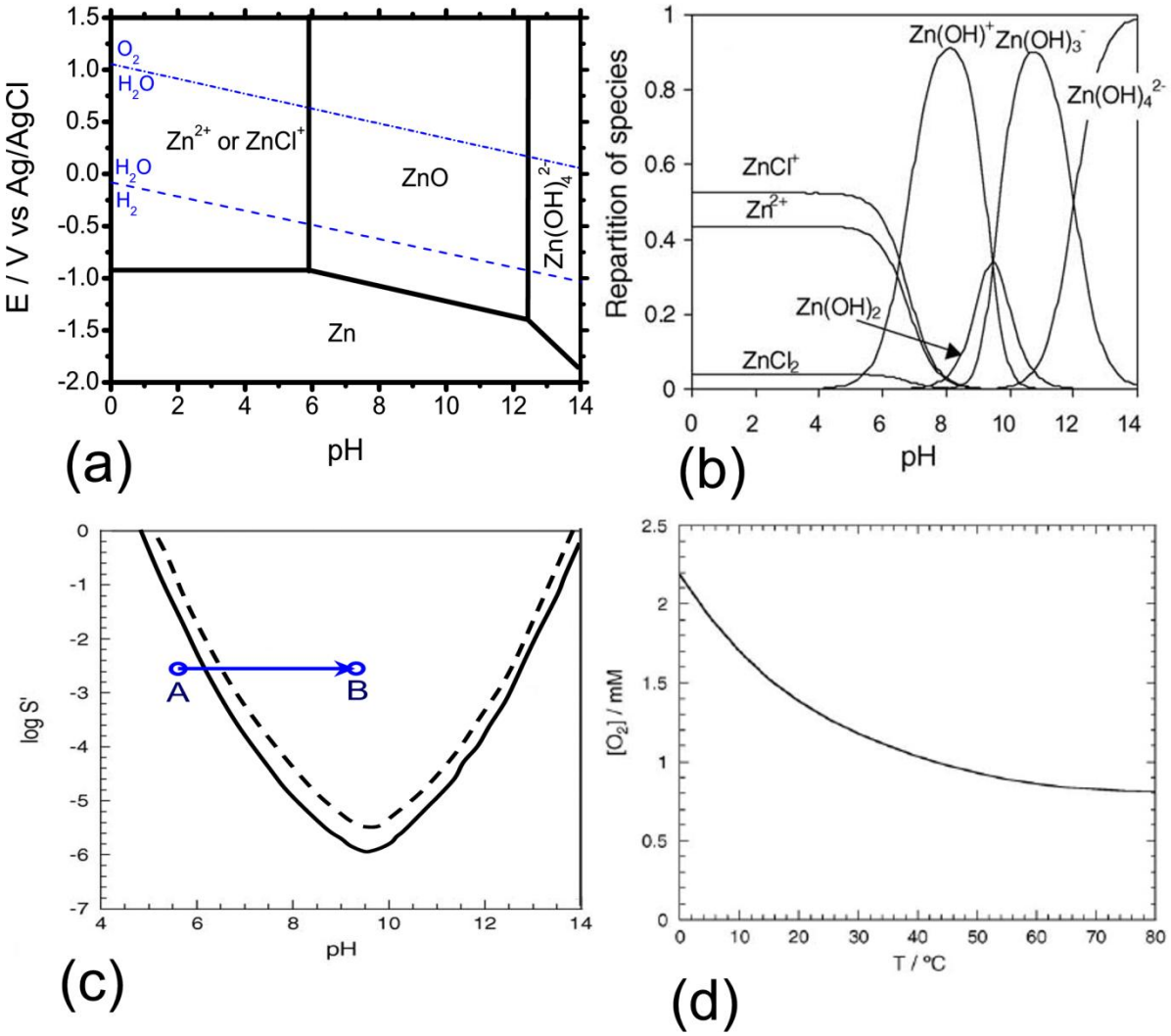


Figure 4.6 Thermochemical calculations from [109] (a) Effect of temperature on potential–pH diagram in the presence of 5mM Zn(II) and 0.1M Cl^- at 70°C. (b) Distribution of the soluble complexes as the function of the solution pH at 60°C. (c) solubility of ZnO (plain line) and $Zn(OH)_2$ (dash line) at 70°C (d) Effect of temperature on the solubility of oxygen at saturation in water

The most stable forms of the zinc soluble species are indicated in the diagram. One can clearly see the amphoterism of ZnO which can act as an acid or as a base according to the following reactions:

$$Zn^{2+} + H_2O \rightarrow ZnO + 2H^+ \qquad \text{(Eq. 4.15)}$$

And

$$Zn(OH)_4^{2-} + 2H^+ \rightarrow ZnO + 3H_2O \qquad \text{(Eq. 4.16)}$$

At 65 ^{o}C ZnO is stable between pH 6 and pH 12.5. For the same temperature, the lower potential limit for the deposition, corresponding to the Zn(II)/Zn(0) redox limit, is −0.95 V versus Ag/AgCl. Theoretically, it should be possible to deposit ZnO from about +0.5 V versus Ag/AgCl. Practically the deposition starts on gold for a potential of about -0.35 V due to the overvoltage and poor catalytic properties of Au for molecular oxygen reduction[111].

Figure 4.5b presents the distribution of the soluble complexes as the function of the solution pH at 60^{o}C. The pH of 5 mM solution of $ZnCl_2$ dissolved in deionised (DI) water is about 5.6. At this pH about 55% of the Zn (II) ions are complexed by one Cl^- ion, 40 % are not complexed and 5% are complexed by two Cl^-. A. Goux et al. determined by Energy-Dispersive X-ray Spectroscopy (EDS) chloride content in the film at various deposition temperatures and conclude that the complexation of Zn^{2+} by chloride ions does not seem to favour the inclusion of Cl in the film[109].

Figure 4.6c presents the solubility of ZnO (plain line) and $Zn(OH)_2$ (dash line) in the presence of 0.1M Cl^-. Compared to other metal oxides, ZnO is more soluble and the deposition reaction of is reversible. Growth under near-equilibrium conditions with fast redissolution steps may explain the formation of large and good structural quality crystals by a dissolution/precipitation mechanism[113]. Point A represents the bulk solution and point B represent a point at the vicinity of the electrode during the deposition[11]. ZnO is less soluble than $Zn(OH)_2$ and therefore should be the compound formed.

Figure 4.6d shows the dramatic change of solubility of O_2 with temperature: the solubility of O_2 decreases sharply with temperature. At 65^{o}C a saturated solution contains 8.10^{-4} M of O_2. Consequently high deposition rate cannot be obtained using oxygen alone as a precursor[114].

4.3 Effect of the Deposition Parameters

4.3.1 Temperature

The nature of the phases depends of the temperature: from a thermochemical point of view, an increase in temperature favours the formation of zinc oxide with respect to zinc

hydroxide[109, 115]. A. Goux et al carried a mechanistic study of the effect of temperature on the growth of ZnO on ITO from a solution containing 5 mM of $ZnCl_2$ and 0.1M of KCl[109]. The deposit crystallographic structures were characterised by X-Ray Diffraction (XRD). They reported that the lowest temperature at which it is possible to deposit crystalline zinc oxide is 34°C. They calculated the average crystallite size with the Scherer formula:

$$D = \frac{0.89\lambda}{b\cos\theta} \qquad \text{(Eq. 4.17)}$$

Where λ is the wavelength of the incident beam, b the full width at half maximum (FWHM) of the diffraction peak and θ is the diffraction angle. They found that increasing the temperature from 34°C to 40°C leads to better crystallised films, the average crystallite size increasing form 20 nm to 60 nm. By comparing the intensity of the (101) and (002) reflection line with powder diffraction standard, they found that texturate of the film with the c-axis perpendicular to the substrate surface is also enhanced with increasing temperature form 50°C to 80°C. The same effect has been reported by Otani et al[115]. In the same experimental conditions, Marí and co-workers report that lowering the temperature from 85°C to 65°C produces longer columns[116, 117]. They report the coalescence of the columns but do not discuss the evolution of the aspect ratio of the nanostructures. No PL emission is observed on these as-deposited films[117]. They report that the change in luminescence after annealing are very dependent on the annealing conditions but are *not* very sensitive to the deposition conditions.

The temperature limit to deposit crystalline ZnO is dependent on the deposition conditions such as the hydroxyl precursor. With much higher concentration of hydroxyl precursor (0.01 M $Zn(NO_3)_2$ and 0.1 M KNO_3) and lower potentials, Zhang et al. report the formation of crystalline ZnO at 0 °C[118]. The as-prepared ZnO film is uniform and ZnO grains are composed of hexagonal grains and/or granular grains with diameters between 10 and 15 nm. They also have carried out a linear voltametry at different temperatures. With the decrease of bath temperature, the onset potential for the reduction of nitrate negatively shifts and the cathodic currents drop significantly at the same potential. One can deduce from their curves that the potential window for the electrodeposition dramatically decreases as temperature decreases: the cathodic current of the nitrate

reduction start at -1 V, -1.3 V and -1.4V vs. Ag/AgCl for a temperature of 70°C, 30°C and 0°C respectively. This is in agreement with the Nernst equation (Eq. 4.18) for the reaction of reduction of the nitrate which predicts a decrease of the reduction potential with temperature.

$$E_{red} = E^0_{red} - \frac{RT}{2F} \ln\left(\frac{[NO_3^-][OH^-]^2}{[NO_3^-]}\right) \quad \text{(Eq. 4.18)}$$

Where E_{red} is the half-cell reduction potential, E^o_{red} is the standard half-cell reduction potential (E^o_{red} =-0.20 V), R is the universal gas constant (R = 8.314 J K^{-1} mol^{-1}), T is the absolute temperature, F is the Faraday constant (F = 9.649×10^4 C mol^{-1}).

4.3.2 Applied Potential or Current Density

The electrodeposition of ZnO was first demonstrated by two groups who worked with different sets of conditions[103, 104]. Most of the following papers have studied the effect of the parameters in one of those sets of conditions. In the first set, a zinc nitrate solution with a concentration of 0.1 M is used. In the second set, $ZnCl_2$ at low concentration (typically 5 mM) and a KCl support electrolyte to insure a good conductivity of the solution is used. The oxygen precursor is either O_2 or H_2O_2. Figure 4.7 summarizes the number of publication as a function of zinc precursor concentration from 1996-2006.

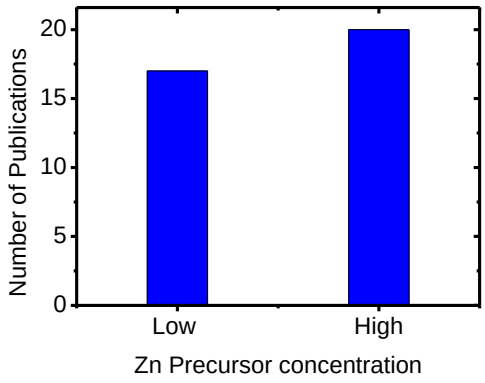


Figure 4.7 Number of published papers from Current Contents Connect data base as a function of zinc precursor concentration (from 1996 to 2006)

As the effects of the parameters are dependent on the type of conditions, we will firstly study the first case (high zinc precursor concentration) and then the second case (low zinc precursor).

4.3.2.1 High Zn Precursor Concentration

The main effect of decreasing the potential is to increase the deposition rate[104, 114, 119, 120]. For High Zn^{2+} concentration, the influence of the potential and the current density on the film orientation is not clear. On one hand, a loss of the preferential (002) orientation is reported for high potential and current densities[104, 119, 120]. On the other hand it is reported in reference [121] that (002) preferential orientation increases with the potential. All the parameters of these 4 papers are very similar apart from the substrate (the deposition is carried out on a Si[121] substrate instead of a conductive transparent oxide[104, 119, 120]). The orientation of the films is dependent of the substrate. A strong influence of the potential on the morphology has been reported[11, 104, 121-127] (see Figure 4.8). A transition from rods to plates to dense films to nodules is observed when the potential is increased from -0.7 V to -1.4 V[104]. The microstructure parameters were calculated by Marotti and co-workers[126]. They calculated the crystallite size using the Williamson-Hall approach:

$$b\cos\theta = \frac{K\,\lambda}{D} + 4\varepsilon\sin\theta \qquad \text{(Eq. 4.19)}$$

Where b is the FWHM, θ is the peak position, λ is the wavelength of the incident beam, K a constant close to unity, D is the crystallite size and ε is the microstrain. Microstrain was found to be of the order of 0.001 (below the uncertainty of the method). No dependence of the crystallite size with potential or current was found within their uncertainty.

4.3.2.2 Low Zn Precursor Concentration

Low zinc concentrations seem to minimise the influence of the potential: the publications [122], [128], [125] and [126] present SEMs of films deposited under similar conditions apart from the applied potential. While varying the potential from -0.5V to -0.85V/NHE no change of morphology type is observed. The films are composed of rods that coalesced with time to form dense films. Decreasing potential increases the

quantity of hydroxide produced. For low zinc concentration the deposition mechanism is more likely to be limited by the diffusion of Zn^{2+}. The rate of production of hydroxide has thus less influence.

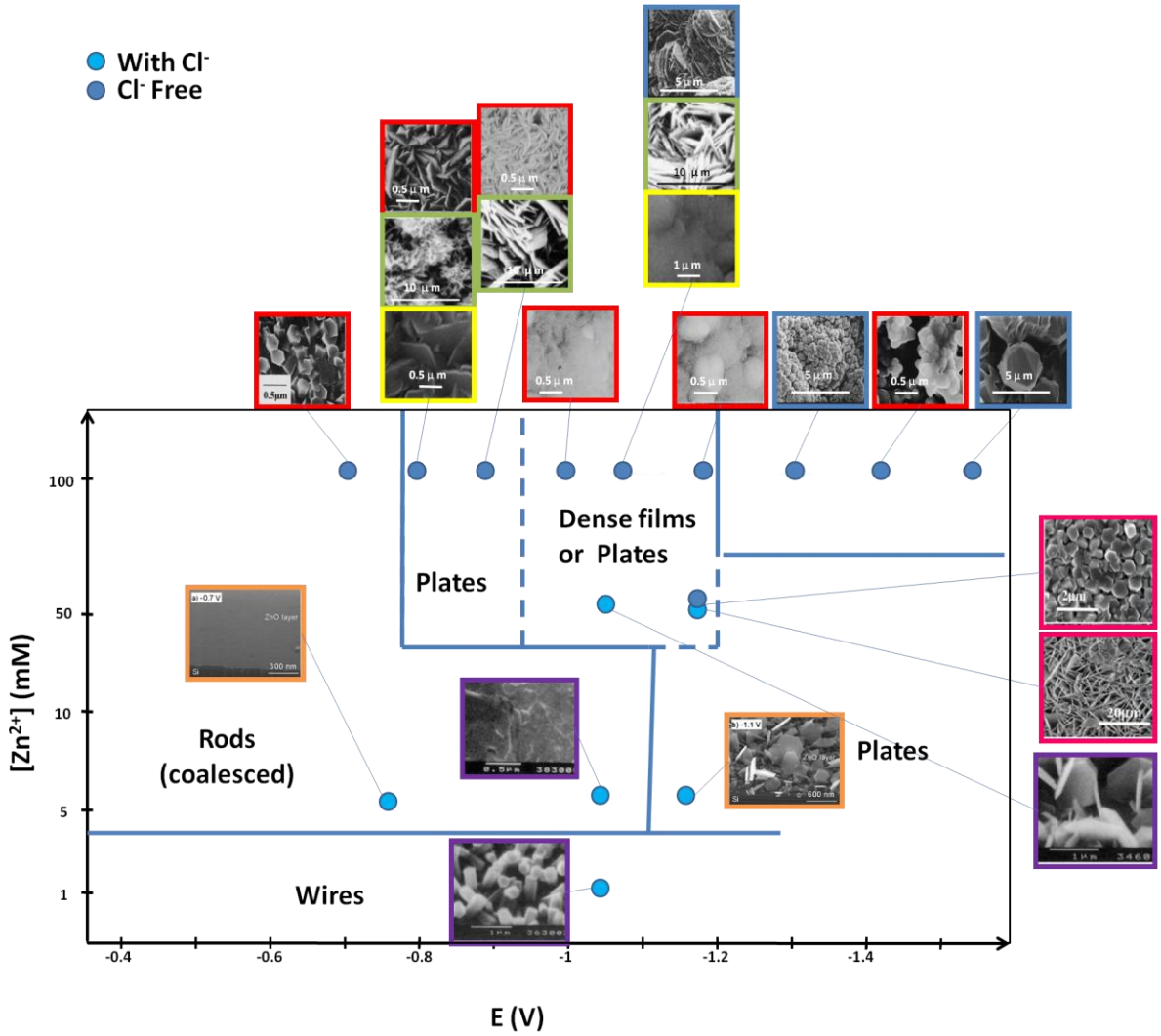


Figure 4.8 Phase Diagrams of the structures obtained by electrodeposition from an aqueous electrolyte containing only $Zn(NO_3)_2$, $ZnCl_2$, O_2 or KCl at temperature ranging from 60°C to 80°C. The colour of the pictures border indicated the source of the images: red[104], purple[11], blue[121], green[123], yellow[126], orange[127], pink[129].

4.3.3 Zinc Precursor Concentration

4.3.3.1 High Zn Precursor Concentration

The deposition rate is maximum for a concentration of 0.1 M of Zn^{2+} [119, 130]. Films prepared from 0.01 to the 0.2M electrolytes were identified as ZnO having a wurtzite structure[130]. The films prepared from 0.03 to 0.1 M electrolytes show a well-defined (001) preferred orientation[130]. For a concentration of zinc nitrate greater than 0.1M the

Zn content in films is 53 wt%, far from the stoichiometry of ZnO (80 wt%). The films prepared from a 0.5M electrolyte have been identified as $Zn_5(NO_3)_2(OH)_8$ -$2H_2O$[130].

4.3.3.2 Low Zn Precursor Concentration

Peulon and Lincot have studied the influence of concentration[11]. They report that there is a saturation of the mass for high zinc concentration (>2.10^{-2} mM). At low concentration they obtained hexagonal zinc oxide rods. The rods are crystalline with a preferential orientation perpendicular to the gold substrate. For high zinc concentration: (>2.10^{-2} mM) they report the formation of zinc hydroxychloride $Zn_5(OH)_8Cl$. For intermediate zinc concentrations, dense films are formed.

Elias and co-workers[131] have carried out a systematic study of the influence of Zn(II) at low concentrations. They explained the formation of 1-D (one dimensional) nano-structures by a limited diffusion of Zn ions which preferentially react at the top of the rods and thus lead to a growth along the c-axis. This explanation has been refuted by Belghiti and co-workers[132] who argue that such a limitation should lead to the formation of conical structures. They explained the formation of wire-like structures at low zinc concentration by a sharp increase of the pH at the beginning of the deposition leading to a change of the growing unit and a preferential growth on the top metastable face of the rods whereas the non-polar side faces are not reactive enough for further growth.

4.3.4 Oxygen Precursor

3.3.4.1 Nitrate

Oshida et al[133] found that the rate of the film growth in the nitrate bath is limited by the charge transfer kinetics. Using the Langmuir absorption model they derived an equation linking the current and the concentration of Zn^{2+} and NO_3^-, and verified this experimentally. They also found that the Zn^{2+} can act as catalyser for the reduction of nitrate. This result has been confirmed by Zhang et al[118].

Nitrate ions are very soluble, but their reduction leads to side reactions that produce nitrite and ammonium ions after further reduction. The accumulation of species in the deposition bath may limit the industrial applications[134].

3.3.4.1 Oxygen

The effect of oxygen has been studied by Lincot and co-workers[11, 111, 135]. They report that a higher oxygen concentration leads to a higher current plateau for the current transient curves. Nevertheless, the deposition rate is not proportional to the oxygen concentration, it saturates with high oxygen concentration. The kinetics is thus not only limited by the diffusion of oxygen, the incorporations of ad-atoms on to the surface can be limiting at high concentration. Increasing the oxygen concentration increase the local supersaturation in the vicinity of the electrode. It increases the density of the nucleation sites and it leads to a smaller grains size.

The use of O_2 does not lead to the formation of by-products that may contaminate the electrodeposition bath during the process but the solubility of O_2 in water is very low (see Figure 4.6d).

4.3.4.2 Hydrogen Peroxide

In order to increase the rate of the electrochemical reaction (hydroxide production), Pauporté and Lincot have used hydrogen peroxide[114, 134]. H_2O_2 is very soluble in water and does not produce by-products, making it suitable for industrial applications. However, high deposition rate have not been obtained due to poor electrochemical kinetics of the hydrogen peroxide reduction. The reduction current of hydrogen peroxide on a gold substrate is more than 50 times higher than on a ZnO substrate[114].

4.3.5 Substrate

Most of the papers report electrodeposition carried out on a transparent conductive oxide, because of their potential opto-electrical applications[11, 104, 109, 114, 116, 117, 119, 122, 123, 128, 129, 135-149]. Nevertheless, transparent conductive oxides, such as indium doped tin oxide do not have a well defined structure and composition. ZnO has also been electrodeposited on to a variety of conductive substrates such as gold[11, 114, 150-152], steel[151], silver[151], copper[126], platinium[111], zinc[13], silicon[121, 127, 153, 154], gallium nitride[125, 155] and boron-doped carbon electrodes[156]. Epitaxial growth of ZnO by a solution process has been reported on gallium nitride (GaN)[125], single-crystalline gold[150] and ZnO single crystal[157].

Pauporté et al[125, 155] emphasize the key role of GaN surface defects on the formation of epitaxial nucleation centres. It also seems that an ammonia pre-treatment is necessary to obtain a good zinc oxide nucleation onto high-quality GaN. They have also studied the current densities as a function of time for different substrates[114]. They show that the electrode behaviour during the first 30–50 s mainly reflects the catalytic properties of the initial substrate for the reduction. After nucleation and growth, they behave similarly to ZnO electrodes.

Illy et al.[13] have shown that the substrate condition strongly influences the deposit morphology through the availability of nucleation sites.

Cembrero et al[117] have compared the characteristics of rods grown under the same condition on two different substrate GaN and fluorine-doped tin oxide glass. The substrate has a clear influence on the aspect ratio and density of the nanorods. They reported that the use of substrates with lower sheet resistances results in a reduction of the size of nanocolumns.

By comparing the results of Canava[128], Peulon[11], Liu[150] and Pauporté[125], which report experiments carried in the same conditions except for the substrate, one can see that the substrate has an influence on the homogeneity, density and size of the nanostructures but *not* on the morphology type.

4.3.6 Influence of the Anions and Surfactant

Surfactants have been used as a templating agent in the deposition solution to control the size and shape of the ZnO nanostructures. There is no simple explanation of how surfactants affect the growth, because the mechanism on the surface is complicated; however it is generally accepted that adsorption on to specific crystal faces can lead to preferential growth and shape development. It has been shown that the morphology can be changed from 1-D structures to 2-D structures by using chloride ions, acetate ions, ethylenediamine or ammonium fluoride [158]. Li and co-workers [159] used citric acid as a shape-control agent and have shown how it modifies nanodendrites. Significantly more work has been carried out with CBD; e.g. phosphate ions have been used to form nanosheets[160]. Yahiro and co-workers have studied the effect of various molecules on the growth of ZnO prepared by CBD in an alkaline solution[161]. They found that acetic

acid had no effect on the morphology under any conditions. They also reported that the presence of citric acid decreased the deposition rate and promoted the formation of a planar morphology. A similar effect of citrate anions have been reported by Tian and co-workers[162,163]. They explained that the change in morphology from rods to plates as due to the preferential absorption of citrate ions on the (002) face restricting (or poisoning) the growth in that direction.

For electrolytes containing a low concentration of Zn precursor, a potassium chloride support electrolyte is added in order to minimize the solution resistance. Tena-Zaera et al. have studied the influence of the support electrolyte[164]. They report that increasing the KCl concentration decreased the rate of O_2 reduction and led to an increase of the deposition efficiency. Increasing the KCl concentration results in an enhancement of the longitudinal growth rate but also favours the lateral growth due to the absorption of Cl^- on the (001) ZnO face. Rods with a lower aspect ratio are obtained.

Pauporté and Lincot[134] have compared the influence of perchlorate and chlorate. The main advantage in using perchlorate instead of chloride ions is that perchlorate is a lower complexing agent and avoids the inclusion of species related to using potassium chloride. Presence of Cl in the films have been reported when using potassium chloride as a support electrolyte[11]. Changing Cl^- to ClO_4^- anions in the solution leads to less well-defined hexagonal crystallites and decrease the band gap from 3.52 eV to 3.38 eV[135]. The use of surfactant molecules appears as a simple way to tune the morphology and properties of the films.

4.4 Field of Research

This work will focus on understanding the deposition mechanism in order to control the growth and so make new, or better defined materials. Electrochemical measurements of ZnO deposition do not provide a clear way to determine the kinetics since the faradaic efficiency for deposition may differ between each experiment. So a direct measure of film growth is required. Our aim is to be able to follow the evolution of the ZnO in real time in order to achieve a complete understanding of the film growth mechanism. Such measurements are difficult because they involve small quantities of materials and short

time scales. The ability of synchrotron radiation to probe materials structure during deposition makes it the ideal tool for the study of nucleation and growth of zinc oxide nanostructures as a function of the processing parameters. Our methods to study the ZnO film growth, based on using X-ray Absorption Near-Edge Structure (XANES) and Grazing Incident X-Ray scattering (GIXS), will be presented in the next chapter.

Due to their potential industrial application, the deposition will be carried using the method developed by Lincot and co-workers[103]. The work will focus on gold substrates because of their good electrical properties and the ease with what well-defined electrodes at a relatively cheap cost can be obtained on a wide range of substrates.

ZnO is probably the richest family of nanostructures among all materials, both in structure and properties. The nanostructures could have novel applications. By mastering the deposition of ZnO, we aim to be able to design new nanostructures and thus get new properties.

Experiments carried out by CBD methods have shown that surfactant and complexing agent greatly influence the crystal shape of ZnO deposited particles. We will study how these chemicals influence the growth of the nanostructures during the electrodeposition. Electrodeposition of doped/mixed zinc oxide films with materials such as Bi[165], Mn[166], Co[167], N[168], Eu[169], In[170], Ce[171] or Al[172], controlled of the morphology by using templates such polycarbonate, aluminium oxide membranes[173] or polystyrene spheres[174] and non-aqueous electrolyte[175] will not be studied.

5 Experimental

This chapter outlines the synthesis techniques that have been used for the deposition of nanostructured zinc oxide as well as the various methods used to understand the mechanism of formation and to characterise the resultant structures. The first part describes the standard electrochemical set-up used to deposit the films. The electron microscopy techniques used to characterize the morphology and the compositions of the films after deposition are described in the second part. In the third part techniques based on synchrotron X-ray radiation are described. The focus is made on the synchrotron techniques in order to show how these techniques can help us to gain a better understanding of the deposition of ZnO. Finally the last part describes how the standard techniques have been adapted and developed in order to be able to study the deposition of ZnO *in-situ.*

5.1 Electrochemistry Techniques

5.1.1 Experimental Set Up

5.1.1.1 Three-electrode Set Up

Two half cells are necessary to study and control an electrochemical process. The electrode of the first half cell must have a controllable potential and insure a good transfer of the electrons. The electrode of the second half cell must have a fixed and well know potential in order to control the potential at the working electrode and it must balance the electrons added by the working electrode. However potential and current are not independent and so it is extremely difficult for an electrode to maintain a constant potential while passing current. To solve this problem a three-electrode set up is used where the role of supplying electron and maintaining a fix potential have been separated: the auxiliary electrode completes the circuit and pass all the current; the reference electrode maintains a fixed potential during the deposition. A gold coated glass slide, a platinum mesh and Ag/AgCl/KCl (3.5 M) reference electrode were used as working, counter and reference electrode respectively. The potential of the reference electrode was +0.025 versus the normal hydrogen electrode at 25°C. All the potentials given in this work are against the Ag/AgCl/KCl (3.5 M) reference electrode. A Princenton VersaSTAT 3 potensiostat connected to a PC was used to control the potential and study the electrochemistry. Figure 5.9 presents a schematic view of the experimental set up.

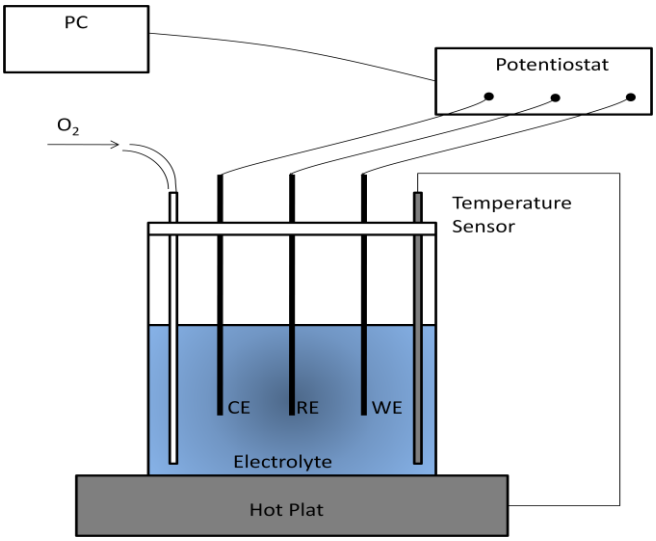


Figure 5.9 Schematic diagram of experimental setup, showing the electrochemical cell with a Pt counter electrode (CE), Ag/AgCl reference electrode (RE), and a gold coated glass slice which acts as the working electrode (WE)

5.1.1.2 Preparation of the Working Electrode

The experiments can be carried out on any conductive substrate. In our experiments, 100 nm sputtered gold films were used. They were sputtered on glass, Mylar© and quartz rods for the home, *in-situ* X-ray absorption and *in-situ* X-ray diffraction experiments respectively. The electrical connection between the sample and an electrical wire was insured by a drop of silver paint for the gold on glass sample. The contact was then covered with copper tape and insulating paint (Miccro Super XP200 Lacquer, Hi Tek Producs ltd, UK). The active area was about 150 mm^2. The preparation of the Mylar© and quartz samples are described in sections 5.4.1 and 5.4.2 respectively. Prior to the deposition, the samples were cleaned with methanol, acetone and deionised (DI) water.

5.1.1.3 Electrolyte

Potassium Chloride (KCl, BDH, 99%) and Calcium Chloride ($CaCl_2$, BDH, 90%) were used as support electrolytes in order to minimize the solution resistance. Zinc nitrate hexahydrate ($Zn(N0_3)_2$ $6H_2O$,Riedel DeHaën, 98%) and Zinc Chloride ($ZnCl_2$, Sigma-Aldrich, 98%) were used as zinc precursors. Sodium acetate ($H_3C_2O_2Na$, BDH, 99%), oxalic acid ($H_2C_2O_4$, BDH, 99.5%), citric acid ($H_8C_6O_7$, BDH, 99.5%) were used in order to study the influence of the carboxylic group. The pH was adjusted by adding a small amount of hydrochloric acid (HCl, BDH, 35.4%) or Potassium hydroxide (KOH, Aldrich, 85%) and was measured at room temperature. Oxygen (O_2, BOC) gas was bubbled 20 minutes prior to, and during, the deposition. Nitrogen (N_2, BOC) gas was used to remove air in order to study the effect of O_2. All the chemicals were used as-received without further purification. The temperature was held constant between room temperature and 90°C with PC-400D 5 x 7" Corning Digital Hot Plate equipped with a temperature sensor for the experiments realised in the standard set up. The accuracy of the control was +/- 1°C. The temperature control for the *in-situ* X-ray absorption and diffraction experience are described in section 5.4.1 and 5.4.2 respectively.

5.1.2 Electrochemical Methods

5.1.2.1 Cyclic Voltammetry (CV)

CV is the most widely used technique for acquiring qualitative information about electrochemical reactions. It offers a rapid location of redox potentials of the electroactive species, and convenient evaluation of the deposition parameters upon the redox process. It consists of a linear ramping in potential of the working electrode versus time. The data can be affected by the presence of uncompensated resistance in the solution phase between the reference and the working electrode and of the working electrode itself[176]. Positioning of the reference electrode close to the working electrode helps to minimise the IR drop between the reference electrode and the working electrode due to the resistivity of the solution phase[176]. The reference electrode must not be in the current path.

5.1.2.2 Electrodeposition

Cathodic electrodeposition (electroplating) is the process of using electrical current to reduce cations of a desired material from a solution and coat a conductive object with a thin layer of the material[177]. The experiments have been realised using a potentiostatic transient technique. The potential of the test electrode is controlled, while the current, the dependent variable, is measured as a function of time. The potential difference between the test electrode and the reference electrode is controlled by a potensiostat. After the deposition was complete, the as-deposited thin films were gently rinsed with de-ionised water and dried in a steam of air.

5.2 Electron Microscopy

A LEO 1525 Field Emission Scanning Electron Microscope (FESEM) equipped with an Oxford Instruments energy dispersive X-ray microanalysis was used for surface topography and quantitative compositional analysis. The electron microscope functions in a similar way to the light microscope except that a beam of electrons is used for imaging instead of a beam of photons. Higher resolution can be obtained due to the shorter wave length of the electron. A field emission gun is used to produce an electron beam that is smaller in diameter, more coherent and brighter. This is necessary because

of the nanoscale features of the material studied, some features being as small as a few nanometres.

5.2.1 Principle

Figure 5.10 shows schematically the optical path and key components of a typical SEM[178].

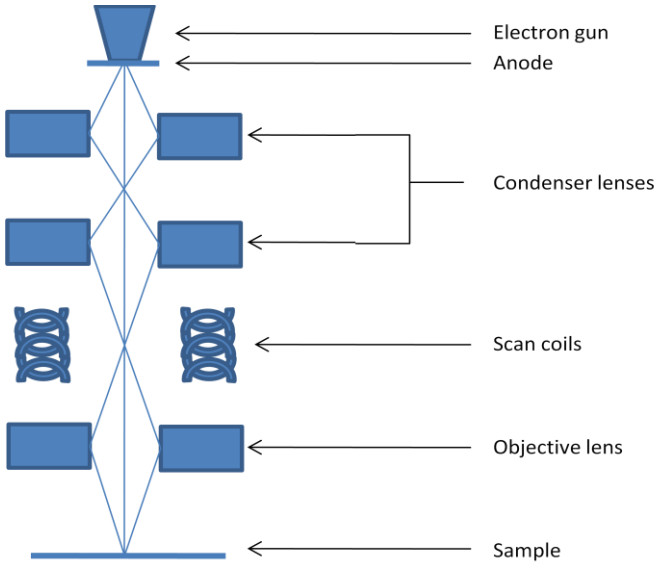


Figure 5.10 Schematic illustration of the electron column of a typical SEM[178]

A field emission gun produces a stream of monochromatic electrons. The electrons produced are then attracted by an anode plate through the condenser lens which produces a beam of limiting current. The condenser aperture eliminates high angle electrons and after passing through a second condenser lens, a thin, coherent beam is formed. An objective aperture further eliminates high angle electrons before a set of coils scan or sweep the beam in a grid fashion over the sample, stopping for specified times in designated locations. The objective lens then focuses the electron beam in a specific plan relative to the specimen. As the beam interacts with the sample, a number of signals are emitted from the point of interaction of the beam (see Figure 5.11)

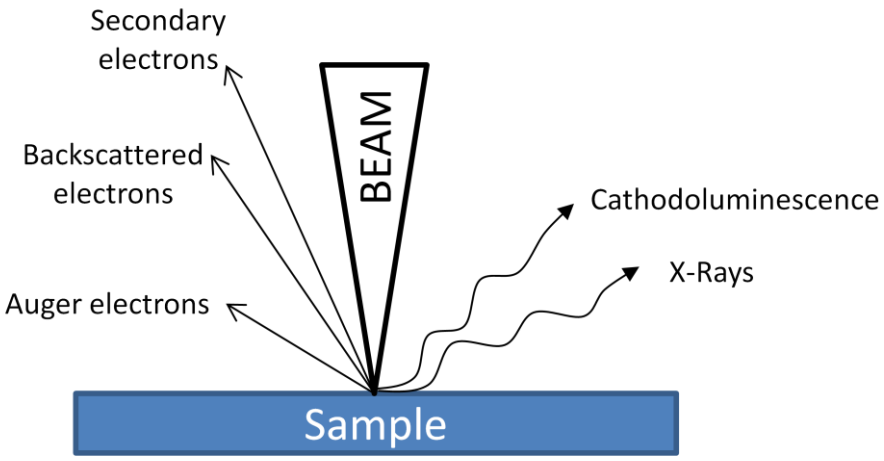


Figure 5.11 Photon and electron emissions from a sample hit with an electron beam[178]

When the electron beam contacts the sample surface each of the signals produced can be collected and amplified as long as the correct detector is used. These signals include the formation of back-scattered electrons (BSE), secondary electrons, x-rays, auger electrons and cathodoluminescence. They are briefly described bellow:

i. **BSE:** BSE are beam electrons that are reflected from the sample by elastic scattering. Backscattering events increases with increasing atomic number and thus can provide information about the distribution of different elements in the sample
ii. **Secondary Electrons:** Secondary electrons are produced as a result of interaction between energetic beam and weakly bound conduction electrons. The information depth is about 1/100 of that for BSE. The number of secondary electrons generated per unit area is much greater than BSE. During the scanning of the surface, they provide information about the local surfaces features and are used for imaging.
iii. **X-rays:** X-rays can be formed during inelastic scattering of the beam electrons. The analytical technique used during this work is described in paragraph 5.2.3.
iv. **Auger electrons**: When an ionized atom undergoes deexcitation, the electron transitions can result in the ejection of an electron (the Auger effect). The energy of the Auger electron is characteristic of the atom. The difference between the properties of characteristic x-rays and characteristic electrons in measuring the composition of the solid has to do with the depth of sampling. The x-ray signal is a measure on average over the whole interaction volume. Auger electrons spectrosocopy can provide a form of surface microanalysis, with a depth of sampling of the order of 1 nm[179].
v. **Cathodoluminescence:** The bombardment of certain materials, such as insulators and semiconductors can create an electron-hole pair. If no bias voltage exists, the electron and hole may recombine, realising the excess energy, which is equal

to the band gap, in the form of a photon. The analyse of the signal can give information about the presence of impurity atoms or crystal defects.

5.2.2 Imaging

The images in this work are formed from the emission of secondary electrons. The number of interactions are then summed and displayed as a pixel on a CRT. This process is repeated at each grid point producing an image which consists of thousands of spots of varying intensity. These spots correspond to the topography of the material being examined.

5.2.3 Energy Dispersive X-ray Spectroscopy (EDS)

EDS is an analytical technique used for the elemental analysis. As the electron beam hits the sample, incident electrons collide with and in some cases displace electrons orbiting around the atoms nuclei. This interaction leaves the atom in an excited state and in order to return to a stable state, an electron from a higher orbital moves into the space in the orbit vacated by the displaced electron. This process involves a reduction in energy through the emission of an x-ray. As each material has a unique atomic structure, the x-rays that are emitted are unique to each elemental material.

5.3 X-ray Absorption and Diffraction Studies

X-ray absorption is used to determine the electronic and atomic environments of a given element. XRD is used to identify the crystalline constituents of a sample. Combined they are a powerful way to study a materials. X-rays are produced either by electronic processes, namely tubes, synchrotron radiation, free electron lasers, or by decay of natural or artificial radioactive isotopes. X-ray tubes and synchrotrons have been both used in this work. The synchrotron experiments will be described in the following chapter.

5.3.1 Tube X-Ray Diffraction

XRD was performed to identify the phases present using a Philips PW 1710 diffractometer with Cu Kα radiation. The continuous spectrum emitted by an X-ray tube is due to the slowing down in the target of the electrons from the filament of the tube. The radiation produced is unpolarized. The intensity of the undesirable components is

decreased relative to the intensity of the Kα radiation by passing the beam through a filter made of Nickel[180]. Each XRD spectrum was collected with a scan step size of 0.04° and a scan step time of 1 s per point.

When X-rays hit a crystal, the electromagnetic waves produces a motion of the electronic clouds relatively to the atoms. The oscillation of the electrons provokes the emission of electromagnetic waves of the same frequency. This phenomenon is known as Rayleigh scattering. Due to the periodical order of the crystal, the phase relations are such that destructive interference occurs in most direction of scattering, but in few directions constructive interference takes place and diffracted beams are formed. This condition can be expressed by Bragg's law:

$$n\,\lambda = 2d\sin\theta \qquad \text{(Eq. 5. 1)}$$

Where n is an integer determined by the order given, λ is the wavelength of x-rays, d is the spacing between the planes in the atomic lattice, and θ is the angle between the incident ray and the scattering planes.

5.3.2 Synchrotron Radiation

5.3.2.1 Synchrotron Sources

Synchrotron radiation is the electromagnetic field radiated by a relativistically accelerated charged particle. For non-relativistic accelerated charges, the energy flux is emitted isotropically around the acceleration, in a large solid angle. At relativistic energies, the radiation pattern becomes sharply peaked in the direction of motion of the radiating charge, as shown in Figure 5.12. Synchrotron radiation is thus highly collimated and an extremely large flux can be obtained[181].

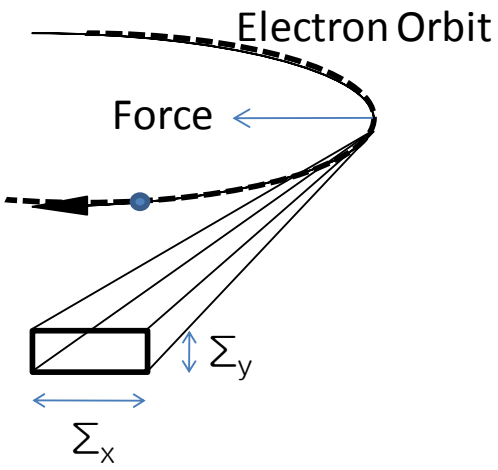


Figure 5.12 Synchrotron radiation emitted by a relativistic electron travelling along a circular orbit. The force is the magnetic field perpendicular to the orbit. $\Sigma_x \Sigma_y$ is the transverse area of the optical source[182].

The brilliance, which represents the flux of photons emitted by the source per solid angle, per unit source area and per bandwidth, is used to compare the performance of different synchrotron radiation facilities. It is up to 10^{17} times higher than traditional X-ray tubes. Such radiation is naturally produced by astrophysical sources in which highly energetic electrons are accelerated along a helical path in the presence of a magnetic field [182]. The energy loss of an electron due to the synchrotron radiation was first theoretically demonstrated in 1898 by Liénard[183]. The radiation was discovered in a General Electric synchrotron accelerator built in 1946 and announced in May 1947[184]. At this time it was considered as a nuisance to particle physics studies causing undesired energy loss. The production of synchrotron radiation by such devices was not taken into consideration until some years later when the possibilities introduced by this discovery were fully understood. The first dedicated generation of synchrotrons was made *via* alterations to accelerators built to study the physic of particle. The SPEAR ring at the Stanford Linear Accelerator Center was one of them. The brilliance was 10^5 higher than the one of an X-ray tube. The increasing imbalance between the demand for synchrotron radiation and its availability led to the creation of the so-called second generation sources, dedicated to the production of synchrotron radiation[185]. The National Synchrotron Light Source at the Brookhaven National Laboratory, where part of the synchrotron experiments have been conducted, is one of them. The first-generation

facilities gradually evolved toward second-generation and the Stanford Synchrotron Radiation Laboratory was created, where the second part of these experiments have been carried out. In the 1990s, high energy facilities optimized to generate brilliant undulator radiation in the hard x-range (1–20 keV) were built and commissioned and these were the first of the third generation synchrotrons[186]. Plans for a 4th generation, based on free electron lasers, are currently set out, the brilliance will be 10^{28} higher than a standard x-ray tube, and the source fully coherent[187].

The components of a synchrotron include an electron gun, linear accelerator, a circular booster ring (to increase the speed of the electrons), storage rings (to re-circulate electrons), and the experimental beamlines. The study of the former involves particle physic which is out of the field of this work. Briefly: the optical system is composed of a source emitting a beam and of optical elements that transform this beam downstream till the samples under study and the following detector. It usually includes the following:

- A slip to shape the beam
- Mirrors to focus the beam
- Monochromators to select particular wavelength bands and absorb other wavelengths
- A beam hutch to protect users from the radiation
- Ion chambers to measure the intensity of the radiations
- A sample stage to position the sample
- A detector
- Computer hardware and software to analyse the results

Synchrotron radiation covers a very wide spectral range, from the infrared to the hard X-rays and has been used to investigate a vast field of science. The remainder of this sections looks at varying techniques that have been used to study the growth mechanism of ZnO in this work.

5.3.2.2 X-Ray Absorption Spectroscopy (XAS)

XAS is the measurement of the of the x-ray absorption coefficient of a given material versus energy. A narrow parallel monochromatic x-ray beam of intensity I_0 passing through a sample of thickness x will emerge with reduced intensity I according to the expression:

$$\ln(\frac{I_0}{I}) = \mu x$$

or $$I = I_0\, e^{-\mu x}$$ (Eq. 5.2)

where μ is the linear absorption coefficient. When the incident x-ray energy matches the binding energy of an electron of an atom within the sample absorption of the material increases dramatically, causing a drop in the transmitted x-ray intensity. This results in the absorption edge in the plot (see Figure 5.13).

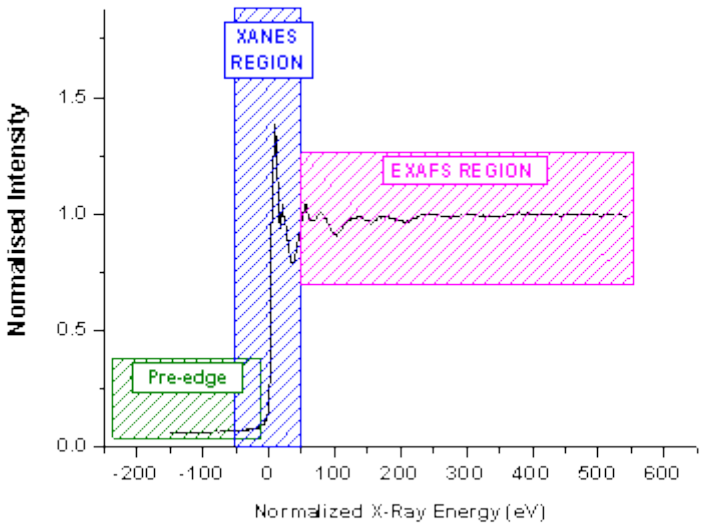


Figure 5.13 Typical X-ray absorption spectrum realised in fluorescence of an ZnO sample deposited during our experiments. The pre-edge, XANES and EXAFS regions are showed.

The XAS spectrum can be quite complex with several regions, as shown above. The different region of the spectrum can be resolved and provide complementary information about the materials:

- The pre-edge region, where the electron has been excited but not emitted, can show features in some elements that can give information on the oxidation state or co-ordination
- The XANES region, up to 50eV beyond the edge, where the electron is slow-moving, provides information on the oxidation state of the atom and the local geometry around the atom.

- The extended X-ray absorption fine structure (EXAFS) region, up to 1keV beyond the edge, the electron is fast moving and give details information about co-ordination numbers and bond lengths.

XAS experiments were conducted on beamline X10C at the National Synchrotron Light Source, Brookhaven National Laboratory, New York. The beamline is designed for XAS with an energy range between 3.5 and 24.7 keV and is equipped for wet chemistry which makes it suitable for the our experiments.

5.3.2.3 Grazing Incidence X-Ray Scattering (GIXS)

XRD carried out in a standard geometry is not well adapted to the study of thin films, because X-ray penetrates through the matter and therefore there is a strong parasite signal from the substrate. To answer this problem we have been using GIXS. The reflection index for X-ray is slightly less than 1. Therefore there is a critical angle below which the X-rays are totally externally reflected[188]. The scattering is limited to the near surface region and the study of thin films is possible. Figure 5.14 illustrates the incident X-ray penetration depth as a function of incidence angle α[189].

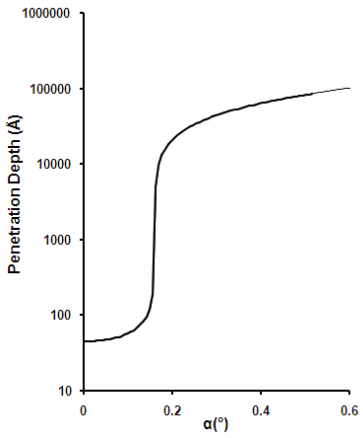


Figure 5.14 incident X-ray penetration depth as a function of incidence angle α from [189]

The main advantage for thin film is to decrease the signal from the substrate. The exit angle β is often small and, thus, the scattering vector, Q, which is the difference between the incident and scattered x-ray vectors (k and k' respectively), is in the plane of the sample; diffraction from planes perpendicular to the sample surface are measured. Figure 5.15 illustrates the geometric aspects of GIXS.

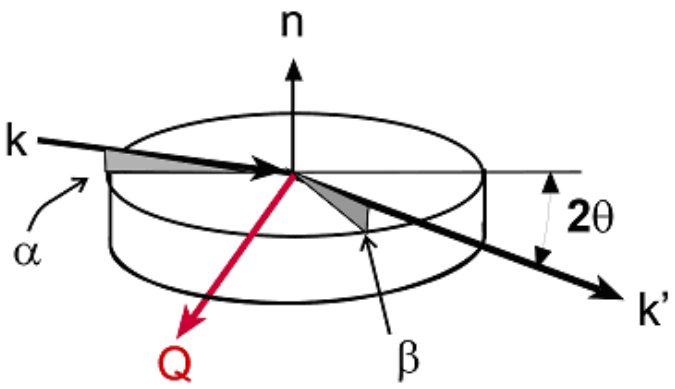


Figure 5.15 schema of the geometry aspect of GIXS from[189].

GIXS experiments were conducted using the area detector on beam line 11-3 of the Stanford Synchrotron Radiation Laboratory at the Stanford Linear Accelerator Center, California.

5.4 Development of *In-Situ* Characterisation Techniques

5.4.1 *In-Situ* X-ray Absorption

The experimental set-up is based on the set up developed by Kerkar et al.[190] (see Figure 5.16). The working electrode consists of a thin Mylar window (6 µm) on which has been sputtered about 100 nm of Au. The electric connection from the electrode to circuit was see by a piece of copper tape. The connection was covered by Devon 5 minute epoxy. Monochromatic x-rays were incident at 45° to the electrode surface and Zn 1s orbital radiation (k-edge) was detected with a solid state detector placed at 90° to the incident x-rays i.e. the signal is measured in fluorescence. This set-up removes the need for thin film cells often used for transmission geometries. In this way a conventional 3-electrode set-up with bulk solution can be used. Radiometer Voltalab PGZ402 potentiostat, was used to control the applied potential. The temperature was held constant using a heating tape wrapping of the cell. The accuracy of the temperature controlled was +/- 2°C. The rest of the electrochemical cell set-up is the same as described in section 5.1.1.

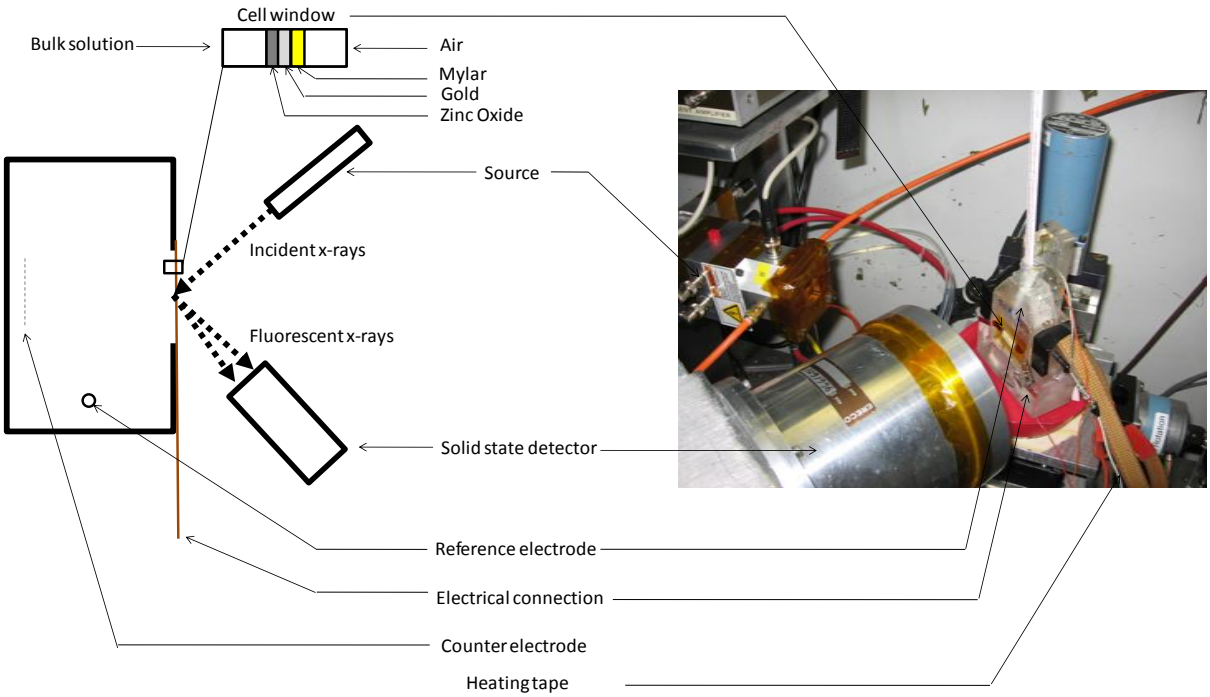


Figure 5.16 Schematic plan and picture of the cell of the *in-situ* XAS set-up.

5.4.2 *In-Situ* Grazing Incidence X-Ray Scattering

XRD experiments were conducted *in-situ* using a custom-made cell on beam line 11-3 at the Stanford Synchrotron Radiation Laboratory. The beam size was 0.15 mm (horizontal) × 0.05 mm (vertical) and the wavelength 0.9736 Å. A LaB6 powder standard was used for calibration. The substrate was a quartz rod covered with 100 nm of sputtered gold; this was positioned in a grazing-incidence geometry with a 2 mm X-ray path length through the solution at the base of the cell and acted as the working electrode. Diffracted X-rays were detected with an MAR345 image plate. Images were taken every 1.5-2 min (10 s to collect and 1.5 min for the detector to read out) in a sequence, with two scans recorded before the potential was applied. A diagram of the cell is shown in Figure 5.17. The cell was held by an aluminium support. Holes were drilled in the support in order to insert heating cartridges (OMEGALUX® CS series). The accuracy of the temperature controlled was +/- 2°C. The electrochemistry was controlled with a Gamry PCI4/300 potentiostat. The rest of the electrochemical cell set-up is the same as described in section 5.1.1.1

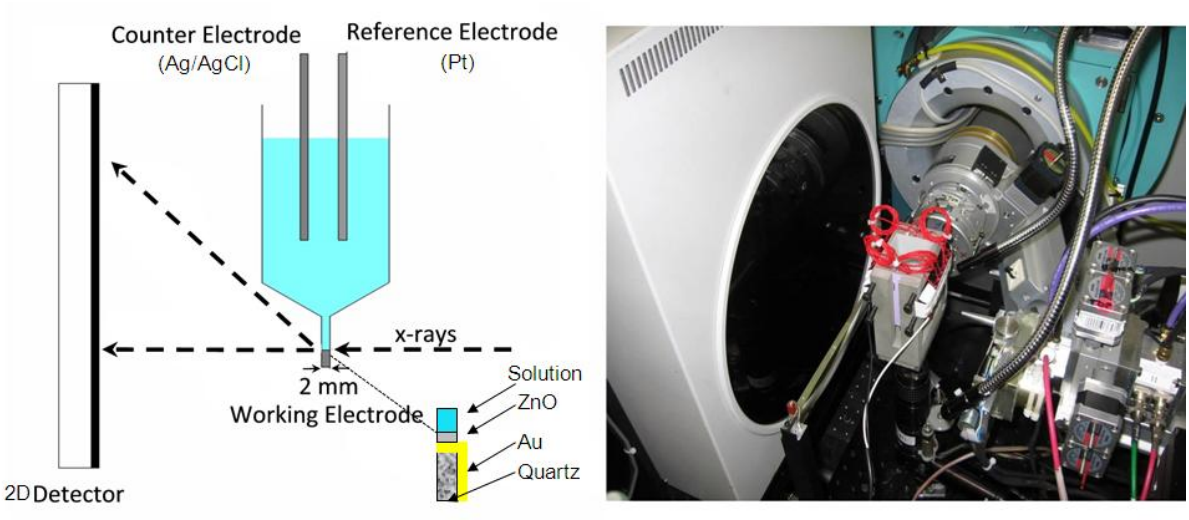


Figure 5.17 Schematic side view and picture of the cell

6 Results and Discussion

6.0 Methodology of Study

The structure and morphology of electrodeposited ZnO films can be controlled by variation of the deposition parameters such as temperature, pH, applied potential, deposition time, zinc precursor concentration, oxygen precursor concentration and concentration of support electrolyte or other molecules in solution. The aim of this project is to understand how these deposition parameters affect the growth, in order to get the desired morphologies and properties. We will study the effect of these parameters by varying one at time and keeping the other ones constant in standard conditions. The standard conditions will be a solution containing 5 mM of zinc nitrate and 0.1 M of KCl at a fixed temperature of 65°C with an applied potential of -0.97 V. The electrodeposition was carried out from a solution containing both nitrate and oxygen. Usually only one is used as oxidant. In this work both precursors have been combined in order to gain a better control on the hydroxide production (see section 6.1.2). Nitrate is not reduced for potentials lower than -0.8V. Table 6.1 summarizes the experimental conditions studied during this work.

	Lower limit	Upper limit
Deposition time	0	90 minutes
Dissolution time	0	5 hours
Potential	-1.8 V	0
Zn(II) concentration	0.5 mM	100 mM
pH	2	6.5
Cl(-I) concentration	0.1	0.2
Capping agent: number of carboxylic groups	0	3

Table 6.1 Summary of the experimental condition used in this work.

The first section will be dedicated to an electrochemical study of the system in the defined standard conditions. In the second section we will discuss the influence of time and check the validity of the methods of characterisation developed in this work. The effect of potential, support electrolyte and concentration will be studied and discussed in the third, fourth and fifth section respectively. The sixth section will be dedicated to the effect of pH and the formation of tubular structures. Finally the last section will be devoted to the effect of carboxylic surfactants. The same methodology will be followed for all the parameters. Firstly, the results from electron microscopy will be presented. Then we will compare our *in-situ* growth measurements based on XANES with the current transient curves. Thirdly we will present the results of our *ex-situ* and *in-situ* XRD measurements. Finally the influence of the parameters will be discussed. The effect of the temperature have not been studied in this work as a clear understanding of its effects can be found in the literature[109].

6.1 Electrochemical Studies of the System in the Standard Conditions

The deposition of ZnO is a coupled reaction with two steps: firstly an electron transfer step, reduction of the oxygen precursor, secondly a chemical step, the precipitation of ZnO. CV is powerful tool to investigate such a system. However we can only have a direct access to the electron transfer step, as no current is associated with the chemical reaction. The most commonly used hydroxide precursors oxygen and nitrate ions, are studied.

6.1.1 Cyclic Voltammetry Studies of the Oxygen Reduction

Table 6.2 presents the standard potential of the stable redox couples the for Zn-Cl-H_2O system at 25°C[109, 191, 192].

Electrode	Reactions	E° (V/AgAgCl)	Ref.
ind.	$O_2 + H_2O + 4e^- \leftrightarrow 4\ OH^-$	0.20	191
	$ZnOOH^- + 2e^- + H_2O \leftrightarrow Zn + 3OH^-$	-0.25	109
ind.	$H_2O + O_2 + 2e^- \leftrightarrow HO_2^- + OH^-$	-0.28	191
	$ZnCl_3^+ + 2\ e^- \leftrightarrow Zn + 3Cl^-$	-0.92	109
	$Zn^{2+} + 2e^- \leftrightarrow Zn$	-0.97	109
	$ZnCl^+ + 2\ e^- \leftrightarrow Zn + Cl^-$	-0.97	109
	$ZnCl_2 + 2\ e^- \leftrightarrow Zn + 2Cl^-$	-0.98	109
	$2\ H_2O + 2e^- \leftrightarrow H_2 + 2OH^-$	-1.03	192
	$ZnOH^+ + 2e^- \leftrightarrow Zn + OH^-$	-1.15	109
	$ZnO + H_2O + 2e^- \leftrightarrow Zn + 2\ OH^-$	-1.26	109
Zn	$Zn(OH)_3^- + 2e^- \leftrightarrow Zn + 3OH^-$	-1.39	191
Zn	$Zn(OH)_4^{2-} + 2e^- \leftrightarrow Zn + 4OH^-$	-1.42	191
Zn	$ZnO_2^- + 2H_2O + 2e^- \leftrightarrow Zn_{(s)} + 4OH^-$	-1.42	191
Zn	$Zn(OH)_2 + 2e^- \leftrightarrow Zn + 2OH^-$	-1.45	191

Table 6.2 Standard potential for the system Zn–Cl–H2O (the column "electrode" gives the electrode on which the value has been measured; if not specified, the value were calculated from the thermodynamic value found in [109]).

Figure 6.18a shows CV curves obtained in KCl solution (0.1M) without oxygen (black curve) and in the presence of oxygen (red curve) at 70°C with a scan rate of 10 mV/s.

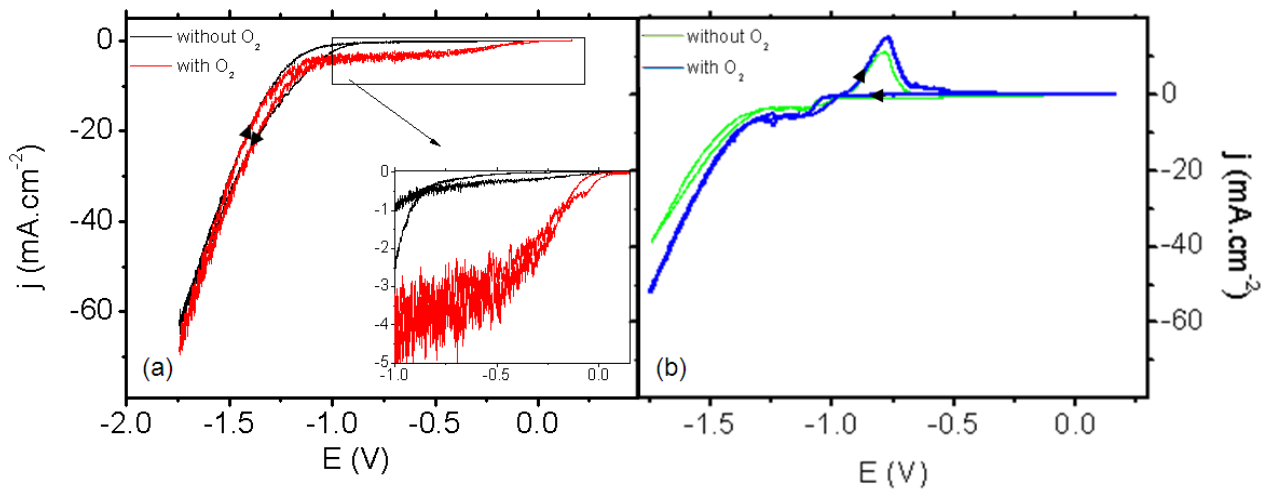


Figure 6.18 CV studies of the Zn-Cl-H_2O system 0.1 M of KCl at 70°C (a) without oxygen (black curve) and with oxygen (red curve) (b) 5 mM $ZnCl_2$ without oxygen (green curve) and with oxygen (blue curve).

Without oxygen, there is no electrochemical reaction observed from 0.1 V to -1V. From -1 to -1.8V, we observe a sharp increase in the cathodic current which can be attributed to the reduction of the solvent according to the following reaction:

$$2H_2O + 2e^- \leftrightarrow H_2 + 2OH^- \qquad E^o = -1.03 \text{ V/AgAgCl} \qquad \text{(Eq. 6.1)}$$

In order to avoid the production of H_2 gas at the working electrode, the applied potential will be kept below -1 V during the deposition.

In the presence of oxygen, the behaviour is modified. From -0.1 to -0.3 V, we observe an increase of the current followed by a plateau between -0.3V and -0.9V. These variations can be assigned to the oxygen reduction according to reactions (6.2) and (6.3) in parallel:

$$O_2 + H_2O + 4e^- \leftrightarrow 4\ OH^- \qquad E^o = 0.2 \text{ V /AgAgCl} \qquad \text{(Eq. 6.2)}$$

$$H_2O + O_2 + 2e^- \leftrightarrow HO_2^- + OH^- \qquad E^o = -0.28 \text{ V/AgAgCl} \qquad \text{(Eq. 6.3)}$$

During the plateau, the reaction is limited by the diffusion of oxygen to the electrode.

Below -0.9 V, the current increases sharply corresponding to solvent reduction.

Figure 6.18b shows experiments performed under the same conditions but with 5 mM of $ZnCl_2$ added to the solution. Without oxygen (green curve), there is no electrochemical reaction from 0.1 to -1 V. At -1 V there is a sharp increase of the current followed by a wavy plateau between -1.1 V and -1.35V. This region corresponds to the zinc metal deposition with high Cl^- concentration (0.1M) according to the reactions (6.4), (6.5) and (6.6)[109].

$$Zn^+ + 2e^- \leftrightarrow Zn \qquad E^o = -0.97 \text{ V /AgAgCl} \qquad \text{(Eq. 6.4)}$$

$$ZnCl^+ + 2\,e^- \leftrightarrow Zn + Cl^- \qquad E^o = -0.97 \text{ V/AgAgCl} \qquad \text{(Eq. 6.5)}$$

$$ZnCl_2 + 2\,e^- \leftrightarrow Zn + 2Cl^- \qquad E^o = -0.98 \text{ V/AgAgCl} \qquad \text{(Eq. 6.6)}$$

Below -1.35 V, the current increases corresponding to solvent reduction (Eq. 6.1) and the zinc deposition according to the reactions (6.1) and (6.4-7)

$$ZnOH^+ + 2e^- \leftrightarrow Zn + OH^- \qquad E^o = -1.15 \text{ V/AgAgCl} \qquad \text{(Eq. 6.7)}$$

The reverse scan follows the same path before -1.1V. An oxidation processes at -1 V, is detected, corresponding to oxidation of the deposit Zn.

In presence of oxygen (blue curve), the curve shows the same variation as the one observed in a zinc free solution with oxygen below -0.9V. This current is due to the reactions (6.2) and (6.3). Above -1.1V, the behaviour is the same as the one observed with an oxygen free solution. This is not surprising; the current associated with the reduction of the solvent is much higher than the other reactions.

One can see that the area of the stripping peak is superior in the case of an oxygen free solution. The area of this peak is proportional to the quantity of element removed during the stripping process, meaning that more reduced zinc species remain on the surface. In this region a zinc oxide layer can be formed on the zinc layer deposited at lower potentials and decrease the oxidation of the Zn metallic atoms.

Identical results have been reported by Peulon[11].

The potential of the second cross-over (-0.98 V) correspond to the equilibrium of the Zn/Zn(II+) reaction (6.6) .In the next chapter the system will be studied up to -1 V, in order to avoid the deposition of Zn metal.

6.1.2 Cyclic Voltammetry Studies of the Effect of Nitrate Anions

Figure 6.19 shows CV curves obtained in KCl solution (0.1M) at 70°C with a scan rate of 10 mV/s, Figure 6.19a presents the CV spectra of a deaerated solution of 0.1 M of KCl with 5 mM $ZnCl_2$ (black curve) and 5 mM $Zn(NO_3)_2$ (red curve). Without NO_3^- (black curves) no electrochemical process is observed between 0.2 V and – 1V. When the nitrate ions are added, a sharp rise is observed at -0.77 V which corresponds to the reduction of the nitrate ions according to the following reaction:

$$NO_3^- + H_2O + 2e^- \leftrightarrow NO_2^- + 2OH^- \qquad E^o=-0.2\ V/AgAgCl \qquad \text{(Eq. 6.8)}$$

At -1V the current value is -0.75 $mA.cm^{-2}$.

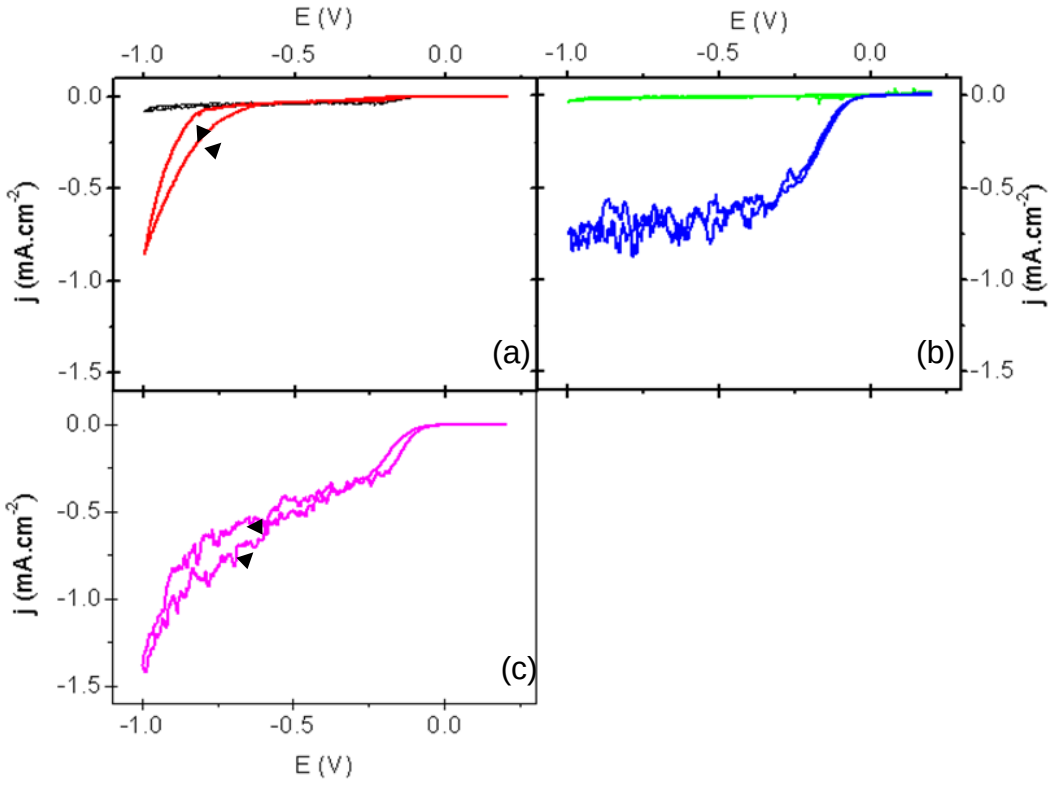


Figure 6.19 CV studies of the nitrate reduction in the Zn-Cl-H_2O-NO_3 system with 0.1 M of KCl at 70°C (a) without oxygen, 5mM of $ZnCl_2$ (black curve) and 5 mM of $Zn(NO_3)_2$ (red curve) ,(b) without oxygen (green curve) and with oxygen (blue curve), (C) 5 mM $Zn(NO_3)_2$ in presence of oxygen.

Figure 6.19b presents the CV spectra of a solution of 0.1 M KCl, without (green curve) and with oxygen, blue cure. Without oxygen no electrochemical process is observed between 0.2 V and – 1V. In the presence of oxygen, we observe an increase of the current at -0.1 V followed by a plateau between -0.3V and -0.9V due to the reaction of oxygen. The current plateau value is about 0.75 $mA.cm^{-2}$.

When oxygen and nitrate are both present in solution (Figure 6.19c, pink curves), the current obtained is equal to the sum of the reduction of nitrate ions and oxygen ions, a small difference is observed due to the catalytic role of Zn to the reduction of nitrate, which increases the associated reduction current[133]. From -0.2 V to -0.75 V, the current is quasi only due to the reduction of oxygen. The ratio of current from the nitrate reduction to the current from the oxygen reduction then increases to reach 1 at -1 V. In the interval of potentials [-1 V, -0.3 V] the current is quasi proportional to the applied potential. Varying the potential in this region is thus an easy way to control the quantity of hydroxide produced at the electrode.

6.1.3 Summary

The upper limit of hydroxide production is -0.2 V. The lower limit to both avoid the formation of Zn metal and the production of gas on the working is -1V. Combining NO_3^- and O_2 in solution is an easy way to have a better control on the hydroxide production and so increase the deposition rate.

6.2 Evolution of the Films with Time: Nucleation and Growth

In this section, the change with time of the deposited films is studied. All the deposition parameters were kept constant in the standard conditions. The *in-situ* synchrotron measurements will be introduced and the validity of these methods will be discussed.

6.2.1 Microscopy

Figure 6.20 presents a cross section of the sample after 1 minute. The films is composed of small rods (<80 nm diameter).

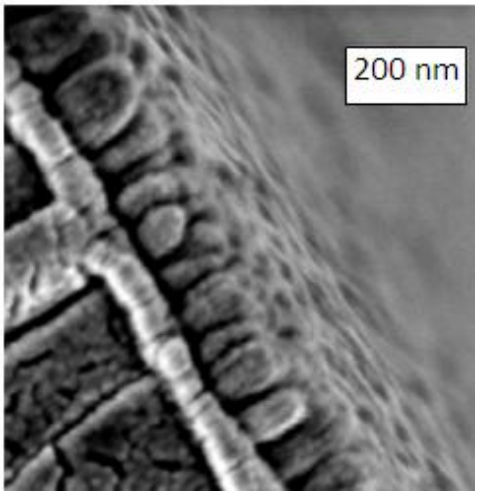


Figure 6.20 FESEM cross-section of a sample after 1 minute. 5 mM of $Zn(NO_3)_2$ and 0.1 M of KCl in a oxygenated aqueous solution at 65°C. The applied potential was -0.97 V.

Figure 6.21 presents top view FESEM characterisation of samples deposited for different times: 15 seconds (a), 1 minute (b), 2 minutes (c), 4 minutes (d), 10 minutes (e) and 45 minutes (f).

For very short time of deposition (Figure 6.21a), the nano-structures have a wide distribution of diameters, comprised between 10 and 80 nm. The nanostructures also differ by their orientation: some of them are orientated perpendicular to the substrate whereas other lie in the plane. The latter disappear with time (see Figure 6.21a-d) and after 4 minutes the substrate is completely covered with structures perpendicular to the substrate. Coalescence is observed from 4 minutes onwards.

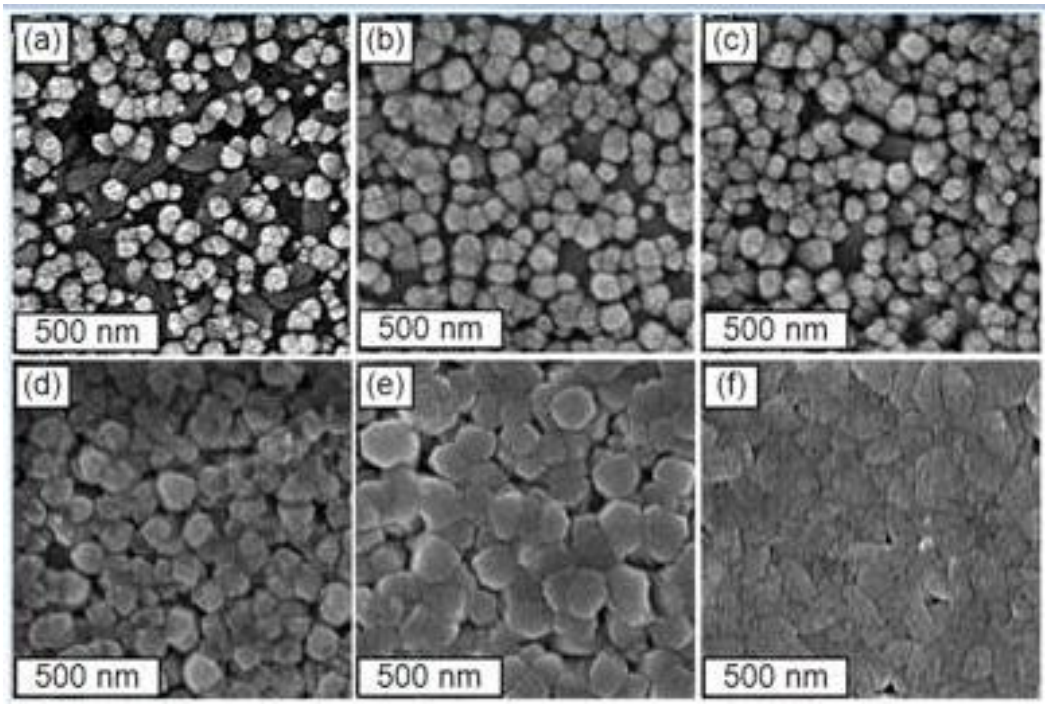


Figure 6.21 Study of the evolution of the structures with time: FESEM images of ZnO nanostructured films deposited for (a) 15 seconds, (b) 1 minute, (c) 2 minutes, (d) 4 minutes, (e) 10 minutes and (f) 45 minutes. 5 mM of $Zn(NO_3)_2$ and 0.1 M of KCl in a oxygenated aqueous solution at 65°C. The applied potential was -0.97 V.

The shape of the structures changes with time. Figure 6.22 shows higher magnification FESEM images of the structures after 1 minute (a) and 10 minutes (b). After 1 minute the rods have a rough conical shape. After 10 minutes the rods have sharper edges and flat top surfaces. The hexagonal shape is altered by the coalescence between adjacent structures.

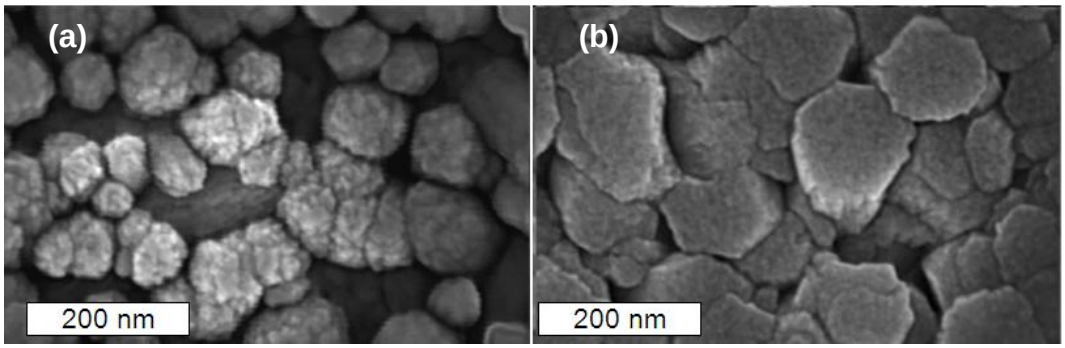


Figure 6.22 FESEM images of samples after 1 minute (a) and 10 minutes (b). 5 mM of $Zn(NO_3)_2$ and 0.1 M of KCl in a oxygenated aqueous solution at 65°C. The applied potential was -0.97 V.

Figure 6.23 shows the evolution of the nanostructure diameter as a function of the deposition time. The width has been obtained by measuring the diameter of the nano-rods from the FESEM images. 800 rods from two samples deposited under the same

conditions were taken for each data point. The error bars are the standard deviations of the sampling distribution. A sharp increase of the diameter is observed at the beginning of the deposition followed by a plateau when the rods coalesced.

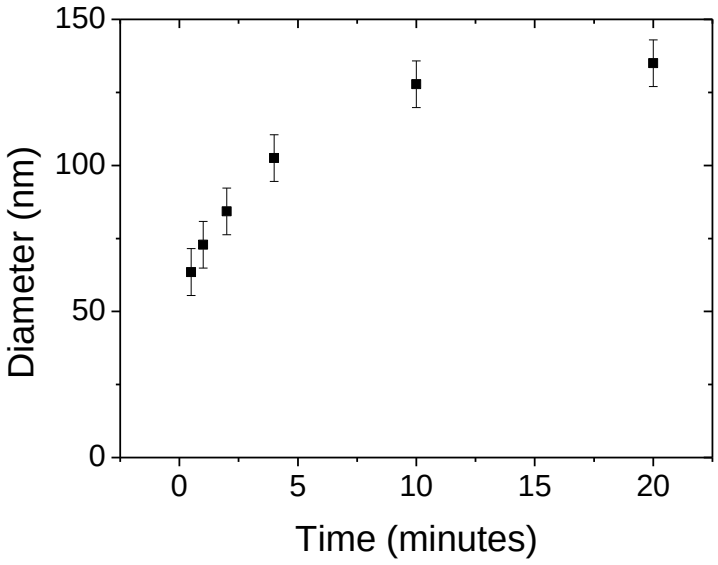


Figure 6.23 Evolution of the nano-structures diameter with time (from the FESEM images). 5 mM of $Zn(NO_3)_2$ and 0.1 M of KCl in a oxygenated aqueous solution at 65°C. The applied potential was -0.97 V.

The coalescence of the nanorods after nucleation has been reported by Lincot and co-workers[134, 155]. A rod diameter of about 150 nm is observed by Peulon et al[11] after one hour of deposition. This is in good agreement with our results. Clement and co-workers have also reported an increase of the rod diameter with time in similar deposition conditions[164].

6.2.2 Evolution of the Current

Figure 6.24 presents a current versus time obtained during the deposition of the film. One can clearly see the drop in current at the beginning of the deposition due to the capacitance effect. The current directly reaches its peak value before decreasing to a plateau value. Neither an induction period nor the increases of the current are observable (see Figure 4.2). The incubation period ([AB]) is not observed because of the relatively high deposition temperature[109]. The ascendant part of the peak ([BC]), corresponding to the nuclei formation and growth is not observed because the surface is

rapidly covered by growth centres as can be seen on the FESEM images at very short deposition times (Figure 6.22).

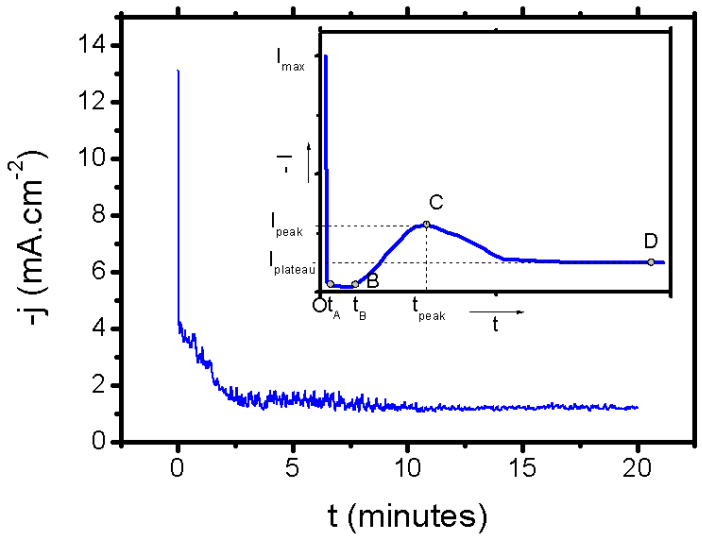


Figure 6.24 Current density as a function of time. 5 mM of $Zn(NO_3)_2$ and 0.1 M of KCl in a oxygenated aqueous solution at 65°C. The applied potential was -0.97 V. Inset : Figure 4.25 Drawing of the general shape of the transients observed for ZnO electrodeposition after [107]. I_{max} is the maximum current observed. t_{peak} and I_{peak} are the coordinate of the peak of current before the plateau whose value is $I_{plateau}$.

6.2.3 Evolution of the Film Thickness

The current density measured during the deposition is related to the reduction reactions 6.2-3 and 6.8. Some information can be inferred from the electrochemical data about the deposition of ZnO, however this is not trivial. For example Faradic current efficiencies ranging from 0.1 to 1 have been quoted in the literature[11, 109, 114, 133]. Some electrochemical quartz crystal microbalance experiments have been performed in attempts to correlate the electrochemical measurements to material deposition[11, 109, 114, 142], but these are not species-specific. While growth is observed, it is not possible to correlate this directly with any particular electrochemical process. We have used synchrotron XAS during film deposition in order to measure directly the rate of deposition on ZnO.

6.2.3.1 Principle of the Methods

In the past[190], the dissolution of material has been followed in real-time by performing XANES scans with as rapid scan rates as possible (2-3 minutes). This same technique was initially applied to monitoring the growth of ZnO nanostructures by repeatedly scanning across the XANES region of the Zn K-edge, on a similar time scale. In this set-up the

incident X-ray beam penetrates the whole of the sample under investigation and so the edge-height in the XANES region is directly proportional to the amount of material present. Figure 6.26 shows a series of XANES scans at the Zn K-edge, taken as ZnO is being deposited from $Zn(NO_3)_2$ solution.

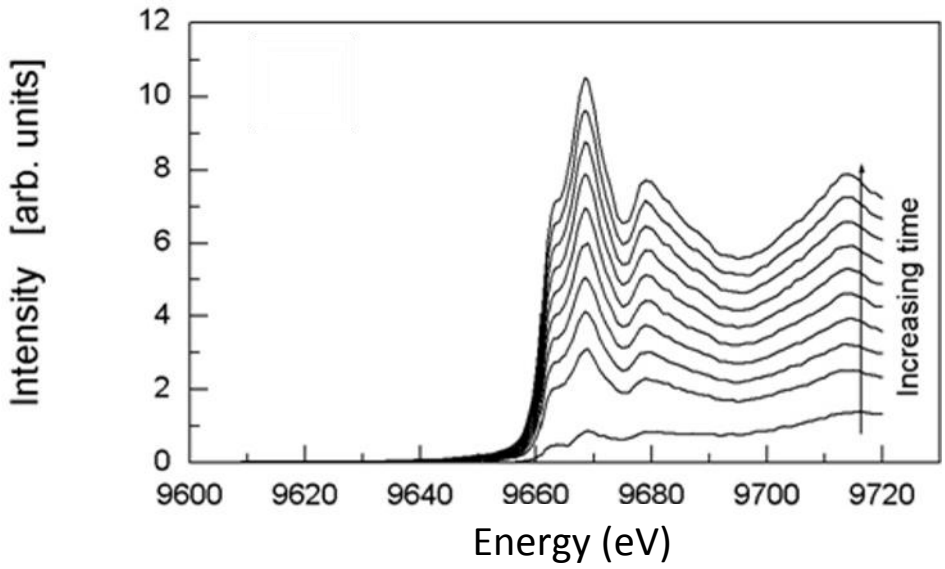


Figure 6.26 Synchrotron XANES recorded during the deposition of ZnO. 5 mM of $Zn(NO_3)_2$ and 0.1 M of KCl in a oxygenated aqueous solution at 65°C. The applied potential was -0.97 V.

The shape of the curves does not change with time and matches that of bulk ZnO. However, at very short times, when the volume of material being added as a proportion of existing material is very large, two problems arise. Firstly, the spectra are more sensitive to this growth and consequently the curves appear to be different. (Indeed, if one assumes linear growth and accounts for this in the first scan by dividing by the time, the curves are identical to ZnO.) Secondly, the nucleation processes, which are thought to dictate the resulting structures, typically occur over a time span of 0-5 minutes. Therefore it is not possible to completely capture this process with successive XANES scans. To extract sensible growth information for these very short times, one needs to utilise a different approach. Ideally, energy-dispersive EXAFS (EDE) would be the tool of choice, however such measurements cannot be performed in fluorescence geometry and the deposition process is not amenable to the thin film cell geometry required for transmission measurements. In these measurements, the time limitation is due to the monochromator movement. Rather than repeatedly scanning the energy over the XANES region (E0 – 50 eV to E0 + 60 eV; where here E0 is the Zn K-edge at 9659 eV), the energy was fixed at a constant value above the edge and the signal in a continuous

fashion (1 second counting time) measured. This is appropriate since we know that the phase formed is not changing with time and so the shape of the XANES remains the same. The fixed energy chosen for these experiments was 9725 eV because the signal varies only slightly between 9720 eV and 9730 eV (see Figure 6.27).

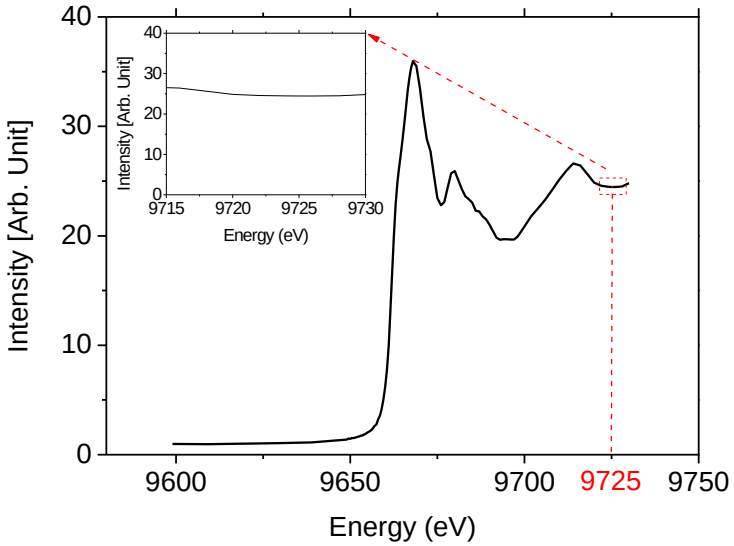


Figure 6.27 Synchrotron XANES recorded during the deposition of ZnO. In-set: region of energy choose for the measurements. 5 mM of $Zn(NO_3)_2$ and 0.1 M of KCl in a oxygenated aqueous solution at 65°C. The applied potential was -0.97 V

Simultaneously, the deposition current density was also monitored, allowing a direct correlation to be made. In addition, full XANES scans were taken before the deposition to record the magnitude of the solution signal. This is used as an internal standard and was calibrated for different concentrations against a ZnO sputtered film of known thickness (see paragraph 6.2.3.2). Another XANES scan was recorded after the deposition to confirm that the correct phase, ZnO, had been formed. EXAFS spectra were also collected post-deposition for further analysis. In this way we obtain all the information of the previous method, but gain extra information on the nucleation and growth processes in real time. This is limited only by the timescale required for measurement of each data point, 1 second.

6.2.3.2 Calibration of Signal

The calibration of the signal was performed by using the solution signal as an internal calibrant in order to convert the intensity measure to the film volume. The monitored

signal is composed of the solution signal, S_s and the film signal S_f. The solution signal is linearly dependent on concentration. The change in concentration due to the deposition of ZnO is negligible, hence the solution signal is constant throughout the deposition. The solution signal and film signal can be expressed has a function of thickness of the solution penetrated e_s and the thickness of the film e_f according to the following equations:

$$S_S = \alpha * A * e_s * C_{Zn(II)} \quad \text{(Eq. 6.9)}$$

$$S_f = \beta * A * e_f \quad \text{(Eq. 6.10)}$$

Where A, α and β are the beam area and two constants respectively.

And thus the ratio of the film signal to the solution signal is equal to:

$$\frac{S_s}{S_f} = \frac{\alpha * e_s}{\beta * e_f} C_{Zn2+} = \frac{\gamma}{e_f} C_{Zn(II)} \quad \text{(Eq. 6.11)}$$

where $\gamma = \frac{\alpha * e_s}{\beta}$

S_s, S_f and $C_{Zn(II)}$ are known, γ was calculated using a 100 nm ZnO film thick sputtered onto a Au/Mylar substrate. XANES scans were performed on this film without any solution, and again with solutions of varying Zn^{2+} concentration. The value measure, the volume of Zn(II) per unit area of surface, as a dimension of a thickness and will be called t_n (nominal thickness) in this work. It is assumed that the ZnO films deposited have the same density as bulk ZnO.

6.2.3.3 Validity of the Method

At energies >50 eV above the absorption edge, the EXAFS oscillations are broader in energy and their amplitude is damped, compared to the oscillations at the absorption edge. The selected energy is still close enough to the edge to be sensitive to an increase in signal, but not so close as to be drastically affected by changes in the oscillations due to a possible change in local structure. While the positions in energy of the EXAFS oscillations of different phases can vary greatly, in all cases for our application

alternative phases (e.g. Zn metal) are undesirable. Indeed by performing the successive scanning experiment first, we have shown that the local structure is not changing over the time frame of our experiments and the increase in intensity can only be due to material deposition.

The self-absorption of the films needs to be considered. At a given energy, the fluorescence signal (I_f) of a film of thickness t, normalised to the incident intensity (I_0), corrected for self-absorption, is[193]:

$$I_f / I_0 \propto [1 - \exp(-(\mu_0 + \mu_e)\, t)\,] / (\mu_0 + \mu_e) \qquad \text{(Eq. 6.12)}$$

Where μ_0 is the absorption at the incident x-ray energy, and μ_e is the absorption at the fluorescent x-ray energy (for Zn $K_{\alpha 1}$, 8639 eV). Therefore the film thickness must be corrected by applying:

$$t_{actual} = -\ln [1 - (\mu_0 + \mu_e) t_{observed}] / (\mu_0 + \mu_e) \qquad \text{(Eq. 6.13)}$$

where $t_{observed} \propto I_f / I_0$, which holds in the limit of Eq. 6.13 for small t. The function is shown in Figure 6.28.

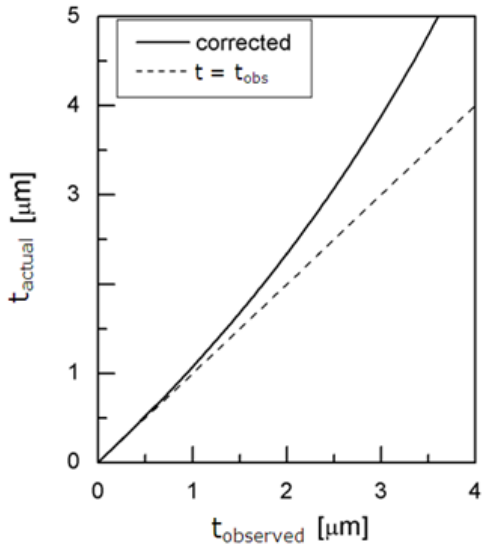


Figure 6.28 Self-absorption correction function for ZnO

At 100 nm, this corresponds to a difference of 0.7%; at 200 nm, 3%; and at 1 µm, 6.7%. The curve saturates for d > 7.6 µm; meaning that thicknesses greater than 7.6 µm cannot be distinguished. The films produced in our work are typically 200-500 nm thick where these effects are minimal; all data presented here are corrected for self-absorption.

6.2.3.4 Evolution of the Nominal Thickness with Time

Figure 6.29 presents the evolution of the nominal thickness with time. Two distinct regions of the curve are observed. Before 2.5 minutes, the growth is linear and the growth rate is closed to 1 $nm.s^{-1}$. After 2.5 minutes, the growth is quasi linear, with a growth rate of 0.3 nm/s which slightly decreases with time.

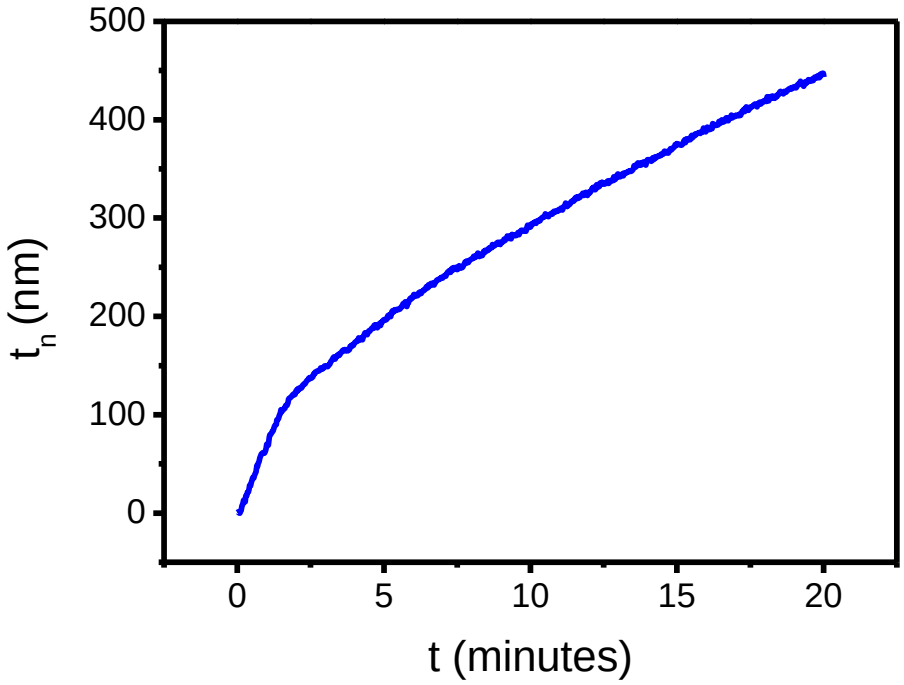


Figure 6.29 Nominal film thickness (t_n) obtained from X-ray fluorescence intensity at 9725 eV. 5 mM of $Zn(NO_3)_2$ and 0.1 M of KCl in a oxygenated aqueous solution at 65°C. The applied potential was -0.97 V.

The transition corresponds *exactly* to the end of the peak in nucleation (see Figure 6.24). FESEM images of sample deposited for 2 minutes, just before the transition (see Figure 6.21c), and for 4 minutes, just after the transition (see Figure 6.21d) shows that the transition corresponds to the coalescence of the nanorods. During the nucleation an increase of diameter as well as of the thickness of the films is observed. When the film coalesces, no further in-plane growth is possible and the film grows only in the direction perpendicular to the substrate. The transition from a 3-D growth regime to a 1-D growth leads to a decrease of the growth rate. The slow decrease of the growth rate observed after the coalescence may be due to the increase of the resistance of the film with the ZnO thickness increasing. Figure 6.30 shows the variation of the faradaic efficiency with time. It is calculated by comparing the amount of material predicted by Faraday's law for the charge passed (t_F, see (Eq. 6.14)) and the volume of material actually deposited.

$$t_F = \frac{Q(t)}{2 * F * S * \frac{d}{M}} \qquad \text{(Eq. 6.14)}$$

where F is the Faraday constant (96500 C.mol-1), d is the zinc oxide density (5.6 $g.cm^{-3}$), S is the surface area of the sample and M represents the molar mass of zinc oxide (81.4 $g.mol^{-1}$).

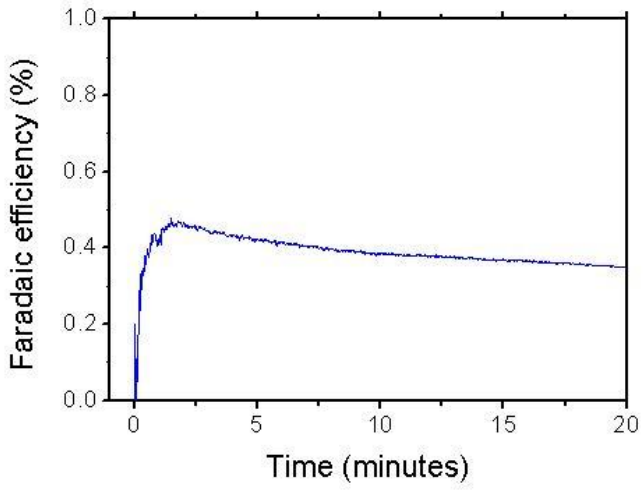


Figure 6.30 Faradaic efficiency as a function of time. 5 mM of $Zn(NO_3)_2$ and 0.1 M of KCl in a oxygenated aqueous solution at 65°C. The applied potential was -0.97 V.

The faradaic efficiency curves exhibit a peak at the point of coalescence. The sharp increase during the first few seconds is due to the capacitance effect generating a drop in current. Then the increase efficiency prior to the peak is due to the decrease of the active gold surface. The noble metal is a better electrode for the reduction of hydroxide precursor zinc oxide[111]. The associated decrease of the current density, while the vicinity of the electrode is still under supersaturation conditions, lead to an increase of the faradaic efficiency.

6.2.4 X-ray Diffraction

6.2.4.1 *Ex-Situ* Measurements

The structure of ZnO films were analyzed by XRD. Figure 6.31 shows XRD pattern of ZnO deposited in the standard conditions. Only the ZnO (002) and (004) peaks are visible, all the other peaks come from the Au substrate. The nanostructured ZnO is strongly textured in the [002] direction. The magnitude of the ZnO (002) peak and Au (111) peak is more than 2 orders of magnitude higher than the other peaks. The XRD patterns are close to the ones obtained on single crystals. Epitaxial growth of ZnO by a solution process has been reported a single-crystalline gold[150]. Zinc oxide has lattice parameters

of a=b=0.3250 nm and c=0.5207 nm. The lattice parameter in the Au [111] plane with face-centred cubic (fcc) crystal structure is 0.2884 nm. The lattice mismatch in this system calculated from (aZnO - aAu)/aAu is -12.7%. The very strong orientation of the zinc oxide is due to the strong (111) orientation of the substrate.

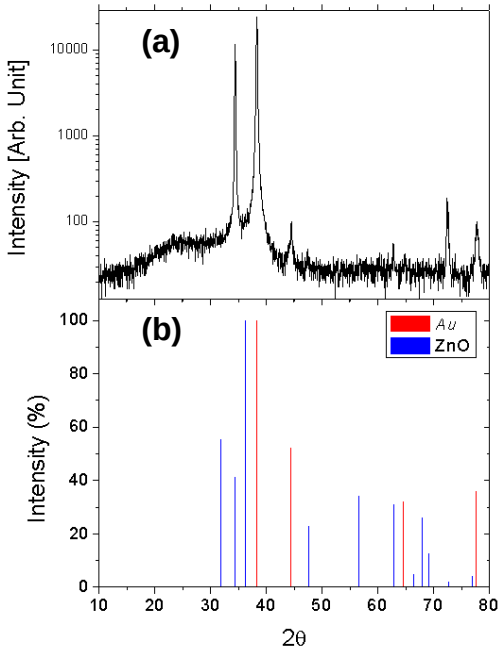


Figure 6.31 Crystallographic study: (a) XRD pattern of a sample after a 20 minutes deposition (b) ZnO wurtzite and Au fcc XRD pattern. 5 mM of $Zn(NO_3)_2$ and 0.1 M of KCl in a oxygenated aqueous solution at 65°C. The applied potential was -0.97 V.

XRD carried out in a standard geometry is not well adapted to the study of thin films, because X-ray penetrates through the matter and therefore there is a strong parasite signal from the substrate. Very long scan time are required (typically 12 hours) to detect a signal coming from material deposited for very short times, which make a systematic study of the effect of the deposition parameters difficult. Moreover some small quantity of crystalline material can remain undetected even with very long scan duration. To answer this problem we have been using GIXS.

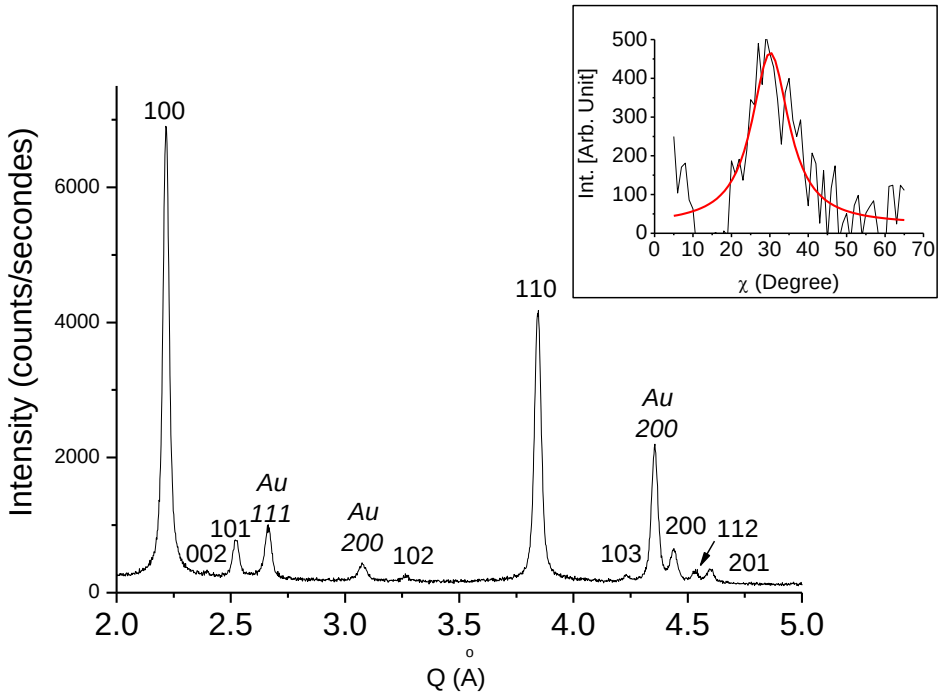


Figure 6.32 *Ex-situ* GIXS scan of a sample deposited for 15 s. The peaks are labelled according to the ZnO wurtzite structure or Au fcc structure (italics). Inset: Intensity vs. polar angle texture scan of the (101) peak with a lorentzian fitting (red line). 5 mM of $Zn(NO_3)_2$ and 0.1 M of KCl in a oxygenated aqueous solution at 65°C. The applied potential during the deposition was -0.77 V.

Figure 6.32 presents an *ex-situ* GIXS scan for a sample deposited for 15 seconds. In the grazing-incidence geometry the incident X-ray beam is at a small angle (0.4°) to the sample surface. The penetration depth of the X-rays into the substrate is consequently low, and one measures diffraction from planes perpendicular to the sample surface. All the peaks have been identified as ZnO wurtzite structures or gold from the substrate. In addition, texture scans were carried out. Since the (100) and (110) are in-plane, the full peak cannot be observed, since no intensity can be measured at χ= 90° (see Figure 6.31) in the grazing incidence geometry. The (002) reflection is not indicative of the true intensity and texture because it is a specular reflection. The (101) reflection was used. Polar scans were fitted to a Lorentzian peak function to obtain the area, position and full width at half maximum. The inset of Figure 6.32 shows the polar plot for the (101) reflection (Q= 2.538 Å), with background subtracted. There is a peak in this plot, which indicates that even at short time (15 s) there is texture present in the nanostructures.

6.2.4.2 *In-Situ* Measurements

Since the nuclei are textured, the question arises as to how the texture changes during the nucleation and subsequence crystal growth. Synchrotron GIXS can be used to obtain crystallographic information during the growth of the nanostructures. Images were taken every 90 s in a sequence. An example of data collected during a scan is given bellow:

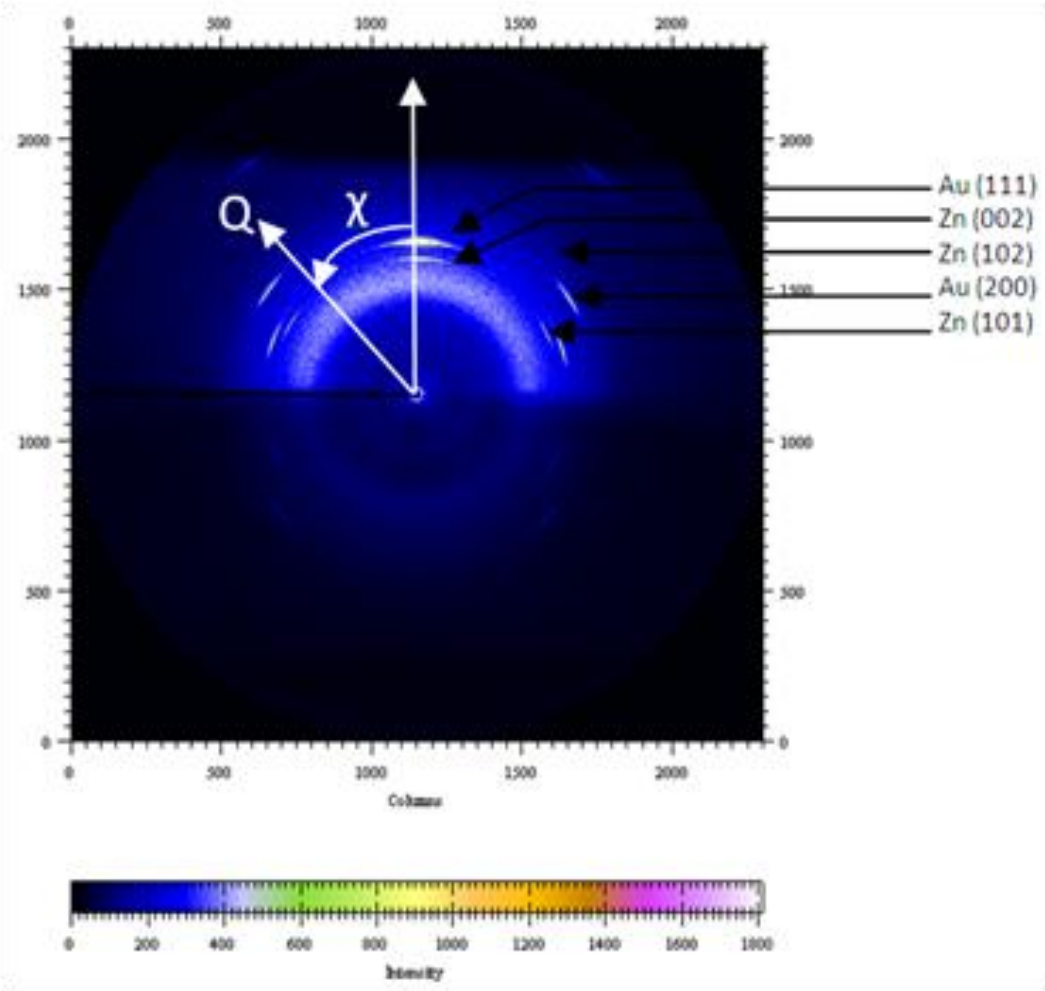


Figure 6.33 Diffraction pattern from an in-situ scan. Each intensity peak corresponds to a specific orientation of either ZnO or Au, as labelled. The data can be read in polar coordinates by using the angle χ from the vertical and the scattering vector Q. 5 mM of $Zn(NO_3)_2$ and 0.1 M of KCl in a oxygenated aqueous solution at 65°C. The applied potential was -0.77 V.

Each arc represents a specific orientation of either the ZnO crystals or the gold upon which it was deposited. (The arcs appear tilted from the normal because the substrate was tilted laterally about the beam.) By using the intensity colour scale, one can see the relative intensities, measured in counts, of each orientation. As the deposition progressed, the ZnO peak intensities increased, corresponding to the amount of

(crystalline) material directly deposited. The width of the arcs indicates the degree of texture present in the nanostructures. The arcs of importance are labelled in Figure 6.33 as follows: ZnO (102), Au (200), Au (111), ZnO (101), and ZnO (002).

The program Fit2d was used to integrate the as-taken data (Figure 6.33) to create the graph shown in Figure 6.34.

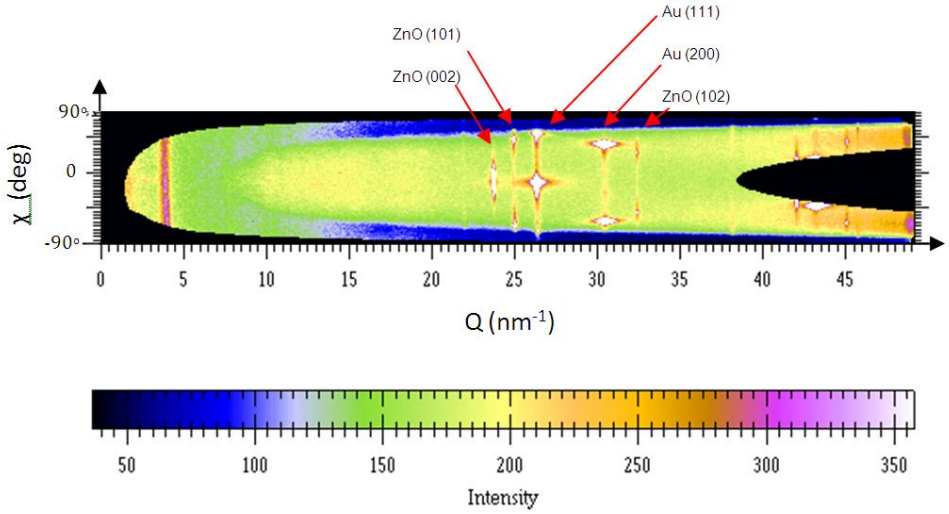


Figure 6.34 Graph resulting of the integration of the data in Figure 6.33 with Fit2d. The polar data (χ, Q) have been converted to a Cartesian referential. The horizontal lines corresponding to the reflection of AU and ZnO have been labelled. 5 mM of $Zn(NO_3)_2$ and 0.1 M of KCl in a oxygenated aqueous solution at 65°C. The applied potential was -0.77V.

This essentially changes the polar coordinates of χ and Q to Cartesian coordinates. The vertical becomes the off-axis angle chi and the horizontal is the magnitude of the scattering vector Q. Using Figure 6.34, one may see more easily the different diffraction peaks, which are once again labelled on the figure and are now horizontal lines.

Cuts were taken along the horizontal lines corresponding to the reflection of the (101) peak (Figure 6.35). The peak can be fitted with Lorentzian curves to obtain the area, which corresponds to the degree of crystallinity along the direction, the centre, and FWHM, which tell us about the strength of the scattering and the variation in texture (preferential orientation). The area and peak width plotted as a function of time are shown in Figure 6.36.

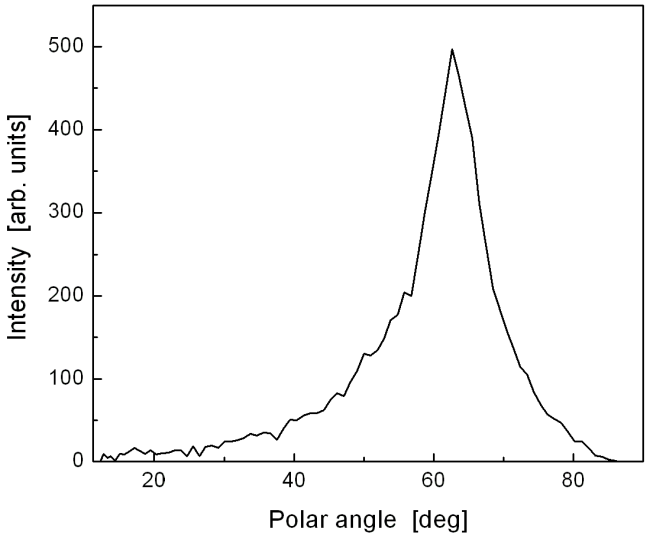


Figure 6.35 Intensity versus angle in omega for the ZnO (101) reflection at the end of a deposition. 5 mM of $Zn(NO_3)_2$ and 0.1 M of KCl in a oxygenated aqueous solution at 65°C. The applied potential was -0.77 V.

The peak area as a function of time (Figure 6.36a) is proportional to the quantity of crystalline material deposited. It increases in a manner similar to that observed previously with in situ XAS (see Figure 6.29). There are two regions of the curve: the initial nucleation regime where material is being deposited rapidly; followed by continuous growth at a slower rate. The azimuthal peak width as a function of time (Figure 6.36b) shows no significant change (within the uncertainties), providing quantitative proof that the texture originates *during* the nucleation. The fwhm is 7.5°, which, compared with Figure 6.32 where the fwhm was 11°, indicates the texture increases slightly after the nucleation stage. The transition between the two regimes of growth is delayed compared to what was observed during the in situ XAS (see Figure 6.29). This is due to the different geometry being used. In the diffraction experiments, the cell is only 2 mm wide in the vicinity of the working electrode, whereas for the X-ray absorption experiments the electrode is open. Figure 6.37 presents the current density recorded in the two experimental set-ups with the same electrochemical parameters.

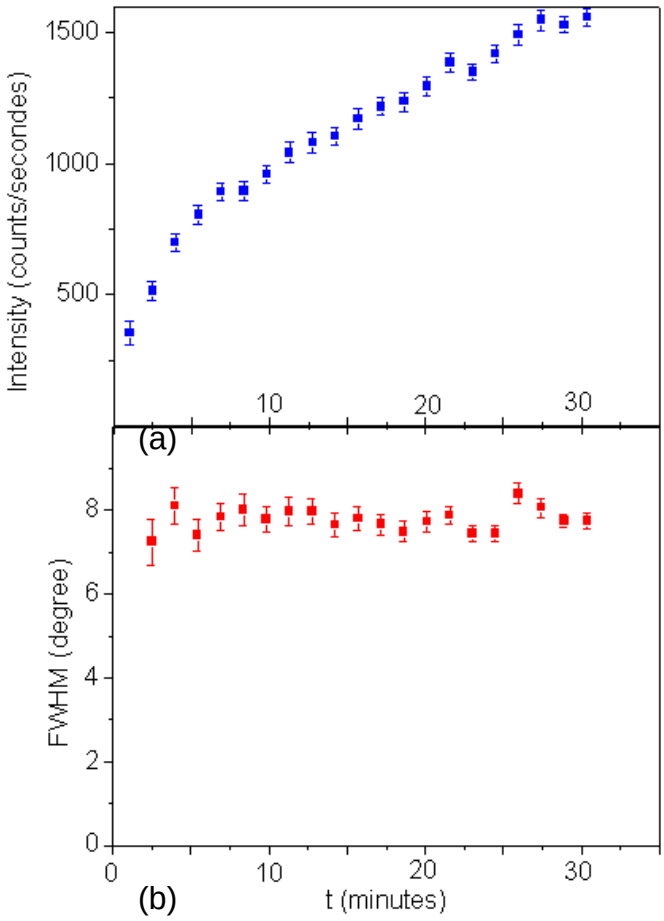


Figure 6.36 *In-situ* measurements of the peak intensity (a) and full width at half-maximum (b) for the (101) reflection as a function of time. The applied potential was -0.77 V

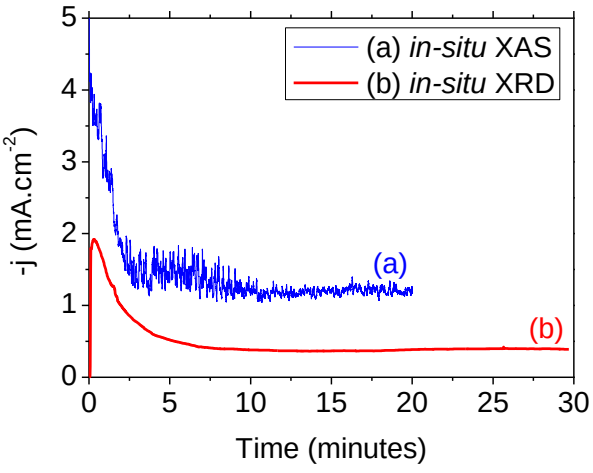


Figure 6.37 Current density as a function of time for (a) in-situ XAS (XAS) set-up and (b) *in-situ* XRD set-up. 5 mM of $Zn(NO_3)_2$ and 0.1 M of KCl in a oxygenated aqueous solution at 65°C. The applied potential was -0.97 V.

The current density is about 3 times lower for the in-situ XRD set-up. The decrease in current is related to the decrease of the diffusion current of the hydroxide precursors as the solution is less agitated at the vicinity of the electrode.

6.2.5 Summary

An *in-situ* crystallographic study of the nucleation of ZnO has been carried out for the first time. The films are covered with crystalline ZnO after only a few seconds. The orientation of these rods perpendicular to the substrate is determined in the first few seconds of deposition, during the nucleation stage. The nuclei are textured in the [002] direction, and this then propagates through the crystallites as the nanostructures grow. The shape of the nanostructures evolves from conical rods which grow in 3-D to hexagonal rods with a 1-D growth. The transition can be clearly observed in the synchrotron in-situ measurements by a change in growth rate. The growth rate observed once the system is in the 1-D regime is lower since no further growth in the direction of the plane can take place. ZnO has a wurtzite structure and exhibits a difference in the polarity of the facets of the rods (see section 3.2.3). The polar top surfaces of the rods are thermodynamically less stable than non-polar faces and tend to grow more rapidly. From a structural point of view, the main effect of the coalescence is to change the reactive surface of the rods in contact with the solution. Before the coalescence, the lateral surface of the rods increases due to the increase of the height of the rod. As soon as the coalescence begins, the exposed area of the lateral faces of the rods decreases. The fact that the variation of the faradaic efficiency is correlated to the variation of the lateral surface is indicative of the difference in reactivity of the different crystal faces of the rods.

6.3 Effect of Potential

In this section, the changes with applied potential are studied. All the other deposition parameters were kept constant. The films were deposited from a solution containing 5 mM of $Zn(NO_3)_2$ and 0.1 M of KCl at 65°C.

6.3.1 Microscopy

Figure 6.38 presents the evolution of the film morphology with time for 4 deposition potentials.

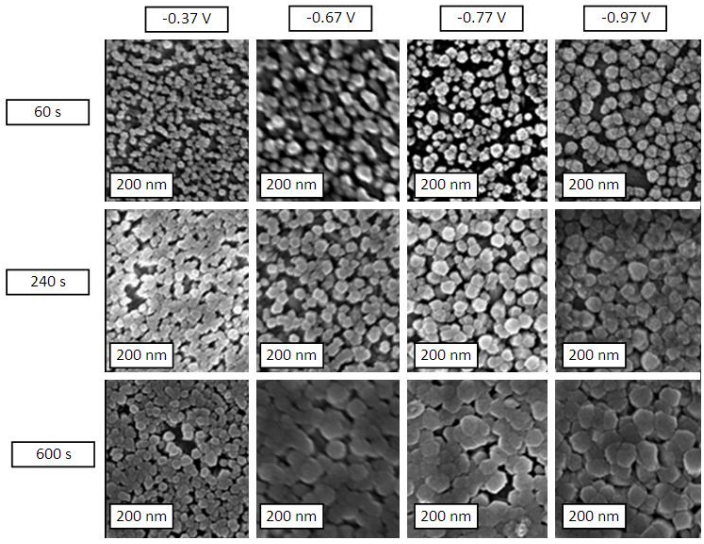


Figure 6.38 Evolution of the film morphology with time for four deposition potentials. 5 mM of $Zn(NO_3)_2$ and 0.1 M of KCl in a oxygenated aqueous solution at 65°C.

All the films are composed of nanorods. Figure 6.39 shows the number and diameter of the nanostructures as a function of time for different potentials. The data for a deposition greater than 10 minutes are not very accurate due to the coalescence of the nanostructures: when the films are dense the boundary between rods may not be clear. For high potentials (-0.37 V), a small linear growth with time is observed. For lower potential a logarithmic growth is observed. The size of the nuclei is about 50 nm and is independent of the applied potential. An increase of the number of nucleation centres is observed when the potential is increased.

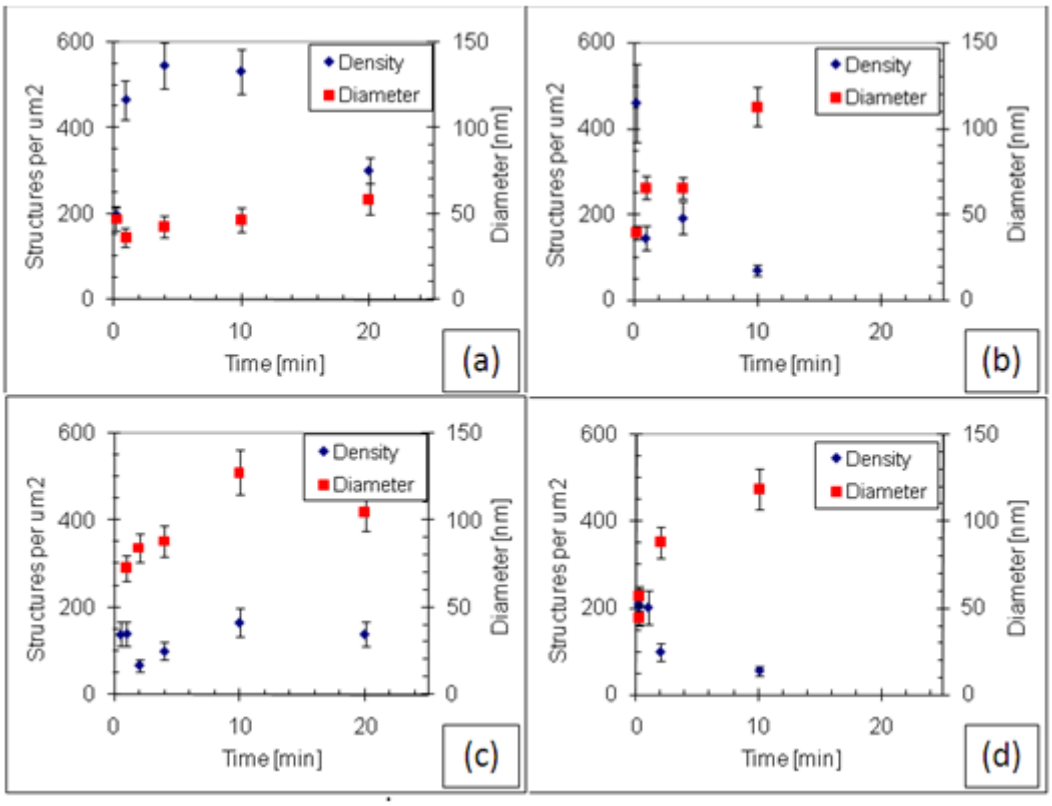


Figure 6.39 Diameter and density of the nanostructures as a function of the potentials and time. (a) -0.37 V, (b) -0.67 V, (c) -0.77 V and (d) -0.97 V. 5 mM of $Zn(NO_3)_2$ and 0.1 M of KCl in a oxygenated aqueous solution at 65°C.

Figure 6.40 presents the diameter and number of nanorods as a function of potential measured from the FESEM images after a 4 minute deposition.

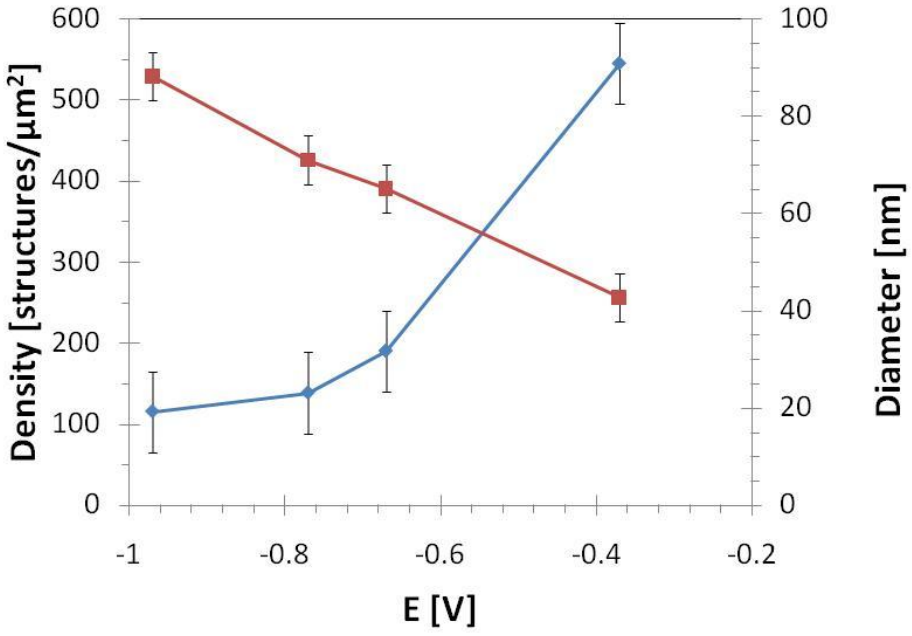


Figure 6.40 Diameter (red squares) and density (blue diamonds) of the nanostructures as a function of the potentials. t=4minutes. 5 mM of $Zn(NO_3)_2$ and 0.1 M of KCl in a oxygenated aqueous solution at 65°C.

When the potential is made more negative, the size of the nanostructures is increased and their density is decreased. The size of nanorods is proportional to the applied potential for a deposition time of 4 minutes. The main effect of the potential is to control the reduction current and thus the pH at the vicinity of the electrode. Low levels of supersaturation lead to the formation of smaller structures.

As far as we know, no effect of potential on the film morphology has been reported for depositions carried out from a deposition bath containing both zinc chloride and oxygen as precursors whereas dramatic changes have been reported with zinc nitrate[104, 121-124]. With oxygen only in solution, the oxygen reduction is limited by the diffusion of O_2 and therefore it is not dependant of the potential.

6.3.2 Electrochemical Measurements

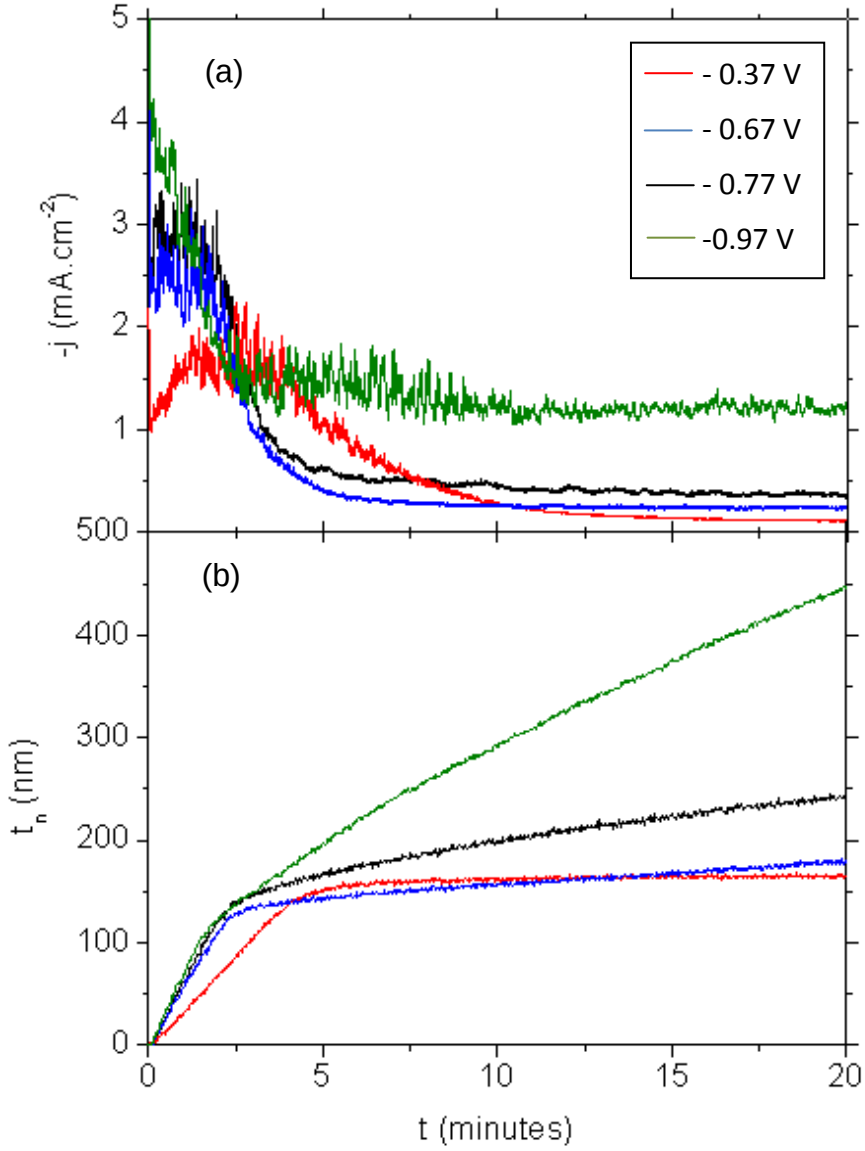


Figure 6.41 Simultaneous current density (a) and nominal thickness (b) measurements as a function of time and potential: -0.37 V (red line), -0.67 V (blue line), -0.77 V (black line) and -0.97 V (green line). 5 mM of $Zn(NO_3)_2$ and 0.1 M of KCl in a oxygenated aqueous solution at 65°C.

Figure 6.41a presents the current density transient as a function of potential. The curves have the same overall shape: a peak region, associated with the nucleation and a plateau, associated with the growth after coalescence. For an applied potential of -0.37, the current transient curve have a clear broad peak. The decrease of the potential toward more negative potential has two effects on the nucleation peak: the duration is decreased and the maximum intensity increases. The ascendant part is dramatically reduced. The plateau value is slightly increased when the potential is decreased from -

0.37 V to -0.77 V. If the potential is further decreases, the ascendant part of the peak disappears and the plateau value is increased, due to the reaction of reduction of the NO_3^{2-}.

Figure 6.41b present the nominal thickness measurement carried out simultaneously with Figure 6.41. One can clearly see the two regimes of growth corresponding to 3-D and 1-D growth as reported in the previous chapter. The sample deposited at -0.37 shows a different behaviour compared to the others. The growth rate during the nucleation is only half as fast. The samples deposited at a lower potential have a quasi identical growth rate during the nucleation. After the nucleation peak, the curves diverge, the growth rate increasing dramatically when the potential is more negative.

The current efficiencies are showed in Figure 6.42. The films deposited at -0.67, -0.77V and -0.97 V only deviate in the nucleation region where the current efficiencies exhibit a peak that is more pronounced at a less negative potential. This corresponds to a protracted nucleation period. At longer times, the efficiency curves are very similar, and there is little difference between the curves obtained for different potentials. The film deposited at -0.37 V exhibit a different behaviour at longer times with a faradaic efficiency 10% lower.

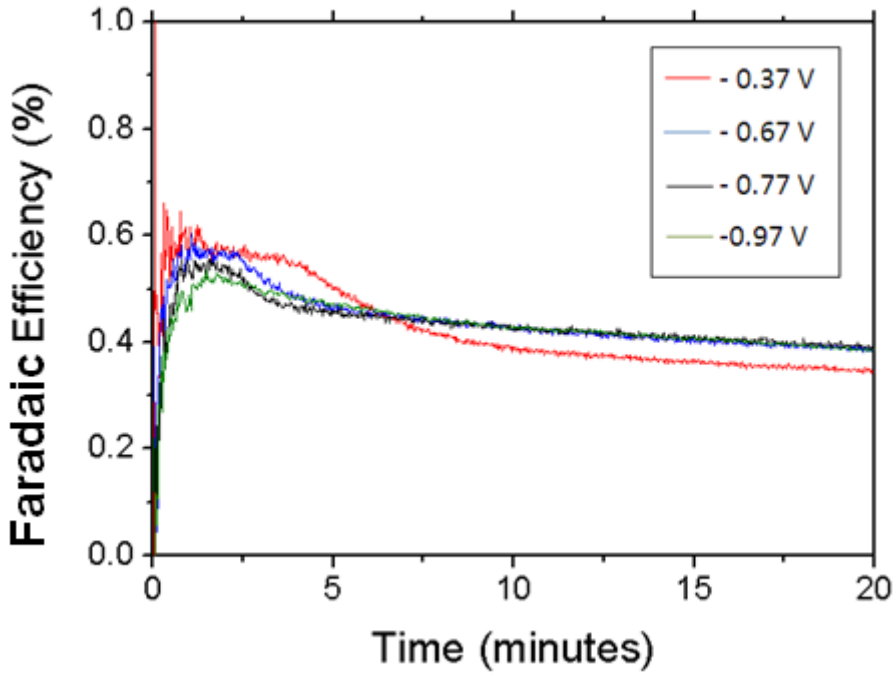


Figure 6.42 Current efficiencies calculated for the films deposited in Figure 6.41 : -0.37 V (red line), -0.67 V (blue line), -0.77 V (black line) and -0.97 V (green line). 5 mM of $Zn(NO_3)_2$ and 0.1 M of KCl in a oxygenated aqueous solution at 65°C.

6.3.3 X-Ray Diffraction

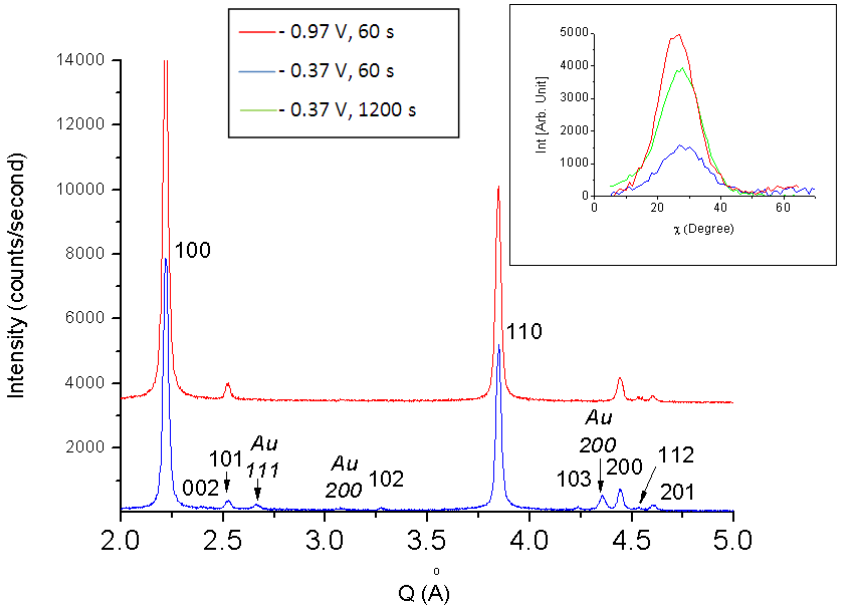


Figure 6.43 *Ex-situ* GIXS scan of a sample deposited for 1 minute at a potential of -0.37 V (blue) and -0.97 V (red). The peaks are labelled according to the ZnO wurtzite structure or Au fcc structure (italics). Inset: Intensity vs. polar angle texture scan of the (101) peak. Green curves: 20 minutes at a potential of -0.37. 5 mM of $Zn(NO_3)_2$ and 0.1 M of KCl in a oxygenated aqueous solution at 65°C.

Figure 6.43 shows the ex-situ GIXS scans of two samples deposited at -0.37 V and -0.97 V respectively. All the peaks have been identified as wurtzite ZnO and fcc gold. The in-set presents (101) texture scan. The area of the peak at -0.37 V is 2.5 times as low as at -0.97 V, which is exactly the ratio of the XANES thickness measurements after 1 minute (Figure 6.41b). The FWHM decrease from 16° at -0.37V to 11.7° at -0.97 V. indicating that the films are more textured at more negative potential or that the texture increases with the thickness. The FWHM at -0.37V after 20 minutes of deposition is 13.3° and are 10 times as thick as the films deposited at -0.97V for 60 s (Figure 6.41b). There is thus an increase of the texture when the potential is more negative.

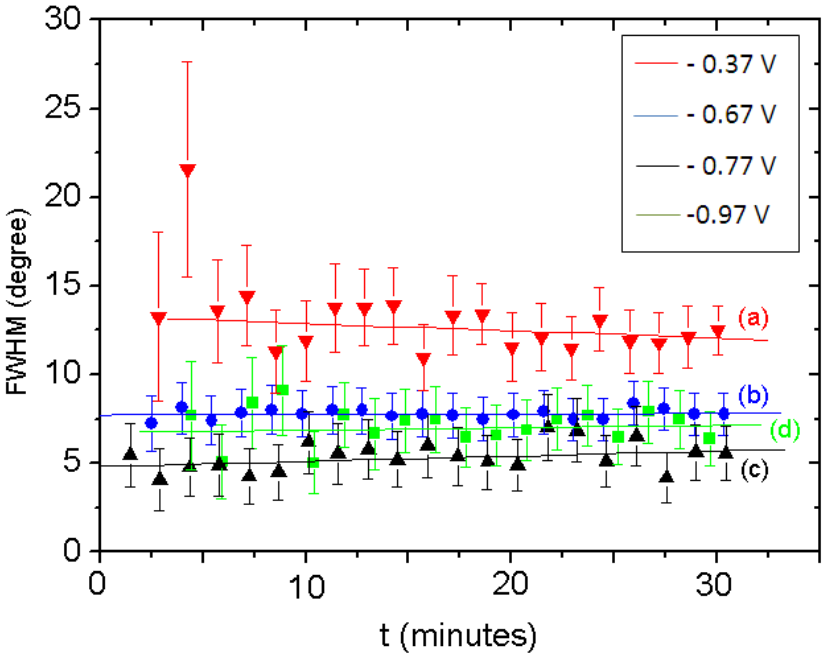


Figure 6.44 *In-situ* measurements of full width at half-maximum for the (101) reflection as a function of potential: (a) -0.37 V, (b) -0.67 V, (c) -0.77 V and (d) -0.77 V. 5 mM of $Zn(NO_3)_2$ and 0.1 M of KCl in a oxygenated aqueous solution at 65°C.

Figure 6.44 presents the variation with time of the FWHM as a function of the applied potential. The points have been fitted with linear curves for clarity. No change with time is observed within the uncertainties.

6.3.4 Discussion

The change in faradaic efficiency with potential can be explained by the variation of hydroxide production. Indeed, the main effect of the potential is to control the production of hydroxide. Hydroxide ions produced at the electrode can either diffuse

toward the bulk or reaction with Zn(II) to produce ZnO[114]. Increasing the potential results in a lower rate of hydroxide production, hydroxide ions have less time to diffuse away from the electrode and an increase of the faradaic efficiency is observed.

The initial size of the nuclei is about 50 nm independent of the applied potential. This is the critical nucleation size for these conditions on a gold substrate.

For high potential (-0.37V), most of the ZnO is deposited during the nucleation, when some gold is in contact with the solution (during a 20 minutes deposition 95% of the material is deposited during the nucleation peak period). Goux et al. have reported surface blocking by oxide deposition intermediate on a ZnO electrode [194]. This blockage is preponderant at high potential due to the low overpotential and the growth is extremely slow when the entire gold surface has been covered with nuclei. The films deposited at -0.37 V are less textured because the growth is limited to the nucleation peak period and we have seen in the section 6.1 that the nuclei exhibit less texture.

For low potential (-0.67 V and lower), the growth rate is very similar during the nucleation phase due to the critical nucleation size. The main effect of potential is to control the growth rate both in the in plane and out of plane directions. As the nanorods grow faster, the coalescence happens faster when the potential is decreased.

6.3.5 Summary

In this section the effect of the deposition potential on the nanostructured ZnO films have been investigated. The mechanism of deposition for high potential (-0.37 V) is different due to surface blocking and low overpotentials. The mechanism for lower potential is very similar, the main effect of potential in this domain is to control the OH^- production which in turn controls the rod dimensionality. The control of the dimensions of ZnO nanostructure is an important step to enhance the performance of devices based on nanostructured materials. Changing the potential appears to be a smart and easy way to control the size of the nanostructures (see Figure 6.39 and Figure 6.40).

6.4 Effect of the Cl^- Concentration.

In this section the effect $[Cl^-]$ is investigated by using two different support electrolytes, KCl and $CaCl_2$ at a concentration of 0.1 M and thus two different $[Cl^-]$ (0.1 M and 0.2 M respectively). Using 0.1 M of $CaCl_2$ instead of 0.2 M of $CaCl_2$ giving a minor the change of conductivity of the solution ($\Lambda^0_{CaCl2}=262.10^{-4}$ $m^2.S.mol^{-1}$, $\Lambda^0_{KCl}=150.10^{-4}$ $m^2.S.mol^{-1}$ where Λ^0 is the conductivity per unit concentration of charges [6]). All the deposition parameters were kept constant. The films were deposited from a solution containing 5 mM of $Zn(NO_3)_2$ at 65°C. The applied potential was -0.97 V.

6.4.1 Microscopy

Figure 6.45 compares the morphology of samples obtained with two different support electrolytes, KCl and $CaCl_2$ at the same concentration (0.1 M) after a ten minute deposition.

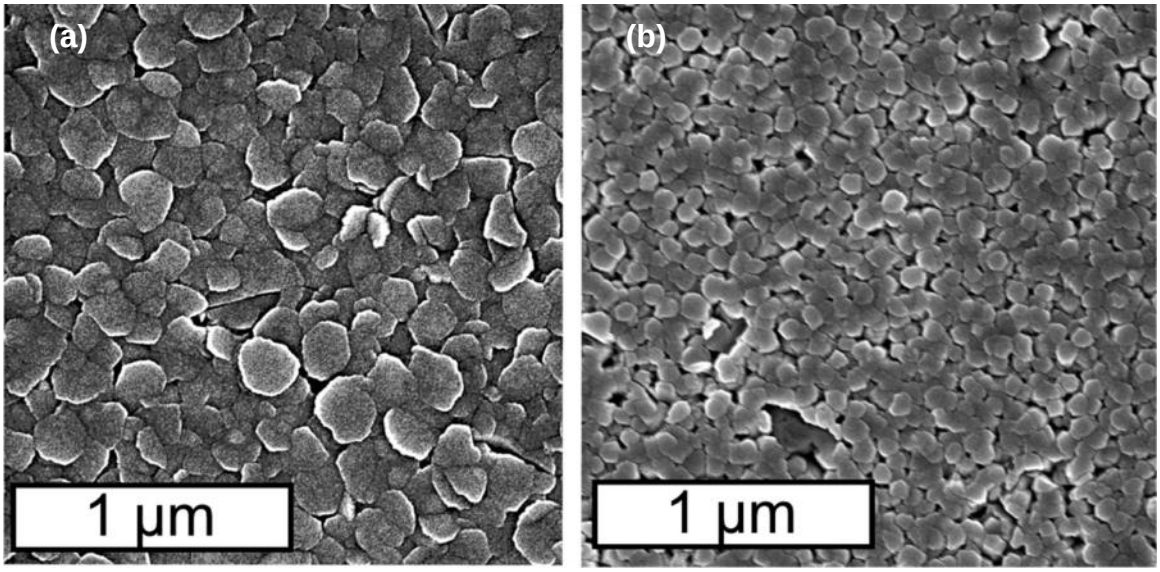


Figure 6.45 Effect of the $[Cl^-]$ on the morphology: 0.2 M of Cl^- (a) and 0.1 M of Cl^- (b). The deposition time was 10 minutes. 5 mM of $Zn(NO_3)$ in a oxygenated aqueous solution at 65°C. The applied potential was -0.97 V.

A striking fact is the change in the diameter of the structures. The films deposited with $CaCl_2$ are three times as big.

6.4.2 Electrochemical Measurements

Figure 6.46 presents the current and nominal thickness vs. time curve obtained with KCl (i) and $CaCl_2$ (ii). Both peak and plateau region, associated with a 3-D and 1-D growth respectively are clearly visible.

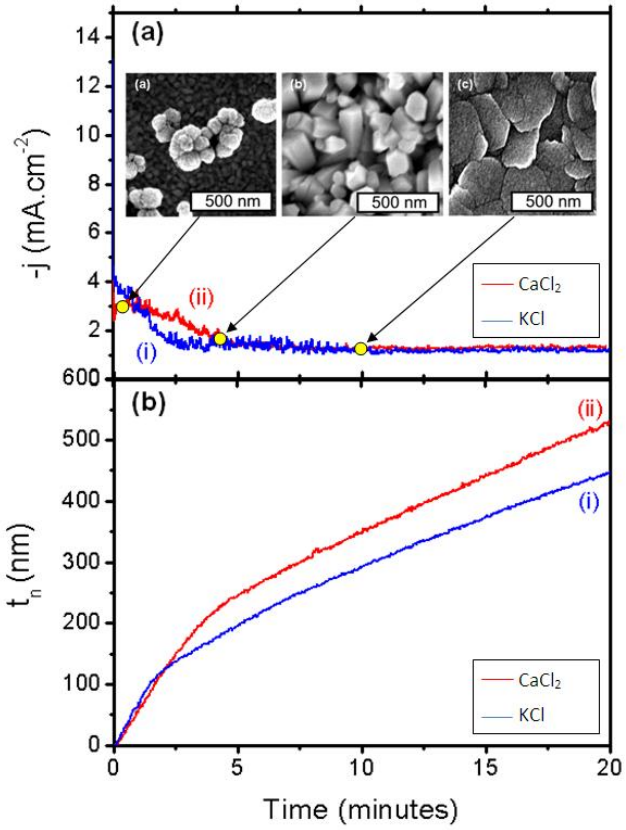


Figure 6.46 Simultaneous (a) current density and (b) nominal thickness measurements as a function of the support electrolyte (i) blue curves, KCl and (ii) red curves, $CaCl_2$. Inset: Evolution of the morphology with timewith a $CaCl_2$ support electrolyte. FESEM images after (a) 25 seconds, (b) 4 minutes and (c) 10 minutes. 5 mM of $Zn(NO_3)$ in a oxygenated aqueous solution at 65°C. The applied potential was -0.97 V.

The duration of the nucleation peak is extended compared to the case of KCl. The current intensities during the plateau region are identical. However a longer nucleation period is clearly visible for $CaCl_2$ on Figure 6.46b. The growth rate during 3-D growth region is slightly higher with KCl. The growth rate during 1-D growth region is slightly higher with $CaCl_2$. The nanostructures presented in the inset of Figure 6.46a are representative of 3 characteristic steps of the deposition: the first nuclei (after 25 s), the films at the end of the nucleation peak (after 4 minutes) and the films during the 1-D growth (10 minutes). The density of nanostructures during the nucleation is smaller for

$CaCl_2$. After 4 minutes the nanorods are not as well orientated as with KCl (see Figure 6.21), but the hexagonal shape of the rod is better defined.

Figure 6.47 presents the faradaic efficiency of two films deposited with 0.1M and 0.2 M of Cl. The faradaic efficiency is similar during the nucleation. For longer time the efficiency is greater with high Cl^- concentration.

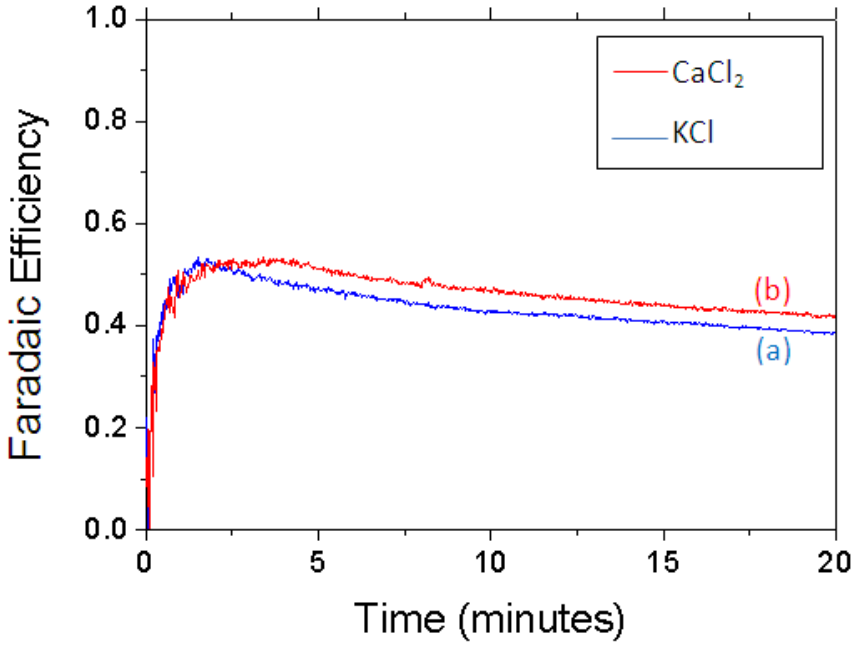


Figure 6.47 Current efficiencies calculated for the films deposited with (a) 0.1 M (blue line) and (b) 0.2 M (red line) of Cl^-. 5 mM of $Zn(NO_3)$ in a oxygenated aqueous solution at 65°C. The applied potential was -0.97 V.

6.4.3 X-Ray Diffraction

Figure 6.48 presents the ex-situ GIXS measurement of film deposited with $CaCl_2$ as a support electrolyte after a 4 minutes deposition. All the peaks have been identified as ZnO and Au.

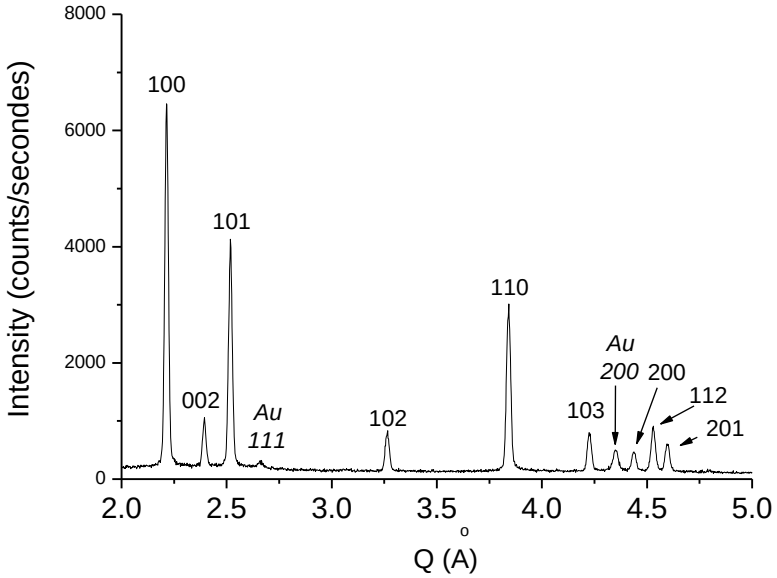


Figure 6.48 *Ex-situ* GIXS scan of a sample deposited for 4 minute. The peaks are labelled according to the ZnO wurtzite structure or Au fcc structure (italics). 5 mM of $Zn(NO_3)$ and 0.1 M of $CaCl_2$ in a oxygenated aqueous solution at 65°C. The applied potential was -0.97 V.

Figure 6.49 presents the in-situ measurements of FHWM of the (101) reflection polar scan. The peak width is broader with a high [Cl^-] indicating a less well-defined texture.

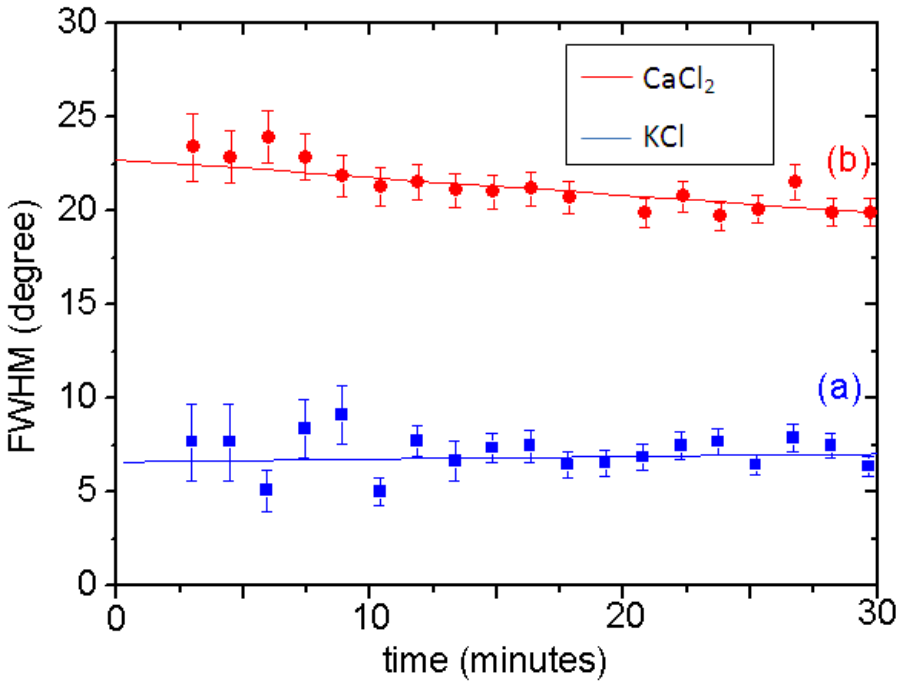


Figure 6.49 *In-situ* measurements of full width at half-maximum for the (101) reflection as a function Cl^- concentration: (a) 0.1 M and (b) 0.2 M. 5 mM of $Zn(NO_3)$ in a oxygenated aqueous solution at 65°C. The applied potential was -0.97 V.

6.4.4 Discussion

The number of nucleation sites is lower with 0.2 M of Cl^-. The density of nucleation sites is linked to the supersaturation of the solution at the beginning of the deposition. Zn^{2+} ions are strongly complexed by Cl^- [109]. Increasing the Cl^- concentration increases the complexation and thus decreases the supersaturation of the solution. Moreover, Tena-Zaera et all[164] have reported increasing [Cl^-] concentration slows down the oxygen reduction reaction. This is in good agreement with Figure 6.46 where a reduction of the initial current with high Cl^- concentration can be seen. The decrease of the hydroxide ions due to the lower rate of the oxygen reduction lead to lower supersaturation level at the beginning of the deposition. These two effects contribute to lower density of nanostructures and lower growth rate observed during the nucleation.

The change in morphology (higher diameter and well defined hexagonal shape of the rods) can be explained by the stabilisation of the polar (002) face by Cl^- has been reported by Xu and co-workers[129]. The decrease in texture may be explain by the repulsion between the negatively charge (002) surfaces and the negatively charged electrode. Tena-Zaera *et al.* have carried out a systematic study of the effects of [Cl^-] in similar deposition conditions[164]. They also observed an increase of rod diameter with increasing [Cl^-].

The texture measurements are in good agreements with the FESEM characterisations. After 4 minutes deposition some nanorods are not orientated perpendicular to the substrate (see Fig 6.20b) and the diameter of the nanostructure is bigger. As the rods are less orientated the surface of the films after coalescence is not flat and the active area is thus higher. The (001) is the most reactive face. This leads to a higher growth rate during the 1-D growth. When the nanorods enter into contact, the growth is directed to a direction perpendicular to the substrate and an increase of the texture is observed.

6.4.5 Summary

Increasing the Cl^- concentration dramatically increased the growth rate in the in-plane direction due to stabilisation of polar (001) face by Cl^- ions. Less textured films are produced with higher Cl concentration.

6.5 Effect of $Zn(NO_3)_2$ Concentration

In this chapter a systematic study of the effect of the concentration of $Zn(NO_3)_2$ in the range [0.1 mM, 50 mM] will be carried out. The other deposition parameter will be fixed to the following value: the temperature is 65°C, the potential is -0.77 V, the support electrolyte is 0.1 M of KCl and the solution is saturated with oxygen. The potential has been decreased in order to be able to study higher concentration range. Indeed with a potential of -0.97 V the formation of parasitic phases are observed from 20 mM. This effect will also be discussed in this chapter.

6.5.1 Effect of the Zinc(II) Concentration on the Solution pH.

Figure 6.50 presents the variation of pH observed when the concentration of $Zn(NO_3)_2$ is increased in solution.

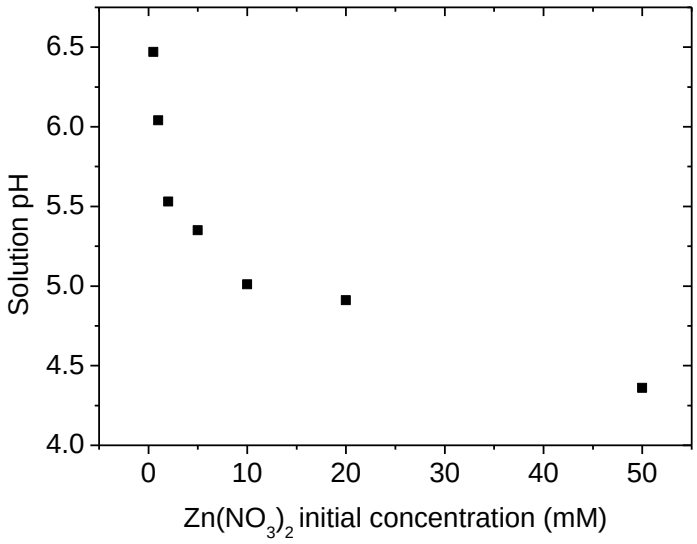


Figure 6.50 Change in the solution pH as a function of initial concentration of $Zn(NO_3)_2$ at 65°C.

The hydrolysis of Zn^{2+} leads to a decrease of the pH according to the reaction:

$$Zn^{2+} + H_2O \leftrightarrow ZnOH^{+} + H^{+} \qquad \text{Eq. 6.15}$$

When the $[Zn^{2+}]$ is increased a dramatic decrease of pH is observed from 6.5 for a concentration of 0.1 mM to 4.25 for a concentration of 50 mM

6.5.2 Microscopy

Figure 6.51 presents the FESEM images of films deposited for 30 minutes with different $Zn(NO_3)_2$ concentrations. For low concentrations (less than 2 mM), the film is composed of isolated rods with a hexagonal shape (see Figure 6.51a, 6.31b and 6.31c). Some rods have a triangular shape because of twinning defects. For intermediate concentrations (between 5 and 20 mM), the film is a dense layer (see Figure 6.51d, 6.31e and 6.31f) formed of coalesced rods. For high concentrations (greater than 20 mM), the film is composed of large sheets (see Figure 6.51g). The sheets are a few microns long and only a few nanometres thick. The concentration regions less than 2 mM; between 2 and 20 mM; and above 20 mM will be called 'low', 'medium' and 'high' concentrations respectively throughout this section.

In order to gain a better understanding of the growth mechanism, the evolution of the morphology of the films with time has been studied. Figure 6.52 presents FESEM images of samples prepared with a low concentration after deposition time of 30 s (Figure 6.52a) and 3600 minutes (Figure 6.52b and Figure 6.52c). The grains of the gold substrate are clearly visible on Figure 6.52a and one can see that the ZnO nuclei have the same size. After one hour of deposition the ZnO nanorods are orientated perpendicular to the substrate, and no coalescence is visible. Pyramid-like structures are clearly visible on the top of the rods. If the concentration is increased to 5 mM, even though the films are still composed of rods (see cross section in Figure 6.51d), the top face of the rod is flat and the substrate is densely covered after a few minutes. Figure 6.52e shows a FESEM image of the film after 15 seconds of deposition. The nuclei have a rough conical shape. Figure 6.52f shown a FESEM image of a film deposited under the same conditions after 20 minutes. The nanostructures now have now a hexagonal shape.

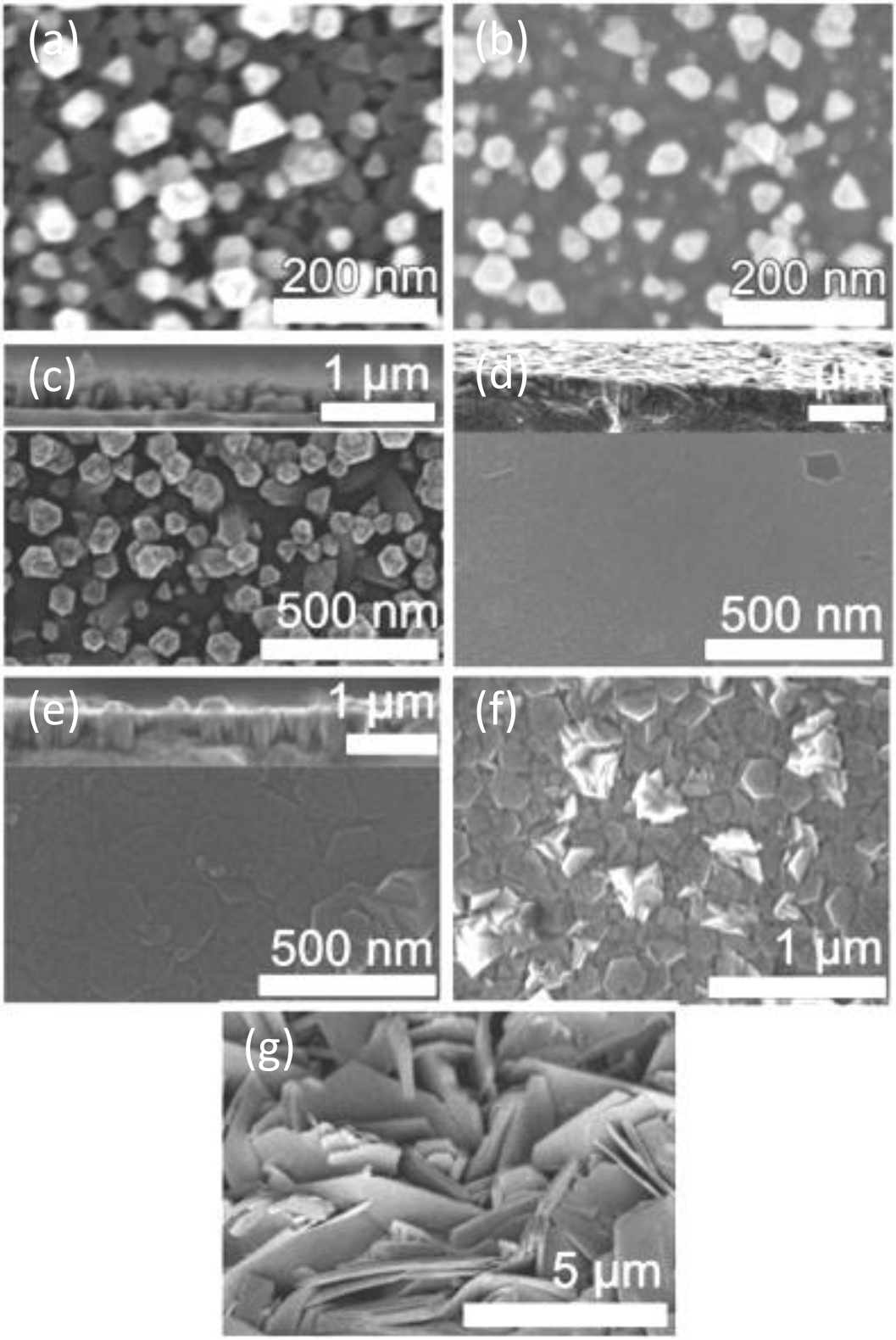


Figure 6.51 Effect of the $Zn(NO_3)_2$ concentration on the morphology of the films. FESEM images of films deposited with an initial concentration of (a) 0.5 mM, (b) 1 mM, (c) 2 mM, (d) 5 mM, (e) 10 mM, (f) 20 mM and (g) 50 mM. The top insert in figures (c), (d), (e) and (g) presents the FESEM cross section of the films. The deposition time was 30 minutes. 0.1 M of KCl in an oxygenated aqueous solution at 65°C. The applied potential was -0.77 V.

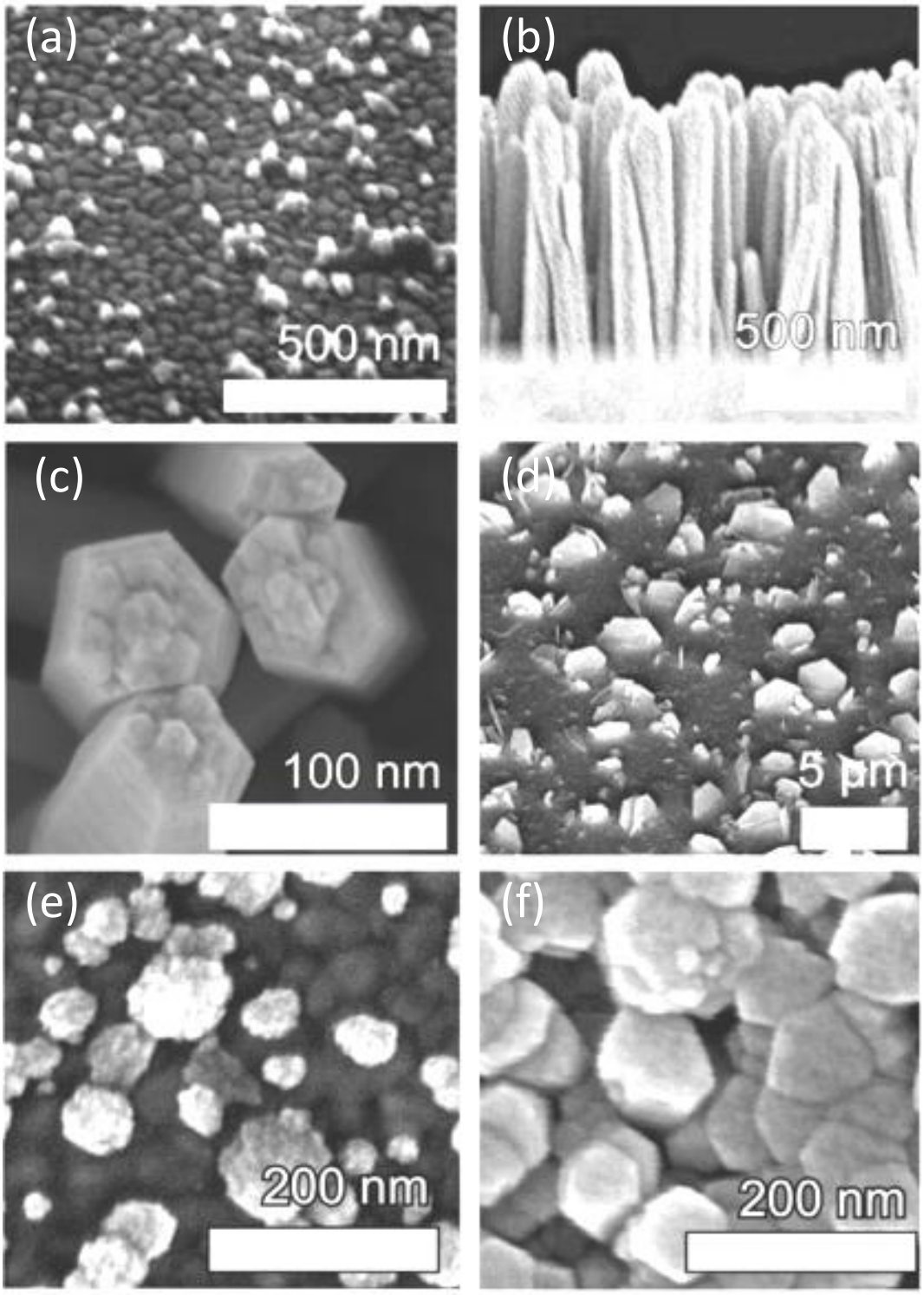


Figure 6.52 Evolution of the film morphology with time as a function of initial concentration of $Zn(NO_3)$. FESEM images: tilt view of a film deposited with (a) 1 mM for 30 seconds, (b) cross section and (c) top view of a film deposited with 1 mM for 60 minutes, (d) tilt view of a film deposited with 50 mM for 30 seconds and top view of films deposited with 5 mM for (e) 30 seconds and (f) 20 minutes. 0.1 M of KCl in an oxygenated aqueous solution at 65°C. The applied potential was -0.77 V.

Figure 6.53 shows the time dependence of the rod diameter for 1 and 5 mM $Zn(NO_3)_2$, which exhibits a dramatic change in the growth habit in going from low to medium concentrations: an increase of the diameter with time is clearly visible in the medium concentration region whereas the diameter is approximatively constant for low concentrations.

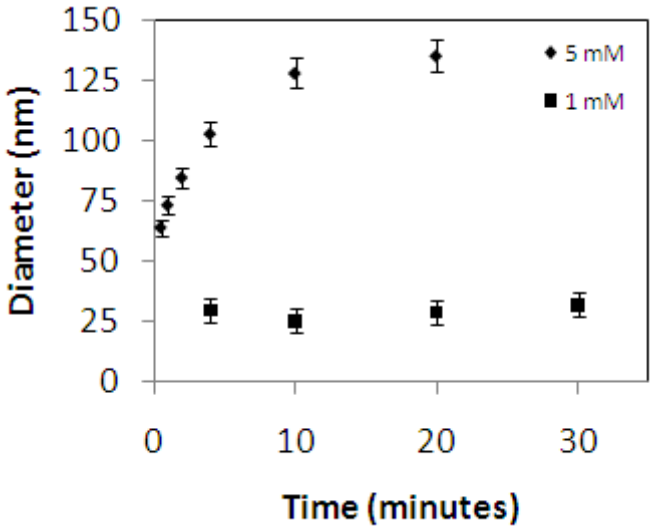


Figure 6.53 Evolution of the rod diameter with time as a function of $Zn(NO_3)_2$ concentration: 1 mM (triangle) and 5 mM (square) of $Zn(NO_3)_2$. The rod diameters have been measured from the FESEM images on two samples deposited in the same conditions. 0.1 M of KCl in an oxygenated aqueous solution at 65°C. The applied potential was -0.77 V.

In the medium concentration region, if the concentration is further increased above 5 mM, the growth direction is progressively shifted away from the direction perpendicular to the substrate (see Figure 6.51e and Figure 6.51f). Figure 6.54 presents the size distribution of the nanorod diameter after 30 minutes of deposition. For low concentrations, the distribution is very narrow. When the concentration is increased, the mean rod diameter increases and the dispersion becomes broader. Thus the rod diameter distribution can be controlled simply by varying the concentration.

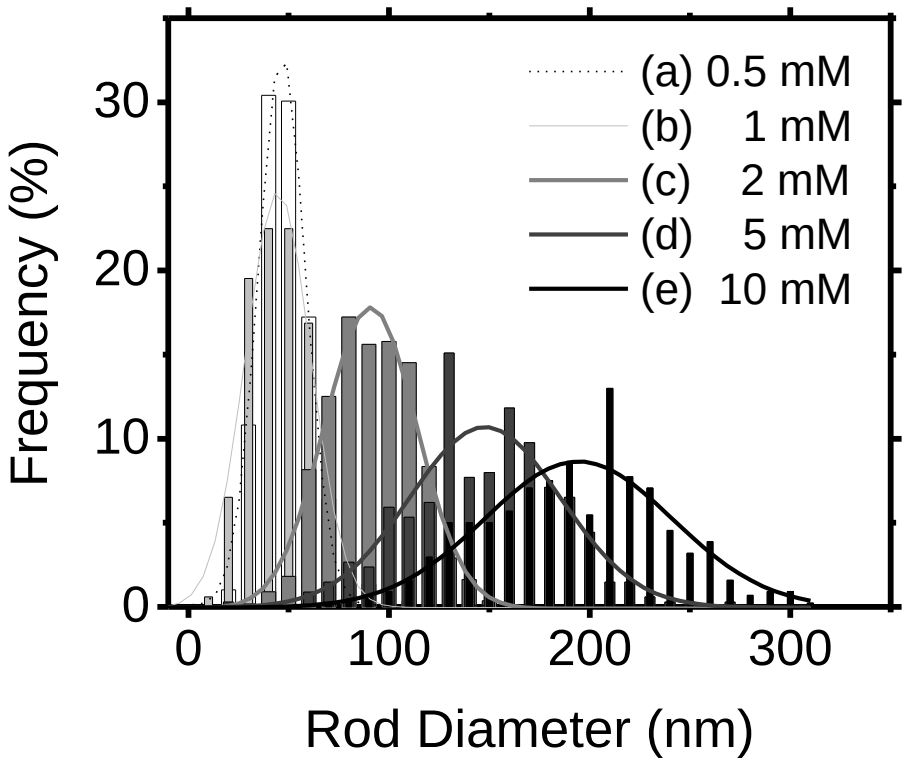


Figure 6.54 Distribution of the nanorod diameters as a function of the $Zn(NO_3)_2$ concentration. (a) 0.5 mM, (b) 1 mM, (c) 2 mM, (d) 5mM and (e) 10 mM. The rod diameters have been measured from the FESEM images on two samples deposited in the same conditions. Gaussian fits of the distributions have been indicated by lines. The deposition time is 30 minutes. 0.1 M of KCl in an oxygenated aqueous solution at 65°C. The applied potential was -0.77 V.

EDS was carried out on the films. The films deposited from an electrolyte containing 5 mM or less of Zn nitrate are entirely composed of Zn and O. For higher concentrations the percentage of Cl in the film increases, up to 7% for 50 mM. After annealing (1 hour at 400°C), these films were Cl free.

6.5.3 Electrochemical Measurements

Figure 6.55a shows the variation with time of the absolute value of the current density as a function of the concentration. The curves obtained for low concentrations are very noisy and remain quite constant with time. When the concentration is medium to high, a peak, followed by a plateau, appears. The peak gets narrower and more intense when the concentration is increased. The increase in the intensity of the peak in the medium and high concentration is related to a change in morphology. Figure 6.52d presents FESEM images of the films after 30 seconds of deposition at high concentrations,

showing the formation of nanosheets. The nanosheets have a very high aspect ratio and thus the active surface for the reduction reaction is higher than the rods and therefore the peak value is also higher. The fact that the peak is narrower indicates that the nucleation rate increases with an increase of the concentration. No peak is visible at low concentrations because there is no coalescence.

Figure 6.55b presents the variation of the volume of Zn(II) per unit area of surface with time. For low concentrations the growth is quasi linear. When the concentration is increased the change in slope of the curves is smoother.

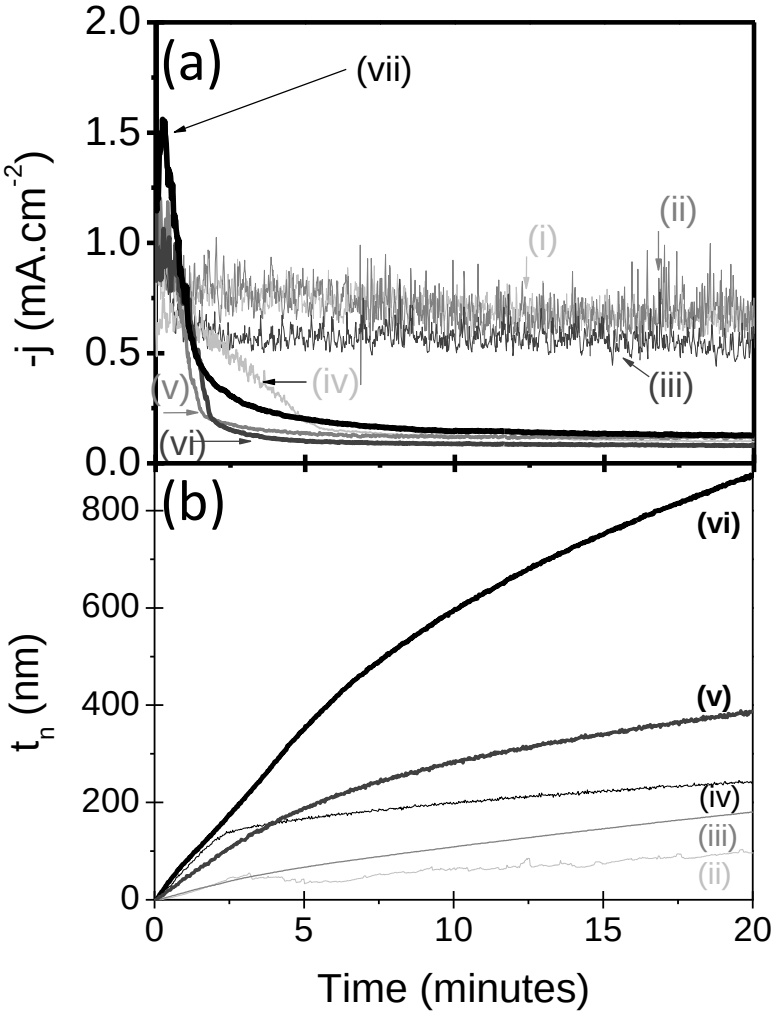


Figure 6.55 Variations of the current density (a) and of the nominal thickness (b) with time as a function of $Zn(NO_3)_2$ concentration: (i) 0.5 mM, (ii) 1 mM, (iii) 2 mM, (iv) 5 mM, (v) 10 mM, (vi) 20 mM and (vii) 50 mM. 0.1 M of KCl in an oxygenated aqueous solution at 65°C. The applied potential was -0.77 V.

Figure 6.56 presents the variation of the faradaic efficiency of the reaction with time. The differences between the three cases can be clearly seen. For low concentrations, the faradaic efficiency is very low, less than 10%. A sharp increase is observed during the first few minutes of deposition. This indicates that the reaction is more efficient on ZnO than on gold. For medium concentrations, the curves have a similar shape to the low concentration curves, but there is a peak in the faradaic efficiency and the plateau value is about 40%. When the concentration is high, the shape of the curve is completely modified. No peak is observed, and the faradaic efficiency increases sharply before reaching a plateau at 70%.

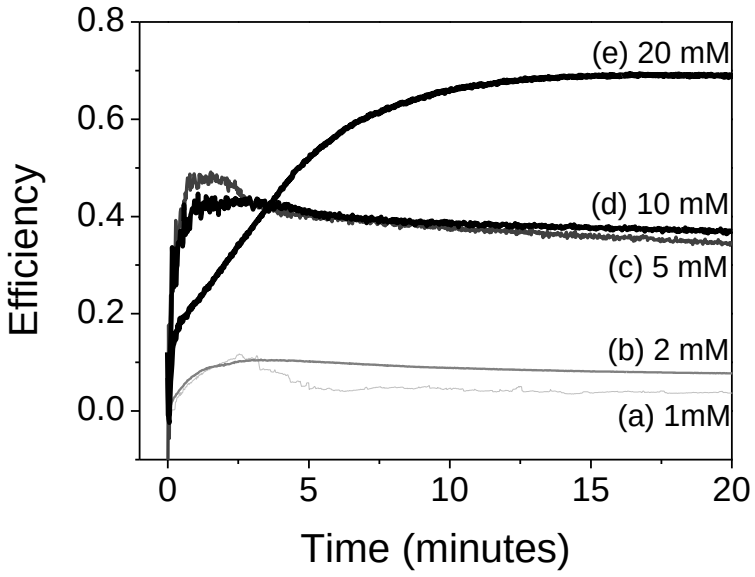


Figure 6.56 Variations of the faradaic efficiency with time as a function of $Zn(NO_3)_2$ concentration: (a) 1 mM, (b) 2 mM, (c) 5 mM, (d) 10 mM, (e) 20 mM. 0.1 M of KCl in an oxygenated aqueous solution at 65°C. The applied potential was -0.77 V.

6.5.4 X-Ray Diffraction

XRD performed at the end of the *in situ* XRD experiments for 1 mM and 5 mM only show peaks from ZnO (see Figure 6.57).

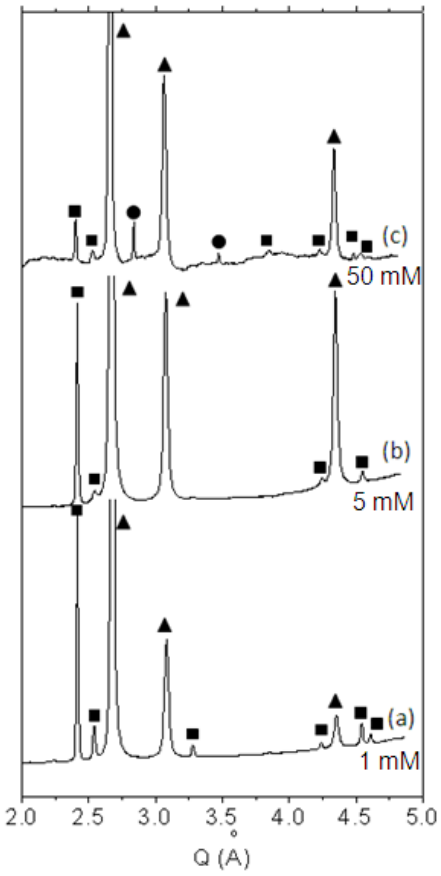


Figure 6.57 *In-situ* grazing incidence XRD scans at the end of a 30 minutes deposition as a function of concentration. (a) low concentration (1 mM), (b) medium concentration (5 mM) and (c) high concentration (50 mM). The peaks corresponding to ZnO, Au and $Zn_5(OH)_8Cl_2$ have been marked the squares, triangles and circle respectively. 0.1 M of KCl in an oxygenated aqueous solution at 65°C. The applied potential was -0.77 V.

For a higher concentrations of $Zn(NO_3)_2$, two extra peaks appear which can be identified as belonging to a $Zn_5(OH)_8Cl_2$[11, 195]. It has been shown that this phase can be removed by annealing at 350 °C for one hour and that the resulting films produce intense green luminescence at room temperature under femtosecond pulse UV light excitation[195]. The formation of the zinc hydroxylchloride is dependent on the relative solubility of zinc oxide and zinc hydroxylchloride species[11] (see Figure 6.58). For a concentration of 50 mM the solubility of ZnO and $Zn_5(OH)_8Cl_2$ are similar.

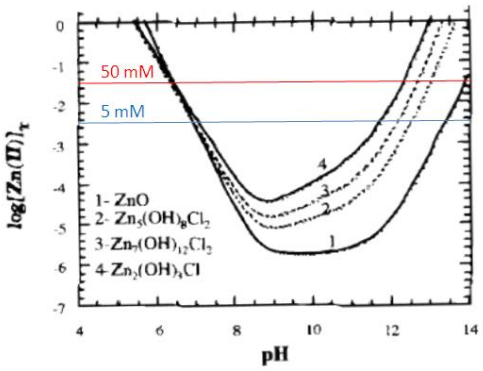


Figure 6.58 Solubility diagrams of zinc oxide and zinc hydroxychloride after 11

This is in good agreement with the EDS measurements showing an increase of the Cl content of the film with the increasing concentrations of $[Zn^{2+}]$. At more negative potentials, the intensity of the ZnO peaks is smaller than $Zn_5(OH)_8Cl_2$ and additional peaks corresponding to other zinc hydroxylchlorite phase appear (Figure 6.59). Increasing the deposition potential can be a simple way to produce purer ZnO materials and reduce the need for annealing. Another way is to decrease the concentration of Cl^- in solution. With the same amount of $Zn(NO_3)_2$ and a smaller amount of Cl^- in solution (0.06M), Xu and co-workers report the direct electrodeposition of ZnO[129].

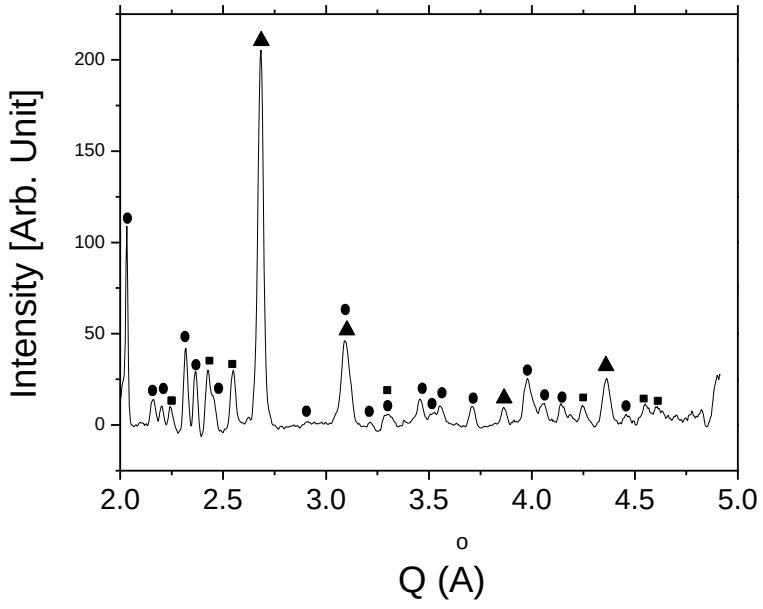


Figure 6.59 *In-situ* grazing incidence XRD scans at the end of a 30 minutes deposition with an applied potential of -0.97 V and $Zn(NO_3)_2$ concentration of 50 mM. 0.1 M of KCl in an oxygenated aqueous solution at 65°C.

The azimuthal peak of the GIXS scans recorded during the deposition were fitted using Lorentzian function. From these fittings the FWHM were obtained as a function of time (Figure 6.60). The crystallite sizes are similar for all concentrations. The crystallite sizes of the nanostructures deposited at low and high concentration appear to be slightly larger. The may be due to an elongation of the grains in the preferential growth direction. Indeed, the growth of the structures deposited at medium concentration is less anisotropic.

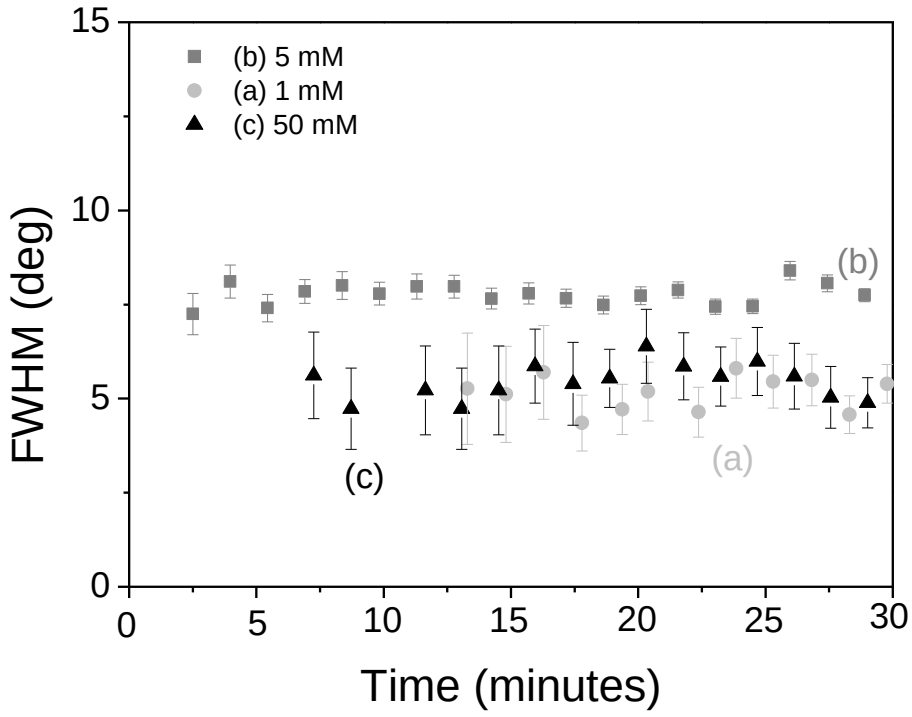


Figure 6.60 Full width at half-maximum (fwhm) calculated from (101) polar angle plots. (a) light grey circles, low concentration (1 mM), (b) gray squares, medium concentration (5 mM) and (c) black triangles, high concentration (50 mM). 0.1 M of KCl in an oxygenated aqueous solution at 65°C. The applied potential was -0.77 V.

6.5.5 Discussion

The influence of $[Zn^{2+}]$ on the growth mechanism is controversial. Elias et al[131] explain the formation of nanowires at low concentration by a Zn^{2+} diffusion limited mechanism. El Belghiti[132] argue that such limitations will lead to the formation of conical structures which reflect the concentration gradient. They propose that the growth along the [002] direction is due to the higher reactivity of the (002) polar faces. Both mechanisms do not

fully explain the formation of the structures observed in this work: anarray of nanowires with a conical ending for low concentrations, dense films for medium concentration and plates for high concentration.

There are two fundamental models of crystal growth mechanism when random nuclei are generated on existing flat surfaces: the Kossel-Stranski-Volmer (KSV) mechanism [196, 197] (2-D nucleation growth) and the Bessel-Cabrera-Frank (BCF) mechanism[198] (spiral growth). In the KSV mechanism, 2-D nucleation occurs preferentially near the edges, kinks and steps of the substrate. When all the high index facets have disappeared, the crystal will continue to grow by 2-D nucleation of new material depositing on the low index facets[198]. In the BCF mechanism, crystal faces grow *via* the outward displacement of a growth spiral originating from screw dislocations in the central region of the face. The former occurs only at relatively high supersaturation levels whereas the latter can happen at low supersaturation levels. The solubility product K_s of ZnO can be written as:

$$K_s=[Zn^{2+}][OH^-]^2 \qquad [4]$$

The saturation of the solution is strongly dependent on the initial concentration of zinc nitrate ($C(Zn(NO_3)_2)$) as it is both a precursor of zinc and hydroxide ions.

Low supersaturation ($C(Zn(NO_3)_2$)< 2 mM)

The supersaturation of the solution is low and the growth follows a BCF mechanism. The pyramidal like structures at the top of the rods are the steps of screw dislocations. The diameter of the rods is set during the nucleation and stays constant during the growth because the growth proceeds from the outside inwards. Similar types of growth have been reported for CBD for low level of supersturation[199].

No change in the morphology and growth kinetics have been observed by varying the applied potential, which promote the formation of hydroxide. The growth is probably limited by the diffusion of Zn(II). The faradaic efficiency is therefore low because the production of hydroxide is faster than the Zn(II) diffusion.

High supersaturation ($C(Zn(NO_3)_2)$**> 20 mM)**

In this domain the supersaturation of the solution is very high. 2-D nucleation of low index faces is more favourable and the growth follows a KSV mechanism. Large plates are formed. The growth rate is dramatically increased (see Figure 6.55b). The comparison of SEM images (see Figure 6.51g and Figure 6.52d) shows that the number and diameter of the nanosheets increase dramatically with time whereas the thickness does not change significantly. The growth perpendicularly to the sheets is blocked by absorption of Cl^-. This happens preferentially on the polar faces and blocks the growth in that direction as reported[129]. The fact that the sheets grow perpendicularly to the substrate may be explained by Coulomb repulsion between the Cl^- terminated (002) face and the negatively polarised substrate[195]. The nucleation is continuous and the growth of new plates stacking next to the former one is observed. The formation of $Zn_5(OH)_8Cl_2$ is observed because for high level of supersaturation its solubility is close to that of ZnO[11]. The faradaic efficiency first increases because the reaction of hydroxide formation is more efficient on ZnO than gold[194]. It is lower than 100% due to the formation of other phases and the diffusion of hydroxide toward the bulk solution.

Medium supersaturation (2 mM < $C(Zn(NO_3)_2)$**< 20 mM)**

In this intermediate region the concentration of the oxygen and zinc precursor are close to stoichiometry and a transition between the two mechanisms reported above is observed. During the nucleation, the pH in the vicinity of the electrode is low and so is the supersaturation. Conical structures are formed following a BCF mechanism. The increase of the pH at the electrode with time leads to an increase of the supersaturation and a transition to a KSV mechanism. The low index faces disappear by the addition of material on the side of the rods and the formation of flat (00l) surfaces with a hexagonal symmetry is observed. An increase of the faradaic efficiency is observed compared to lower concentration because of the increase of the concentration of Zn(II) in solution and thus a decrease of the diffusion limitation.

6.5.6 Summary

Three concentration regions have been identified where the deposition behaviour of ZnO nanostructures differs notably. For low Zn^{2+} concentrations (less than 2 mM) the

nanorods grow along screw dislocations: pyramidal structures are observed on top of the rods, and over time the rods maintain a constant diameter and do not coalesce. For medium Zn^{2+} concentrations (2 mM to 20 mM) the nanorods grow in a 3-D fashion and ultimately coalesce. The growth rate behaviour clearly shows an initial nucleation process followed by 3-D growth. For high Zn^{2+} concentrations (above 20 mM) large nanosheets are formed and Cl^- ions absorb to the surface to form zinc hydroxylchloride phases. By controlling the zinc concentration in solution, highly tailored morphologies can be produced.

6.6 Effect of pH, Dissolution and Formation of Nanotubes

In this chapter we will first study the effect of pH in the range [2; 6]. The other deposition parameter will be fixed to the following value: the temperature is 65°C, the potential is -0.97 V, $[Zn^{2+}]$ is 5 mM, the support electrolyte is 0.1 M of KCl and the solution is saturated with oxygen. We will then study the dissolution of the nanostructures as a function of time before discussing the effect of time, potential, $[Zn^{2+}]$ and $[Cl^-]$ on the dissolution and formation of nanotubes. All the dissolution experiments were performed in the deposition solution at the open circuit potential.

6.6.1 Effect of pH on the Growth

6.6.1.1 Microscopy

Figure 6.61 presents FESEM images for films deposited under the same conditions apart from the pH. The structures deposited at pH 4 have shaper edges and a lower density. The diameter is increased for a solution pH of 6.

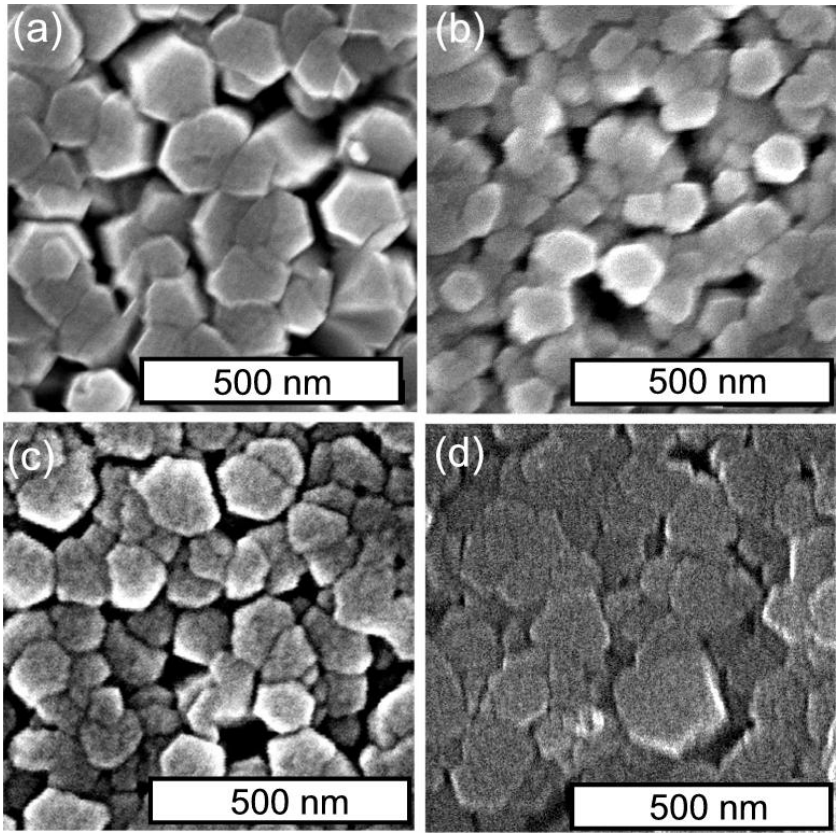


Figure 6.61 Effect of pH. FESEM images after a 20 minute deposition and the film immediately removed from solution. (a) pH=4, (b) pH=5, (c) pH=5.3 and (d) pH=6. 5 mM of $Zn(NO_3)_2$ and 0.1 M of KCl in an oxygenated aqueous solution at 65°C. The applied potential was -0.97 V.

6.6.1.2 Electrochemical Measurements

Figure 6.62 shows the current density vs. time curves for different initial pH values. The current is generated by the reduction of dissolved oxygen and nitrate ions (see Eqs. (6.2-3) and (6.8)).

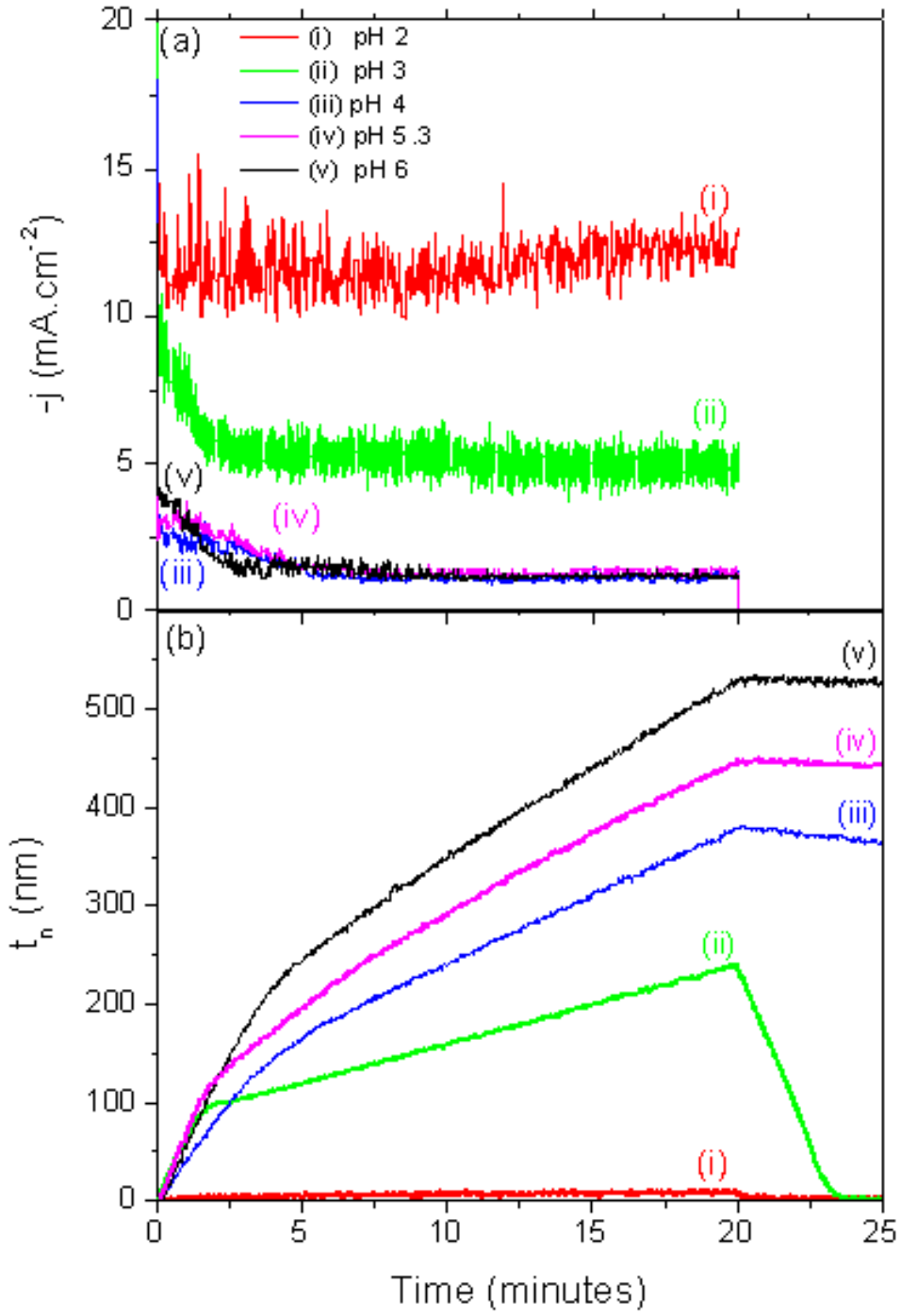


Figure 6.62 Simultaneous current density (a) and nominal thickness (b) measurements as a function of the pH (i) pH=2, (ii) pH=3, (iii) pH=4, (iv) pH=5.3, (v) pH=6. 5 mM of $Zn(NO_3)_2$ and 0.1 M of KCl in an oxygenated aqueous solution at 65°C. The applied potential was -0.97 V.

From pH 2 to pH 4, the current decreases when the pH is increased. Decreasing the pH is equivalent to consuming OH^-, which is the product of reactions (6.2-3) and (6.8), and so the reaction is promoted. The effect becomes negligible when the pH is greater than 4. A peak in the current followed by a plateau is observed below pH 3. As the peak in current

happens instantaneously, this means that the surface is immediately active. Figure 6.62b shows the variation of the nominal thickness with time. The change in the magnitude of the Zn(II) signal was also followed for 5 minutes after the 20 minute deposition time (i.e. with no potential applied). The deposition curves are in perfect accord with the current transient curves. Three growth regimes can be identified. When the pH is less than 2, precipitation does not occur and no nucleation peak is observed. When the pH is between 2 and 4, precipitation does occur, but as soon as the applied potential is removed the film is quickly dissolved. For pH 4 or higher, precipitation occurs and the film is quite stable. It is not surprising that the rate of dissolution increases when the pH decreases based on the solubility behaviour of bulk ZnO with solution pH[109]. A decrease in pH, shifts the equilibrium of the deposition reaction (3.1) toward the left and thus the dissolution rate increases.

6.6.1.3 X-Ray Diffraction

Figure 6.63 presents the end scan of the *in-situ* GIXS measurements with the solution removed as a function of pH. All the peaks have been identified has ZnO wurtzite and Au. Figure 6.64 presents the in-situ measurements of FHWM of the (101) reflection polar scans. There is little significant variation with time or pH within the uncertainty in measurement.

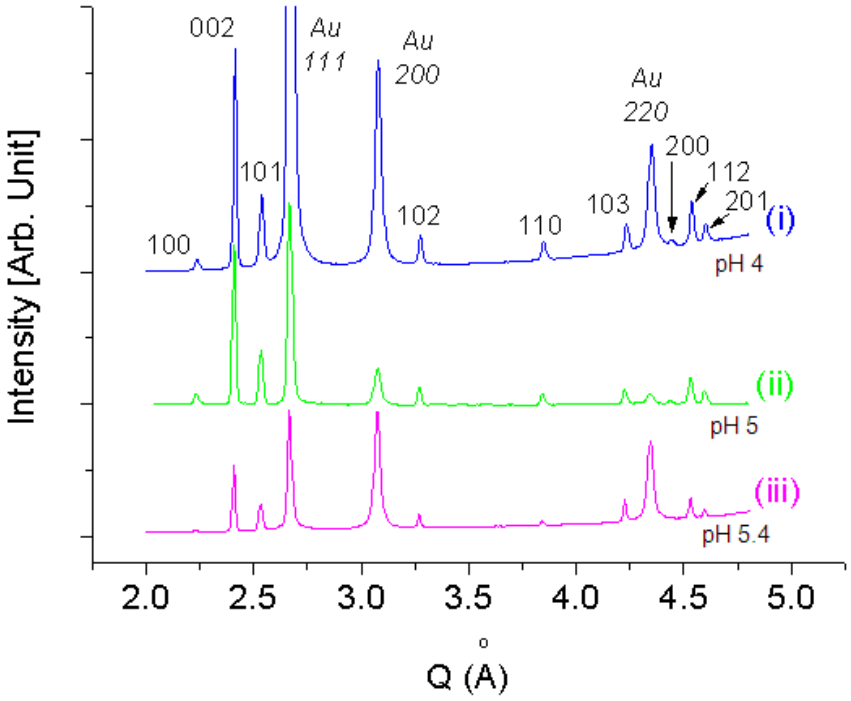


Figure 6.63 *In-situ* end GIXS scan with removed solution as a function of pH: (i) pH=4, (ii) pH= 5, (iii) pH=5.4. The peaks are labelled according to the ZnO wurtzite structure or Au fcc structure (italics). 5 mM of $Zn(NO_3)_2$ and 0.1 M of KCl in an oxygenated aqueous solution at 65°C. The applied potential was -0.97 V.

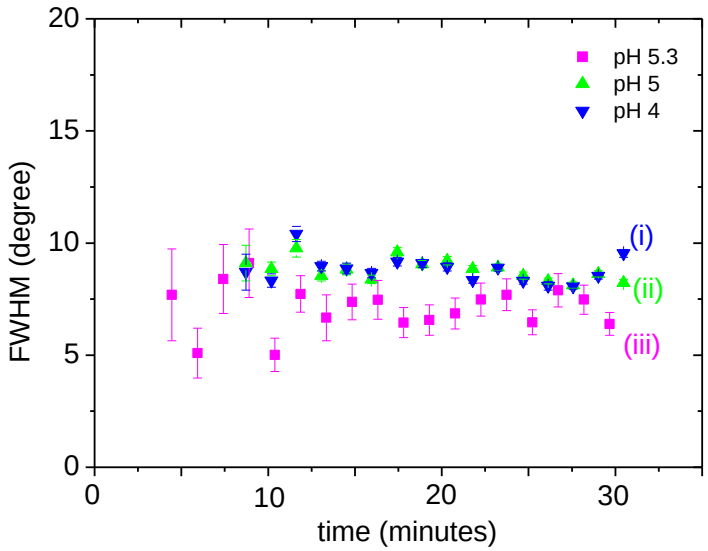


Figure 6.64 *In-situ* measurements of full width at half-maximum for the (101) reflection as a function of pH: (i) pH=4, (ii) pH=5 and (iii) pH=5.3. 5 mM of $Zn(NO_3)_2$ and 0.1 M of KCl in an oxygenated aqueous solution at 65°C. The applied potential was -0.97 V.

6.6.2 Dissolution and Formation of Nanotubes.

6.6.2.1 Introduction

Figure 6.62 clearly show the dissolution of the films when the applied potentials is removed. A very interesting fact is that the dissolution process is anisotropic. Figure 6.65 presents combined nominal thickness measurements with FESEM images of two films deposited in the same conditions expect that the one of them was left in solution for 40 minutes after the deposition was halted.

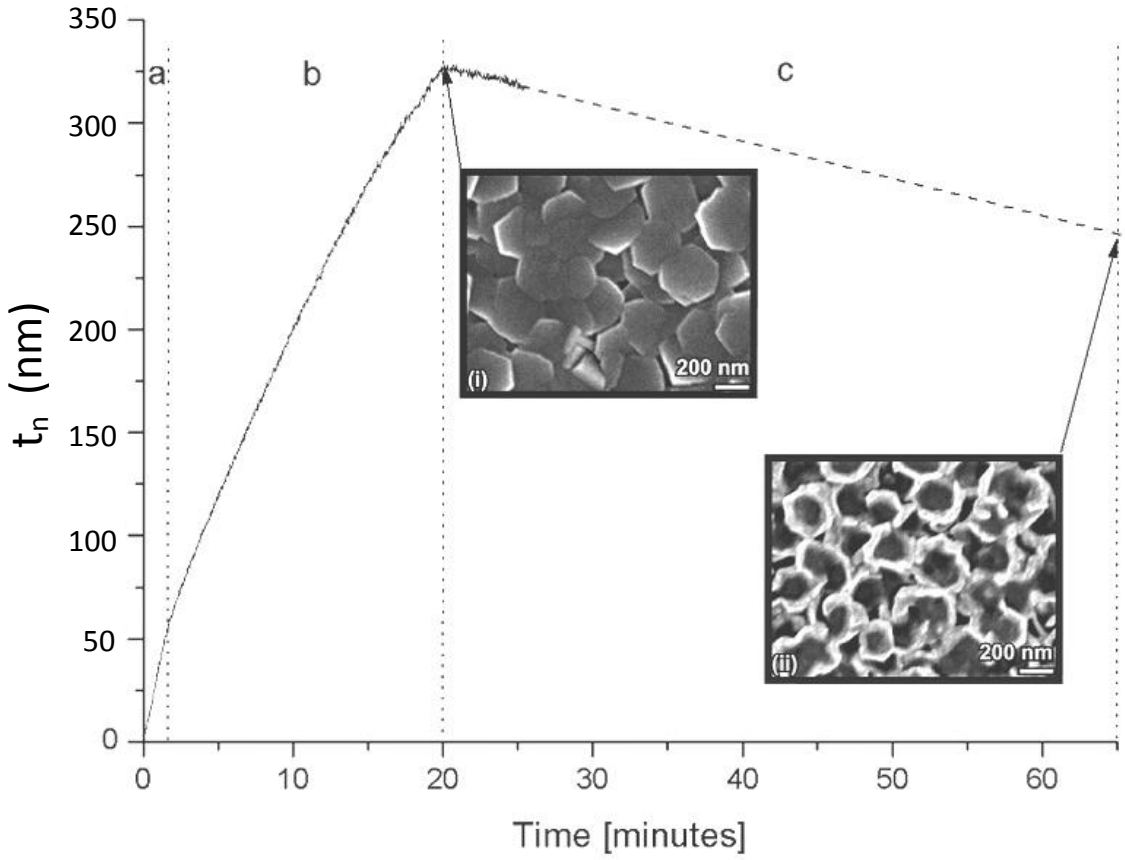


Figure 6.65 Nominal thickness as a function of time, for a ZnO film deposited from 10 mM Zn(NO3)2 solution with 0.1 M KCl as the electrolyte at 65°C. The applied potential was -0.77 V. Region (a) corresponds to nucleation, (b) to 1d growth, and (c) to open-circuit dissolution. The inset micrographs correspond to the end of deposition (20 minutes, i) and dissolution (40 minutes, ii).

In Figure 6.65 the nominal thickness increases during the deposition is apparent; a 2-stage growth (regions a and b) occurs, characteristic of a transition from 3-D to 1-D growth in the nanostructured films. The total volume of material is then seen to slowly

decrease at an effective rate of about 1 nm per minute as soon as the cell is returned to open circuit conditions.

Inset (i) in Figure 6.65 shows a typical FESEM image of a dense film of nanorods removed from the electrolyte immediately at the end of deposition and inset (ii) the corresponding structure after 40 minutes dissolution at open circuit in the same solution. Before the dissolution the film is composed of an array of coalesced nanorods oriented perpendicular to the substrate as a result of anisotropic growth along the c-axis. The rod length is about 320 nm normal to the substrate. The micrograph inset (ii), corresponding to the end of the process, shows the dramatic inhomogeneous nature of the dissolution process: holes are formed in the centre of the initial nanorods and preferential etching of the rod interior proceeds. To understand the formation of these ZnO nanotubes, it is necessary to consider the ZnO crystal structure. To form tubular structures from the rods requires a preferential dissolution on the (002) metastable plane. The formation of nanotubes by aging process have been first reported by Vayssieres et al[200] which were using a chemical bath deposition method. This method was requiring long preparation times, the formation of tubes was observed after 2 days. This process is remarkably quick and reproducible over large areas and for various experimental conditions as shown in Figure 6.66.

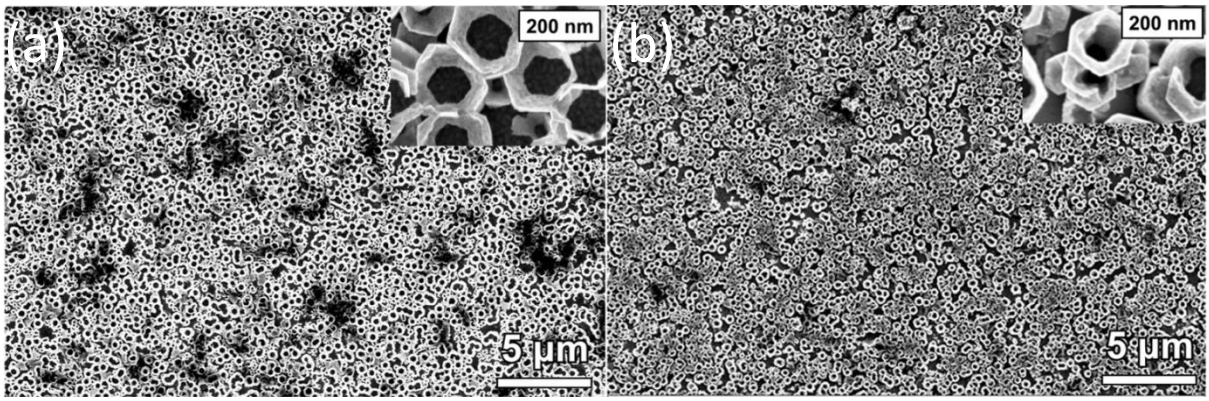


Figure 6.66 Formation of tube structures occurs over large areas. The dimensions such as tube diameter, tube high and wall thickness can be tailored by varying the deposition parameters. The insets show close-up of the nanotubes. (a) The applied potential was -870 mV using a 5 mM $Zn(NO_3)_2$ solution and 0.1 M $CaCl_2$ electrolyte. (b) The applied deposition potential was -770 mV. The solution was 5 mM $Zn(NO_3)_2$ with 0.1 M $CaCl_2$ electrolyte. The dissolution time is 270 minutes in both cases.

The formation of nanotubes is strongly dependent on the deposition conditions and the dimension (tube diameter, tube hight and wall thickness) can be tailored by varying the

deposition parameters. In the following paragraph we will discuss the influence of time, potentials, Zn(II) concentrations and Cl^- concentration on the morphology of the films. Table 2 summarize the growth and dissolution rates measured as a function of the potential (E), $[Cl^-]$, $[Zn^{2+}]$ and pH.

	E (V)	[Cl-]	$[Zn^{2+}]$	pH	Growth Rate* nm/min	Dissolution Rate* nm/min
Variation in E	-0.37	0.1 M	5 mM	5.4	0.21±0.02	-1.53±0.04
	-0.97	0.1 M	5 mM	5.4	15.43± 0.04	-1.19± 0.07
Variation in $[Cl^-]$	-0.97	0.1 M	5 mM	5.8	15.43± 0.04	-1.19± 0.07
	-0.97	0.2 M	5 mM	6	17.99± 0.05	-0.67 ± 0.04
Variation in $[Zn^{2+}]$	-0.97	0.1 M	1 mM	6	1.27 ± 0.01	-0.66 ± 0.11
	-0.97	0.1 M	5 mM	5.4	15.43 ± 0.07	-1.19 ± 0.14
	-0.97	0.1 M	10 mM	5	25.45 ± 0.17	-3.30 ± 0.21
Variation in pH	-0.97	0.1 M	5 mM	3	8.06 ± 0.04	-70.96 ± 0.37
	-0.97	0.1 M	5 mM	4	13.71 ± 0.05	-3.20 ± 0.12
	-0.97	0.1 M	5 mM	5	15.44 ± 0.07	-1.19 ± 0.14

Table 6.3 Growth and dissolution rates for ZnO nanostructured films formed under a range of conditions. *Rates are calculated from in situ x-ray absorption measurements such as shown in Figure 6.65

6.6.2.2 Microscopy

6.6.2.2.1 Evolution of the Film Morphology with Time

Fig 6.67 shows samples deposited in the same conditions and dissolved for different durations. One can clearly see the formation of pit-holes and the progressive dissolution of the top face. After 4.5 hours, all the rods have been transformed to tubes of length ~ 250 nm and wall width ~ 40 nm. The films were totally dissolved after 5 hours.

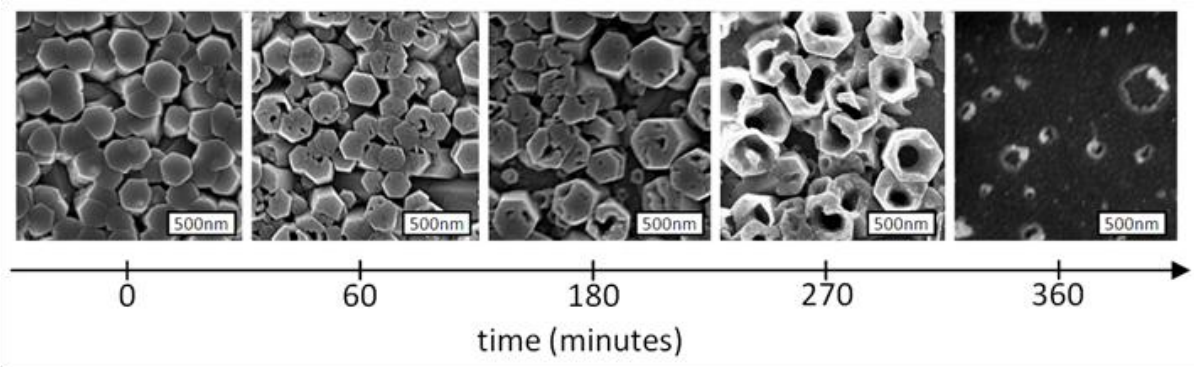


Figure 6.67 Evolution of the film morphology with increasing dissolution time. The samples were prepared from a solution with 5 mM of $Zn(NO_3)_2$ and 0.1 M of$CaCl_2$ at 65°C

6.6.2.2.2 Effect of Deposition Potential.

The dissolution behaviour is similar to the case presented in the above paragraph for an applied potential between -1 V and -0.5 V. For higher potentials the *dissolution* mechanism is different. Figure 6.65 shows the film before and after dissolution for a film deposited with a high potential (-0.37 V). The film after dissolution has been coated with Au. No sign of anisotropic dissolution is seen. We have seen that the structures grown at high potential have a smaller diameter. No anisotropic dissolution has been observed for structures with a diameter less than 50 nm.

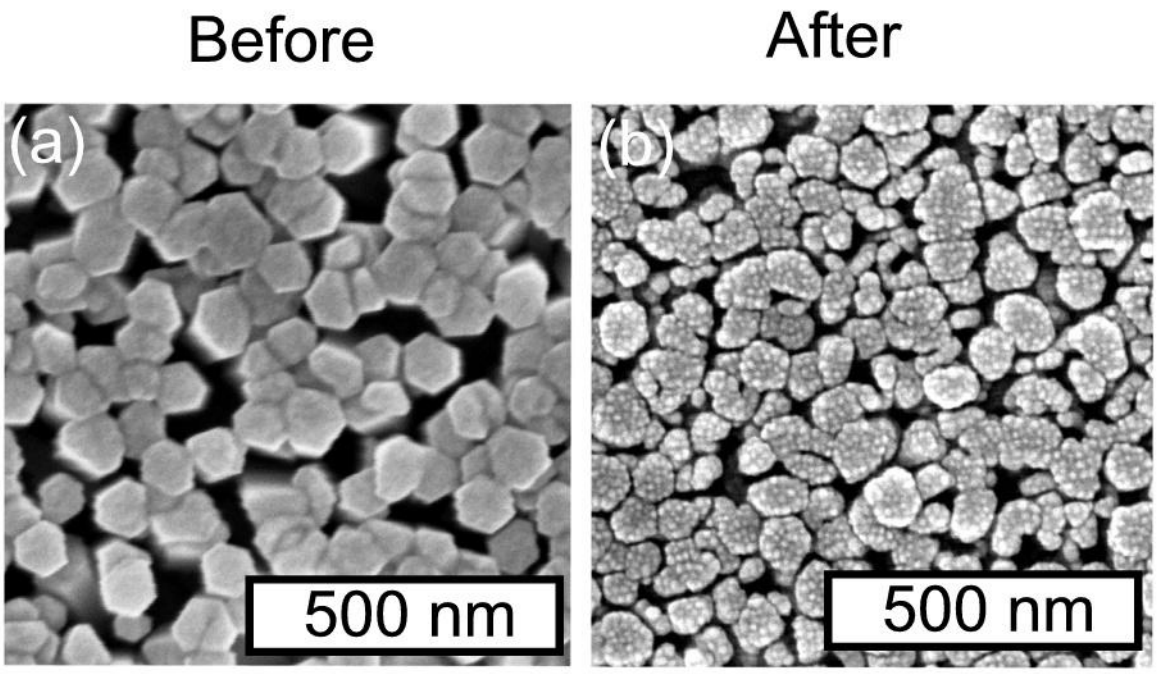


Figure 6.68 Evolution of the film morphology before and after a one hour long dissolution for high deposition potential (-0.37 V). The samples were prepared from a solution with 5 mM of $Zn(NO_3)_2$ and 0.1 M of KCl at 65°C. The small pots on fig (b) are due to the gold coating.

6.6.2.2.3 Effect of Cl Concentration

Changing the concentration of Cl^- from 0.1 to 0.2 M changes both the growth and dissolution kinetics as shown in Table 6.3. The growth rate *increases* from ~15 to 18 nm/min and the dissolution rate *decreases* from 1.2 to 0.7 nm/min. The FESEM images in Figure 6.69 clearly show that the nanostructures are modified by the amount of Cl^-.

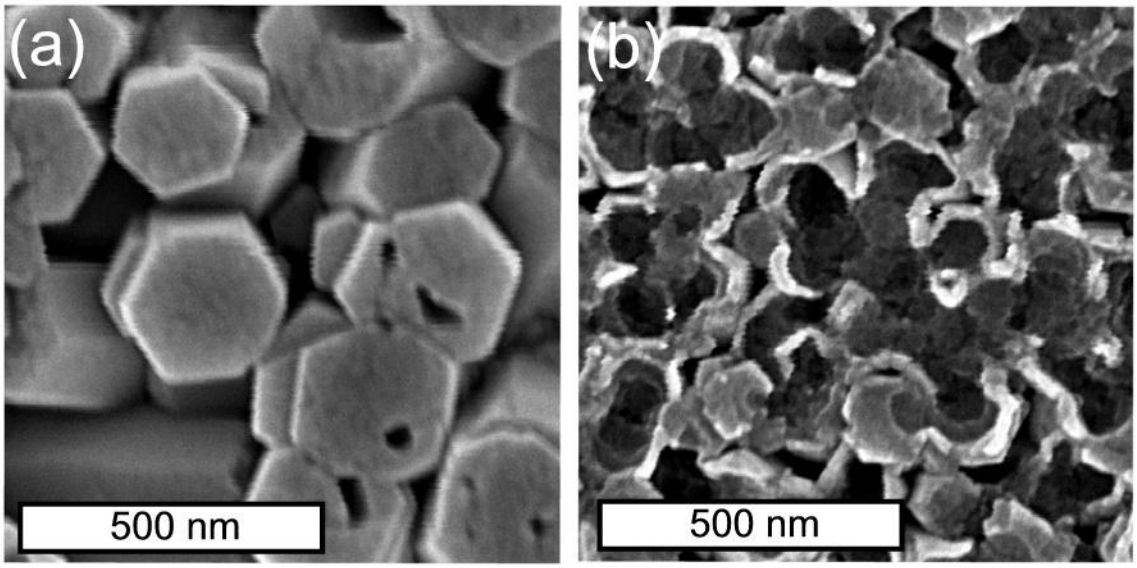


Figure 6.69 Influence of chloride ion concentration. FESEM images of films deposited at -0.770 V at 65°C from 5 mM $Zn(NO_3)_2$ solution for 20 minutes after 1 hour long dissolution: (a) 0.1 M Cl^- (b) 0.2 M Cl^-

Firstly the Cl^- affects the size and density of the nanorods: with 0.2 M Cl^- as a support electrolyte the rod diameter is doubled in comparison to 0.1 M Cl^- (250 nm vs. 120 nm). Figure 6.69 show the FESEM images after 60 minutes dissolution. One can clearly see that the dissolution behaviour is completely different. At low Cl^- the dissolution is more homogeneous and faster. With 0.2 M Cl^-, pits are formed at the top of the rods. Furthermore the lateral faces of the rods appear 'sharper'. Both of these effects are a result of the Cl^- anion in the stabilization of the (001) polar plane. During the deposition, stabilization of the top face allows continued lateral growth and the resulting rods are wider. During the dissolution process, the top face is again stabilized and the dissolution is slower. As the dissolution rate is very slow for higher Cl^- concentrations the dissolution time was increased to 270 minutes to observe to resultant morphology (Figure 6.67): all the rods have been transformed to tubes of length ~ 250 nm and wall width ~ 40 nm.

6.6.2.2.4 Effect of Zn(II) Concentration

1. Medium concentration

The dissolution rate is found to increase, by a factor of ~3, by increasing [Zn^{2+}] from 5 to 10 mM. This is contrary to what would be expected by simply considering the equilibrium condition for Eq. 3.1 but probably due partly to the change in pH generate by the change in zinc concentration (see Figure 6.50). Moreover, changing the [Zn^{2+}] is also found to affect the morphology of the deposited film, producing larger diameter rods. These low aspect ratio rods have a significantly higher proportion of metastable, polar surface and this leads to much more rapid dissolution of the structure. As can be seen in Figure 6.70 under such rapid dissolution the sides of the tubes may start to collapse resulting in a more disordered porous structure.

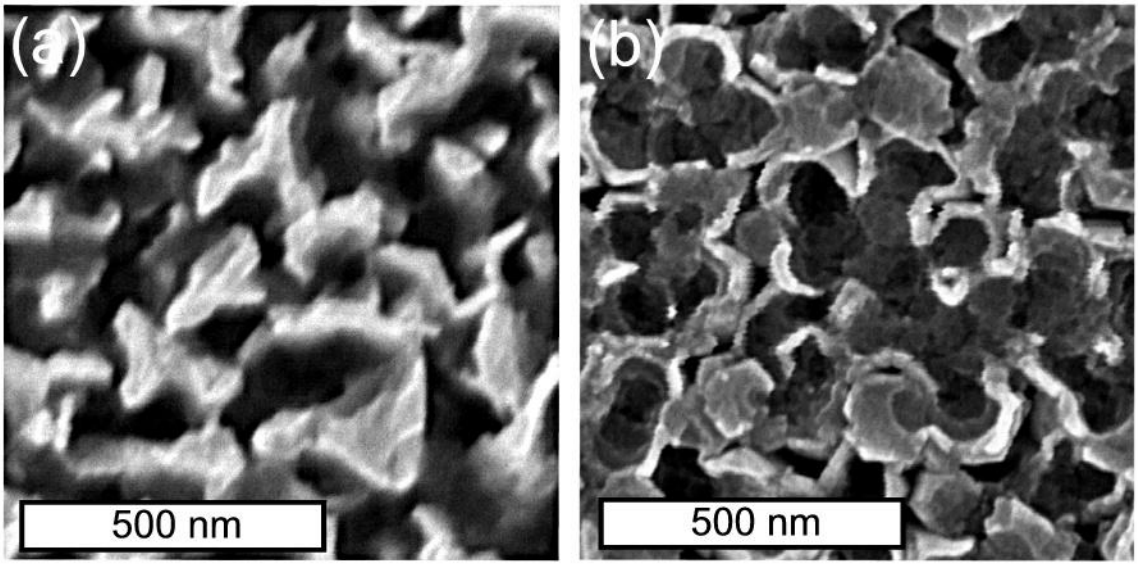


Figure 6.70 Influence of chloride ion [Zn^{2+}]. FESEM images of films deposited at -770 mV at 65°C with KCl support electrolyte for 20 minutes after 1 hour dissolution: (a) 10 mM of [Zn^{2+}] and (b) 5 mM of [Zn^{2+}]

2. Low and High Concentration

The dissolution rate data show a strong dependence on the cation concentration (Table 6.3). The dissolution rate is also found to increase, by a factor of ~5, by increasing [Zn^{2+}] from 1 to 10 mM. This is due to the strong change in pH associated with the change in zinc nitrate concentration. Figure 6.71a and 6.49b Show the images of nanostructures

deposited with low zinc nitrate concentration (1 mM). The dissolution is anisotropic, an important decrease in diameter is observed while the length is not dramatically altered. As the rods in this condition have a conical ending, there is no (002) face in contact with the solution. The dissolution happens preferentially along the *side* faces of the rods and thinner rods can be obtained.

A similar effect is observed for high zinc nitrate concentration. The thickness of the plates is constant whereas a decrease of the diameter is observed. The rate of dissolution of the faces parallel to the sheet is slower than perpendicular. This is due to the stabilisation of the (002) by the adsorbed Cl^- as discussed and in the section 6.5.

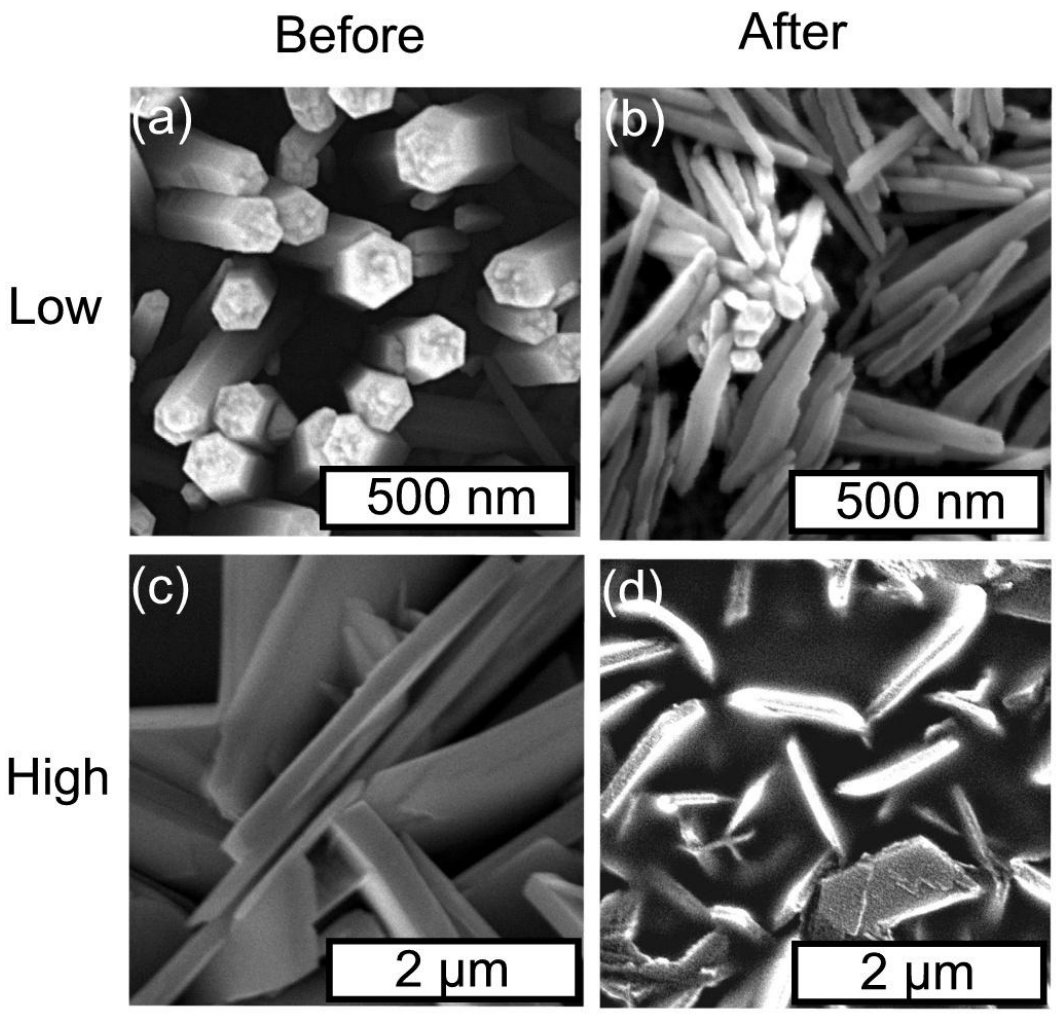


Figure 6.71 Study of the dissolution: influence of concentration. Deposition conditions for (a) and (b): 5 mM $Zn(NO_3)_2$, 0.1 M $CaCl_2$ at 65^{0}C for 90 minutes. The applied potential was -0.77 V. The samples shows in (b) have been dissolved for 3.5 hours. Deposition conditions for (c) and (d): 50 mM $Zn(NO_3)_2$, 0.1 M KCl at 65^{0}C for 30 minutes. The applied potential was -0.77 V. The samples shows in (d) have been dissolved for 1 hour.

6.6.2.3 X-Ray Diffraction

In order to gain a better understanding of the crystallographic effects, XRD measurements were performed. Figure 6.72 shows *ex-situ* grazing incidence scans of two films deposited from a 10 mM $Zn(NO_3)_2$ solution with 0.1 M KCl electrolyte at 65°C and an applied potential of -0.77 mV, one removed from solution immediately after 20 minutes deposition and the other subsequently dissolved for 45 minutes.

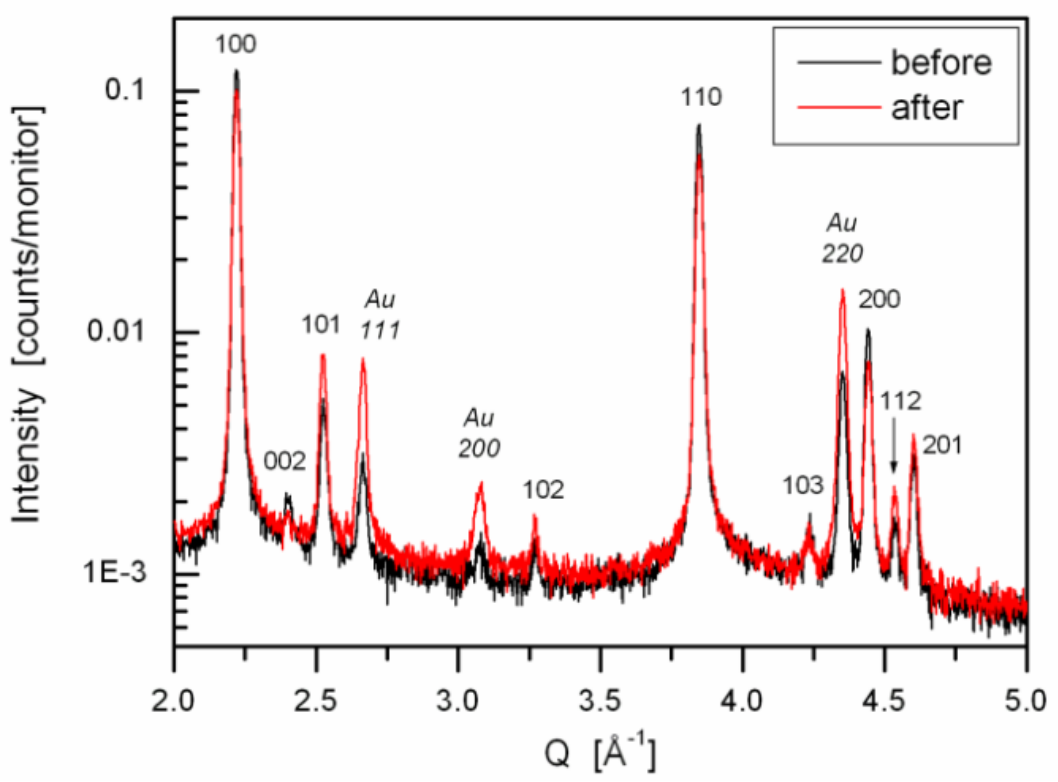


Figure 6.72 Grazing incidence XRD scans of two films deposited for 20 minutes from a 10 mM $Zn(NO_3)_2$ solution with 0.1 M KCl electrolyte at 65°C and an applied potential of -770 mV, one removed from solution immediately after deposition but before dissolution (black), and the other subsequently dissolved for 45 minutes (red). The peaks are labelled according to the ZnO wurtzite structure or Au fcc structure (italics). Note that the intensity is shown on a log scale

All the peaks have been identified as wurtzite ZnO or substrate Au and are labelled accordingly. In addition, texture scans were performed on a the (101) peak. The (101) has both in-plane and out-of-plane components and shows a 49% reduction which is consistent with the XANES result obtained under the same conditions.

6.6.3 Summary

A simple process for the formation of ZnO nanotubes from nanorods in aqueous solutions has been demonstrated. Selective etching of the (002) surface results in anisotropic dissolution and the formation of tubular structures. Care must be taken in

fast-etching regimes to avoid collapse of the tubes. The dimensionality of the tubes can be controlled by an appropriate choice of the deposition parameters and post-deposition solutions. Here we have considered a one-step approach where films have been formed and dissolved under the same conditions; variation of the solution during this process would allow for more careful tuning of the tube structures.

The deposition and dissolution processes are related to the solubility product for ZnO in the relevant solution, coupled with stabilizing effects of specific anions such as Cl^- on the polar faces of the ZnO nanostructures. With this in mind it is possible to modify the kinetics of both the deposition and dissolution processes by simple changes to the electrolyte environment, such as anion concentration and solution pH. In addition the formation of tube-like structures shows strong dependence on the potential and concentration at which the *nanorods are formed*.

6.7 Effect of Capping Agent

The effect of carboxyl groups on the growth has been studied by comparing acetate, oxalate and citrate groups. The structures of the molecules used and the experiments performed are summarised in Table 6.4.

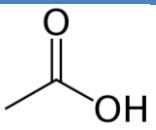
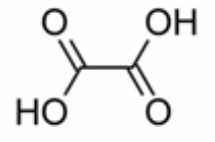
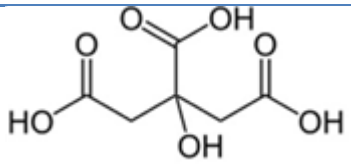
Additive	Structure	pH	Concentration (mM)
Acetic Acid		4,5, 5.4 and 6	0.1 and 1
Oxalic Acid		4, 5, 5.4 and 6	0.1 and 1
Citric Acid		5.4	0.01, 0.1 and 1

Table 6.4 Summary of structures used and conditions studied

Acetic acid, oxalic acid and citric acid have 1, 2 and 3 carboxyl groups respectively and therefore they are good candidates to systematically study how the groups affect the growth. All the other deposition parameters were kept constant. The films were deposited from a solution containing 5 mM of $Zn(NO_3)_2$ and 0.1 M of KCl at 65°C. The applied potential is -0.97V.

Table 6.4 presents the variation of relative concentration of the acid base couple with pH. Increasing the pH from 4 to 6 increases the concentration of the base in solution by a factor 100 and it is thus an easy way to vary the concentration of negatively charge carboxylate groups.

Organic molecules such as acetate ions[158], ethylenediamine[158] and citric acid[159] have been used to changed the morphology of electrodeposited zinc oxide. The effect of organic molecules have also been extensively studied[160-163] for CBD. Changed from 1-D structures to 2-D have been explain by the poisoning of the polar (002) due to the preferential absorption compared to the non-polar faces.

pH	R1	R2
4	6	2
5	0.6	0.2
5.3	0.2	0.1
6	0.06	0.02

Table 6.5 Ratio of the acid concentration to base concentration for the acido-basic couple $[HCH_3CO_2]/[CH_3CO^{2-}]$ (R1) and $[HC_2O_4]/[C_2O^{4-}]$ (R2) as a function of pH.

6.7.1 X-Ray Diffraction

Adding new molecules in solution increases the risk of depositing other phases than ZnO. As the deposition of ZnO is the main goal in this work, XRD characterisations and EDS measurements were first performed to check the phase purity. Figure 6.19 shows the XRD data of films deposited with different carboxylic groups at fixed pH (5.4).

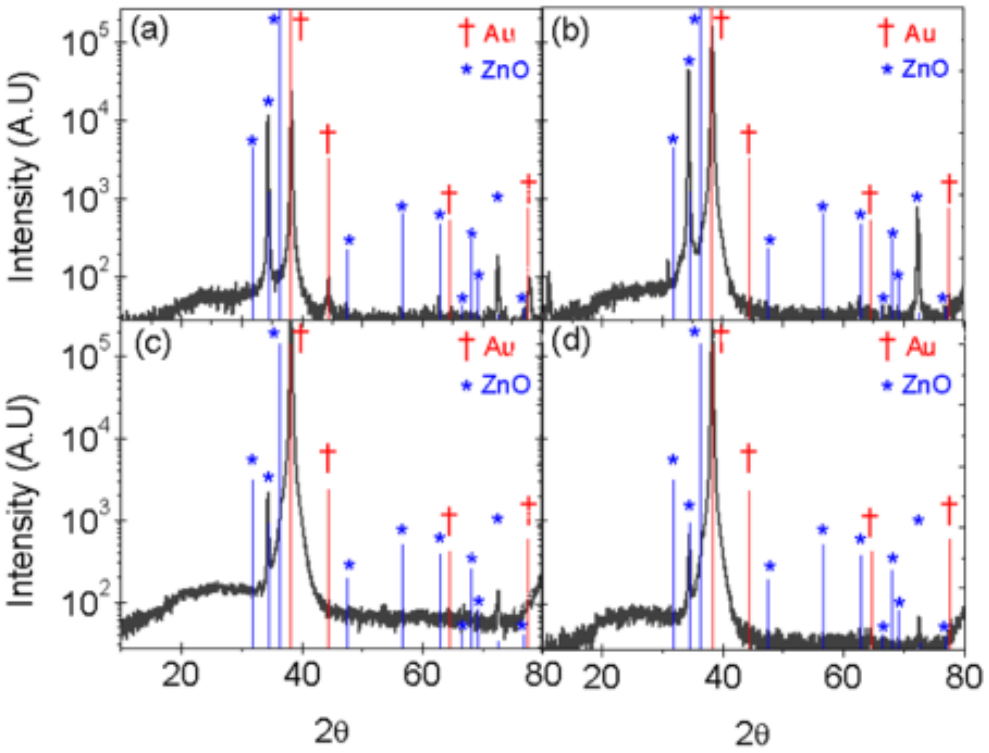


Figure 6.73 Comparison of the XRD pattern for different surfactant. (a) no surfactant, (b) 1 mM of sodium acetate, (c) 1 mM of oxalic acid and (d) 0.1 mM of citric acid. Red and blue lines correspond to cubic gold (from the substrate) and hexagonal zinc oxide patterns respectively. 5 mM of $Zn(NO_3)_2$ and 0.1 M of KCl in an oxygenated aqueous solution at 65°C. The applied potential was -0.97 V.

All peaks have been identified as zinc oxide or gold (substrate). The peaks due to the gold substrate are indicated by stars in the figure. All the other peaks can be indexed as wurtzite ZnO (crosses). The ZnO nanostructures have a strong (002) preferential orientation, as evidenced by the (00l) lines being very strong and all other peaks very weak.

These results are in good agreement with the EDS measurements (see Figure 6.74). All the films execpt one deposited with oxalic acid were composed of Zn, O and a concentration of Cl^- below 2 at. %. The one deposited with oxalic acid contained C between 10 and 17 at% depending on the pH. As C is a very light element, EDS provides a rough estimation of the C content.

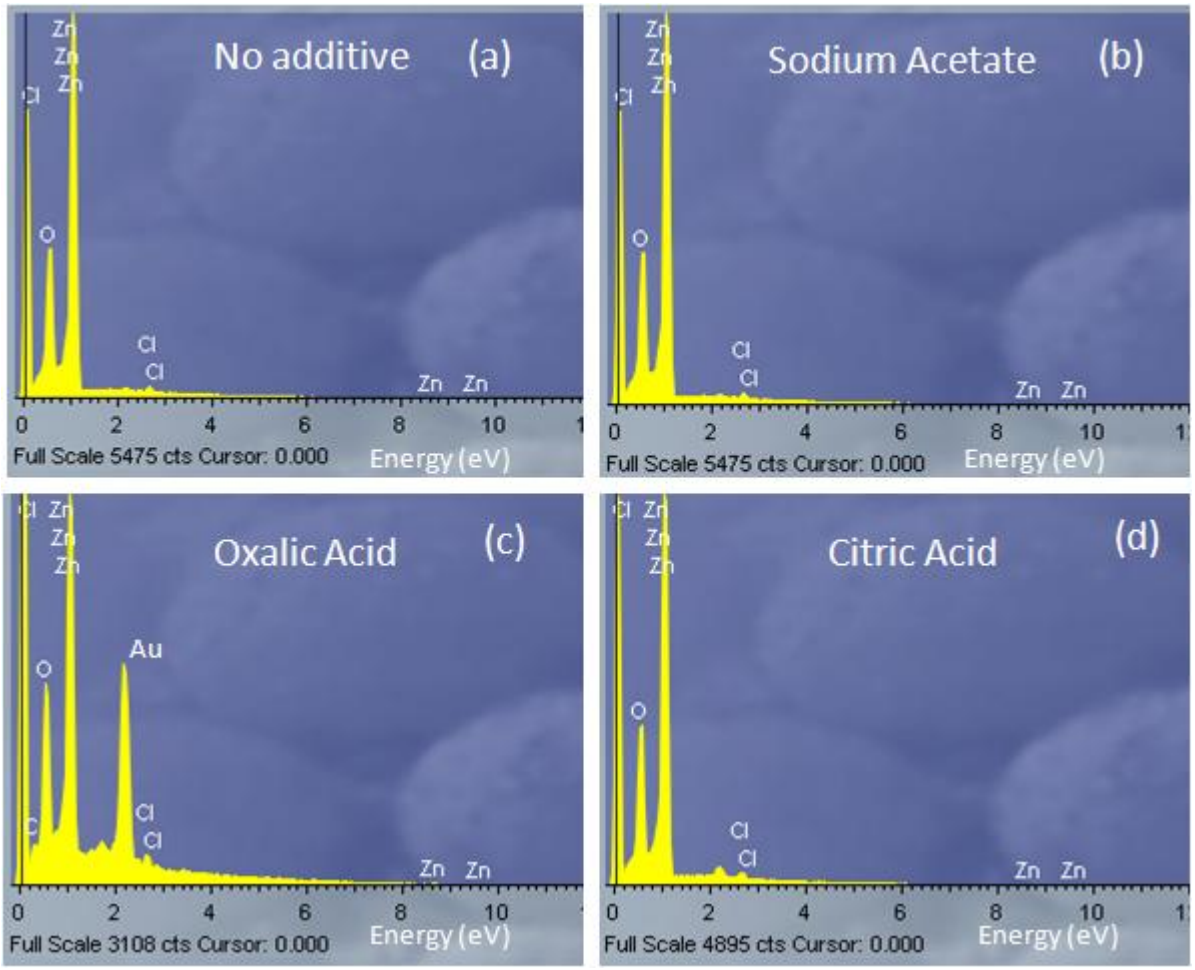


Figure 6.74 EDS spectrum with and without additive. (a) no additive, (b) 1 mM of sodium acetate, (c) 1 mM of oxalic acid and (d) 0.1 mM of citric acid. The peak are indexed with the corresponding elements. 5 mM of $Zn(NO_3)_2$ and 0.1 M of KCl in an oxygenated aqueous solution at 65°C. The applied potential was -0.97 V. pH was 5.4.

6.7.1 Acetic Acid

6.7.1.1 Microscopy

Figure 6.75 presents the FESEM images of the film obtained after 20 minutes of deposition.

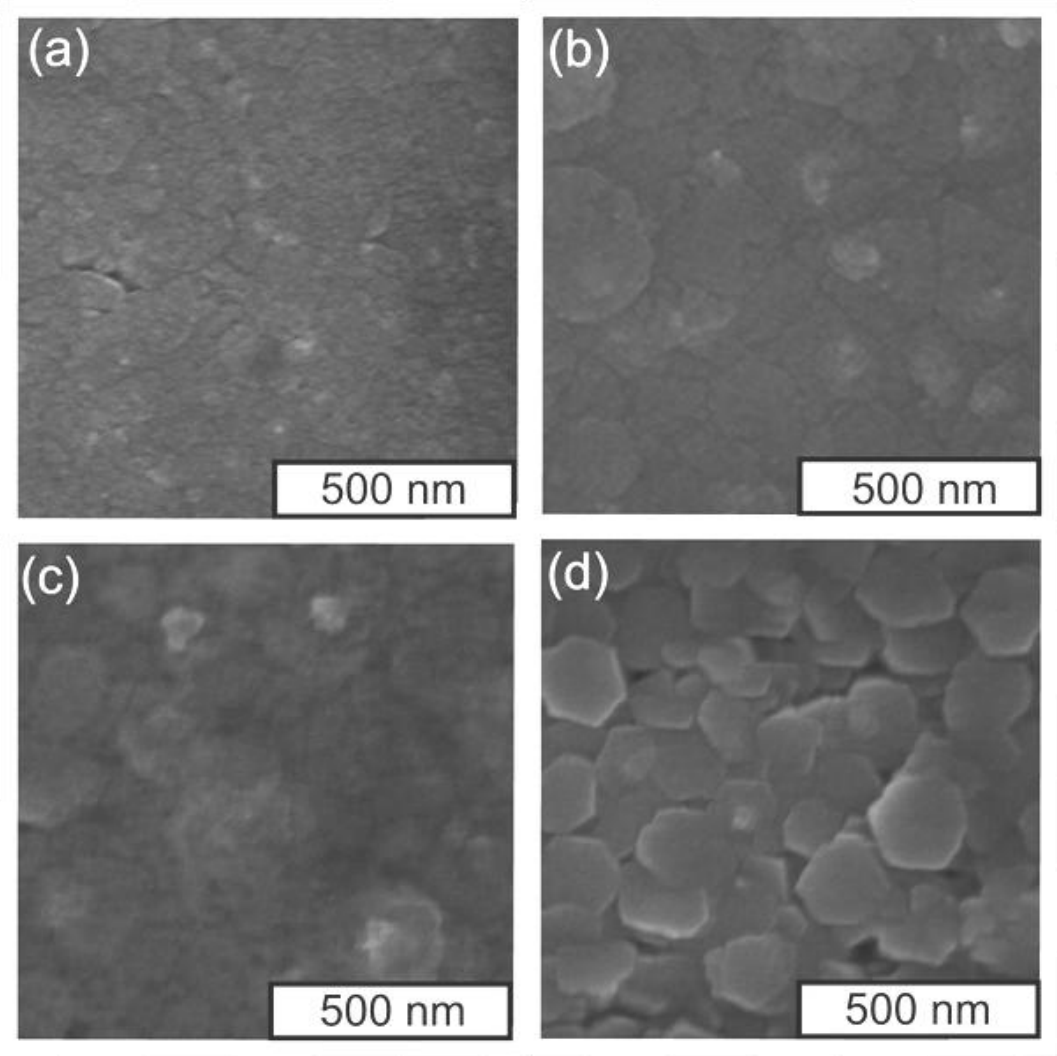


Figure 6.75 Effect of pH on the film morphology in presence of 1 mM of sodium acetate. FESEM images after a 20 minute deposition. (a) pH=4, (b) pH=5, (c) pH=5.3 and (d) pH=6. 5 mM of $Zn(NO_3)_2$ and 0.1 M of KCl in an oxygenated aqueous solution at 65°C. The applied potential was -0.97 V.

At pH 4, 5 and 5.4 the film is comprised of small, aggregated nanostructures. The films are very dense. At pH 6 the film is comprised of particles with a hexagonal shape.

6.7.1.2 Electrochemical Measurements

Figure 6.76 presents the influence of pH on the current density vs. time curves and the nominal thickness of Zn(II). The curves all have the same overall shape. The nucleation

period is not affected by the bulk pH. The deposition curves obtained at pH 4 and 5 are similar. Increasing the pH further slightly decreases the deposition rate.

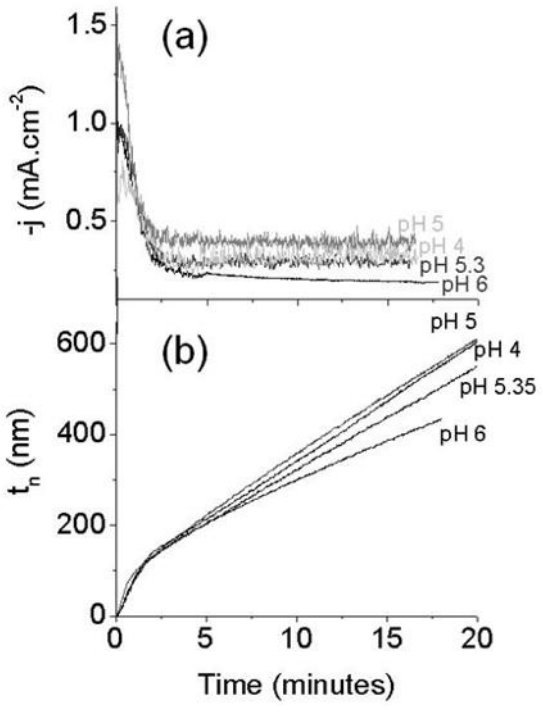


Figure 6.76 Deposition studies with 1mM of sodium acetate showing the effect of pH. (a) current vs. time (b) nominal thickness vs. time. 5 mM of $Zn(NO_3)_2$ and 0.1 M of KCl in an oxygenated aqueous solution at 65°C. The applied potential was -0.97 V.

The only face with a hexagonal symmetry in the wurtzite structure is the (001), which is a polar face (see Figure 3.1). Increasing the pH is equivalent to increasing the concentration of negatively charged acetate ions compared to neutral acetic acid molecules (see Table 6.5). At more alkaline pH the acetate ions stabilise the positively charged top polar surface (001). This has two effects. On one hand, the diameter of the nanostructures is increased due to the stabilization of the (001) face. On the other hand the acetate ions poison growth normal to that face and slow down the overall growth of the crystal.

6.7.2 Oxalic Acid

6.7.2.1 Microscopy

Figure 6.77 presents electron microscopy images of the nanostructures obtained. They consist of sheets with a width of 500 nm for pH 4 and 5 and a width of 2 and 3 µm for pH

5.4 and 6 respectively. The thickness in all cases is less than 20 nm. The increase of the size of the sheet with the pH is not surprising and is related to the increase of oxalate anions in solution.

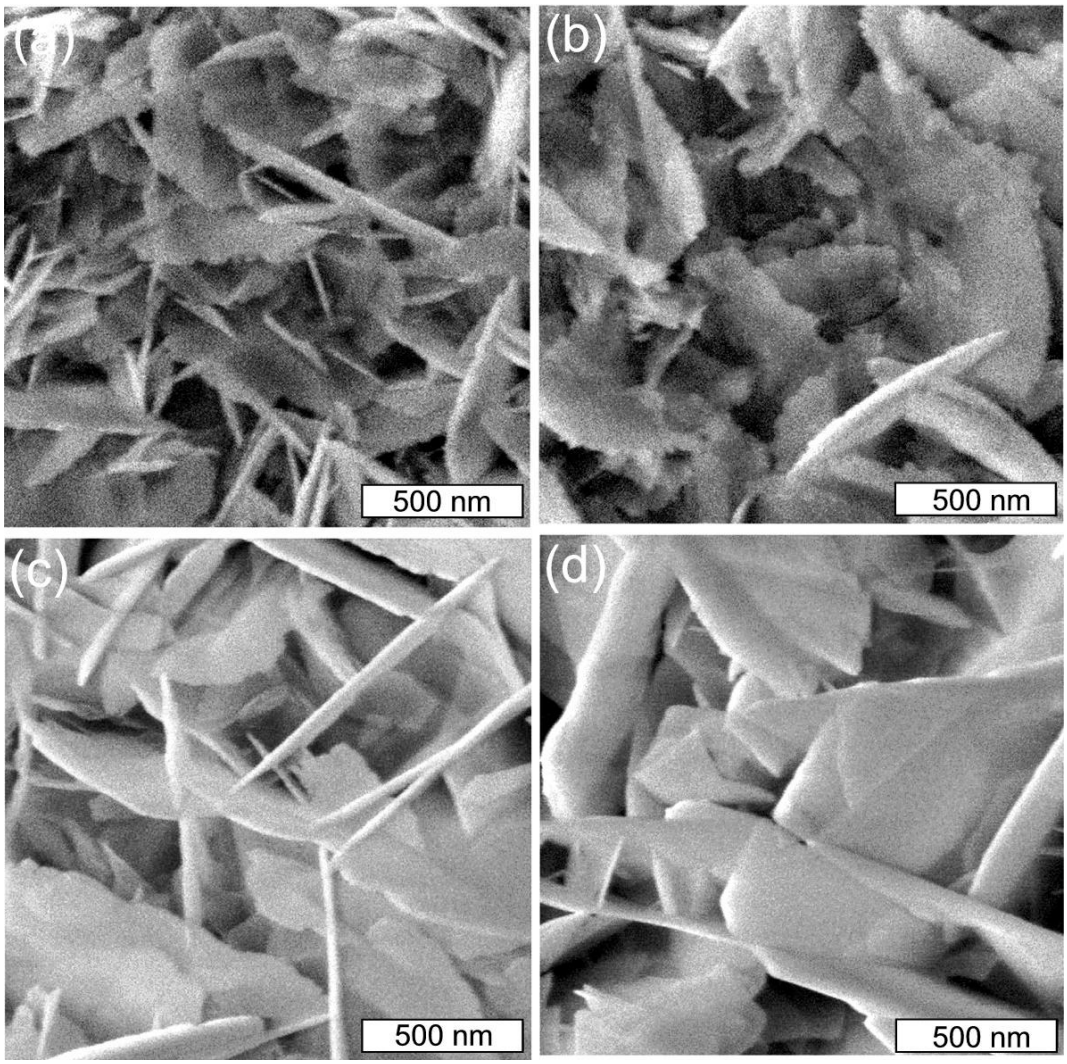


Figure 6.77 Effect of pH on the film morphology in presence of 1 mM of oxalic acid. FESEM images after a 20 minute deposition. (a) pH=4, (b) pH=5, (c) pH=5.3 and (d) pH=6. 5 mM of $Zn(NO_3)_2$ and 0.1 M of KCl in an oxygenated aqueous solution at 65°C. The applied potential was -0.97 V.

EDS composition measurements have been carried out on the samples. The films deposited with oxalic acid show a high concentration in carbon (up to 17%) whereas all the other films are carbon free. This could be due to trapping of electrolyte in-between the sheets or to strongly adsorbed or co-deposited molecules. To test whether the oxalate was incorporated, the film deposited from a solution of 1mM of oxalic acid was annealed in air at 450°C for 30 minutes. Figure 6.78 presents a FESEM picture of the resultant structure.

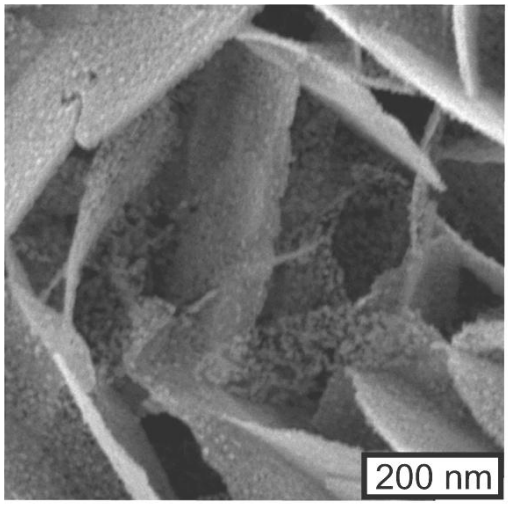


Figure 6.78 FESEM image of a film deposited in presence of 1mM of oxalic acid after annealing, showing the formation of nanopores in the ZnO sheets. 5 mM of $Zn(NO_3)_2$ and 0.1 M of KCl in an oxygenated aqueous solution at 65°C. The applied potential was -0.97 V.

It can be clearly seen that the original morphology has been altered. The plates have holes with dimensions of a few nanometres, consistent with removal of oxalate ions during the annealing process. The two carboxylate groups of the oxalate molecule can be absorbed into the ZnO matrix by chelation to two Zn atoms. Similar structures have been reported by F. Wang et al [195] after annealing a film deposited from a aqueous solution of 0.05M $Zn(NO_3)_2$ and 0.1M KCl. They carried out photovoltaic measurements and associated nano-pits with an intense green emission instead of a broad UV emission which favour for the photoelectric effects. Moreover the increase of surface area makes it a good candidate for dye sensitized or hybrid solar cells.

Figure 6.79 presents the evolution of the morphology when the concentration of oxalic is changed. There is a transition from nano-rods (a) to a mixture of nano-rods and nano-sheets (b) to a structure completely comprised of nano-sheets (c). As before this is most likely due to the stabilisation effect of the two carboxylic groups of oxalic acid on the polar surface.

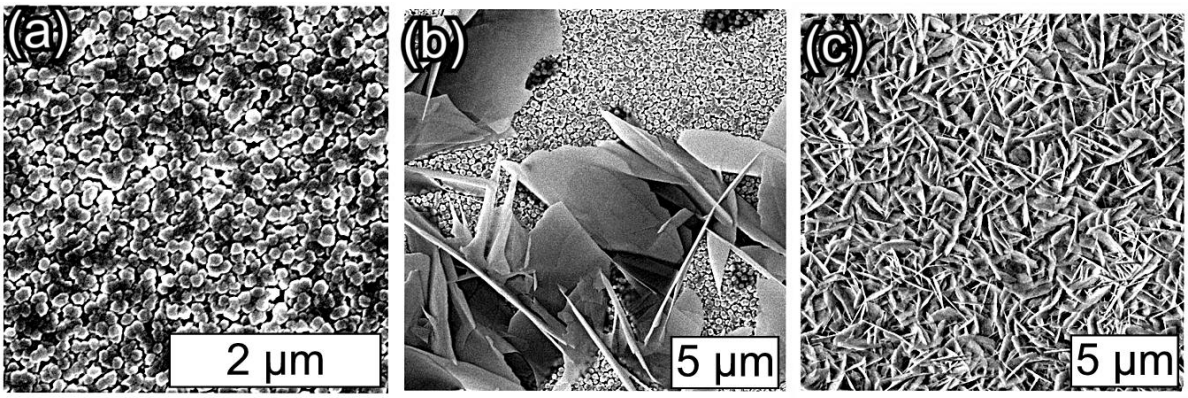


Figure 6.79 Effect of oxalic acid concentration on the film morphology in presence at pH 5.3. (a) no oxalic acid (b) 0.1 mM and (c) 1 mM. 5 mM of $Zn(NO_3)_2$ and 0.1 M of KCl in an oxygenated aqueous solution at 65°C. The applied potential was -0.97 V.

6.7.2.2 Electrochemical Measurements

Figure 6.80a presents the effect of pH on the current transient curves for a film deposited from a solution containing 1 mM of oxalic acid.

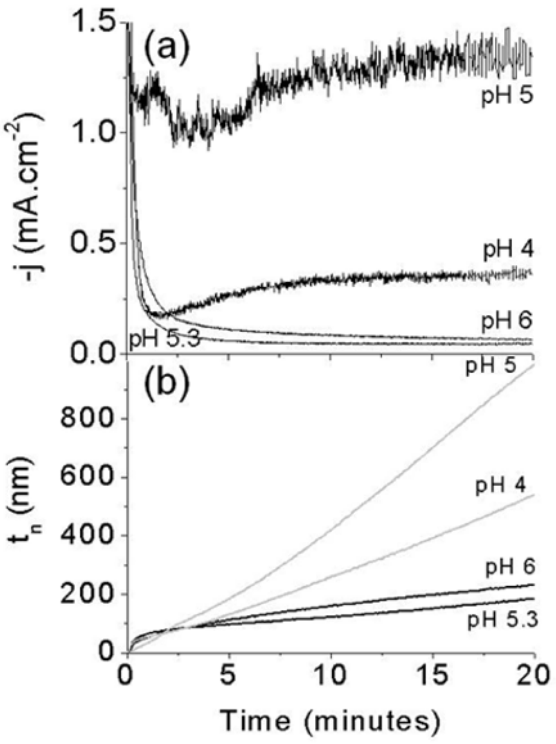


Figure 6.80 Deposition studies with 1mM of oxalic acid: effect of pH. (a) current vs. time, (b) nominal thickness vs. time. 5 mM of $Zn(NO_3)_2$ and 0.1 M of KCl in an oxygenated aqueous solution at 65°C. The applied potential was -0.97 V.

One can clearly see that the pH has a dramatic effect on growth. Two regimes can be seen. Firstly for pH 4 and 5, the current transient curves slowly increase after reaching a minimum. For pH 5.3 and 6 the current decreases sharply and then more slowly; no extrema are observed. Figure 6.22b presents the nominal thickness vs. time curves. The curves obtained for pH 5.4 and 6 are similar.

Figure 6.81a presents the current transient curves as a function of the oxalic acid concentration.

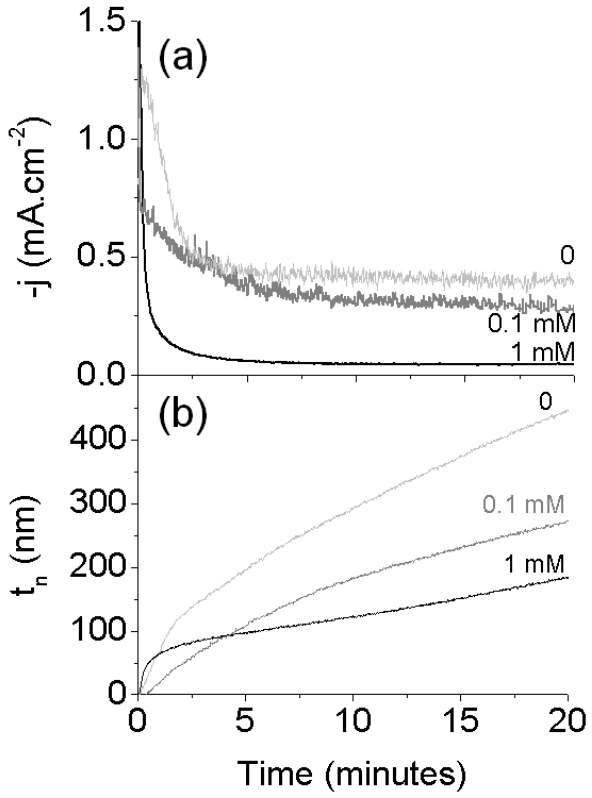


Figure 6.81 Deposition studies: effect of oxalic acid concentration. (a) Current vs. time, (b) nominal thickness vs. time. 5 mM of $Zn(NO_3)_2$ and 0.1 M of KCl in an oxygenated aqueous solution at 65°C. The applied potential was -0.97 V.

The addition of 0.1 mM oxalic acid decreases the magnitude of the initial current peak and the value of the plateau. If 1 mM is added the curve is completely changed: no peak is observed and the plateau value decreases. A similar effect is observed on the nominal thickness vs. time (see Figure 6.81b). The addition of 0.1 mM oxalic acid leads to a decrease in the deposition rate. At 1 mM the growth curve is changed. The film growth is rapid at the beginning of deposition and then the growth is slower.

6.7.3 Citric Acid

6.7.3.1 Microscopy

The changes observed when citric acid is added to the solution are even more dramatic (see Figure 6.82). A small addition of citric acid results in the formation of a thin sheet resembling a lacy network. Increasing the concentration of acid to 0.1 mM leads to an increase in the pore size. No deposit is observed with 1 mM in solution.

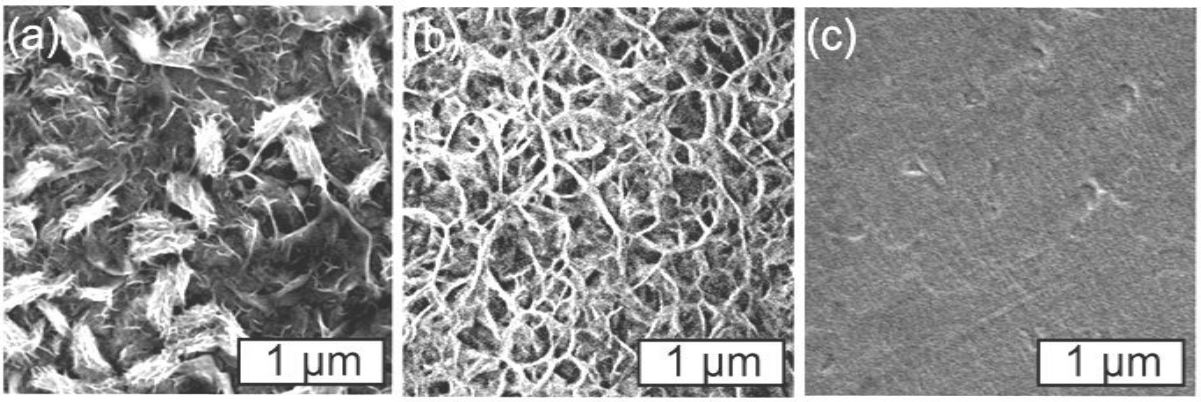


Figure 6.82 Effect of citric acid concentration on the film morphology. (a) 0.01 mM, (b) 0.1 mM and (c) 1 mM. FESEM images after a 20 minute deposition. 5 mM of $Zn(NO_3)_2$ and 0.1 M of KCl in an oxygenated aqueous solution at 65°C. The applied potential was -0.97 V.

6.7.3.2 Electrochemical Measurements

Figure 6.83 shows the effect of citric on combined current density and nominal thickness. The peak in the current is delayed, and only occurs after about 5 minutes (Figure 6.83a). The induction time is clearly visible on the nominal thickness vs. time curve: the nominal thickness is constant during the first minutes of the deposition (Figure 6.83b). There is no deposition when 1mM citric acid is added. The effect of citric acid is three-fold. Firstly, the positively charged top surface is poisoned and thus the growth along the non polar faces is favoured. This explains the change in morphology from rods to planar structures. Secondly, zinc ions can form two chelate rings because citric acid has 3 carboxyl and 3 hydroxyl groups. This favours the connection of the nanosheets and the formation of a lacy network. Thirdly, the gold surface is strongly stabilized by the citric acid molecules[201], which decreases the reactivity of the gold surface and delays the nucleation. When the concentration of citric acid in solution is increased, the number of nucleation sites is decreased and the distance between ZnO

nuclei also increases, and thus so too does the pore diameter. At 1 mM, the gold surface is completely covered with surfactant and no growth is observed.

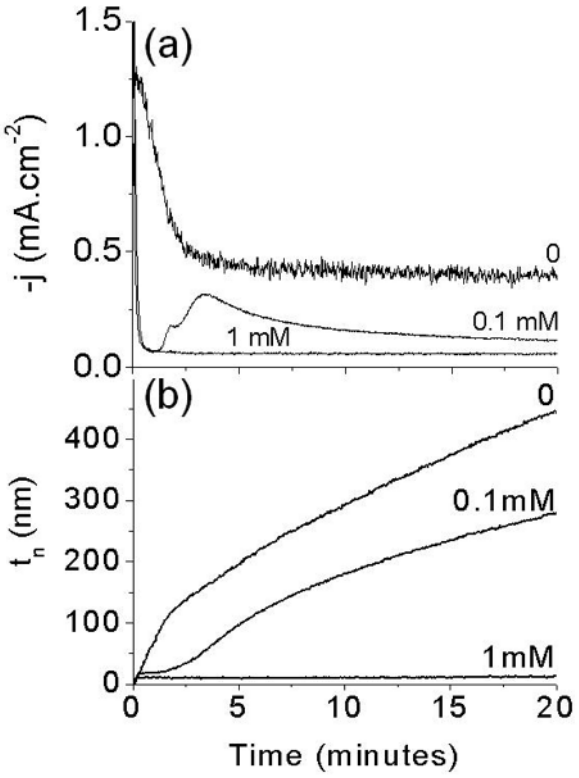


Figure 6.83 Deposition studies: effect of citric acid concentration. (a) Current vs. time, (b) nominal thickness vs. time. 5 mM of $Zn(NO_3)_2$ and 0.1 M of KCl in an oxygenated aqueous solution at 65°C. The applied potential was -0.97 V.

6.7.4 Summary

We report a systematic study of the effect of carboxylate groups on the growth behaviour of ZnO. The measurement of the dissolution rate of ZnO in aqueous solution as a function of the pH is reported for the first time. It is shown that the morphology of zinc oxide can be altered by changing the number of carboxyl group in capping molecules, and the concentration of the carboxylate species in solution. Nanoporous structures with a typical pore diameter of less than 5 nm can be easily obtained by removing trapped molecules by post-deposition annealing. The ability to alter the nanostructures through the use of surfactants has far-reaching implications on the

ability to tune these materials for use in optoelectronic applications *via* quantum confinement effects.

7. Conclusions and Future Work

7.1 Conclusions

ZnO nanostructured films fabricated by electrochemical deposition exhibit a variety of morphologies which can find huge commercial applications in a wide range of domains. This work has been dedicated to the systematic study of the effect of the deposition parameters in order to control the morphology and thus the properties of the films. The effects of time, potential, chloride concentration, zinc nitrate concentration; pH and carboxyl groups have been studied. The film growth has been investigated using two new *in-situ* methodologies.

A modified procedure for collecting real-time x-ray absorption data during the *in situ* electrochemical deposition of ZnO nanostructured films has been described. This enables a direct correlation to be made between the growth as observed from an increase in the fluorescence signal above the absorption edge, and the electrochemical current response. Comparisons with *ex-situ* measurements have proven the validity of the method.

A new methodology to study the development of crystal formation and texture evolution has been developed using synchrotron XRD. The orientation of these rods perpendicular to the substrate is determined in the first few seconds of deposition, during the nucleation stage. The nuclei are textured in the [002] direction, and this then propagates through the crystallites as the nanostructures grow. The shape of the nanostructures evolves from conical rods which grow in 3 dimensions to hexagonal rods with a 1-D growth. The texture is increased during this process.

Decreasing the supersaturation of the solution during the nucleation leads to the formation of smaller nanorods. For potentials higher than ~-0.4 V, no growth is observed

after coalescence of the nanostructures due to surface blockage on the ZnO electrode. For potential higher than ~-1.1 V the formation of metallic zinc is observed. In between this interval the diameter of the rods can be controlled by changing the potential.

The effect of Cl^- anions is described in terms of its absorption on to the (002) polar faces which leads to an increase of the rod diameter and a decrease of [002] orientation. Less textured films are produced with higher Cl^- concentration.

Three concentration regions have been identified where the deposition behaviour of ZnO nanorods differs strongly. For low $Zn(NO_3)_2$ concentrations (less than 2 mM) the nanorods grow along screw dislocations: pyramidal structures are observed on top of the rods, and over time the rods maintain a constant diameter and do not coalesce. For medium $Zn(NO_3)_2$ concentrations (2 mM to 20 mM) the nanorods grow in a 3-D fashion and ultimately coalesce. The growth rate behaviour clearly shows an initial nucleation process followed by 3-D growth. For high $Zn(NO_3)_2$ concentrations (above 20 mM) large nanosheets are formed and Cl^- anions absorb on to the surface to form zinc hydroxylchloride phases. By controlling the supersaturation in solution, highly tailored morphologies can be produced.

Initial solution pH has a strong influence on the growth and dissolution rate. Tubular structures can be simply produced by selective etching of the (002) surface. The dimensionality of the tubes can be controlled by an appropriate choice of the deposition parameters and post-deposition solutions.

Carboxylic molecules added to the electrolyte can dramatically alter the morphology of the deposited ZnO films. There is a strong interaction between the carboxylic groups and the ZnO polar faces. For the case of the oxylate ion evidence of molecular incorporation into the growing ZnO nanostructure was found. Nanoporous structures with a typical

pore diameter of less than 5 nm were obtained by removing these trapped molecules by post-deposition annealing.

7.2 Further Research and Development of this Topic

The *in-situ* X-ray absorption and X-ray diffraction methodology developed during this work have been proven to be a very useful technique to study the nucleation and growth mechanism of ZnO. These techniques could easily be transferred to the study of other systems.

Information for time lower than 4 minutes could not have been obtained with the *in-situ* XRD measurements due to some experimental limitations:

- the high noise to signal ratio for very short time due to the intrinsic noise of the image plate detector
- the read-out time of the image plate detector
- Absorption of the solution directly proportional to the thickness crossed by the beam

State of the art detectors do not have intrinsic noise and can have higher reading times, but there are very expensive and not commonly found at the beamlines.

The thickness of the solution crossed by the beam cannot by reduced in the present set up due to the diffusion limitation. The easier way to decrease this limitation will be to force the solution flow close to the widow of the cell with a pump in order to have similar transport of the molecules as in the *ex-situ* set-up. Next generation synchrotron source with higher available flux will allow thicker cells to be used without loss of data quality.

ZnO is a promising material for a wide range of applications but have not yet fulfilled expectations. For example, in solar cell applications, far better efficiencies are currently obtained with tin oxide. The properties of nanostructured zinc oxide are strongly related

to the surface defects due to its high surface to volume ratio. The polar and non-polar surface, as well as the defects and stress in the nanostructures, have not been fully characterised. Imaging of the surface by high-resolution transmission electron microscopy (HRTEM) should provide very useful insights. The recent development in nano focused X-ray beam of synchrotron techniques should allow the direct measurement on a single nanostructure without the problems associated of the sample preparation for HRTEM studies.

For cheap photovoltaic applications, the structures deposited in this work should be fully characterised with a wide range of functional material for light absorption and hole conduction. Infiltration of the nanoporous films with functionalising molecules may be problematic and should be studied.

Most of the characterisation for sensing applications has been on 1-D nanostructures. Other geometries such has nano plates should be investigated. Large polar (002) surfaces have promising sensing capabilities.

Deposition of high quality film on flexible subtracts have been achieved during this work. This opens up the possibility for scaled up deposition and roll-to-roll production; this should be investigated in order to reach low cost industrial application.

ZnO nanostructured materials are quite new and long term stability of the nanostructured still needs to be determined. Film degradation with time may restrict the applications. Nano materials are very new on the market and some health concerns have been raised about their potential toxicity. In the public opinion, they are commonly associated with asbestos. Health and safety studies should be carried out before large scale applications.

8. References

(1) What is Nanotechnology? http://www.nano.gov/html/facts/whatIsNano.html
(2) FAQs: Nanotechnology. http://www.nano.gov/html/facts/faqs.html
(3) Faloon, D., *Zinc Oxide: History, Manufacture and Properties as a Pigment*. ed.; D. Van Nostrand: 1925.
(4) P. Yang, H. Y., S. Mao, R. Russo, J. Johnson, R. Saykally, N. Morris, J. Pham, R. He, H.-J. Choi,, Controlled Growth of ZnO Nanowires and Their Optical Properties. *Advanced functional materials* 2002, 12, (5), 323-331.
(5) Gu, Y.; Kuskovsky, I. L.; Yin, M.; O'Brien, S.; Neumark, G. F., Quantum confinement in ZnO nanorods. *Applied Physics Letters* 2004, 85, (17), 3833-3835.
(6) Ryu, Y. R.; Kim, W. J.; White, H. W., Fabrication of homostructural ZnO p-n junctions. *Journal of Crystal Growth* 2000, 219, (4), 419-422.
(7) Chang, P.-C.; Fan, Z.; Chien, C.-J.; Stichtenoth, D.; Ronning, C.; Lu, J. G., High-performance ZnO nanowire field effect transistors. *Applied Physics Letters* 2006, 89, (13), 133113.
(8) Dulub, O.; Diebold, U.; Kresse, G., Novel Stabilization Mechanism on Polar Surfaces: ZnO(0001)-Zn. *Physical Review Letters* 2003, 90, (1), 016102.
(9) Wander, A.; Harrison, N. M., An ab-initio study of ZnO(1120). *Surface Science* 2000, 468, (1-3), L851-L855.
(10) Labuayai, S., Synthesis and optical properties of nanocrystalline ZnO powders prepared by a direct thermal decomposition route. *Applied physics. A, Materials science & processing* 2009, 94, (4), 755-761.
(11) Peulon, S.; Lincot, D., Mechanistic Study of Cathodic Electrodeposition of Zinc Oxide and Zinc Hydroxychloride Films from Oxygenated Aqueous Zinc Chloride Solutions. *Journal of The Electrochemical Society* 1998, 145, (3), 864-874.
(12) Konenkamp, R.; Word, R. C.; Dosmailov, M.; Meiss, J.; Nadarajah, A., Selective growth of single-crystalline ZnO nanowires on doped silicon. *Journal of Applied Physics* 2007, 102, (5).
(13) Illy, B.; Shollock, B. A.; MacManus-Driscoll, J. L.; Ryan, M. P., Electrochemical growth of ZnO nanoplates. *Nanotechnology* 2005, 16, (2), 320-324.
(14) Li, G.-R.; Lu, X.-H.; Qu, D.-L.; Yao, C.-Z.; Zheng, F.-l.; Bu, Q.; Dawa, C.-R.; Tong, Y.-X., Electrochemical Growth and Control of ZnO Dendritic Structures. *The Journal of Physical Chemistry C* 2007, 111, (18), 6678-6683.
(15) Sun, Y.; Riley, D. J.; Ashfold, M. N. R., Mechanism of ZnO nanotube growth by hydrothermal methods on ZnO film-coated Si substrates. *Journal of Physical Chemistry B* 2006, 110, (31), 15186-15192.
(16) Zhang, T.; Dong, W.; Keeter-Brewer, M.; Konar, S.; Njabon, R. N.; Tian, Z. R., Site-Specific Nucleation and Growth Kinetics in Hierarchical Nanosyntheses of Branched ZnO Crystallites. *J. Am. Chem. Soc.* 2006, 128, (33), 10960-10968.
(17) Kong, X. Y.; Ding, Y.; Yang, R.; Wang, Z. L., Single-Crystal Nanorings Formed by Epitaxial Self-Coiling of Polar Nanobelts. *Science* 2004, 303, (5662), 1348-1351.
(18) Kong, X. Y.; Wang, Z. L., Spontaneous Polarization-Induced Nanohelixes, Nanosprings, and Nanorings of Piezoelectric Nanobelts. *Nano letters* 2003, 3, (12), 1625-1631.
(19) Chen, Z.; Shan, Z.; Cao, M. S.; Lu, L.; Mao, S. X., Zinc oxide nanotetrapods. *Nanotechnology* 2004, (3), 365.
(20) Wang, Z., Novel nanostructures of ZnO for nanoscale photonics, optoelectronics, piezoelectricity, and sensing. *Applied physics. A, Materials science & processing* 2007, 88, (1), 7-15.
(21) Brown, H. E., *Zinc Oxide Properties and Applications*. ed.; Pergamon, New York: 1976.
(22) Peterson, R. B.; Fields, C. L.; Gregg, B. A., Epitaxial Chemical Deposition of ZnO Nanocolumns from NaOH Solutions. *Langmuir* 2004, 20, (12), 5114-5118.
(23) Wama, R.; Utiyama, M.; Plashnitsa, V. V.; Miura, N., Highly sensitive impedance-based propene sensor using stabilized zirconia and zinc oxide sensing-electrode. *Electrochemistry Communications* 2007, 9, (12), 2774-2777.
(24) Qin, Y.; Wang, X.; Wang, Z. L., Microfibre-nanowire hybrid structure for energy scavenging. *Nature* 2008, 451, (7180), 809-813.
(25) Lee, J.-B.; Lee, H.-J.; Seo, S.-H.; Park, J.-S., Characterization of undoped and Cu-doped ZnO films for surface acoustic wave applications. *Thin Solid Films* 2001, 398-399, 641-646.
(26) Kropp, R. Solar Expected to Maintain its Status as the World's Fastest-Growing Energy Technology. http://www.socialfunds.com/news/article.cgi/2639.html (2009),
(27) Yoshida, T.; Zhang, J.; Komatsu, D.; Sawatani, S.; Minoura, H.; Pauporté, T.; Lincot, D.; Oekermann, T.; Schlettwein, D.; Tada, H.; Wöhrle, D.; Funabiki, K.; Matsui, M.; Miura, H.; Yanagi, H., Electrodeposition of Inorganic/Organic Hybrid Thin Films. *Advanced functional materials* 2009, 19, (1), 17-43.
(28) Olson, D. C.; Shaheen, S. E.; Collins, R. T.; Ginley, D. S., The Effect of Atmosphere and ZnO Morphology on the Performance of Hybrid Poly(3-hexylthiophene)/ZnO Nanofiber Photovoltaic Devices. *The Journal of Physical Chemistry C* 2007, 111, (44), 16670-16678.
(29) Moet, D. J. D.; Koster, L. J. A.; de Boer, B.; Blom, P. W. M., Hybrid Polymer Solar Cells from Highly Reactive Diethylzinc: MDMO–PPV versus P3HT. *Chemistry of materials* 2007, 19, (24), 5856-5861.
(30) Beek, W. J. E.; Wienk, M. M.; Kemerink, M.; Yang, X.; Janssen, R. A. J., Hybrid Zinc Oxide Conjugated Polymer Bulk Heterojunction Solar Cells. *The Journal of Physical Chemistry B* 2005, 109, (19), 9505-9516.

(31) Zhang, R.; Kumar, S.; Zou, S.; Kerr, L. L., High-Density Vertically Aligned ZnO Rods with a Multistage Terrace Structure and Their Improved Solar Cell Efficiency. *Crystal Growth & Design* 2008, 8, (2), 381-383.
(32) Zhao, Q.; Xie, T.; Peng, L.; Lin, Y.; Wang, P.; Peng, L.; Wang, D., Size- and Orientation-Dependent Photovoltaic Properties of ZnO Nanorods. *The Journal of Physical Chemistry C* 2007, 111, (45), 17136-17145.
(33) Olson, D. C.; Lee, Y.-J.; White, M. S.; Kopidakis, N.; Shaheen, S. E.; Ginley, D. S.; Voigt, J. A.; Hsu, J. W. P., Effect of Polymer Processing on the Performance of Poly(3-hexylthiophene)/ZnO Nanorod Photovoltaic Devices. *The Journal of Physical Chemistry C* 2007, 111, (44), 16640-16645.
(34) Takanezawa, K.; Hirota, K.; Wei, Q.-S.; Tajima, K.; Hashimoto, K., Efficient Charge Collection with ZnO Nanorod Array in Hybrid Photovoltaic Devices. *The Journal of Physical Chemistry C* 2007, 111, (19), 7218-7223.
(35) Huang, M. H.; Mao, S.; Feick, H.; Yan, H.; Wu, Y.; Kind, H.; Weber, E.; Russo, R.; Yang, P., Room-Temperature Ultraviolet Nanowire Nanolasers. *Science* 2001, 292, (5523), 1897-1899.
(36) Li, Y. Y.; Li, Y. X.; Wu, Y. L.; Sun, W. L., Preparation and photoluminescent properties of zinc oxide phosphor. *Journal of Luminescence* 2007, 126, (1), 177-181.
(37) Huang, X.-J.; Choi, Y.-K., Chemical sensors based on nanostructured materials. *Sensors and Actuators B: Chemical* 2007, 122, (2), 659-671.
(38) Gong, H.; Hu, J. Q.; Wang, J. H.; Ong, C. H.; Zhu, F. R., Nano-crystalline Cu-doped ZnO thin film gas sensor for CO. *Sensors and Actuators B: Chemical* 2006, 115, (1), 247-251.
(39) Kang, B., Hydrogen and ozone gas sensing using multiple ZnO nanorods
APPLIED PHYSICS A-MATERIALS SCIENCE & PROCESSING. *Applied physics. A, Materials science & processing* 2005, 80, (5), 1029-1032.
(40) Shinde, V. R.; Gujar, T. P.; Lokhande, C. D.; Mane, R. S.; Han, S.-H., Use of chemically synthesized ZnO thin film as a liquefied petroleum gas sensor. *Materials Science and Engineering: B* 2007, 137, (1-3), 119-125.
(41) Shinde, V. R.; Gujar, T. P.; Lokhande, C. D.; Mane, R. S.; Han, S.-H., Development of morphological dependent chemically deposited nanocrystalline ZnO films for liquefied petroleum gas (LPG) sensor. *Sensors and Actuators B: Chemical* 2007, 123, (2), 882-887.
(42) Zhang, Y.; Yu, K.; Jiang, D.; Zhu, Z.; Geng, H.; Luo, L., Zinc oxide nanorod and nanowire for humidity sensor. *Applied Surface Science* 2005, 242, (1-2), 212-217.
(43) Wang, H. T.; Kang, B. S.; Ren, F.; Tien, L. C.; Sadik, P. W.; Norton, D. P.; Pearton, S. J.; Lin, J., Hydrogen-selective sensing at room temperature with ZnO nanorods. *Applied Physics Letters* 2005, 86, (24), 243503-3.
(44) X. Jiaquiang; C. Yuping; L. Yadong; Jianian, S., *Journal of Materials Science* 2005, 40, 2019.
(45) Galeazzo, E.; Peres, H. E. M.; Santos, G.; Peixoto, N.; Ramirez-Fernandez, F. J., Gas sensitive porous silicon devices: responses to organic vapors. *Sensors and Actuators B: Chemical* 2003, 93, (1-3), 384-390.
(46) Fan, Z.; Wang, D.; Chang, P.-C.; Tseng, W.-Y.; Lu, J. G., ZnO nanowire field-effect transistor and oxygen sensing property. *Applied Physics Letters* 2004, 85, (24), 5923-5925.
(47) Fan, Z.; Lu, J. G., Gate-refreshable nanowire chemical sensors. *Applied Physics Letters* 2005, 86, (12), 123510-3.
(48) Wan, Q.; Li, Q. H.; Chen, Y. J.; Wang, T. H.; He, X. L.; Gao, X. G.; Li, J. P., Positive temperature coefficient resistance and humidity sensing properties of Cd-doped ZnO nanowires. *Applied Physics Letters* 2004, 84, (16), 3085-3087.
(49) M. H. Huang, Y. W., H. Feick, N. Tran, E. Weber, P. Yang,, Catalytic Growth of Zinc Oxide Nanowires by Vapor Transport. *Advanced Materials* 2001, 13, (2), 113-116.
(50) Lettieri, S.; Bismuto, A.; Maddalena, P.; Baratto, C.; Comini, E.; Faglia, G.; Sberveglieri, G.; Zanotti, L., Gas sensitive light emission properties of tin oxide and zinc oxide nanobelts. *Journal of Non-Crystalline Solids* 2006, 352, (9-20), 1457-1460.
(51) Wang, J. X.; Sun, X. W.; Wei, A.; Lei, Y.; Cai, X. P.; Li, C. M.; Dong, Z. L., Zinc oxide nanocomb biosensor for glucose detection. *Applied Physics Letters* 2006, 88, (23), 233106-3.
(52) Kang, B. S.; Ren, F.; Heo, Y. W.; Tien, L. C.; Norton, D. P.; Pearton, S. J., pH measurements with single ZnO nanorods integrated with a microchannel. *Applied Physics Letters* 2005, 86, (11), 112105-3.
(53) Safaa, M. A.-H.; Al-Mofarji, R. T.; Klason, P.; Willander, M.; Gutman, N.; Sa'ar, A., Zinc oxide nanorods grown on two-dimensional macroporous periodic structures and plane Si as a pH sensor. *Journal of Applied Physics* 2008, 103, (1), 014302.
(54) Safaa, M. A.-H.; Willander, M.; Anita, O.; Peter, S., ZnO nanorods as an intracellular sensor for pH measurements. *Journal of Applied Physics* 2007, 102, (8), 084304.
(55) Al-Hilli, S. M.; Al-Mofarji, R. T.; Willander, M., Zinc oxide nanorod for intracellular pH sensing. *Applied Physics Letters* 2006, 89, (17).
(56) Zhang, F.; Wang, X.; Ai, S.; Sun, Z.; Wan, Q.; Zhu, Z.; Xian, Y.; Jin, L.; Yamamoto, K., Immobilization of uricase on ZnO nanorods for a reagentless uric acid biosensor. *Analytica Chimica Acta* 2004, 519, (2), 155-160.
(57) Lin, K.-C.; Chen, S.-M., The electrochemical preparation of FAD/ZnO with hemoglobin film-modified electrodes and their electroanalytical properties. *Biosensors and Bioelectronics* 2006, 21, (9), 1737-1745.
(58) Zhao, G.; Xu, J.-J.; Chen, H.-Y., Interfacing myoglobin to graphite electrode with an electrodeposited nanoporous ZnO film. *Analytical Biochemistry* 2006, 350, (1), 145-150.
(59) Du, T.; Song, H.; Ilegbusi, O. J., Sol-gel derived ZnO/PVP nanocomposite thin film for superoxide radical sensor. *Materials Science and Engineering: C* 2007, 27, (3), 414-420.

(60) Ohno, H., Making Nonmagnetic Semiconductors Ferromagnetic. *Science* 1998, 281, (5379), 951-956.
(61) Prinz, G. A., Magnetoelectronics. *Science* 1998, 282, (5394), 1660-1663.
(62) Sowing the seeds of spin: FERROMAGNETISM. *Materials Today* 2002, 5, (12), 9-9.
(63) Sharma, P.; Gupta, A.; Rao, K. V.; Owens, F. J.; Sharma, R.; Ahuja, R.; Guillen, J. M. O.; Johansson, B.; Gehring, G. A., Ferromagnetism above room temperature in bulk and transparent thin films of Mn-doped ZnO. *Nat Mater* 2003, 2, (10), 673-677.
(64) Xu, C. X.; Sun, X. W.; Dong, Z. L.; Yu, M. B.; Xiong, Y. Z.; Chen, J. S., Magnetic nanobelts of iron-doped zinc oxide. *Applied Physics Letters* 2005, 86, (17), 173110-3.
(65) Hays, J.; Reddy, K. M.; Graces, N. Y.; Engelhard, M. H.; Shutthanandan, V.; Luo, M.; Xu, C.; Giles, N. C.; Wang, C.; Thevuthasan, S.; Punnoose, A., Effect of Co doping on the structural, optical and magnetic properties of ZnO nanoparticles. *Journal of Physics: Condensed Matter* 2007, (26), 266203.
(66) Snure, M.; Kumar, D.; Tiwari, A., Ferromagnetism in Ni-doped ZnO films: Extrinsic or intrinsic? *Applied Physics Letters* 2009, 94, (1), 012510-3.
(67) Shore, R. E., Overview of Radiation-induced Skin Cancer in Humans. *International Journal of Radiation Biology* 1990, 57, (4), 809 - 827.
(68) Willander, M.; Nur, O.; Lozovik, Y. E.; Al-Hilli, S. M.; Chiragwandi, Z.; Hu, Q. H.; Zhao, Q. X.; Klason, P., Solid and soft nanostructured materials: Fundamentals and applications. *Microelectronics Journal* 2005, 36, (11), 940-949.
(69) Kong, L., Sol-gel glass-coated zinc oxide for varistor applications. *Journal of materials science letters* 1998, 17, (9), 769.
(70) Granqvist, C. G., Transparent conductors as solar energy materials: A panoramic review. *Solar Energy Materials and Solar Cells* 2007, 91, (17), 1529-1598.
(71) Lu, J. G.; Chang, P.; Fan, Z., Quasi-one-dimensional metal oxide materials--Synthesis, properties and applications. *Materials Science and Engineering: R: Reports* 2006, 52, (1-3), 49-91.
(72) Park, S. S.; Lee, J. M.; Yoon, S. I.; Lee, D. G.; Kim, S. J.; Kim, S. H.; Maeng, S.; Kim, S. W. In *Low-temperature synthesis of one-dimensional ZnO nanostructures on screen-printed carbon nanotube films*, Symposium on Electron Transport in Low-Dimensional Carbon Structures/Science and Technology of Nanotubes and Nanowires, Strasbourg, FRANCE, May 28-Jun 01, 2007; Elsevier Science Bv: Strasbourg, FRANCE, 2007; pp 2526-2530.
(73) Yanagida, T.; Marcu, A.; Matsui, H.; Nagashima, K.; Oka, K.; Yokota, K.; Taniguchi, M.; Kawai, T., Enhancement of Oxide VLS Growth by Carbon on Substrate Surface. *Journal of Physical Chemistry C* 2008, 112, (48), 18923-18926.
(74) Mustafa, D.; Biggemann, D.; Wu, J.; Coffer, J. L.; Tessler, L. R. In *Structural characterization of ZnO/Er2O3 core/shell nanowires*, Symposium on ZnO and Related Materials held at the 2006 EMRS Spring Meeting, Nice, FRANCE, May 29-Jun 02, 2006; Academic Press Ltd Elsevier Science Ltd: Nice, FRANCE, 2006; pp 403-408.
(75) Willander, M.; Nur, O.; Zhao, Q. X.; Yang, L. L.; Lorenz, M.; Cao, B. Q.; Perez, J. Z.; Czekalla, C.; Zimmermann, G.; Grundmann, M.; Bakin, A.; Behrends, A.; Al-Suleiman, M.; El-Shaer, A.; Mofor, A. C.; Postels, B.; Waag, A.; Boukos, N.; Travlos, A.; Kwack, H. S.; Guinard, J.; Dang, D. L., Zinc oxide nanorod based photonic devices: recent progress in growth, light emitting diodes and lasers. *Nanotechnology* 2009, 20, (33), 40.
(76) Chen, Y. X.; Lewis, M.; Zhou, W. L., Zno nanostructures fabricated through a double-tube vapor-phase transport synthesis. *Journal of Crystal Growth* 2005, 282, (1-2), 85-93.
(77) Iribarren, A.; Fernandez, P.; Piqueras, J. In *Cathodoluminescence characterization of ZnO : Te microstructures obtained with ZnTe and TeO2 doping*, 7th International Conference on Physics of Ligh-Matter Coupling in Nanostructures (PLMCN7), Havana, CUBA, Apr 12-17, 2007; Academic Press Ltd Elsevier Science Ltd: Havana, CUBA, 2007; pp 600-604.
(78) Miao, L.; Ieda, Y.; Tanemura, S.; Cao, Y. G.; Tanemura, M.; Hayashi, Y.; Toh, S.; Kaneko, K., Synthesis, microstructure and photoluminescence of well-aligned ZnO nanorods on Si substrate. *Sci. Technol. Adv. Mater.* 2007, 8, (6), 443-447.
(79) Wu, X. F.; Xu, C. X.; Zhu, G. P.; Ling, Y. M., ZnO nanorods produced by the method of arc discharge. *Chinese Physics Letters* 2006, 23, (8), 2165-2168.
(80) Yu, K.; Zhang, Y. S.; Ouyang, S. X.; Zhang, Q. J.; Luo, L. Q.; Zhang, Q. X.; Chang, Z. K.; Li, L. J.; Zhu, Z. Q., Synthesis and field emission of ZnO nanostructures on CuO catalyzed porous silicon substrate. *Chinese Physics Letters* 2005, 22, (9), 2411-2414.
(81) Lee, W.; Jeong, M. C.; Myoung, J. M., Catalyst-free growth of ZnO nanowires by metal-organic chemical vapour deposition (MOCVD) and thermal evaporation. *Acta Mater.* 2004, 52, (13), 3949-3957.
(82) Chen, Z.; Shan, Z. W.; Cao, M. S.; Lu, L.; Mao, S. X., Zinc oxide nanotetrapods. *Nanotechnology* 2004, 15, (3), 365-369.
(83) Leprince-Wang, Y.; Wang, G. Y.; Zhang, X. Z.; Yu, D. P., Study on the microstructure and growth mechanism of electrochemical deposited ZnO nanowires. *Journal of Crystal Growth* 2006, 287, (1), 89-93.
(84) Trindade, T.; Dejesus, J. D. P.; Obrien, P., PREPARATION OF ZINC-OXIDE AND ZINC-SULFIDE POWDERS BY CONTROLLED PRECIPITATION FROM AQUEOUS-SOLUTION. *Journal of Materials Chemistry* 1994, 4, (10), 1611-1617.
(85) Liu, X.; Afzaal, M.; Ramasamy, K.; O'Brien, P.; Akhtar, J., Synthesis of ZnO Hexagonal Single-Crystal Slices with Predominant (0001) and (000(1)over-bar) Facets by Poly(ethylene glycol)-Assisted Chemical Bath Deposition. *Journal of the American Chemical Society* 2009, 131, (42), 15106-+.

(86) Yan, Z. J.; Zeng, D. W.; Xie, C. S.; Wang, H. H.; Song, W. L., Nanostructured ZnO network films deposited on Al2O3 substrates by chemical bath deposition. *Thin Solid Films* 2009, 517, (5), 1541-1545.
(87) Ku, C. H.; Wu, J. J., Chemical bath deposition of ZnO nanowire-nanoparticle composite electrodes for use in dye-sensitized solar cells. *Nanotechnology* 2007, 18, (50), 9.
(88) Peiro, A. M.; Ayllon, J. A.; Peral, J.; Domenech, X.; Domingo, C., Microwave activated chemical bath deposition (MW-CBD) of zinc oxide: Influence of bath composition and substrate characteristics. *Journal of Crystal Growth* 2005, 285, (1-2), 6-16.
(89) Cao, B. Q.; Cai, W. P.; Li, Y.; Sun, F. Q.; Zhang, L. D., Ultraviolet-light-emitting ZnO nanosheets prepared by a chemical bath deposition method. *Nanotechnology* 2005, 16, (9), 1734-1738.
(90) Tang, W.; Cameron, D. C., Aluminum-doped zinc oxide transparent conductors deposited by the sol-gel process. *Thin Solid Films* 1994, 238, (1), 83-87.
(91) Chang, S. Y.; Yang, N. H.; Huang, Y. C., Hydrothermal Growth and Interface Correlation of Highly Aligned ZnO Nanorod Arrays on UV-Activated Sol-Gel Transparent Conducting Films. *Journal of The Electrochemical Society* 2009, 156, (11), K200-K204.
(92) Hossain, M. F.; Takahashi, T.; Biswas, S., Nanorods and nanolipsticks structured ZnO photoelectrode for dye-sensitized solar cells. *Electrochemistry Communications* 2009, 11, (9), 1756-1759.
(93) Nian, H.; Hahn, S. H.; Koo, K. K.; Shin, E. W.; Kim, E. J., Sol-gel derived N-doped ZnO thin films. *Materials Letters* 2009, 63, (26), 2246-2248.
(94) Lee, J.; Yoon, M., Synthesis of Visible Light-Sensitive ZnO Nanostructures: Subwavelength Waveguides. *Journal of Physical Chemistry C* 2009, 113, (27), 11952-11958.
(95) Gerard, D.; Graziella, G., Sovothermal Processes in Materials Synthesis. *MATERIALS RESEARCH SOCIETY SYMPOSIUM PROCEEDINGS* 2005.
(96) Y. Sun, G. M. F., N. A. Fox, D. J. Riley, M. N. R. Ashfold,, Synthesis of Aligned Arrays of Ultrathin ZnO Nanotubes on a Si Wafer Coated with a Thin ZnO Film. *Advanced Materials* 2005, 17, (20), 2477-2481.
(97) Lojkowski, W.; Gedanken, A.; Grzanka, E.; Opalinska, A.; Strachowski, T.; Pielaszek, R.; Tomaszewska-Grzeda, A.; Yatsunenko, S.; Godlewski, M.; Matysiak, H.; Kurzydowski, K. J., Solvothermal synthesis of nanocrystalline zinc oxide doped with Mn2+, Ni2+, Co2+ and Cr3+ ions. *J. Nanopart. Res.* 2009, 11, (8), 1991-2002.
(98) Ghoshal, T.; Biswas, S.; Paul, M.; De, S. K., Synthesis of ZnO Nanoparticles by Solvothermal Method and Their Ammonia Sensing Properties. *Journal of Nanoscience and Nanotechnology* 2009, 9, (10), 5973-5980.
(99) Xu, L.; Hu, Y. L.; Pelligra, C.; Chen, C. H.; Jin, L.; Huang, H.; Sithambaram, S.; Aindow, M.; Joesten, R.; Suib, S. L., ZnO with Different Morphologies Synthesized by Solvothermal Methods for Enhanced Photocatalytic Activity. *Chemistry of materials* 2009, 21, (13), 2875-2885.
(100) Li, Y.; Liu, X.; Zou, Y.; Guo, Y., The growth morphology of ZnO hexangular tubes synthesized by the solvothermal method. *Mater. Sci.* 2009, 27, (1), 187-192.
(101) Cheng, H. M.; Chiu, W. H.; Lee, C. H.; Tsai, S. Y.; Hsieh, W. F., Formation of Branched ZnO Nanowires from Solvothermal Method and Dye-Sensitized Solar Cells Applications. *Journal of Physical Chemistry C* 2008, 112, (42), 16359-16364.
(102) Bellis, M. The History of Electroplating. http://inventors.about.com/od/estartinventions/a/Electroplating.htm
(103) Peulon, S.; Lincot, D., Cathodic electrodeposition from aqueous solution of dense or open-structured zinc oxide films. *Advanced Materials* 1996, 8, (2), 166-170.
(104) Izaki, M.; Omi, T., Transparent zinc oxide films prepared by electrochemical reaction. *Applied Physics Letters* 1996, 68, (17), 2439-2440.
(105) D. Pletcher, S. E. G., Southampton electrochemistry group, *Instrumental Methods in Electrochemistry*. ed.; Horwood Publishing: 2001; p 442 pages.
(106) Vayssieres, L., Advanced semiconductor nanostructures. *Comptes Rendus Chimie* 2006, 9, (5-6), 691-701.
(107) Abyaneh, M. Y.; Fleischmann, M., The electrocrystallisation of nickel: Part I. Generalised models of electrocrystallisation. *Journal of Electroanalytical Chemistry* 1981, 119, (1), 187-195.
(108) Inamdar, A. I.; Mujawar, S. H.; Sadale, S. B.; Sonavane, A. C.; Shelar, M. B.; Shinde, P. S.; Patil, P. S., Electrodeposited zinc oxide thin films: Nucleation and growth mechanism. *Solar Energy Materials and Solar Cells* 2007, 91, (10), 864-870.
(109) Goux, A.; Pauporte, T.; Chivot, J.; Lincot, D., Temperature effects on ZnO electrodeposition. *Electrochimica Acta* 2005, 50, (11), 2239-2248.
(110) Scharifker, B.; Hills, G., Theoretical and experimental studies of multiple nucleation. *Electrochimica Acta* 1983, 28, (7), 879-889.
(111) Goux, A.; Pauporté, T.; Lincot, D., Oxygen reduction reaction on electrodeposited zinc oxide electrodes in KCl solution at 70 °C. *Electrochimica Acta* 2006, 51, (15), 3168-3172.
(112) Mandin, P.; Cense, J. M.; Picard, G.; Lincot, D., Simplified kinetic modelling and numerical simulation of a metal oxide chemical bath electro deposition process at a rotating electrode. *Electrochimica Acta* 2006, 52, (3), 1296-1308.
(113) Lincot, D., Electrodeposition of semiconductors. *Thin Solid Films* 2005, 487, (1-2), 40-48.
(114) Pauporte, T.; Lincot, D., Hydrogen peroxide oxygen precursor for zinc oxide electrodeposition II--Mechanistic aspects. *Journal of Electroanalytical Chemistry* 2001, 517, (1-2), 54-62.

(115) Otani, S., Effect of bath temperature on the electrodeposition mechanism of zinc oxide film from zinc nitrate solution. *Journal of The Electrochemical Society* 2006, 153, (8), C551-C556.
(116) Marí, B.; Mollar, M.; Mechkour, A.; Hartiti, B.; Perales, M.; Cembrero, J., Optical properties of nanocolumnar ZnO crystals. *Microelectronics Journal* 2004, 35, (1), 79-82.
(117) Cembrero, J.; Elmanouni, A.; Hartiti, B.; Mollar, M.; Marí, B., Nanocolumnar ZnO films for photovoltaic applications. *Thin Solid Films* 2004, 451-452, 198-202.
(118) Zhang, L.; Chen, Z.; Tang, Y.; Jia, Z., Low temperature cathodic electrodeposition of nanocrystalline zinc oxide thin films. *Thin Solid Films* 2005, 492, (1-2), 24-29.
(119) Mahalingam, T.; John, V. S.; Sebastian, P. J., Growth and characterization of electrosynthesised zinc oxide thin films. *Materials Research Bulletin* 2003, 38, (2), 269-277.
(120) Izaki, M.; Omi, T., Characterization of Transparent Zinc Oxide Films Prepared by Electrochemical Reaction. *Journal of The Electrochemical Society* 1997, 144, (6), 1949-1952.
(121) Dalchiele, E. A.; Giorgi, P.; Marotti, R. E.; Martín, F.; Ramos-Barrado, J. R.; Ayouci, R.; Leinen, D., Electrodeposition of ZnO thin films on n-Si(1 0 0). *Solar Energy Materials and Solar Cells* 2001, 70, (3), 245-254.
(122) Gu, Z. H.; Fahidy, T. Z., Electrochemical Deposition of ZnO Thin Films on Tin-Coated Glasses. *Journal of The Electrochemical Society* 1999, 146, (1), 156-159.
(123) Mahalingam, T.; John, V. S.; Raja, M.; Su, Y. K.; Sebastian, P. J., Electrodeposition and characterization of transparent ZnO thin films. *Solar Energy Materials and Solar Cells* 2005, 88, (2), 227-235.
(124) Cao, B., Fabrication of large-scale zinc oxide ordered pore arrays with controllable morphology. *Chemical communications* 2004, (14), 1604-1605.
(125) Pauporte, T.; Cortes, R.; Froment, M.; Beaumont, B.; Lincot, D., Electrocrystallization of Epitaxial Zinc Oxide onto Gallium Nitride. *Chemistry of materials* 2002, 14, (11), 4702-4708.
(126) Marotti, R. E.; Guerra, D. N.; Bello, C.; Machado, G.; Dalchiele, E. A., Bandgap energy tuning of electrochemically grown ZnO thin films by thickness and electrodeposition potential. *Solar Energy Materials and Solar Cells* 2004, 82, (1-2), 85-103.
(127) Rappich, J.; Fahoume, M., Nonradiative recombination and band bending of p-Si(100) surfaces during electrochemical deposition of polycrystalline ZnO. *Thin Solid Films* 2005, 487, (1-2), 157-161.
(128) Canava, B., Nucleation effects on structural and optical properties of electrodeposited zinc oxide on tin oxide. *Journal of applied electrochemistry* 2000, 30, (6), 711-716.
(129) Xu, L.; Guo, Y.; Liao, Q.; Zhang, J.; Xu, D., Morphological Control of ZnO Nanostructures by Electrodeposition. *The Journal of Physical Chemistry B* 2005, 109, (28), 13519-13522.
(130) Izaki, M.; Omi, T., Electrolyte Optimization for Cathodic Growth of Zinc Oxide Films. *Journal of The Electrochemical Society* 1996, 143, (3), L53-L55.
(131) Elias, J.; Tena-Zaera, R.; Lévy-Clément, C., Electrochemical deposition of ZnO nanowire arrays with tailored dimensions. *Journal of Electroanalytical Chemistry* 2008, 621, (2), 171-177.
(132) H. El Belghiti, T. P., D. Lincot,, Mechanistic study of ZnO nanorod array electrodeposition. *physica status solidi (a)* 2008, 205, (10), 2360-2364.
(133) Yoshida, T.; Komatsu, D.; Shimokawa, N.; Minoura, H., Mechanism of cathodic electrodeposition of zinc oxide thin films from aqueous zinc nitrate baths. *Thin Solid Films* 2004, 451-452, 166-169.
(134) Pauporte, T.; Lincot, D., Hydrogen Peroxide Oxygen Precursor for Zinc Oxide Electrodeposition I. Deposition in Perchlorate Medium. *Journal of The Electrochemical Society* 2001, 148, (4), C310-C314.
(135) Pauporté, T.; Lincot, D., Electrodeposition of semiconductors for optoelectronic devices: results on zinc oxide. *Electrochimica Acta* 2000, 45, (20), 3345-3353.
(136) Zhang, Y.; Weng, J.; Zhang, Y.; Xu, L.; Xu, J.; Huang, X.; Chen, K., Effects of the electrochemical deposition conditions on the properties of ZnO polycrystalline thin film. *Physica E: Low-dimensional Systems and Nanostructures* 2005, 27, (1-2), 183-187.
(137) Weng, J.; Zhang, Y.; Han, G.; Zhang, Y.; Xu, L.; Xu, J.; Huang, X.; Chen, K., Electrochemical deposition and characterization of wide band semiconductor ZnO thin film. *Thin Solid Films* 2005, 478, (1-2), 25-29.
(138) O'Regan, B.; Sklover, V.; Gratzel, M., Electrochemical Deposition of Smooth and Homogeneously Mesoporous ZnO Films from Propylene Carbonate Electrolytes. *Journal of The Electrochemical Society* 2001, 148, (7), C498-C505.
(139) Lee, J.; Tak, Y., Electrodeposition of ZnO on ITO Electrode by Potential Modulation Method. *Electrochemical and Solid-State Letters* 2001, 4, (9), C63-C65.
(140) Li, M.; Zhai, J.; Liu, H.; Song, Y.; Jiang, L.; Zhu, D., Electrochemical Deposition of Conductive Superhydrophobic Zinc Oxide Thin Films. *The Journal of Physical Chemistry B* 2003, 107, (37), 9954-9957.
(141) Luo, H.; Zhang, J.; Yan, Y., Electrochemical Deposition of Mesoporous Crystalline Oxide Semiconductor Films from Lyotropic Liquid Crystalline Phases. *Chemistry of materials* 2003, 15, (20), 3769-3773.
(142) Lee, J., On the origin of electrodeposition mechanism of ZnO on ITO substrate. *The Korean Journal of Chemical Engineering* 2005, 22, (1), 161-164.
(143) Mei, Y. F.; Siu, G. G.; Fu, R. K. Y.; Chu, P. K.; Li, Z. M.; Tang, Z. K., Room-temperature electrosynthesized ZnO thin film with strong (0 0 2) orientation and its optical properties. *Applied Surface Science* 2006, 252, (8), 2973-2977.

(144) Johnson, J. C.; Yan, H.; P., Y.; Saykally, R. J., Optical Cavity Effects in ZnO Nanowire Lasers and Waveguides. *The journal of physical chemistry. B, Condensed matter, materials, surfaces, interfaces & biophysical* 2003, 107, (34), 8816-8828.
(145) B. Marí, J. C., F. J. Manjón, M. Mollar, R. Gómez,, Raman measurements on nanocolumnar ZnO crystals. *physica status solidi (a)* 2005, 202, (8), 1602-1605.
(146) Katayama, J., Observation of photocurrent generation in electrodeposited zinc oxide layers. *Journal of applied electrochemistry* 2000, 30, (7), 855-858.
(147) Chen, Q. P.; Xue, M. Z.; Sheng, Q. R.; Liu, Y. G.; Ma, Z. F., Electrochemical growth of nanopillar zinc oxide films by applying a low concentration of zinc nitrate precursor. *Electrochemical and Solid State Letters* 2006, 9, (3), C58-C61.
(148) Michaelis, E.; Wöhrle, D.; Rathousky, J.; Wark, M., Electrodeposition of porous zinc oxide electrodes in the presence of sodium laurylsulfate. *Thin Solid Films* 2006, 497, (1-2), 163-169.
(149) Marotti, R. E.; Giorgi, P.; Machado, G.; Dalchiele, E. A., Crystallite size dependence of band gap energy for electrodeposited ZnO grown at different temperatures. *Solar Energy Materials and Solar Cells* 2006, 90, (15), 2356-2361.
(150) Liu, R.; Vertegel, A. A.; Bohannan, E. W.; Sorenson, T. A.; Switzer, J. A., Epitaxial Electrodeposition of Zinc Oxide Nanopillars on Single-Crystal Gold. *Chemistry of materials* 2001, 13, (2), 508-512.
(151) Leprince-Wang, Y.; Yacoubi-Ouslim, A.; Wang, G. Y., Structure study of electrodeposited ZnO nanowires. *Microelectronics Journal* 2005, 36, (7), 625-628.
(152) Izaki, M.; Watase, S.; Takahashi, H., Room-temperature ultraviolet light-emitting zinc oxide micropatterns prepared by low-temperature electrodeposition and photoresist. *Applied Physics Letters* 2003, 83, (24), 4930-4932.
(153) Liu, Y. L.; Liu, Y. C.; Liu, Y. X.; Shen, D. Z.; Lu, Y. M.; Zhang, J. Y.; Fan, X. W., Structural and optical properties of nanocrystalline ZnO films grown by cathodic electrodeposition on Si substrates. *Physica B: Condensed Matter* 2002, 322, (1-2), 31-36.
(154) Liu, Y.; Liu, Y.; Zhang, J.; Lu, Y.; Shen, D.; Fan, X., ZnO hexagonal prisms grown onto p-Si (1 1 1) substrate from poly (vinylpyrrolidone) assisted electrochemical assembly. *Journal of Crystal Growth* 2006, 290, (2), 405-409.
(155) Pauporte, T.; Lincot, D., Heteroepitaxial electrodeposition of zinc oxide films on gallium nitride. *Applied Physics Letters* 1999, 75, (24), 3817-3819.
(156) Chatterjee, A.; Foord, J., Electrochemical deposition of nanocrystalline zinc oxide at conductive diamond electrodes. *Diamond and Related Materials* 2006, 15, (4-8), 664-667.
(157) Kawano, T.; Yahiro, J.; Maki, H.; Imai, H., Epitaxial growth of wurtzite ZnO crystals in an aqueous solution system. *Chemistry letters* 2006, 35, (4), 442-443.
(158) Xu, L., Morphological control of ZnO nanostructures by electrodeposition
JOURNAL OF PHYSICAL CHEMISTRY B. *Journal of Physical Chemistry B* 2005, 109, (28), 13519-13522.
(159) Li, G., Electrochemical growth and control of ZnO dendritic structures. *Journal of physical chemistry. C* 2007, 111, (18), 6678-6683.
(160) Yamabi, S.; Yahiro, J.; Iwai, S.; Imai, H., Formation of cellular films consisting of wurtzite-type zinc oxide nanosheets by mediation of phosphate anions. *Thin Solid Films* 2005, 489, (1-2), 23-30.
(161) Pauporte, T., Luminescence of nanostructured Eu3+/ZnO mixed films prepared by electrodeposition. *Journal of physical chemistry. C* 2007, 111, (42), 15427-15432.
(162) Tian, Z. R.; Voigt, J. A.; Liu, J.; Mckenzie, B.; Mcdermott, M. J., Biomimetic Arrays of Oriented Helical ZnO Nanorods and Columns. *Journal of the American Chemical Society* 2002, 124, (44), 12954-12955.
(163) Tian, Z. R.; Voigt, J. A.; Liu, J.; McKenzie, B.; McDermott, M. J.; Rodriguez, M. A.; Konishi, H.; Xu, H., Complex and oriented ZnO nanostructures. *Nat Mater* 2003, 2, (12), 821-826.
(164) Tena-Zaera, R.; Elias, J.; Wang, G.; Levy-Clement, C., Role of Chloride Ions on Electrochemical Deposition of ZnO Nanowire Arrays from O2 Reduction. *The Journal of Physical Chemistry C* 2007, 111, (45), 16706-16711.
(165) Lan, C., Bi-doped ZnO layer prepared by electrochemical deposition. *Journal of The Electrochemical Society* 2007, 154, (3), D117-D121.
(166) Li, G.-R.; Qu, D.-L.; Zhao, W.-X.; Tong, Y.-X., Electrochemical deposition of (Mn, Co)-codoped ZnO nanorod arrays without any template. *Electrochemistry Communications* 2007, 9, (7), 1661-1666.
(167) Abid, M., Ferromagnetism at room temperature on electrodeposited Co2+-doped ZnO thin film. *Journal of The Electrochemical Society* 2006, 153, (8), D138-D142.
(168) Cao, P.; Zhao, D. X.; Zhang, J. Y.; Shen, D. Z.; Lu, Y. M.; Fan, X. W.; Wang, X. H., N-doping-related room temperature ferromagnetism of electrodeposited ZnCoO films. *Physica B: Condensed Matter* 2007, 392, (1-2), 255-258.
(169) Pauporté, T.; Goux, A.; Kahn-Harari, A.; de Tacconi, N.; Chenthamarakshan, C. R.; Rajeshwar, K.; Lincot, D., Cathodic electrodeposition of mixed oxide thin films. *Journal of Physics and Chemistry of Solids* 2003, 64, (9-10), 1737-1742.
(170) Machado, G.; Guerra, D. N.; Leinen, D.; Ramos-Barrado, J. R.; Marotti, R. E.; Dalchiele, E. A., Indium doped zinc oxide thin films obtained by electrodeposition. *Thin Solid Films* 2005, 490, (2), 124-131.
(171) Lu, X.-H.; Li, G.-R.; Zhao, W.-X.; Tong, Y.-X., A simple electrochemical deposition route for the controllable growth of Ce4+-doped ZnO nanorods. *Electrochimica Acta* 2008, 53, (16), 5180-5185.

(172) Wellings, J. S.; Samantilleke, A. P.; Warren, P.; Heavens, S. N.; Dharmadasa, I. M., Comparison of electrodeposited and sputtered intrinsic and aluminium-doped zinc oxide thin films. *Semiconductor Science and Technology* 2008, (12), 125003.
(173) Wang, J.-G.; Tian, M.-L.; Kumar, N.; Mallouk, T. E., Controllable Template Synthesis of Superconducting Zn Nanowires with Different Microstructures by Electrochemical Deposition. *Nano letters* 2005, 5, (7), 1247-1253.
(174) Yang, Y.; Yan, H.; Fu, Z.; Yang, B.; Zuo, J.; Fu, S., Enhanced photoluminescence from three-dimensional ZnO photonic crystals. *Solid State Communications* 2006, 139, (5), 218-221.
(175) Gal, D.; Hodes, G.; Lincot, D.; Schock, H.-W., Electrochemical deposition of zinc oxide films from non-aqueous solution: a new buffer/window process for thin film solar cells. *Thin Solid Films* 2000, 361, 79-83.
(176) Scholz, F., *Electroanalytical Methods: Guide to Experiments and Applications* ed.; Springer: 2002.
(177) Paunovic, M.; Schlesinger, M., *Fundamentals of Electrochemical Deposition*. Second edition ed.; Wiley: 2006.
(178) Watt, I., *The principles and practice of electron microscopy* ed.; Cambridge University Press: 1997.
(179) Goldstein, J.; Newbury, D.; Joy, D.; Lyman, C.; Echlin, P.; Lifshin, E.; Sawyer, L. C.; Michael, J. R., *Scanning Electron Microscopy and X-ray Microanalysis*. ed.; Plenum Press, New York: 1981.
(180) Authier, A., *Dynamical Theory of X-Ray Diffraction*. ed.; Oxford University Press: 2001.
(181) *Neutron and Synchrotron radiation for condensed matter studies*. ed.; Les Editions de Physique Springer Verlag: 1993; Vol. Volume I, Theory, Instruments and Methods.
(182) Paganin, D., *Coherent X-Ray Optics*. ed.; Oxford University Press: 2006.
(183) Liénard, A.-M., Champ électrique et magnétique, produit par une charge électrique concentrée en un point et anime d'un mouvement quelconque. *L'Eclairage Electrique* 1898, 16, 5-14 ; 53-59 ; 106-112.
(184) Elder, F. R.; Gurewitsch, A. M.; Langmuir, R. V.; Pollock, H. C., Radiation from Electrons in a Synchrotron. *Physical Review* 1947, 71, (11), 829.
(185) Robinson, A., *History of Synchrotron Radiation*. ed.; Center for X-ray Optics and Advanced Light Source, Lawrence Berkeley National Laboratory: 2001.
(186) Bilderback, D., Review of third and next generation synchrotron light sources
Journal of Physics B-Atomic Molecular And Optical Physics. *Journal of physics. B, Atomic, molecular, and optical physics* 2005, 38, (9), S773-S797.
(187) Saldin, E. L.; Schneidmiller, E. A.; Yurkov, M. V.; Ieee In *Gigawatt-class vacuum ultraviolet free electron laser at DESY paves the way for the fourth-generation x-ray source*, International Conference on Computer as a Tool (EUROCON 2007), Warsaw, POLAND, Sep 09-12, 2007; Ieee: Warsaw, POLAND, 2007; pp 1705-1713.
(188) Toney, M., Near-Surface Alignement of Polymers in Rubbed Films. *Nature* 1995, 374, (6524), 709-711.
(189) Toney, M. Grazing Incidence X-ray Scattering and Diffraction on Thin Films http://ssrl.slac.stanford.edu/materialscatter/scatter-grazing.html
(190) Kerkar, M.; Robinson, J.; Forty, A. J. In *In situ structural studies of the passive film on iron and iron/chromium alloys using X-ray absorption spectroscopy*, General Discussion on Structure of Surfaces and Interfaces as Studied Using Synchrotron Radiation, Manchester, England, Apr 04-06, 1990; Royal Soc Chemistry: Manchester, England, 1990; pp 31-40.
(191) Milazzo, G.; Caroli, S., *Tables of standard Electrode Potentials*. ed.; Wiley-Interscience Publication: 1978.
(192) Lide, D. R., *The Handbook of Chemistry & Physics 85th Ed*. ed.; National Institute of Standards & Technology: 2003.
(193) Hooth, C. H.; Bridges, F., *Physica Scripta* 2005, (T115), 202.
(194) Goux, A.; Pauporte, T.; Lincot, D., Oxygen reduction reaction on electrodeposited zinc oxide electrodes in KCl solution at 70 [degree sign]C. *Electrochimica Acta* 2006, 51, (15), 3168-3172.
(195) Wang, F.; Liu, R.; Pan, A.; Cao, L.; Cheng, K.; Xue, B.; Wang, G.; Meng, Q.; Li, J.; Li, Q.; Wang, Y.; Wang, T.; Zou, B., The optical properties of ZnO sheets electrodeposited on ITO glass. *Materials Letters* 2007, 61, (10), 2000-2003.
(196) Kossel, W., *Zur Theorie des Kristallwachstums, Nachr.* ed.; Ges. Wiss. Götingen: 1927.
(197) Stranski, Zur Theorie des Kristallwachstums, Nachr. *Z. Phys. Chem* 1928, A136, 259-278.
(198) Burton, W. K.; Cabrera, N.; Frank, F. C., The Growth of Crystals and the Equilibrium Structure of their Surfaces. *Philosophical Transactions of the Royal Society of London. Series A, Mathematical and Physical Sciences* 1951, 243, (866), 299-358.
(199) Govender, K.; Boyle, D. S.; Kenway, P. B.; O'Brien, P., Understanding the factors that govern the deposition and morphology of thin films of ZnO from aqueous solution. *Journal of Materials Chemistry* 2004, 14, (16), 2575-2591.
(200) Vayssieres, L.; Keis, K.; Hagfeldt, A.; Lindquist, S. E., Three-Dimensional Array of Highly Oriented Crystalline ZnO Microtubes. *Chem. Mater.* 2001, 13, (12), 4395-4398.
(201) Teobaldi, G., Adsorption of organic molecules on gold electrodes
JOURNAL OF PHYSICAL CHEMISTRY C. *Journal of physical chemistry. C* 2007, 111, 13879-13885.

9. Appendix: 3D schematic views and technical drawings of in-situ GIXS cell

9.1 Reservoir and Cover

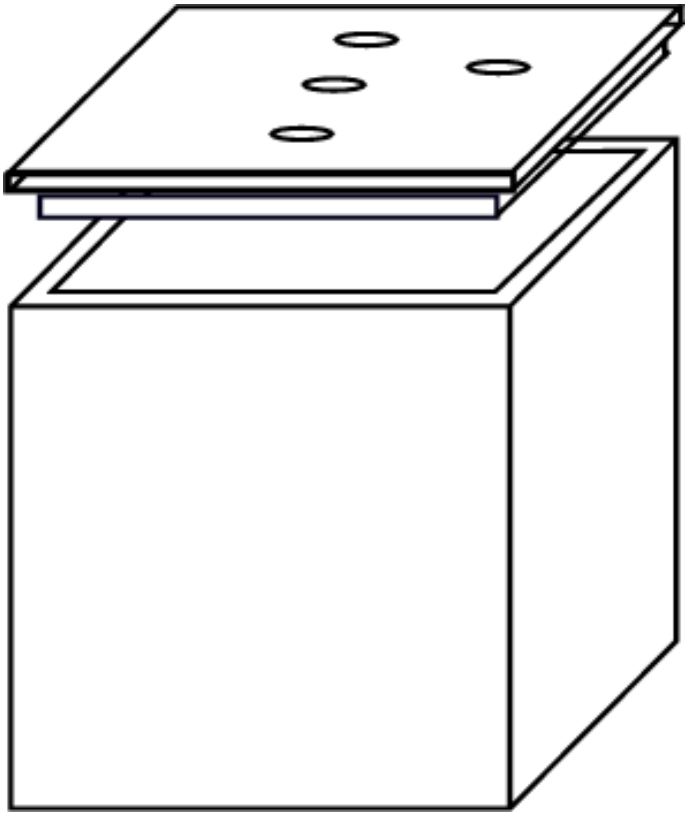


Figure 9.1 3D schematic view of the reservoir and its cover.

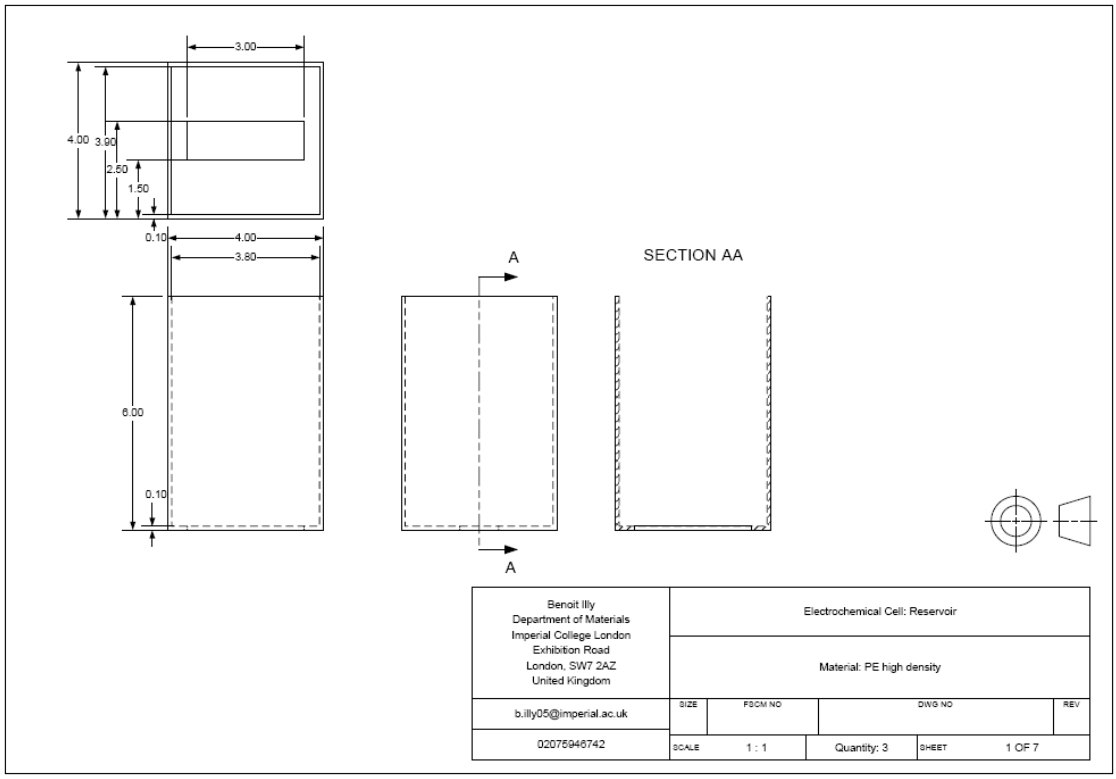


Figure 9.2 Technical drawing of the reservoir.

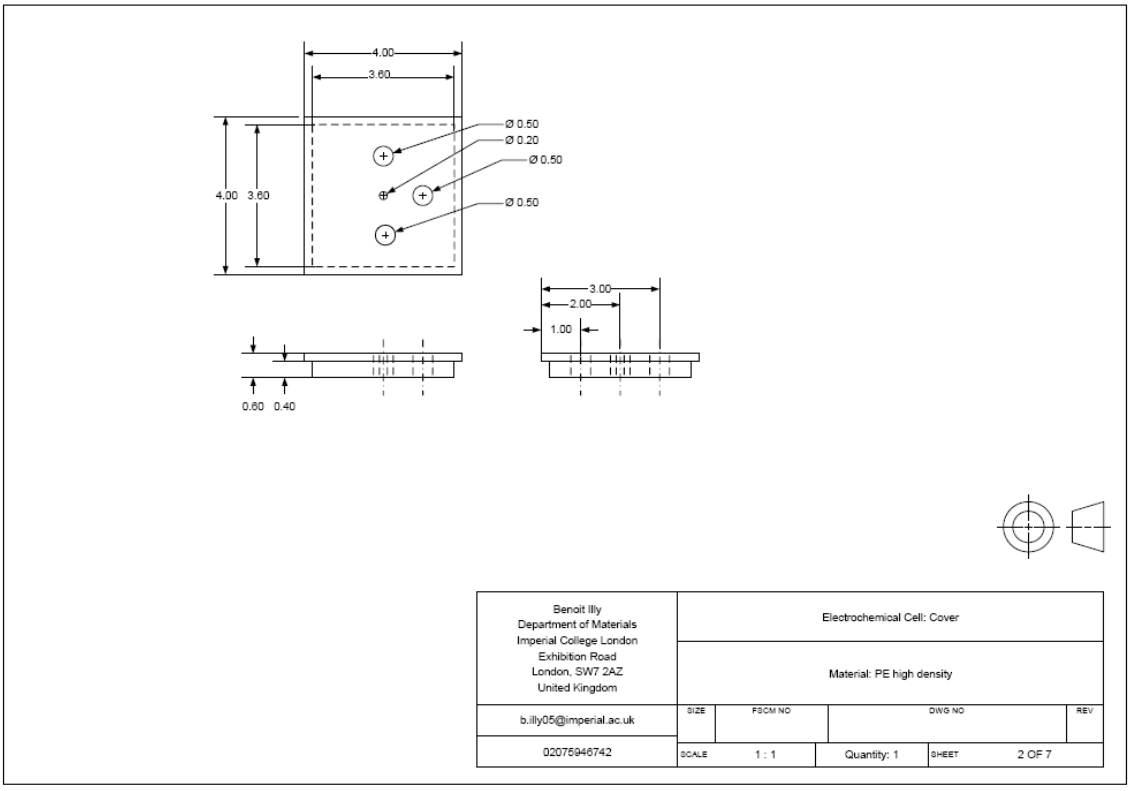


Figure 9.3 Technical drawing of the cover.

9.2 Kapton and Sample Holders

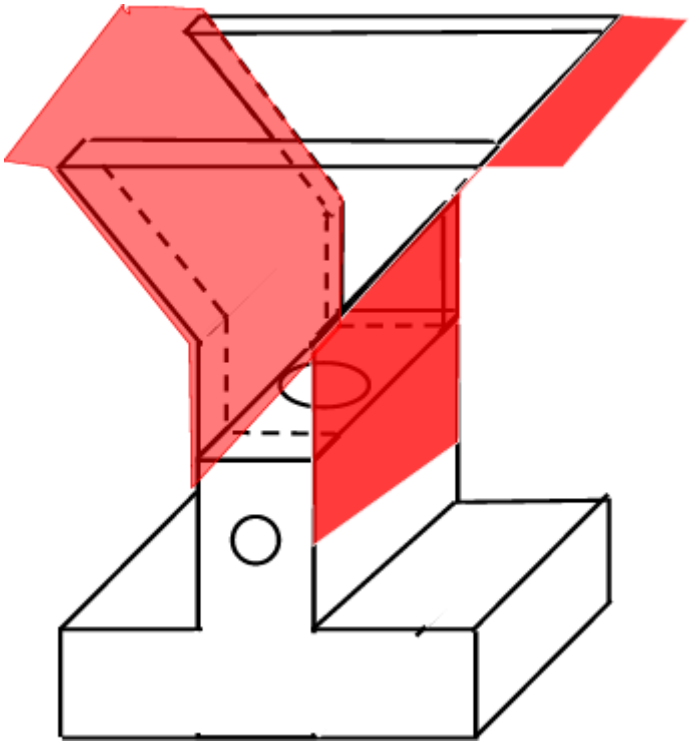


Figure 9.4 3D Schematic views of the Kapton and sample holders.

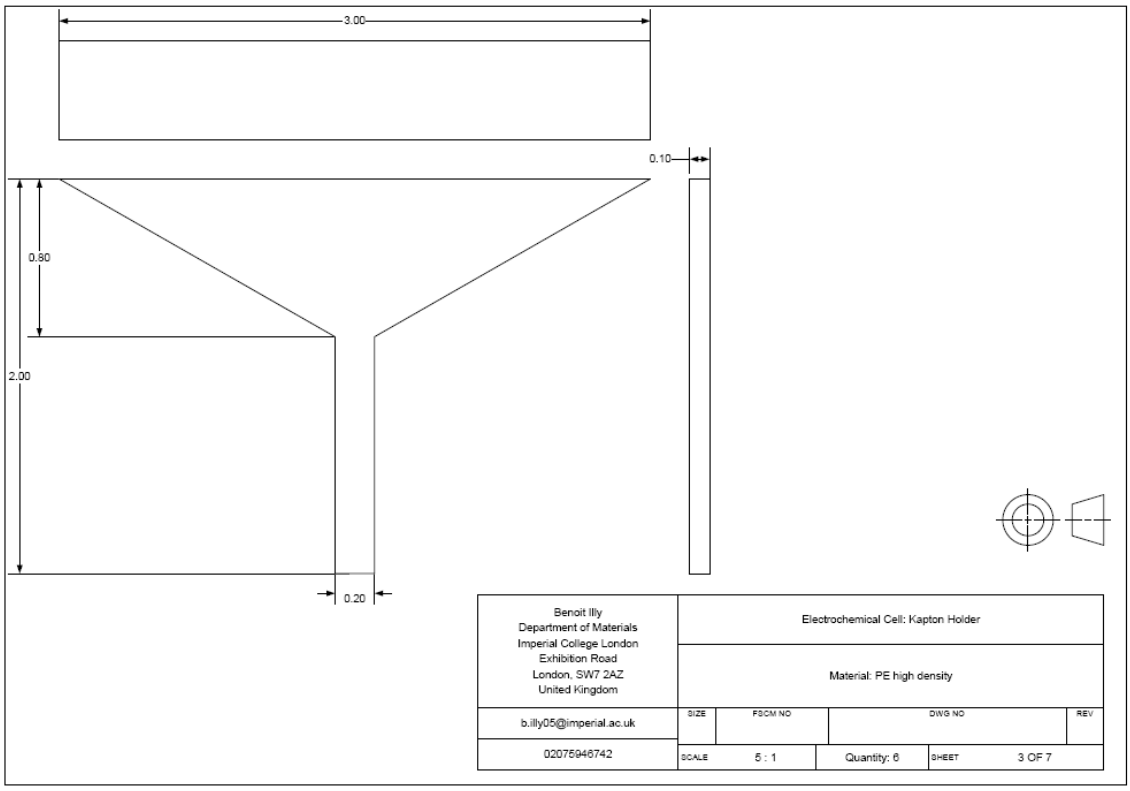


Figure 9.5 Technical drawing of the Kapton holder.

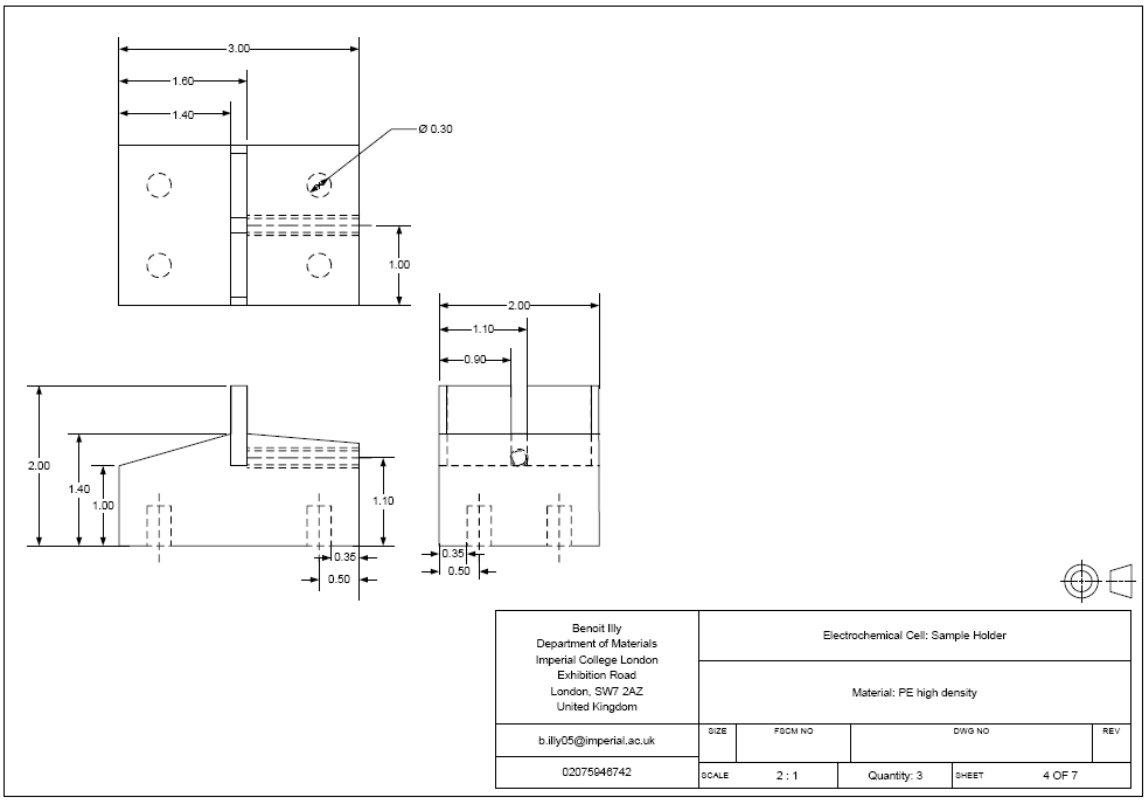


Figure 9.6 Technical drawing of the sample holder.

9.2 Heating System

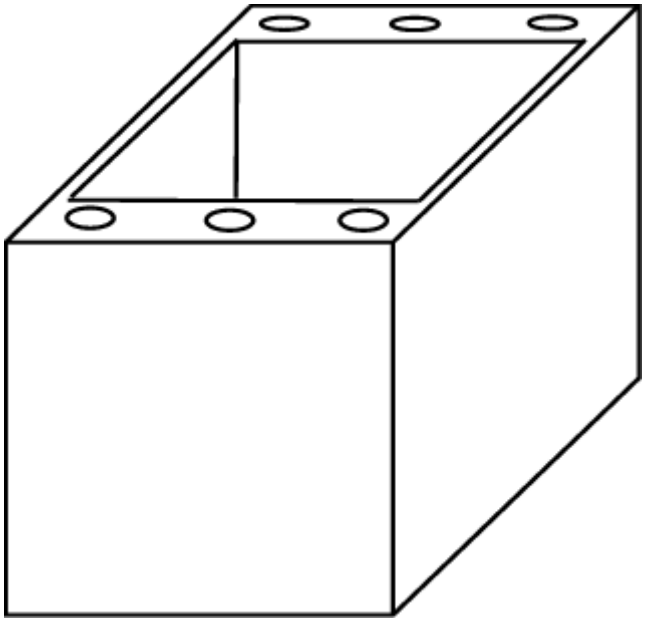


Figure 9.7 3D schematic view of the heating system.

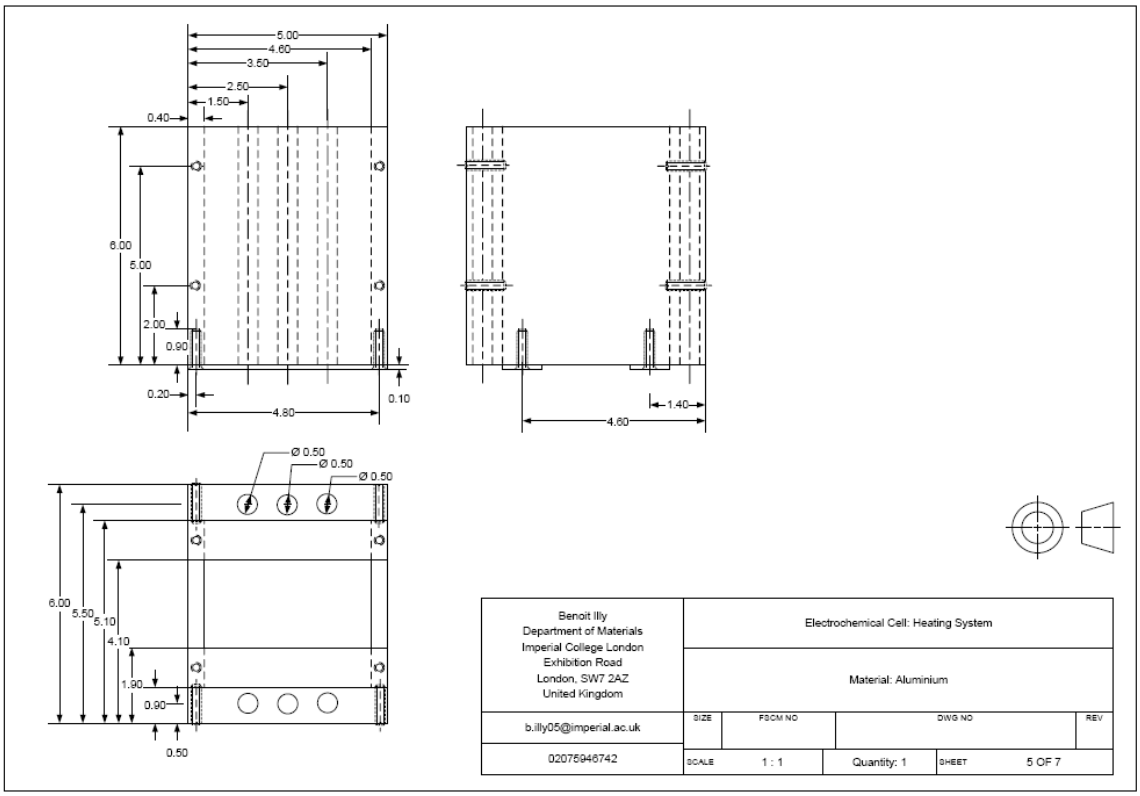


Figure 9.8 Technical drawing of the heating system.

9.3 Cell Support

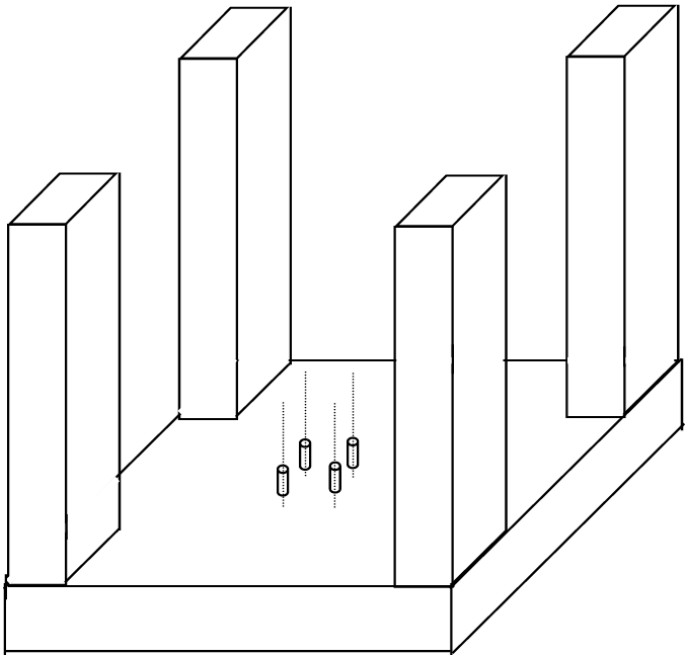


Figure 9.9 3D Schematic view of the cell support.

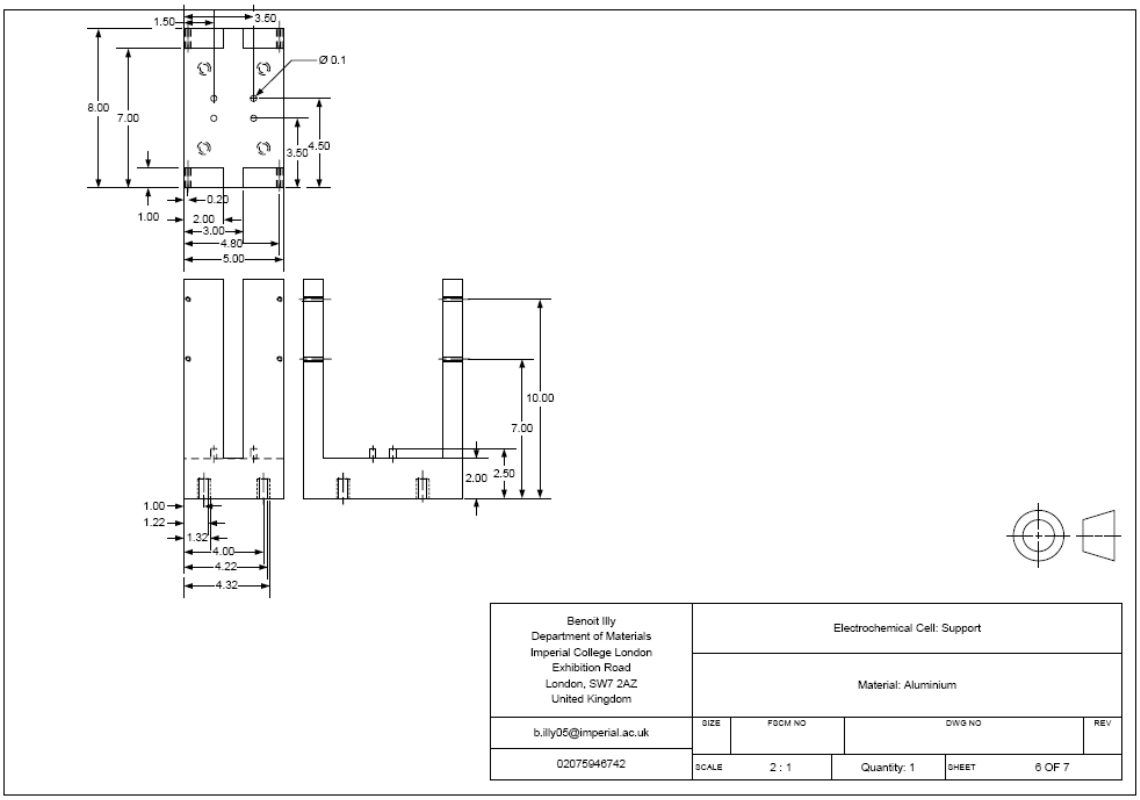


Figure 9.10 Technical drawing of the cell support.